PhD-FSTC-2018-17
The Faculty of Sciences, Technology and Communication

DISSERTATION

Defence held on 20/02/2018 in Luxembourg

to obtain the degree of

DOCTEUR DE L'UNIVERSITÉ DU LUXEMBOURG

EN PHYSIQUE

by

Erika ROBERT

Born on 20 July 1990 in Grenoble (France)

INVESTIGATION OF THE $CU_2(SN,GE)S_3$ TERNARY ALLOY FOR THIN FILM SOLAR CELLS

Dissertation defence committee

Dr Phillip DALE, dissertation supervisor
Associate Professor, Université du Luxembourg

Dr Jessica DE WILD
Researcher, IMEC Belgium

Dr Jan LAGERWALL, Chairman
Professor, Université du Luxembourg

Dr Edgardo SAUCEDO
Researcher, IREC Barcelona

Dr Daniel ABOU-RAS, Vice Chairman
Private lecturer, Helmholtz-Zentrum Berlin

Acknowledgements

First and foremost I would like to thank my PhD supervisor, Phillip Dale, who supported me during the four years of my PhD in the Laboratory of Energy Materials. His guidance, regular feedback and share of ideas were valuable, particularly when exploring a new material.

I would also like to thank Susanne Siebentritt for her active help in organising my return to the University of Luxembourg as well as her support as leader of the Laboratory of Photovoltaics group for all the time being.

Moreover, I would also like to express my gratitude to my PhD defence committee including Phillip Dale, as well as Jessica de Wild, Daniel Abou-Ras, Edgardo Saucedo and Jan Lagerwall, for their dedication and effort in ensuring my PhD studies.

Jessica de Wild has been the 'other half' of the project for three years as a postdoctoral researcher. She is deeply thanked for her positive suggestions, support and contributions.

I gratefully acknowledge the funding grant from the Fonds National de la Recherche under the agreement C13/MS/5898466, that made my PhD work possible, allowing visits to several international conferences and collaborations with various institutes and universities across Europe, contributing to the enhancement of the knowledge on the 'CTGS' materials.

In particular, I am grateful to Susan Schorr, Daniel Abou-Ras and their respective teams for welcoming me during my visits at the Helmholtz-Zentrum in Berlin. Hereby, I want to thank René Gunder for the patience, email support and assistance with the X-ray characterisation.

I would also like to thank Levent Gütay, Alex Redinger, Robert Treharne and João Malaquias for the deposition of different metal precursors via sputtering and electrodeposition in Oldenburg, Berlin, Liverpool and Leuven. At the University of Luxembourg, Ludger Wirtz and Henrique Miranda are deeply acknowledged for their calculations of Raman modes as well as their general guidance and manuscript reviews.

This PhD could not be today, without the cooperation of a big international family of solar cell scientists at the University of Luxembourg in the Laboratory of Energy Materials and Photovoltaics groups. Numerous discussions, suggestions, weekly group meetings in a friendly atmosphere.

I want to thank again those of you I have not already mentioned who contributed to this work, still members, or previous group members:

- Maxime Thevenin and Michele Melchiorre for their careful sample analysis at the microscope and device finishing,
- Hossam Elanzeery for performing the electrical measurements,
- Conrad Spindler and Finn Babbe for performing the photoluminescence measurements and the discussions and advice which followed,
- Alexandre Crossay for the guidance with the electrodeposition and the old oven at the start of the project,
- Diego Colombara for the valuable and comprehensive scientific advice, ideas, and writing skills. A source of inspiration!
- Fang Fang Wu and Daniel Siopa for the annealing rounds and the quest for tin (!),
- Erwin Reiter for performing some Raman measurements on CGS in the frame of his bachelor project.

Brahime El Adib and Constance Toulouse from the Luxembourg Institute of Science and Technology are also acknowledged for their help with the Raman setup and measurements together with Mael Guennou for his valuable advice on the matter. Thanks to Nathalie Valle for the SIMS measurements and Yves Fleming together with Inmaculada Peral Alonso for the last minute advice and help regarding the X-ray diffraction.

Huge thanks to Thomas Schuler, our Professor, and Patricia Ramoa for their proactive and endless support in technical as well as administrative matters.

Special thanks also go to the ones that did not only share work meetings and discussions but time outside work, in particular, I will mention the initiators: Connie, Sara, Jo and Alex. And the dear officemates of the best-office-in-the-world for the past five years!
’A l’amitié!’

Finally, I want to thank the eternal outside-of-work moral support, which gives me strength for the rest: my family, my international friends from the University and outside (the rock climbers, hikers, runners, musicians..) for the great times in Luxembourg and around the world.

Villmols merci!

Table of Contents

Abstract

This thesis examines material properties of the novel $Cu_2(Sn,Ge)S_3$ alloy, from the perspective of a solar cell scientist searching for a new light absorbing material to produce highly efficient thin-film devices.

The main part of this thesis is divided into 4 chapters describing the facile production of thin films of Cu_2SnS_3 and Cu_2GeS_3 materials **(i)**, the better light-emitting properties and reduced disorder of the material when synthesised at temperatures above 500°C **(ii)**, the bandgap tuning of Cu_2SnS_3 to the optimum spectral region of 1.1 to 1.4 eV by alloying with 30 to 70% of Ge **(iii)**, the low solar cell performance of device completed from absorbers grown at temperatures above 500°C, attributed to large bulk and interface recombinations of photogenerated charge carriers **(iv)**.

(i) Single phase Cu_2SnS_3 and Cu_2GeS_3 films of copper and sulphur-poor compositions can be prepared with a simple two-step synthesis route, which only requires the annealing of thin copper films in vapours of chalcogen, S, and group IV chalcogenide, SnS or GeS. Both species are important, together with a reduced background pressure, to prevent decomposition of the semiconductor and the segregation of secondary phases.

(ii) The structure of Cu_2GeS_3 films is studied with X-ray diffraction and photoluminescence, as a function of the annealing temperature. As in Cu_2SnS_3, a low-temperature structure (cubic) and a higher temperature structure (monoclinic) are identified where the latter is the most ordered, with a larger bandgap and higher luminescence yield. Novel Raman signature of the cubic material is recorded, which together with calculations of phonon modes in monoclinic Cu_2GeS_3 allow to confirm the predominance of the monoclinic structure at temperatures above 500°C.

(iii) Single phase $Cu_2(Sn,Ge)S_3$ films of various Ge compositions are produced at annealing temperatures above 500°C. Their lateral and in-depth uniformity allows to study structural and electronic properties as function of the Ge content, with Le Bail refinement of X-ray data and photoluminescence. The films are also measured to be p-type, but show however a high hole concentration of about 10^{18} cm^{-3}, around two orders of magnitude too high compared to high efficient record devices.

(iv) Cu_2SnS_3 and Cu_2GeS_3 absorber layers are completed into solar cell devices, where modelling of external quantum efficiency spectra demonstrate low minority carrier diffusion lengths space-charge region widths, as suggested by the high doping values. A depth-gradient is engineered in $Cu_2(Sn,Ge)S_3$ from which a device power conversion efficiency of 2.9% is obtained.

Work done in collaboration with others

The work presented in this thesis was carried out by the author, with the following exceptions:

1. The Mo-coated soda-lime glass (SLG) substrates were provided by Maxime Thevenin or Dr. Michele Melchiorre (University of Luxembourg). The Mo was sputtered on SLG.
2. The Cu-Sn precursor stacks sputtered on Mo-coated SLG and used in Chapters 4 and 7 were provided by Dr. Alex Redinger (Helmholtz Zentrum Berlin).
3. The Cu-Sn-Ge containing precursors sputtered on Mo-coated SLG used in Chapter 6 were provided by Dr. Robert Treharne (University of Liverpool) and Dr. Levent Gütay (University of Oldenburg).
4. The Cu-Sn-Ge precursors electrodeposited from an organic solvent on Mo-coated SLG and used in Chapter 4 were provided by Dr. João Malaquias (KU Leuven).
5. Copper was directly coated on SLG by Dr. Jessica de Wild (University of Luxembourg) with a wet-chemical method, allowing to perform transmission measurements on Cu_2GeS_3 films in Chapter 5.
6. All scanning electron microscopy (SEM) measurements (cross-sections/EDX/WDX) were performed either by Maxime Thevenin, Dr. Michele Melchiorre, Dr. Jessica de Wild or Daniel Siopa (University of Luxembourg).
7. Photoluminescence (PL) measurements presented in Chapter 5 were performed by Dr. Jessica de Wild. Measurements presented in Chapter 6 were performed by Conrad Spindler and Finn Babbe. All were done at the University of Luxembourg.
8. Depth-resolved grazing incidence X-ray diffraction (GI-XRD) measurements presented in Chapter 6 were performed in the X-ray CoreLab (Helmholtz Zentrum Berlin) with the help of René Gunder. The other GI-XRD measurements were performed by the author within the Luxembourg Institute of Science and Technology (LIST).
9. The Raman measurements presented in Chapter 5 were performed by the student Erwin Reiter and the ones in Chapter 6 by Brahime El Adib (LIST).
10. The theoretical phonon modes in $Cu_2(Sn, Ge)S_3$ presented in Chapters 5 and 6 were calculated by the theoretical physicists Dr. Henrique Miranda and Dr. Ludger Wirtz (University of Luxembourg).

11. The capacitance-voltage (CV) measurements presented in Chapter 6 were performed by Hossam Elanzeery (University of Luxembourg).
12. The secondary ion mass spectroscopy (SIMS) measurement presented in Chapter 7 was performed by Dr. Nathalie Valle (LIST).
13. The CdS buffer, ZnO window layers and front contacts Al:ZnO and Ni:Al grids for device finishing in Chapter 7 were deposited either by Maxime Thevenin or Dr. Michele Melchiorre (University of Luxembourg) by chemical bath deposition (CBD), sputtering and evaporation methods, respectively.

The evaluation of all results was carried on by the author.

List of publications

Here follows the list of publications that were generated during the course of this PhD project:

U. Berner, D. Colombara, J. de Wild, **E.V.C. Robert**, M. Schütze, F. Hergert, N. Valle, M. Widenmeyer and P. J. Dale, ”13.3% efficient solution deposited $Cu(In,Ga)Se_2$ solar cells processed with different sodium salt sources” in *Progress in Photovoltaics, Research and Applications*, 24(6): 749-759, 2015

E.V.C. Robert, J. de Wild and P. J. Dale ”Cu_2SnS_3-based thin film solar cell from electrodeposition - annealing route” in *IEEE Proceedings 42nd*, 15664737, 2015

E.V.C. Robert, J. de Wild and P. J. Dale ” Reaction chemistry of group IV containing copper chalcogenide semiconductors Cu_2MX_3 (M = Sn,Ge and X = S,Se)” in *Journal of Alloys and Compounds*, 695: 1307-1316, 2016

J. de Wild, **E.V.C. Robert**, B. El Adib, D. Abou-Ras and P. J. Dale ”Secondary phase formation during monoclinic Cu_2SnS_3 growth for solar cell application” in *Solar Energy Materials and Solar Cells*, 157: 259-265, 2016

E.V.C Robert, J. de Wild, D. Colombara and P. J. Dale ”Crystallographic and optoelectronic properties of the novel thin film absorber Cu_2GeS_3” in *Proceedings of SPIE 9936*, Thin Films for Solar and Energy Technology VIII, 993607, 2016

J. de Wild, E. Kalesaki, **E.V.C Robert** and P. J. Dale, ”Quantum efficiency measurements and modelling to monitor air annealing of Cu_2SnS_3 solar cells” in *IEEE Journal of Photovoltaics*, 7(1): 268-272, 2016

H. Elanzeery, F. Babbe, M. Melchiorre, **E.V.C. Robert**, A. Zelenina and S. Siebentritt ”Potassium fluoride ex-situ treatment on both Cu-rich and Cu-poor $CuInSe_2$ thin film solar cells” in *IEEE Journal of Photovoltaics*, 7(2): 684-689, 2017

J.C. Malaquias, M. Wu, J. Lin, **E.V.C. Robert**, J. Sniekers, K. Binnemans, P.J. Dale and J. Fransaer ”Electrodeposition of germanium-containing precursors for $Cu_2(Sn,Ge)S_3$ thin film solar cells” in *Electrochimica Acta*, 251: 651-659, 2017

J. de Wild, F. Babbe, **E.V.C Robert**, A. Redinger and P. J. Dale, ”Silver doped Cu_2SnS_3 absorber layers for solar cell applications” in *IEEE Journal of Photovoltaics*, 8(1): 299-304, 2017

E.V.C. Robert, R. Gunder, J. de Wild, C. Spindler, F. Babbe, H. Elanzeery, B. El Adib, R. Treharne, H. P.C. Miranda, L Wirtz, S. Schorr and P. Dale, ”Synthesis, theoretical and experimental characterisation of thin film $Cu_2Sn_{1-x}Ge_xS_3$ ternary alloys ($x = 0$ to 1): homogeneous intermixing of Sn and Ge” in *Acta Materialia*, 151, 125-136, 2018.

CHAPTER 1

Introduction

In 2016 the primary energy consumption for electricity generation reached 13.3 gigatonnes of oil equivalent, representing an increase of 20% over the past decade [1]. 85% of the consumed energy comes from the burning of fossil fuels (oil, natural gas and coal) which emits carbon dioxide, CO_2, and other greenhouse gases and therefore drives global warming and climate change. Further economic and population growth are predicted to double the world's energy demand by 2040 [2], likely accelerating the finite fossil fuel use. To solve the energy crisis, a radical energetic transition from fossil fuels to renewable energies is mandatory. The most powerful clean energy source available is the sun which provides at noon each day about 1000 Watts per meter squared on the Earth. By its power, the sun drives the climate system on Earth and makes it hospitable for life. Harnessing its energy could feed the rising demand. The harnessing of sunlight and its conversion into electrical power is done by means of solar cells and described as 'photovoltaics'. The solar cells contain several semiconductors with stringent material properties, in general, two: one which absorbs the light and the other which is there to allow separation of the photogenerated charge carriers and current extraction. Such solar cells already exist but further improvement would consist in finding the optimal absorbing semiconductor material: one that is both Earth-abundant and economically competitive. In this thesis $Cu_2(Sn, Ge)S_3$ is investigated as a candidate material for thin film solar cells. This chapter aims to provide an introduction to thin film solar cells and a literature review on $Cu_2(Sn, Ge)S_3$ at the start of this work. Finally, the research questions are outlined and an overview of the thesis is given.

Why thin film photovoltaics?

Nowadays the photovoltaic market is dominated by crystalline silicon (c-Si)-based solar cells which can transform around 26% of the incoming photon energy into usable electrical energy [3]. But their high manufacturing costs, toxic waste, as well as handling issues bring researchers to think about other possible material options.

Inorganic thin film solar cells based on semiconductor materials with direct bandgaps are thinner than c-Si wafer cells and thus have lower processing costs. Their reduced thickness of around 2 microns allows more flexibility and thus offers more variability for terrestrial and spatial applications in photovoltaic modules. Thin film solar cells consist of a p-n junction where the p-type doped layer is described as the 'absorber layer', which as its name suggests should absorb most of the solar spectrum illuminating the cell. The n-type doped material completes the junction and device finishing is done by addition of electrical contacts around the junction. Thin film photovoltaics is seen as a promising field for future energy needs, [4, 5] with the p-type CdTe and ternary alloy $Cu(In, Ga)Se_2$ (CIGSe) as absorber layers, reaching device power conversion efficiencies up to 22.9% [6, 7]. Fig. 1.1 shows the abundance of common chemical elements used for thin film solar cells in the Earth's crust and their market price. As shown in Fig. 1.1 the scarcity of Te is predicted to lead to a material shortage of CdTe, bringing inevitably to the search of other compounds, preferably based on Earth-abundant elements [4, 8].

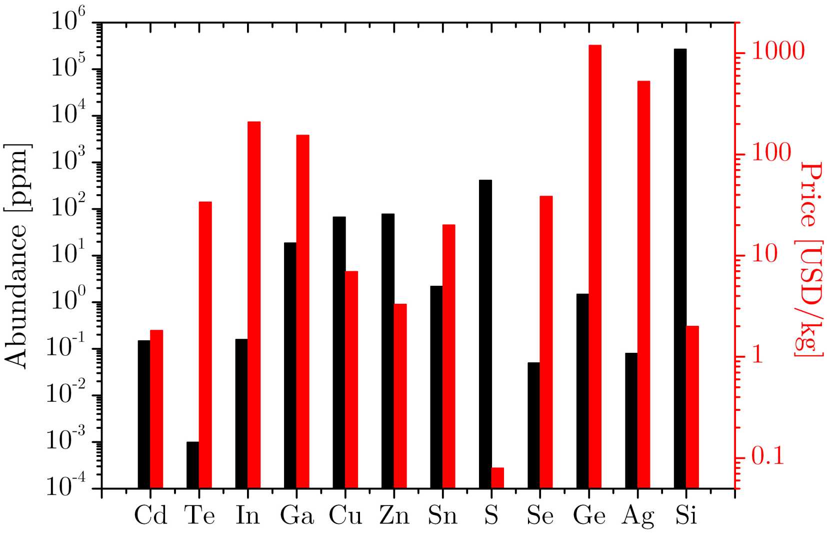

Figure 1.1: Abundance in the Earth's crust [9] and market price of common chemical elements used for thin film solar cells (prices from October 2017 for Cu, Sn, Zn and Ag [10] or averaged over the year 2016 for the other elements [11, 12]).

Alternative earth-abundant Cu-based materials for thin film photovoltaics

Despite being one of the market leaders, CIGSe thin films contain the expensive indium In and Ga elements, as shown by current market prices in Fig. 1.1. The optimal situation would be to find an alternative p-type semiconductor compound with Earth-abundant and cheaper elements that also could produce efficient solar cell devices. CIGSe is a ternary alloy obtained by alloying $CuInSe_2$ (CISe) with Ga, thus substituting part of the In atoms by Ga.

Fig 1.2 shows the derivation of CIGSe from the structure of pure Si (diamond). Starting from Si, a family of compounds is obtained by isoelectronic exchange of the chemical elements with respect of the octet rule. Fig 1.2 presents two units cells of Si on top of each other. The unit cell of Si is cubic with each Si atom (4 valence electrons) bonded to four other Si atoms, thus respecting the octet rule. The zinc blende structure (CdTe (II-VI) and GaAs (III-V)) is obtained by replacement of the Si atoms by charged ions, keeping the tetrahedral coordination. Goodman [13] and Parthe [14] have shown that families of multinary compounds can be predicted by isoelectronic ion cross-substitution in the zinc blende structure, also shown in Fig. 1.2. This cross-substitution maintains an average number of four valence electrons per atomic site. Additionally, each anion is bonded to four cations and each cation to four anions.

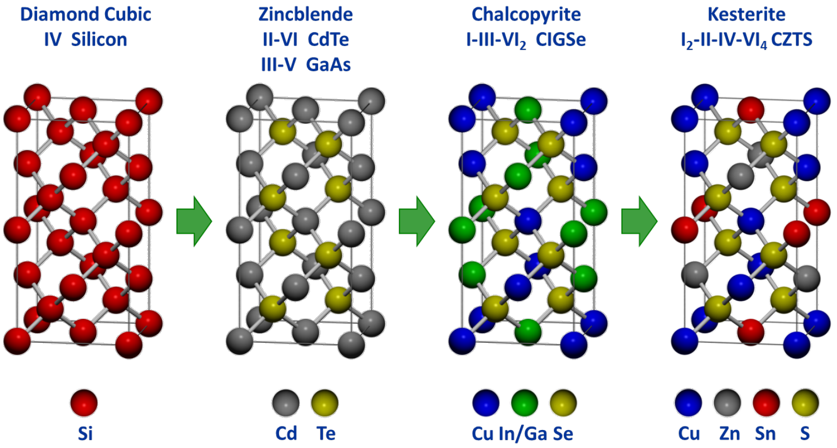

Figure 1.2: Ion cross-substitution in the zinc blende structure produces the chalcopyrite (CIGSe) and kesterite (CZTS) crystals. The anions are shown in yellow, the cations in grey, blue, green and red. Figure reproduced from [15].

The derivations of the CISe and CZTS multinary compounds are also presented in Fig. 1.2, by cross-substitution of ions in the zinc blende structure of CdTe. Cation cross-substitution is done by replacing the four Cd atoms in the zinc blende structure (group II) by two atoms of Cu (group I) and two of In (group III). The Te anions are replaced by Se anions. When the two In atoms in CISe are further replaced by one Zn atom (group II) and one Sn atom (group IV), one obtains the quaternary compound CZTS. CZTS is composed of the cheaper and earth-abundant tin, Sn, and zinc, Zn, elements, together with sulphur, S, as shown in Fig. 1.1.

The quaternary CZTS is a p-type semiconductor material with a direct bandgap E_G of about 1.45 eV and a high absorption coefficient of $10^4\,\mathrm{cm}^{-1}$ [16] at the conduction band edge which is sufficient for the film to be incorporated into thin film solar cell devices as a two micron thick layer. However, CZTS has many drawbacks in its properties which make it difficult to track down the main culprit currently limiting the device efficiencies to below 13% [17]. These properties include the difficulty to grow single phase material due to the high number of constituent elements leading to a large number of possible secondary phases, the different possible arrangements of the Cu and Zn cations in lattice planes and various deep defects [18–20]. As an alternative to finding the main culprit, one could just attempt to reduce the number of drawbacks and thus research a new ternary compound that only contains Earth-abundant elements.

The $Cu_2(Sn,Ge)S_3$ alloy as thin film absorber candidate for solar cells

A new ternary semiconductor compound based on Earth-abundant elements can be constructed from the quaternary CZTS under Zn-poor conditions. The resulting I_2-IV-VI_3 ternary compound is Cu_2SnS_3 (abbreviated as CTS), poorly investigated at the start of this thesis but suggested to be the most suited for photovoltaic applications, among all other Cu-Sn-S ternary compounds [21]. However, first material evaluations have suggested it could be a good light-harvesting semiconductor with a light absorption coefficient in the order of 10^4 cm^{-1} [22] and a direct bandgap, E_G, with an energy in the optimal range for photovoltaic cells [23]. The optimal range for the cells is defined by the calculations of Schockley and Queisser [24] on the maximum device efficiency reachable for a p-n junction device, as a function of E_G, as shown in Fig. 1.3. The absorption lines in the solar spectrum 'AM1.5G' used to compute the Schockley-Queisser limit (SQ) lead to the presence of two close maxima: 33% for E_G = 1.35 eV and 32.8% for E_G = 1.15 eV [25]. The cell record efficiencies for c-Si, GaAs, CdTe, CZTSSe and CIGSe-based devices are also reported in Fig. 1.3. Alloying CISe with Ga (in CIGSe) is feasible because In and Ga belong to the same group III of the periodic table so the number of valence electrons in the bonds is maintained by the replacement. The latter allows to tune E_G between about 1.0 eV in CISe to 1.6 eV in pure CGSe, as highlighted by the red dotted line. The region highlighted in pink in Fig. 1.3 presents the bandgap values for which one could ideally obtain the highest efficiencies.

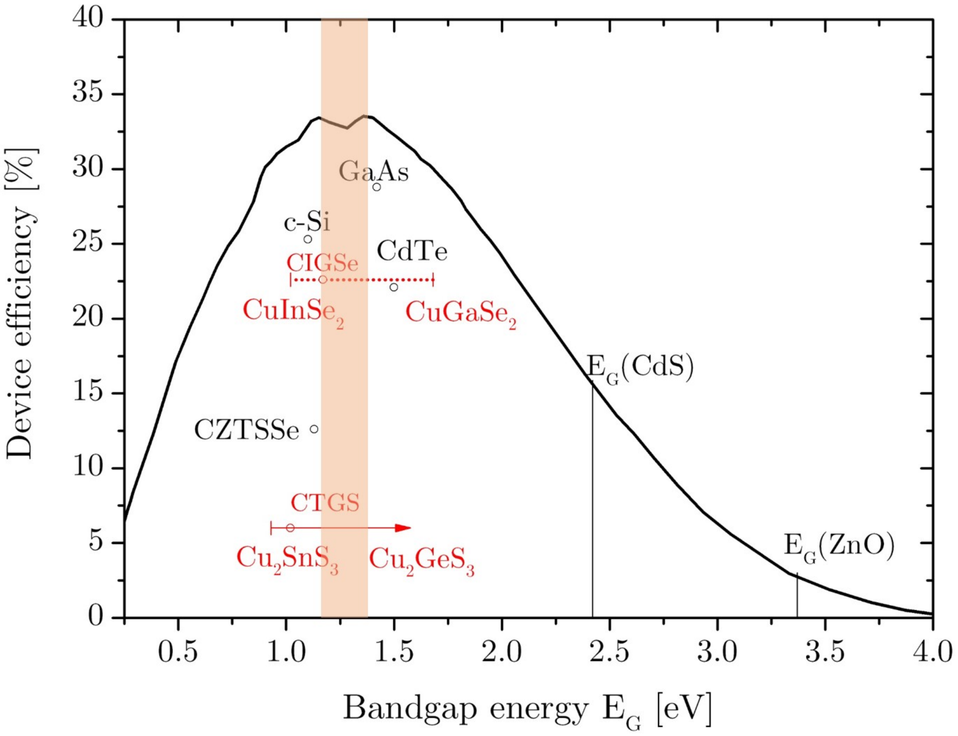

Figure 1.3: Maximum device efficiency calculated by Schockley and Queisser and reported in [5] for single p-n junction devices, as a function of the bandgap, E_G, of the p-type absorber layer. The highest efficiencies are reported with dots for c-Si-, GaAs-, CdTe- and CZTSSe-based devices. The two ternary alloys CIGSe and CGTS are also reported and the pink region represents the bandgap values that could lead to the highest efficiencies in the SQ limit. The bandgap energies of the standard top layers in solar cells, CdS and ZnO, are also shown.

One sees that the CIGSe alloy with current best efficiency (shown with the dot along the dotted line) lies in this optimum bandgap region. The best CTS-based p-n junction devices had demonstrated device efficiencies up to 2.84% [26] at the start of this work. All devices presented have the same typical device structure used for CIGSe, and presented in Fig. 1.4 as applied to CTGS, namely: Mo/CTS/CdS/i:ZnO/Al:ZnO/Ni:Al. The cadmium sulphide layer, CdS, is the n-type layer of the p-n junction, deposited by chemical bath onto the CTGS absorber layer [27]. The electrical contacts are made of molybdenum, Mo, at the back, sputtered onto a soda-lime glass (SLG) substrate [28] and n-type zinc oxide, ZnO, as front contact, sputtered on top of the CdS buffer layer. The bandgaps of CdS and ZnO are large enough to be transparent to the lower energy photons, as seen in Fig. 1.3. Ni:Al grids are then deposited by e-beam evaporation onto the device.

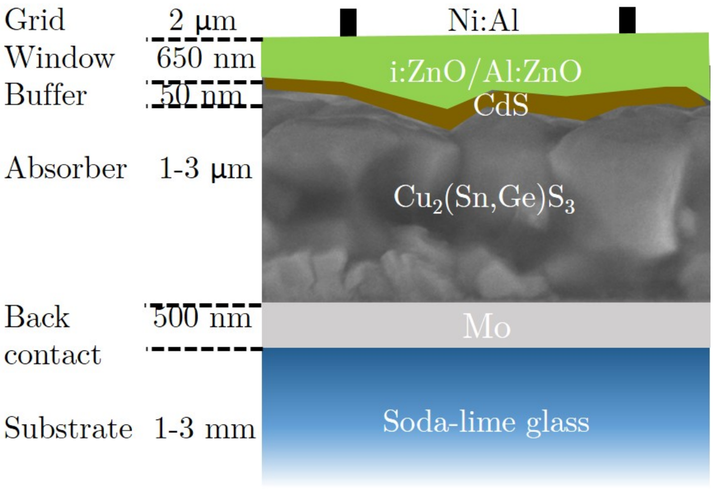

Figure 1.4: Typical structure of a CIGSe-based solar cell in substrate configuration, where here the $Cu_2(Sn,Ge)S_3$ absorber replaces the CIGSe absorber. All solar cell layers are shown with their average thicknesses. i:ZnO indicates intrinsically doped ZnO and Al:ZnO is ZnO doped with Al.

The highest performance is obtained for a CTS absorber alloyed with 17% germanium [29] (CTGS), as also seen in Fig. 1.3. Ge is one of the most expensive elements in thin-film photovoltaics as it can be noticed in Fig. 1.1 but it belongs to the group IV of the periodic table like Sn. There could be compromises to make between expenses and device performance, as for CIGSe, if alloying with Ge was also producing very good CTS devices. The addition of Ge to CTS appears to increase the bandgap above 1 eV in a similar way to Ga in CIGSe, and highlighted by the red arrow in Fig. 1.3.
The best device efficiencies η to be reported at the start of this work for pure CTS-based thin film devices and Ge-alloyed CTS are presented in Table 1.1 with respective device parameters: open circuit voltage V_{oc}, short-circuit current density J_{sc}, fill factor FF and bandgap energy E_G of the absorber layer, where η corresponds to the product of FF, J_{sc} and V_{oc} divided by incident light power. There was no report of a Cu_2GeS_3-based device at the start of this work. The CTS films of the reported devices were grown on Mo in very similar ways, from two-step approaches where Cu-Sn precursors (deposited on Mo via electrodeposition, sputtering or electron beam evaporation) are further annealed in sulphur atmosphere only (or both sulphur and germanium disulphide atmospheres [29]) at temperatures between 550 and 580°C.

At this stage, more emphasis was put on making devices with CT(G)S films than understanding material properties. The modest device efficiencies were due to both low current collection with J_{sc} of only a few mA, as well as a low V_{oc} compared to the bandgap energy $E_G \sim 1$ eV.

Absorber layer	Year	Reference	E_G [eV]	J$_{sc}$ [mA/cm^2]	V$_{oc}$ [mV]	FF [%]	η [%]
Cu_2SnS_3	2012	[30]	0.93	17	104	30	0.5
Cu_2SnS_3	2012	[26]	≤ 1	29	249	39	2.8
Cu_2SnS_3	2012	[22]	0.96-1.00	28	211	43	2.5
$Cu_2Sn_{1-x}Ge_xS_3$ $(x = 0.17)$	2013	[29]	1.02	30	355	56	6.0

Table 1.1: Some of the best device efficiencies reported for CTS at the start of this work, together with bandgap energies and device parameters. The absorber layer of the best CTGS-based device shows a bandgap E_G above 1 eV.

Since then, in 2015, CTS has reached a new record of 4.6% by alkali doping (NaF) of the CTS absorber layer [31]. However, knowledge of the material properties remains fairly low. The little literature available on the characterisation of CTS films reports conflicting bandgaps from 0.93 eV up to 1.35 eV [32, 33]. There is also the report of a metallic form of CTS [34]. Those differences in E_G were suggested to correlate to changes in the crystallographic structure, and vary with the synthesis method [35] but without much consensus. What is also unknown at the start of this work is E_G as function of the composition in Ge, starting from pure CTS, constituting one main research question of this thesis. This thesis thus aims to bring more understanding of CT(G)S properties.

Research questions and overview of this thesis

This thesis has the ambition of increasing the knowledge on the sulphide CTGS materials, which show very poor consensus at the start of this work as for any newly investigated materials. Previous research has shown CTGS films are good light harvesters able to produce working solar cell devices as p-type absorbers, but a better knowledge of material properties could help on deciding whether studies on the CTGS material are worth pursuing and how to carry on with further investigations to approach the Shockley-Queisser limit in future years. The next paragraphs describe the research questions and overview of the thesis, divided into eight chapters, of which four are result chapters.

Research questions

As demonstrated by the few CTS and CTGS absorbers at the start of this work, further completed into working p-n heterojunction devices with CdS, I am convinced that it is possible to form near-stoichiometric CT(G)S absorber layers by cost-efficient two-step synthesis methods, as also largely employed for CIGS and CZTS-based technologies. This two-step method involves the annealing of previously deposited metallic precursors, in a chalcogen vapour atmosphere.
To form CTGS alloys of various Ge compositions via an annealing step, I believe that a better knowledge of the reaction path and assessment of the vapour pressures of the elements are required. I hypothesise that the kinetics of vapour-solid (precursor) reactions within the annealing furnace are of huge importance and will act upon the final composition of the CT(G)S film. I wish to establish kinetics conditions that are sufficient to form films of uniform phase and com-

position that are reproducible from any type of precursor. In this topic I extend the study to the selenide compound Cu_2SnSe_3 (CTSe), which contrarily to Cu_2GeSe_3 [36, 37], shows despite a lower bandgap of about 0.8 eV [38, 39] a similar absorption coefficient to CTS and CGS [40, 41] and could also be of use for photovoltaic purposes, as bottom cell in tandem devices.

Multiple bandgaps are reported for CTS films and a careful literature analysis suggests they arise due to different synthesis conditions. I hypothesise that temperature is an important factor in the synthesis which could affect the crystallographic structure of CTS and thus its bandgap. A similar model is likely to exist for CGS. I wish to pursue this hypothesis by annealing films at different temperatures and study the resulting dominant crystallographic structure. If I can prove that one of the polymorphs shows better photovoltaic properties than another, I could reduce their study to a single crystallographic phase.

The most performing device reported at the time of writing is one based on a CTGS alloy with 17% of Ge, where Ge has been incorporated into the absorber during reactive annealing of precursors in the presence of a Ge-containing vapour. Therefore alloys could be formed by reactive annealing. However, the single composition formed does not necessarily mean a broad solution range of CTGS exists. Thus I wish to study the existence of the width of the solid solution which, if a larger range of alloys is shown to exist, would allow to build a library of structural and electronic properties of CTGS.

Finally, a high doping density of the material could affect the collection of charge carriers in a solar cell device, which instead of being collected to generate electrical current, are lost by recombination. I would like to check whether the performance of CTGS devices could be affected by high doping densities.

Overview of the thesis

The thesis starts in **Chapter 2** with a presentation of all the characterisation techniques that are of use within this work for compositional, morphological, crystallographic and optoelectronic analysis of the films and solar cell devices.
Chapter 3 describes the deposition methods of the precursors via electrodeposition and sputtering. Those films will be further annealed to form C(T,G)S. The chapter first explains the electrodeposition from aqueous electrolytes which has been used to deposit stacks of Cu and Sn on Mo substrates. It also describes the alternative physical method of sputtering used for developing various stackings of Ge-containing precursors. The chapter ends with a presentation of the possible alloys that might form in the Cu-Sn-Ge system at room temperature and/or during light pre-alloying.
Chapter 4 is dedicated to the study of the annealing of precursors inside the furnace where the kinetic conditions that are necessary to form CTS and CGS films that are uniform in composition are established, showing the importance of background pressure in this process, with dramatic effects when selenised CTSe films are prepared. In parallel, the chemical route to CTS and CGS formation is given. It is also shown that CTGS alloys of uniform composition are the most likely to be produced from Ge-containing precursors annealed in presence of group IV chalcogenide vapours.
Chapter 5 investigates the structural and electronic properties of Cu_2GeS_3 which in the model

of Cu_2SnS_3 also shows a transition from a disordered cubic phase to a more ordered monoclinic phase when annealed above 500°C. The bandgaps and Raman spectra of the cubic phase are reported for the first time. Photoluminescence measurements suggest the monoclinic phase is less defective than the cubic one.

The annealing route to form the monoclinic phase is therefore chosen for **Chapter 6** which deals with the compositional, crystallographic and electrical characterisation of films of the CTGS alloys. The chapter shows the rapid kinetics of Ge and Sn intermix in the precursor and the existence of a broad compositional range for CTGS solid solution. In-depth bandgap gradients as for well performing CIGS devices thus have to be engineered.

Chapter 7 presents the completion of $Cu_2Sn_{1-x}Ge_xS_3$ into devices and attempts to give a route to explain the large performance losses observed, starting from the high doping densities measured in Chapter 6. A 2.9% efficient device is produced from a depth-graded CTGS absorber.

Chapter 8 presents the conclusion of this work and suggestions for further research and progression.

CHAPTER 2

Characterisation techniques for thin films and solar cells

This chapter presents the theoretical background for all precursor, absorber and solar cell characterisation techniques used in this thesis. Precursor and absorber characterisation techniques are presented first, where the absorber is a semiconductor compound in the form of thin polycrystalline films. They cover in this order: composition, morphology, phase analysis, light absorption, doping density. The composition of CTGS was studied with **Energy Dispersive and/or Wavelength Dispersive X-ray spectroscopy (EDX/WDX)** whilst morphology was analysed with a **Scanning Electron Microscope (SEM)**. Finally, the structural phase analysis of the bulk material was performed with **X-ray diffraction (XRD)** whilst its surface was studied with **Raman spectroscopy**. Light absorption was measured with **Visible-NIR spectroscopy**. Estimation of net majority carrier doping densities in the absorber layer was carried out with **Capacitance- Voltage measurements (CV)**. In a second part, the solar cell characterisation techniques are presented: **Current density-Voltage (J-V)** curves followed by the **External Quantum Efficiency (EQE)**. Reference to the appropriate literature on the techniques is given in each subsection, together with specific details of measurements conditions employed.

2.1 Characterisation of precursor and absorber layer

2.1.1 Composition and morphology

Scanning electron microscopy

The scanning electron microscope (SEM) is a multi-functional tool widely used in material science for imaging and compositional analysis. This section gives an overview of the working principles of the SEM as applied to the study of thin films. It is described extensively in textbooks, [42, 43], to which the reader is referred for more information. The SEM makes use of an electron beam which can explore nanoscale material while visible light can only get down to resolutions of several hundreds of nm due to its larger wavelength range. An SEM therefore consists of a microscope column with an electron gun and a separate control console. The electron gun can accelerate electrons down the column to energies between 0.1 and 30 keV. The electron path crosses various lenses that are focusing the beam into a reasonably sharp beam of about 1 μm width. To create an image of the sample the beam is swept across the sample surface with a resolution defined by the beam size. The electron beam interacts with the sample in various ways as pictured in Fig. 2.1a). A scintillator detector measures the particles that are scattered out of the sample: secondary electrons (abbreviated as SE), Auger electrons, backscattered electrons deeper in the bulk (abbreviated as BSE) together with X-ray emission. For an image of the surface to be produced one looks most frequently at the emitted secondary electrons or backscattered electrons (abbreviated as SE and BSE, respectively). To get information about the surface morphology the detector can be oriented such as mostly SE are collected, which is possible since BSE follow more defined directions.

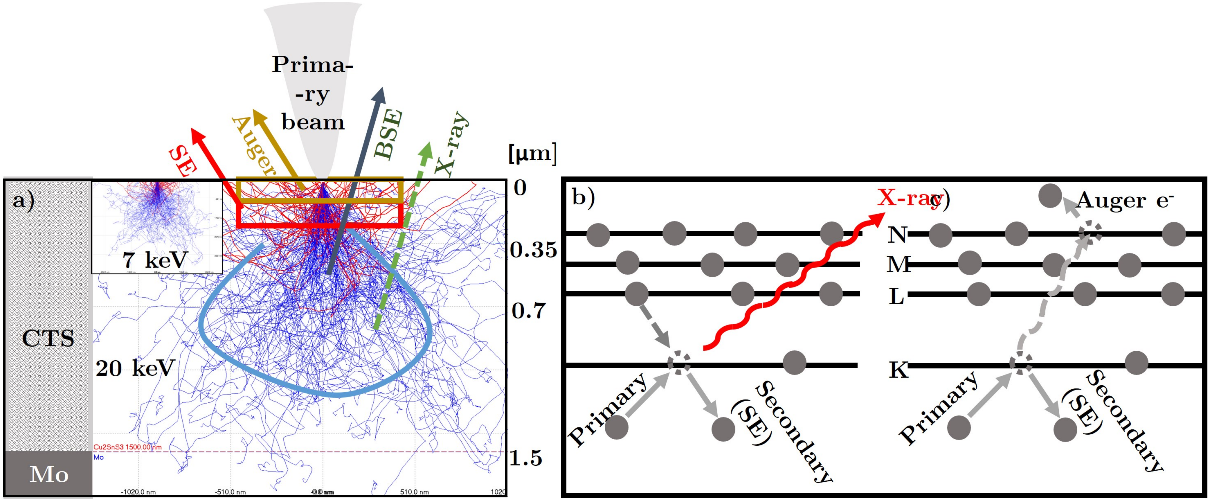

Figure 2.1: a) CASINO simulation [44] of the interaction of an electron beam of 20 keV with a thin Cu_2SnS_3 film of 1.5 microns deposited on a standard 500 nm thick Mo substrate. The trajectories of the scattered electrons in the first hundreds of nm are shown in red (i.e the secondary electrons (SE)) and deeper in blue (i.e the backscattered electrons (BSE),) leading to the emission of characteristic X-rays, from the volume of interaction defined by the blue solid line. Additionally, Auger electrons can also be emitted from the surface. The inset (shown to-scale) shows the respective beam-sample interactions for a primary electron beam of 7 keV. b) Schematic representation of the generation mechanism of X-rays, via interaction of the primary electron beam with electron shells (K, L, M...) in the sample. c) Schematic representation of the mechanism of generation of an Auger electron via similar interactions.

BSE that are beam electrons, scattered elastically by the sample, would be collected to get information on compositional contrasts, as the number of BSE depends on the atomic number Z of the atoms probed. As heavier atoms have larger scattering cross sections than lighter atoms, and thus emit more BSE, their measurement results in brighter spots in the final image. To reach larger depths in the sample, the acceleration of primary electrons should be increased to higher acceleration voltages to probe a bigger volume, so that BSE can be emitted. For surface morphology information, however, smaller acceleration voltages are sufficient, as pictured in Fig. 2.1a) at 7 keV. The top view images and cross-sections obtained within the scope of this work were measured with a Hitachi SEM (SU-70). SEM images were usually recorded in SE mode with an acceleration voltage of the primary electron beam of 7 keV.

Energy/wavelength dispersive X-ray spectroscopy

Besides the analysis of morphological and elemental contrasts with the SEM by detection of the emitted SE and BSE, the relative composition of elements in a sample can be determined by analysis of the energy quanta of emitted X-rays. The technique is described as energy dispersive X-ray spectroscopy (abbreviated as EDX). As sketched in Fig. 2.1b), X-rays are emitted when an electron from a higher energetic shell falls into an empty and lower state of a SE which has been knocked out of its shell by the primary electron beam (the transition is here sketched from the L to the K shell). As the spacing between the electron shells differs with the chemical element, the emitted quanta of energy are thus characteristic of the elements present in the sample. By analysis of the integrated intensity of each energy peak of the resulting spectrum, quantitative information on the elemental ratios in the sample can also be obtained. Energies of the possible elements to be found in CTGS on Mo (i.e Mo, Cu, Ge, Sn and S) are reported in table 2.1.1 together with Se, as Cu_2SnSe_3 films are also measured in Chapter 4.

Nature of emission line/Atom	Mo	Cu	Ge	Sn	S	Se
K_α line [keV]	17.480	8.048	9.887	25.272	2.308	11.223
L_α line [keV]	2.293	0.930	1.188	3.444	(-)	1.379

Table 2.1: X-ray emission lines for Mo, Cu, Ge, Sn, S and Se in keV.

An EDX spectrum measured on a CTGS thin film on Mo with an acceleration voltage of 30 keV is shown in Fig 2.2a). To measure a specific emission line, the acceleration voltage has to be higher than the energy of this line. Since the depth probed depends on the acceleration voltage, it also means that different volumes probe different elements. It can be seen in Table 2.1.1 that the K line of S and the L line of Mo are very close to each other, only separated by 15 eV, which is likely below the spectral resolution (130 eV for the Mn K-line at about 6 keV [42]). Therefore, although new generations of EDX detectors with better deconvolution algorithms effectively separate the Mo and S signals, the measurement system used in this work requires the use of wavelength dispersive X-ray spectroscopy (abbreviated as WDX) to quantify the relative Mo/S amounts, with a ten times better spectral resolution than EDX, as shown in Fig. 2.2b). If only Cu/(Sn+Ge) or Ge/(Sn+Ge) ratio are measured, EDX is sufficient.

If EDX and WDX are performed separately, it is important to use the same acceleration voltage if one wants to compare the output compositional ratio, especially if the sample has a compositional depth gradient. As seen in Fig. 2.1a) for 20 and 7 keV there is a large difference in interaction volume for different voltages. All EDX/WDX measurements performed in this work were performed with a Hitachi SEM (SU-70), in most cases done with an acceleration voltage of 20 keV on $\sim 1\mu$m points or $\sim 60\mu m^2$ area. It happened however that films were sometimes a bit thicker and thus 30 keV were employed as well to test for the depth uniformity of the sample. WDX was only performed additionally to the EDX in the cases where the films are thin enough for the beam to penetrate the Mo, and thus inhibit the correct quantification of the S/(Cu+Sn+Ge) ratio. In Chapter 4 EDX mappings were recorded and overlaid with SEM top views, allowing to study both elemental distribution and surface morphology.

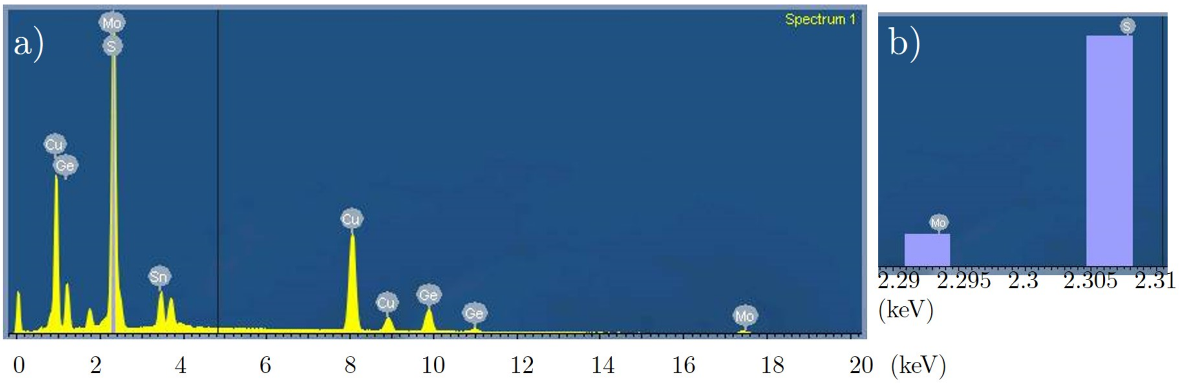

Figure 2.2: a) EDX spectrum (EDX counts vs energy E) measured on a SLG/Mo/CTGS sample. One can see the K lines of Cu, Ge and S at 8.048, 9.887, and 2.308 keV, respectively, and the L lines of Cu, Ge, Sn, and Mo at 0.930, 1.188, 3.444 and 2.293 keV, respectively. b) WDX spectrum measured on the same sample (WDX counts vs energy E) done in parallel with sufficient resolution to separate the L line from the Mo substrate and the K line from S in the absorber layer.

2.1.2 Phase identification

The understanding of the phases present in a crystalline material together with their structure is of key importance in physics and material sciences. To find out the nature of these phases and their relative atomic positions in the polycrystalline films, the interaction of light with the material is investigated. X-rays have a wavelength in the tenth of nanometer range, which is in the order of interatomic distances. The general background of the X-ray diffraction technique is described here but more details on the technique can be found in textbooks [43, 45].

X-ray diffraction

Crystal structures The smallest unit of atomic periodicity within a crystal lattice is termed the unit cell, which has dimensions a, b and c separated by the angles α, β, γ, denoted the lattice parameters. The variation of lattice parameters defines seven crystal systems, as referred here in table 2.1.2 by increasing order of symmetry. More details can be found in crystallography textbooks such as Ref.[46]. As CTGS is a relatively new material, confirming in which system it lies is essential, and is studied in Chapters 5 and 6.

X-ray diffraction technique With a wavelength $\lambda \sim 1$ Å comparable to the interatomic distance in a crystal, X-rays are the perfect investigators of crystalline structures. In this work, the X-ray source is an X-ray tube with a copper target, meaning the X-ray beam is described by the Cu$_{K\alpha}$ transition with a wavelength $\lambda = 1.54056$ Å. When X-rays impinge on a solid its electrons start to oscillate with the same frequency, emitting electromagnetic radiation scattered in all directions. Both constructive and destructive interferences of the scattered radiation occur symmetrically around the sample. Bragg's law of diffraction (Eq. (2.1)). describes the condition for constructive interference, in a geometrical configuration (illustrated in [45]) where atoms in the solid are periodically arranged on parallel planes separated by the interplanar distance d_{hkl}.

Lattice system	Lattice constants	Angles
Triclinic	$a \neq b \neq c$	$\alpha \neq \beta \neq \gamma \neq 90$
Monoclinic	$a \neq b \neq c$	$\alpha = \gamma = 90°$, $\beta \neq 90°$
Orthorhombic	$a \neq b \neq c$	$\alpha = \beta = \gamma = 90°$
Tetragonal	$a = b \neq c$	$\alpha = \beta = \gamma = 90°$
Hexagonal	$a = b \neq c$	$\alpha = \beta$ = 90°, γ = 120°
Rhombohedral (or trigonal)	$a = b = c$	$\alpha = \beta = \gamma \neq 90°$
Cubic	$a = b = c$	$\alpha = \beta = \gamma$ = 90°

Table 2.2: Seven existing lattice systems with their lattice parameters (a,b,c,α, β, γ) arranged by increasing symmetry: the triclinic is the least symmetric system and the cubic the most symmetric.

Each crystallographic plane is characterised by the Miller indices h, k and l. Bragg's law states:

$$n\lambda = 2d_{hkl}sin(\theta) \tag{2.1}$$

with n an integer number of wavelength and θ the incidence angle of the X-rays onto the sample. Bragg's law is the ground rule of X-ray diffraction (abbreviated as XRD). An X-ray diffractogram is measured by varying the angle θ: this is done either by scanning the X-ray source and the detector radially around the sample, or by rotating the sample itself. The resulting scattered X-rays reaching the detector are measured as a number of counts, which produce a pattern of Bragg peaks as a function of 2θ. The most common setup geometry to measure XRD is a θ - 2θ scan, as presented in Fig. 2.3a), where the incident and scattered beams each form an angle θ to the planar surface of the sample.

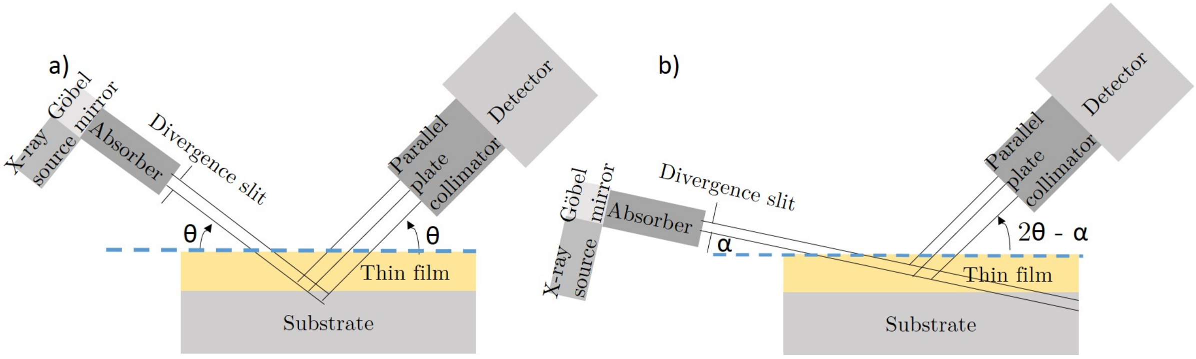

Figure 2.3: Experimental setups for a) a θ - 2θ scan and b) a grazing incidence X-ray diffraction scan, where α is the grazing angle and θ the scanning angle.

In the θ - 2θ geometry, Bragg's equation (2.1) is only verified for the diffraction of X-rays by lattice planes that are parallel to the sample planar surface. This geometry is not the best suited for the measurement of thin films because the X-rays only travel a short distance within the thin film and a larger distance in the substrate. Thus the highest contribution observed in the resulting XRD pattern is from the substrate. To solve this issue, an alternative geometry, the grazing

incidence XRD (abbreviated as GI-XRD), is commonly used to analyse thin films and presented in Fig. 2.3b). In this configuration, the X-ray beam penetrates the sample with a small and constant incidence angle α while the detector moves around the sample as previously. The small fixed incidence angle increases the path length of X-rays within the film, which is beneficial to any phase and structural identification. It is possible to evaluate the X-ray penetration depth in the film for any incidence angle α. This is done by means of the Beer-Lambert law which expresses the intensity decay of the X-rays after their absorption in the material. Details of the calculation are given in paragraph 2.1.2 for CTGS films. It is seen in Fig. 2.4 that it is perfectly reasonable to use α values between 0.5 and 6° to probe from the few hundred nm of the surface to the full depth of a three micron film. However, it is not recommended to use values below 0.5°, which is around the critical angle of total reflection. Incidence angles below the critical angle probe the first few nm of the film but lead to weak intensities and systematic peak shifts.
The X-ray diffractograms present Bragg peaks at specific angles 2θ. The amplitude of Bragg peaks is directly proportional to the square of the structure factor, F_{hkl}. F_{hkl} is the Fourier transform of the scattering density. Assuming that the scattering is localised on the atom centres, F_{hkl} can also be calculated as the sum of all individual scattering amplitudes f_n (also called form factor) of each atom n in the unit cell, as given in Eq. (2.2):

$$F_{hkl} = \sum_{n=1}^{N} f_n \exp(2\pi i(hx_n ky_n lz_n)) \tag{2.2}$$

where each atom is represented by its positions in the unit cell defined by the fractional coordinates (x_n, y_n, z_n) and the Miller indices (hkl) of the lattice plane on which it lies.
Each peak in a diffractogram can be assigned to a specific plane (hkl), and thus a crystal structure assigned to a sample. These may be cross-compared with existing databases with diffractogram patterns of similar compounds. Most measurements in this work (i.e Chapter 4) were performed in grazing incidence configuration GI-XRD, such as in Fig. 2.3b), with a Bruker D8 DISCOVER. The divergence slit used on the X-ray source arm is 1.2 mm together with a soller slit. Furthermore, the grazing angle α was set to 0.5°. The GI-XRD measurements discussed in Chapter 6 were obtained on a PANAlytical XPert Pro MPD diffractometer, using a soller slit as well as a $\frac{1}{4}^0$ divergence slit at the source arm. α was set to 0.5, 3 or 6°. Before each measurement, a height alignment of the sample was performed in order to avoid peak shifts. The typical scan range for the investigation of CTGS thin films and their possible secondary phases was between 10 and 90°. Phase identification is based on the 2016 PDF database from the International Centre for Diffraction Data (ICDD PDF-2016) [47].
Deeper investigations on the structure and microstructural properties of the films can also be performed via refinement of the crystal structure. This refinement consists in the attempt to match a calculated XRD with the experimental data thanks to an XRD-specific computing software [48] based on the Rietveld algorithm [49]. The Rietveld refinement method can provide a whole lot of information (lattice parameters, atomic coordinates, occupancy of atomic positions, preferential orientation, isotropic thermal parameters and estimations for strain and stress effects) but it also requires a structural model (i.e all atomic positions) from which the structure factor F_{hkl} can be computed. In this work, a simpler model of crystal structure refinement named Le Bail refinement is used. It is simpler because it does not require any structural model [50] but only the attribution of an appropriate space group and initial unit cell parameters, which constrain the Bragg peak positions to specific 2θ values. The parameters being fitted include

the unit cell parameters, the instrumental zero error, the peak width and peak shape parameters. Le Bail refinement exploits the following Rietveld decomposition formula (Eq. (2.3)) in an iterative manner to estimate the structure factor F^2_{hkl} for unknown atomic positions. The formula states for the pattern intensity I_K:

$$I_K = \sum_j w_{j,K} \cdot F^2_{hkl} \cdot \frac{y_j(obs)}{y_j(calc)} \tag{2.3}$$

where $w_{j,K}$ is a measure of the contribution of the Bragg peak at position $2\theta_K$ to the diffraction profile y_j at position $2\theta_j$ and y_j(calc) is the calculated total intensity profile at position $2\theta_j$ from all contributing Bragg peaks. The sum is over all $y_j(obs)$ that can theoretically contribute to the intensity I_K. Initially, all F^2_{hkl} are set to an arbitrary equal value and I_K values for each Bragg peak are calculated with Eq. (2.3). Those I_K values are then used to determine new F^2_{hkl} values by iteration. The process is repeated until the fit is in good agreement with the experimental data. This method yields basic information as the cell parameters, refines the background and the peak shape. As mentioned space groups and lattice parameters have to be input in the Fullprof software. The diffractograms are thus fitted to the space group C1c1 for CTGS and Im$\overline{3}$m for the contribution of the Mo substrate, as explained in Chapter 6. The lattice parameters for CTS, CGS and Mo used are taken from the database 2016 of the International Centre for Diffraction Data [47]. The refinement process begins with background fitting, for which points are fixed manually within the FullProf software. FullProf is then run to calculate the initial model of the intensity profile with an arbitrary structure factor for all peaks, as explained previously. Iterations were run on a basis of a maximum of 100 cycles with one parameter being refined at a time in the following sequence: the unit cell, the full width at half maximum, the zero point of the detector. Refinement of the unit cell parameters a, b, c and β is performed in Chapter 6 in the monoclinic unit cell of CTGS. Thus changes in the unit cell with the composition of Ge can be quantified.

Sampling depth of grazing incidence X-ray diffraction in CTGS films Average X-ray penetration depths z in grazing incidence geometry can be calculated by means of the attenuation law. z describes the depth at which the X-ray intensity reaches 37% $(=\frac{1}{e})$ of the incident X-ray intensity I_0. The attenuation law expresses the intensity at the distance x in the film as a function of I_0, such as:

$$I(x) = I_0 \exp(-\mu\rho x) \tag{2.4}$$

with μ the mass attenuation coefficient and ρ the material density. In the GI geometry presented in Fig. 2.3b), the incident beam path length L_i in the material before reflection and the path length after reflection L_r can be expressed as function of the penetration depth z as follows:

$$L_i = \frac{z}{\sin(\alpha)}, L_r = \frac{z}{\sin(2\theta - \alpha)}, \tag{2.5}$$

with $L_i + L_r$ the total distance travelled in the film by the beam, and thus replaces x in Eq. (2.4). The penetration depth z can be finally calculated for any incident angle α as function of 2θ as:

$$z = \frac{1}{\mu\rho}\left(\frac{1}{\sin\alpha} + \frac{1}{\sin(2\theta - \alpha)}\right) \tag{2.6}$$

For example, and for the experimental investigation in Chapter 6, z is calculated for the pure CTS, CGS and a CTGS alloy for α = 0.5, 3 and 6°. For each compound:

$$\mu(CTGS) = \rho(CTGS)\Sigma\frac{M_i}{M(CTGS)}\frac{\mu}{\rho}_i \tag{2.7}$$

where $\frac{\mu}{\rho}_i$ is the elemental attenuation coefficient found in databases (NIST) and the approximate density $\rho(CTGS)$ is calculated from the volume of a monoclinic unit cell (with the unit cell data found in [51] considering it contains 4 formula units.)

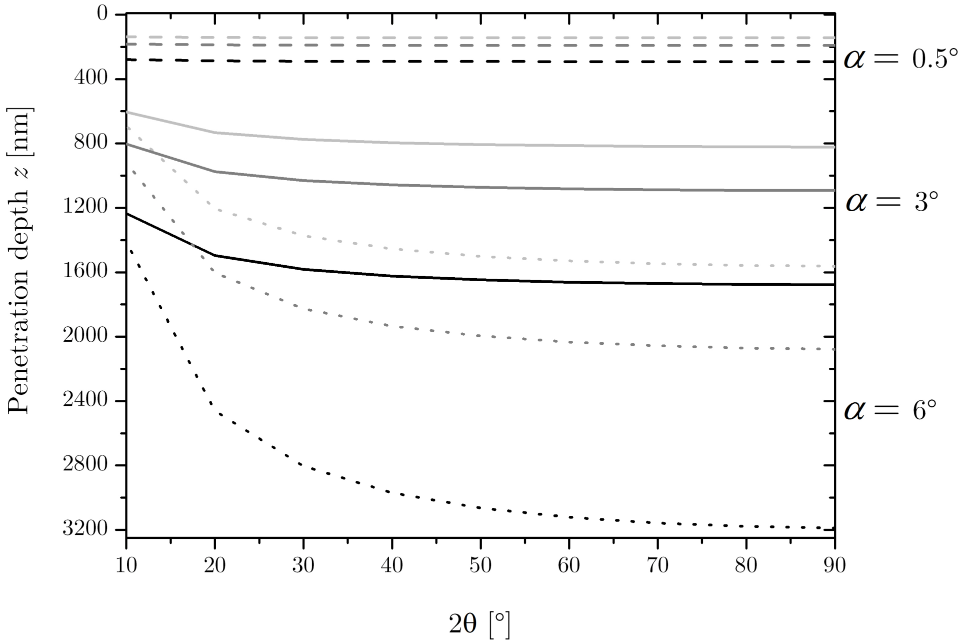

Figure 2.4: X-ray penetration depth z (nm), calculated for pure Cu_2SnS_3 (light grey), a $Cu_2Sn_{1-x}Ge_xS_3$ alloy (x=0.5) (dark grey) and pure Cu_2GeS_3 (black) as function of 2. The calculation is done for grazing incidence geometry angles of α = 0.5 (dashed lines), 3.0 (solid lines) and 6.0°(dotted lines), following the attenuation law.

Fig. 2.4 confirms that $\alpha = 6°$allows to reach a depth of 3 microns.

Raman spectroscopy

Raman spectroscopy is an optical and non-destructive technique using monochromatic laser light to obtain information on the bonding state of atoms inside a material. The nature of the bonds gives hints on the crystal structure and composition of the sample. For more details, one should refer to [43]. When laser light impinges on a material, a small fraction of its photons ($< 1\%$) is scattered by the material. Scattering occurs both elastically and inelastically, and Raman measures both signals as a function of their frequency. Elastic scattering, where energy is conserved, occurs due to the electromagnetic nature of light. The applied oscillating field induces a time-dependent polarisation in the material, and thus the material radiates energy at the same frequency. In the resulting Raman spectrum, a high signal from the elastic scattering is always visible which is called Rayleigh signal and at a frequency equal to the frequency of the incident beam. Fig. 2.5a) shows a Raman spectrum measured on crystalline silicon Si, where the most intense signal corresponds to the Rayleigh peak. Two peaks of lower intensity are also visible. They relate to inelastic scattering and are the peaks of interest in a Raman measurement. Inelastic scattering occurs due to the offset between the atomic polarisation fields in the material (the atoms oscillating with a certain frequency for $T > 0\,K$) and the external electric field. This offset is described as Raman shift. The two Raman signals seen in Fig. 2.5 around the Rayleigh peak show this Raman shift and correspond each to the creation of a phonon with the energy Ω ("Stokes") or annihilation of a phonon with the energy Ω ("Anti-Stokes"). The creation of a phonon within the crystal results in the emission of photons of lower energy, while emitted photons have a higher energy when a phonon is annihilated. Among the two, the Stokes line is used for analysis due to its higher intensity. The intensity of the Raman signal can be enhanced to some extent by increasing the intensity of the laser light. It can also be increased together with the concentration of Raman active species. Eventually, it also varies with the polarisability of the considered atomic species, explained by group theory.

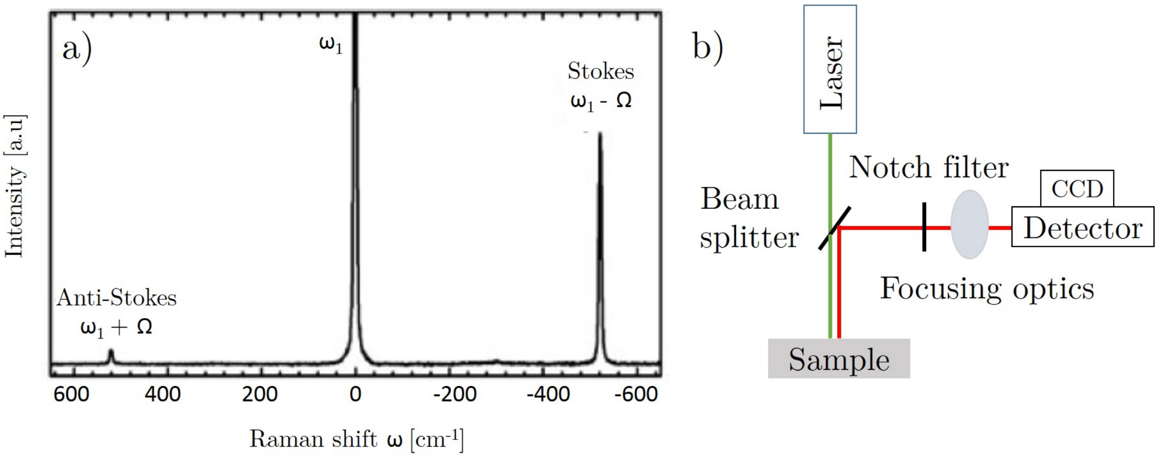

Figure 2.5: a) Raman spectrum of crystalline Si (found in [43]) showing the elastic (Rayleigh) and inelastic (Stokes and Anti-Stokes) scattered signals, b) Sketch of a typical instrumental setup used for Raman and photoluminescence measurements.

In this thesis, CTGS thin films are analysed with Raman spectroscopy in parallel to XRD, in Chapters 5 and 6. The measurements are performed with incident wavelengths λ of 442, 532, 633 and 785 nm in Chapter 5, and 633 nm in Chapter 6, with respective laser powers 41, 21, 84 and 45 µW in order of increasing λ. These were carefully selected in order not to inappropriately heat the sample and result in peak shifts. Prior to measurement λ was calibrated with an integrated Si-sample. A typical Raman setup is presented in Fig. 2.5b). Raman being a surface sensitive technique, the beam only probes the first 80 to 150 nm of the film. The laser beam is focused on the sample with a diameter of about 1 micron. This resolution is defined by choice of the spectrometer focal length, the diffractometer grating, the incident λ and the pixel size of the detector. The radiation scattered from the sample is refocused and measured thanks to a charge-coupled device detector (CDD).

2.1.3 Optical characterisation with photoluminescence

Photoluminescence (abbreviated as PL) is a suitable and widely employed optical technique to investigate the quality of an absorber layer for solar cells. PL allows to study the radiative recombination processes in the semiconductor and conclude on the defect levels existing within the bandgap. Detailed information on photoluminescence and its application to thin film solar cells can be found in Ref.[43].

When a solid is irradiated with light of energy E superior to the bandgap of the semiconductor, i.e $E > E_G$, light is absorbed by the semiconductor material and its electrons are excited from the valence band (VB) to high energy states in the conduction band (CB), leaving behind holes in a broad range of states of the VB. The excited electrons in the CB, and holes in the VB, rapidly thermalise to the conduction band minimum (CBM) and valence band maximum (VBM), respectively, or to defect states within the bandgap. After thermalisation, electrons recombine with holes either radiatively or non-radiatively via deep defects within the bandgap. PL consists in looking at the radiative emission where recombination occurs with the emission of a photon. A PL measurement consists in measuring the energy and intensity of the emitted photon flux or luminescence. PL can be measured both at room temperature (RT) and low temperature (low T), depending on the transition one is interested to investigate. Examples of common recombination pathways measurable at LT and RT are drawn in the band diagram of Fig. 2.6.

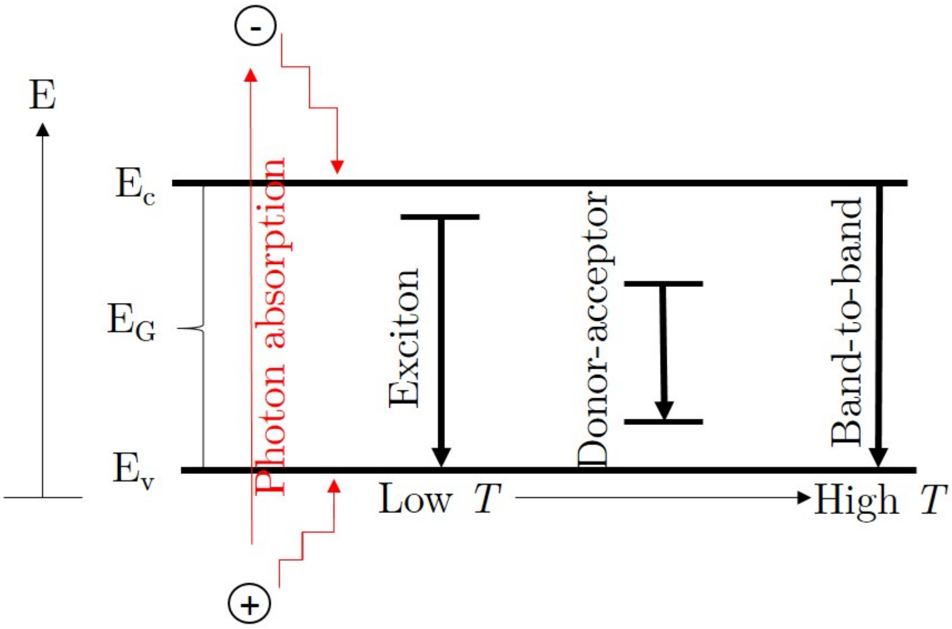

Figure 2.6: Examples of radiative recombination pathways (excitonic, donor-acceptor and band-to-band transitions) drawn with black arrows, occurring in a PL experiment after photon absorption and thermalisation of the generated electron-hole pair to the band edges E_c and E_V (both drawn in red).

Excitonic and donor-acceptor transitions are defect transitions that can be observed in PL done at low T. At RT enough thermal energy is available for the shallow donor and acceptor states to be ionised and the excitons to dissociate, which means only band-to-band transitions or transitions between donor and acceptor states that are deeper in the bandgap are measurable. Thus PL measurements done at RT typically allows to determine the bandgap energy E_G of the CTGS samples, mostly underestimated by the donor-acceptor transition. When PL is measured at room temperature (RT) the measured photon flux Y_{PL} outside the sample can be expressed as [52]:

$$Y_{PL} = \frac{2\pi}{h^3c^2}\frac{E^2 \cdot a(E)}{\exp(\frac{E-\triangle\mu}{kT}) - 1}[=]\frac{\text{photon}}{\text{area} \cdot \text{time} \cdot \text{bandwidth}} \tag{2.8}$$

with T the temperature, $\triangle\mu$ the quasi-Fermi level splitting (QFLS) and $a(E)$ the absorptivity. $\triangle\mu$ describes the difference between the Fermi levels E_F of the conduction and valence bands under illumination. $a(E)$ is function of the front surface reflectivity R_f, the absorption coefficient α_{abs} and the laser penetration depth x, such as:

$$a(E) = (1 - R_f)(1 - \exp(-\alpha_{abs}(E)x)). \tag{2.9}$$

where for λ = 514 and 660 nm, $x \sim$ 80 and 250 nm in CTGS, respectively [53].
Y_{PL} is mostly determined by the exponential decay in Eq. (2.8). Thus a higher Y_{PL} of the band-to-band transition results in a larger QFLS, and a higher device open-circuit voltage V_{oc} can be expected in the corresponding solar cell device. The prospective V_{oc} can be calculated from $\triangle\mu$ if it can be obtained via fitting of the high energy wing of the PL peak, which in our data is not feasible due to large tailing of the peak.

PL measurements presented in Chapter 5 were carried out at RT on a home-built setup with an excitation wavelength of 514.5 nm using an Argon ion laser, with a spot size of 80μm dispersed with a 303 mm spectrograph. The measurements were spectrally corrected using a calibrated halogen lamp. The measurements presented in Chapter 6 were performed at RT as well with an excitation wavelength of 660 nm and 80μm spot size.

2.1.4 Visible-near infrared spectroscopy

Reflectance and transmittance of CTGS films was measured with Visible-Near Infrared spectroscopy (Vis-NIR) from a tungsten-halogen lamp. Ultraviolet (UV) measurements are also possible with radiation from a deuterium lamp but are not performed in this thesis where one focuses on materials with bandgaps below 3 eV. More information on the technique can be found in Refs.... The measurements presented in this thesis in Chapter 2 were carried out using a Perkin Elmer Lambda 950 UV/Vis/NIR spectrometer. The transmission T and reflection R are measured as a function of the incident wavelength on the sample, in this work between 680 (visible, red) to 1550 nm (NIR), selected thanks to a monochromator. The monochromatic light is split into two beams of equal intensity. The reference beam goes to the detector and the second beam is focused onto the sample. For the reflection measurement, the sample is placed within an integrating sphere, a hollow spherical cavity covered on the interior with white reflecting coating. This sphere ensures that any light reflected from the sample surface is scattered evenly within the cavity. This diffuse light is then detected using a photomultiplier tube and InGaAs detectors which are positioned within the sphere. In the case of transmission measurements, the sample is mounted at the front of the integrating sphere blocking the entrance point of the irradiating light. Any light that passes through the sample into the integrating sphere is detected. From the measured T and R the absorption coefficient α of the CTGS material can be calculated following:

$$\alpha = -\frac{1}{x}\log(\frac{T}{1-R}), \tag{2.10}$$

with x the thickness of the film.
Before any measurement, zero values of T and R must be determined for calibration. In this aim, T and R are measured over the desired wavelength range with two white boards instead of the sample.
To be able to measure T the CTGS films should be detached from the opaque Mo substrate and stuck onto a transparent soda-lime glass substrate. This prerequisite limits the usability of this technique on the layers annealed in this thesis which show a high adherence to the substrate. Thus, to be able to evaluate α it would be easier to have CTGS directly deposited on SLG instead of SLG/Mo, thus the Cu,Sn,Ge-containing precursors should be deposited on SLG. To study light absorption in Cu_2GeS_3 in Chapter 5, copper was directly deposited on soda-lime glass using a wet-chemical method with copper formate as an organic salt, and further annealed in a GeS and S atmosphere, as described in Chapter 4. One might refer to Ref.[54] for more details on the precursor deposition method. In this work, one makes sure that the resulting Cu_2GeS_3 film after annealing is identical to the ones prepared on Mo, so one can make use of the $T-R$ measurements.
The inflection points of the absorption spectrum, determined from its derivative $\frac{\mathrm{d}\alpha}{\mathrm{dE}}$, are known to give a fair estimation of the optical bandgap E_G [55]. The optical bandgap of CTGS can also be determined from the plot of the product $(\alpha \cdot E)^2$ as a function of the incident photon energy E, which is described as a 'Tauc plot'. E_G is extracted from the linear extrapolation of the Tauc plot to the x-axis.

2.1.5 Electrical characterisation with capacitance-voltage measurements

Capacitance-voltage measurements (abbreviated as CV) yield information on the net doping density of majority carriers and densities of electrically active defects, in a semiconductor [56]. The capacitance (per unit area) is defined as the change of charge Q (per unit area) by a change of applied voltage V, such as:

$$C = \frac{dQ}{dV} \tag{2.11}$$

In this thesis, the Mott-Schottky technique is employed in CV measurements to determine the net doping density of CTGS films. The CTGS semiconductor film is layered within two metallic layers: the standard Mo substrate at the back and a 3 micron thick aluminium layer at the front surface. The Mo-CTGS interface is considered to be ohmic, thus not presenting an appreciable barrier to hole transfer across the interface. Electronic transport at the metal-semiconductor interface Al-CTGS is controlled through the Schottky model where a charge depleted region occurs in the semiconductor, causing band bending. By varying the applied voltage, one changes the built-in voltage V_{bi} at the junction, described the magnitude of the bending. The relationship between the interface capacitance C and the applied potential V is described by the

Mott-Schottky equation:

$$\frac{1}{C^2} = \frac{2}{q\varepsilon A N_A}(V_{bi} + V - \frac{k_b T}{q}) \tag{2.12}$$

with N_A the doping density (1/cm^3), q the elementary charge, A the surface area of the sample and ε the dielectric constant of the material.
A plot of $\frac{1}{C^2}$ as a function of V should have a linear region. N_A is obtained from the slope V_{bi} from the extrapolation to the x-axis. C-V measurements have been performed in this thesis on the SLG/Mo/CTGS films presented in Chap. 6, with Al evaporated on the surface of the film with a Ferrotech Electron-beam evaporation tool. The SLG/Mo/CTGS/Al samples were then mounted in an evacuated cryostat at a temperature of 300 K and left there in the dark for at least 8 hours before the C-V measurements were carried out with an Agilent E4980A Precision LCR Meter at a frequency of 100 kHz. The apparent doping was extracted from the slope of the resulting Mott-Schottky plots (cf. Eq. (2.12)).

2.2 Characterisation of solar cells

Photovoltaic devices may be fabricated out of the produced CTGS absorber layers, following the structure presented in Fig. 1.4. Device characterisation is performed by measurement of the device response to photoexcitation, which allows the determination of its power conversion efficiency. The theoretical background of current density-voltage and external quantum efficiency analysis presented in this section are found in Ref.[43], to which the reader might refer for more information.

2.2.1 Current density-voltage characteristics

A solar cell device is characterised by its power conversion efficiency η. η expresses the ratio between the maximal electrical power P_{max} generated by the device and the incident light power P_{in} irradiating the device, as:

$$\eta = \frac{P_{max}}{P_{in}} \tag{2.13}$$

η could reach in an ideal case the limit of about 33% established from the calculations of Schockley and Queisser [24] for an absorber layer with a bandgap E_G of 1.4 eV. To measure η, current-voltage (I-V) characteristics are evaluated: in this aim, the sample is illuminated with known power P_{in} and its current response I (in Amps) is measured under application of a range of voltages V (in Volts). The same measurement is repeated without illumination, i.e in the dark. More often, the current is expressed in terms of current density J, with $J = \frac{I}{A}$ with A the surface area of the sample in cm^2, which results in J-V curves. An example of a set of J-V curves, measured in the dark and under illumination, is presented in Fig. 2.7.

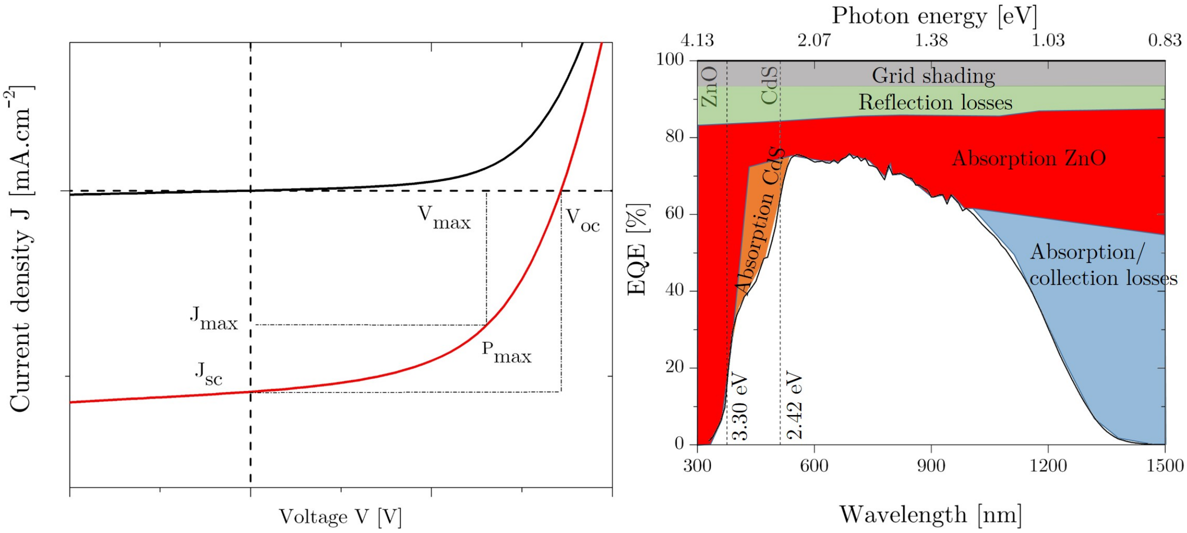

Figure 2.7: a) Exemplary set of J-V curves of a thin film-based solar cell device measured in the dark (black) and under illumination (red). The maximum power point P_{max} of the J-V curve under illumination is highlighted as the crossing point of J_{max} and V_{max}. The theoretical maximum power point is also shown at the crossing of J_{sc} and V_{oc}, b) An external quantum efficiency (EQE) measurement of a thin-film based device (here CZTS) showing optical and collection losses with their origins highlighted on the graph [25]. The bandgaps of the CdS and ZnO layers are also indicated.

The current density of the solar cell in the dark, J_d, describing the dark J-V curve in Fig. 2.7a), is given by the diode equation (2.14):

$$J_d = J_0(\exp{(\frac{qV}{nk_bT})} - 1), \tag{2.14}$$

with J_0 the diode saturation current density and n the diode quality factor. n describes how closely any investigated diode obeys the ideal diode equation [57] and thus equals 1 for ideal devices. k_bT/q is the thermal voltage, giving the temperature dependence of the curve with k_b the Boltzmann constant and q the elementary charge. The J-V curve measured under illumination is equivalent to the dark J-V curve, shifted by a negative and constant current value, as seen in Fig. 2.7a). This value is described as the short-circuit current density J_{sc} corresponding to the current flow at zero applied bias, $V = 0\,\text{V}$. For for $V \neq 0\,\text{V}$, J_{sc} can be approximated as the photocurrent density J_{ill}, considering that charge carrier collection is independent of the applied bias. Under illumination, Eq. (2.14) is modified to describe the resulting photocurrent density J as:

$$J = J_0(\exp{(\frac{qV}{nk_bT})} - 1) - J_{ill}. \tag{2.15}$$

The voltage measured at zero current is the open-circuit voltage V_{oc} as represented in Fig. 2.7a) and as extracted from Eq. (2.15) for $J = 0$, can be expressed as follows:

$$V_{oc} = \frac{nk_bT}{q} \ln \frac{J_{ill}}{J_0}. \tag{2.16}$$

The minimum value of J_0 occurs when there is only radiative (band-to-band) recombination in the device. Non-radiative recombination leads to an increase of J_0 and thus a decrease of the V_{oc}.

The electrical output power P (in Watts) defined as product of I and V reaches a maximum value P_{max} at the maximum power point $(I_{max},\ V_{max})$ on the J-V curve:

$$P_{max} = I_{max} \cdot V_{max} : \tag{2.17}$$

In an ideal assumption where the device could deliver a constant current density J_{sc} until the open circuit voltage [57], thus showing a rectangular J-V curve, the maximal power point would be at the crossing between the short-circuit current density J_{sc} and the open-circuit voltage V_{oc}. A dimensionless entity called the fill factor (FF) ($0 < FF < 1$) and usually described as a percentage exists as:

$$FF = \frac{J_{max} \cdot V_{max}}{J_{sc} \cdot V_{oc}} \tag{2.18}$$

describing how close the measured J-V curve is to the square shape delimited by J_{sc} and V_{oc}, as seen on the schematic J-V curve in Fig. 2.7a). The power conversion device efficiency η (cf Eq. (2.13) can be rewritten considering Eq. (2.17) as:

$$\eta = \frac{J_{max} \cdot V_{max}}{P_{in}}, \tag{2.19}$$

which with Eq. (2.18) gives finally:

$$\eta = \frac{J_{sc} \cdot V_{oc} \cdot FF}{P_{in}}. \tag{2.20}$$

Power losses in the device and thus deviations from ideality are described by the diode ideality factor n as well as both series and shunt (parallel) resistances, R_s and R_{sh}. These parasitic resistances reduce solar cell efficiency by dissipating power, and thus decrease the fill factor. The diode equation under illumination (Eq. 2.15) is modified to account for the power dissipation, as:

$$J = J_0(\exp\frac{q(V - AJR_s)}{nk_bT} - 1) + \frac{V - AJR_s}{R_{sh}} - J_{ill}. \tag{2.21}$$

with A the surface area of the solar cell.

Eq. (2.21) assumes that the charge carrier recombination rate is directly proportional to the product of electron and hole generation with a sufficiently high charge carrier mobility for charge carrier collection at any voltage bias. Change in the magnitude or type of recombination is reflected in the diode factor, $n > 1$.

Magnitudes of R_s and R_{sh} can be extracted from the dark J-V curve. R_s and R_{sh} are roughly estimated from the inverse slopes of the J-V curves at voltages more positive than the V_{oc} and near the J_{sc}, respectively. In an ideal device, R_{sh} is infinite and R_s is 0 Ω.

The J-V measurements done in this work were performed at RT both in the dark and under illumination, using a OAI Trisol Standard Solar Simulator with a Keithley current voltage source calibrated by a silicon reference solar cell (WPVS-Cell, RS-ID-3, Serial No. 006-2007, from ISE/S. Brachmann) and with a four probe configuration.

2.2.2 External quantum efficiency

Solar cell devices are subject to both optical and electrical losses that can be analysed with external quantum efficiency measurements (abbreviated as EQE). An EQE measurement consists in irradiating the solar cell with monochromatic light varying over a given wavelength spectral range $\mathrm{d}\lambda$ and measuring the collected current for each λ. Without voltage bias, the collected current equals I_{sc}. The standard EQE plot is obtained by ratio of the wavelength-dependent number of collected electrons $\mathrm{d}I_{sc}/e$ to the incident photon flux $\mathrm{d}\phi$, such as:

$$EQE(\lambda) = \frac{\mathrm{d}I_{sc}(\lambda)}{q \cdot \mathrm{d}\phi(\lambda)}, \tag{2.22}$$

with q the elementary charge. The short-circuit current density of a solar cell can be therefore be obtained by integrating the product of the EQE spectrum with the incident photon flux over all wavelengths, following:

$$J_{sc} = \frac{I_{sc}}{A} = \int q \cdot EQE \cdot \Phi \mathrm{d}\lambda. \tag{2.23}$$

A standard EQE plot is presented in Fig. 2.7b) for a $Cu_2ZZnSnSe_4$ device with report of the origin of optical and electrical losses on the spectrum. The Gärtner equation [58] (Eq.(2.24)) expresses the low energy side (high λ) of the EQE in terms of the absorption coefficient α, the space charge region width W, and the minority carrier diffusion length L_d:

$$\mathrm{EQE} = 1 - \frac{\exp(-\alpha W)}{1 + \alpha L_d} \tag{2.24}$$

Under the assumption that in small grained polycrystalline materials, $\alpha \cdot L_d << 1$, Eq.(2.24) becomes [59]:

$$\mathrm{EQE} = 1 - \exp(-\alpha(W + L_d)), \tag{2.25}$$

where for highly doped material, it is very likely that $W << L_d$. For incident photon energies $E = \nu$ near the bandgap E_G of a direct bandgap material such as CTGS, α can be expressed as:

$$\alpha h\nu = A(h\nu - E_G)^{\frac{1}{2}} \tag{2.26}$$

with A a constant. Replacing α in Eq. (2.25) by its expression in Eq. (2.26) leads to Eq. (2.27):

$$-h\nu \ln(1 - EQE) = (W + L_d)A(h\nu - E_G)^{\frac{1}{2}} \tag{2.27}$$

A plot of $(h\nu \ln(1 - EQE))^2$ against $h\nu$ gives a straight line allowing to extract the bandgap value E_G. E_G corresponds to the intercept of this line with the x-axis.

EQE measurements presented in this work were made at RT in a home-built setup using chopped monochromatic light source (beam area 1×1 mm) from a Xenon ($300 \leq \lambda \leq 800\,\mathrm{nm}$) and a Tungsten lamp ($800 \leq \lambda \leq 1650\,\mathrm{nm}$). The two light sources are calibrated with a Si and an InGaAs photodiode and the resulting photocurrent is measured using a lock-in amplifier.

CHAPTER 3

$Cu_2Sn_{1-x}Ge_xS_3$ precursor fabrication

This chapter introduces the procedures employed for **precursor fabrication**. For the growth of CTGS absorber layers, or more accurately, $Cu_2Sn_{1-x}Ge_xS_3$ with $0 \leq x \leq 1$, precursor fabrication corresponds to the **deposition of copper Cu, tin Sn and germanium Ge thin films** on a Mo-coated soda-lime glass (SLG) substrate. The sulphur is only incorporated later during post-deposition annealing of the precursors where their crystallisation into the final ternary alloy occurs, as illustrated here and investigated in chapter 4.

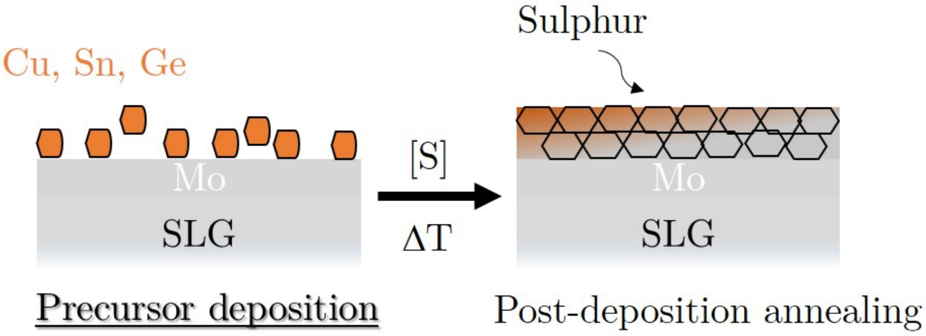

Two different procedures were used for metal deposition, on SLG/Mo:

1. Electrodeposition
2. Sputtering

This chapter starts with the introduction of the theoretical concepts of the electrodeposition process. The electrodeposition was done two ways: either from aqueous solvents or from organic solvents which are known to facilitate the deposition of germanium and the reasons for this are explained in the second part of the chapter. Thirdly, the concepts of DC magnetron sputtering will be shortly introduced. This method allows for various stacking orders that will be presented. Finally, the concept of alloying is introduced for the Cu-Sn, Cu-Ge and Ge-Sn binary systems.

3.1 Basic principles of electrodeposition

Electrochemical deposition (or electrodeposition) is a low-cost technique for the deposition of stacked elemental layers, metal alloys or chalcogenide compounds onto a conductive substrate. The method is acknowledged for its easy upscaling for industrial purposes and often used alternatively to expensive vacuum techniques (e.g Physical Vapour Deposition (PVD)) for thin film deposition [60]. In this thesis stacks of elemental Cu and Sn metallic layers were electrodeposited on conductive Mo-coated SLG substrates. The first section of this chapter describes the basics of the electrodeposition process, before applying this knowledge to the deposition of Cu and Sn layers on Mo. More details on the electrodeposition process can be found in Ref.[61].

3.1.1 Redox reactions at the anode and cathode

Electrodeposition makes use of oxido-reduction (redox) reactions to coat a metallic layer on a conductive substrate. The deposition process of the metal M occurs on the substrate via electrochemical reduction of metal cations M^{n+} present in an electrolyte, as follows:

$$\mathrm{M}^{\mathrm{n}+}_{(\mathrm{aq})} + \mathrm{ne}^- \rightarrow \mathrm{M}_{(\mathrm{s})} \tag{3.1}$$

The reduction is thus a gain of electrons, with n the integer number of required electrons e^- required for the cation M^{n+} to form one M atom on the substrate. The reduction occurs at the solid-liquid interface that is the interface between the substrate to be coated and the electrolyte in which it is immersed. The electrolyte is prepared by dissolving metal salts in a solvent and thus contains both cations and anions, where only the cations contribute to the redox reaction. The electrons are provided via an electrical circuit connecting the substrate to a power supply. In this electrical circuit the substrate corresponds to the negative electrode, also called the cathode or working electrode (WE). Fig 3.1 shows the considered electrical setup.

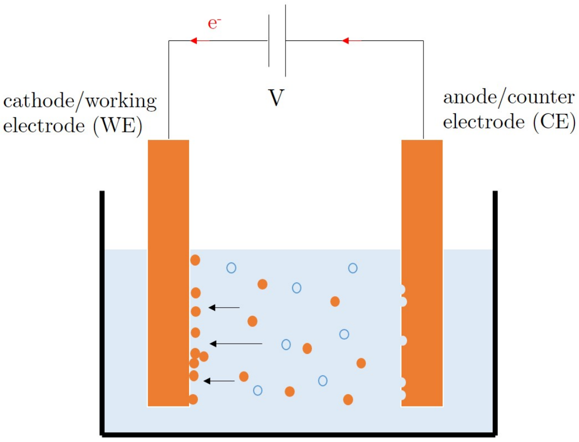

Figure 3.1: Electrodeposition setup with the coating of metal M occurring at the cathode via reduction of M^{n+} cations present in the electrolyte. The cations in solution are drawn as orange circles while the anions are represented by blue circles. In parallel, oxidation occurs at the anode where the species to be oxidised (often the same M) loses electrons. In this case, the anode dissolves and is thus sacrificial. The red arrows indicate the direction in which electrons flow.

Any reduction reaction (gain of electrons) at the cathode occurs together with an oxidation reaction (loss of electrons) at the positive electrode of the circuit, as represented in Fig 3.1. The positive electrode is called anode, or counter electrode (CE), and undergoes oxidation (i.e a loss of n electrons) following:

$$\mathrm{M_{(s)}} \rightarrow \mathrm{M^{n+}_{(aq)}} + \mathrm{ne^-}, \tag{3.2}$$

Both reduction and oxidation reactions require the transfer of n electrons, maintaining charge neutrality. This necessary current flow is induced by application of a potential difference between the cathode and the anode. To understand why a potential difference is applied, it is relevant to look at what happens at a single electrode-electrolyte interface directly after the electrode is immersed.

3.1.2 Immersion of electrode in electrolyte: open-circuit potential

At immersion of the electrode in the electrolyte, the system is in equilibrium with the Fermi levels of both the metal of the immersed electrode, E_F, and of the redox species in the electrolyte, $E_{F,\,redox}$, at the same energy. Therefore the net electron transfer is zero as illustrated in Fig. 3.2a). The energy levels of the redox species are described as ”Lowest Unoccupied Molecular Orbital” (LUMO) and ”Highest Occupied Molecular Orbital” (HOMO). If the Fermi level of the metal $E_F > E_{LUMO}$ an electron is transferred from the metal to the redox species and reduction of the cation in solution occurs, as seen in Fig. 3.2b). If $E_F < E_{HOMO}$ oxidation of the species in solution occurs in which an electron is transferred from the redox species to the metal, as seen in Fig. 3.2c).

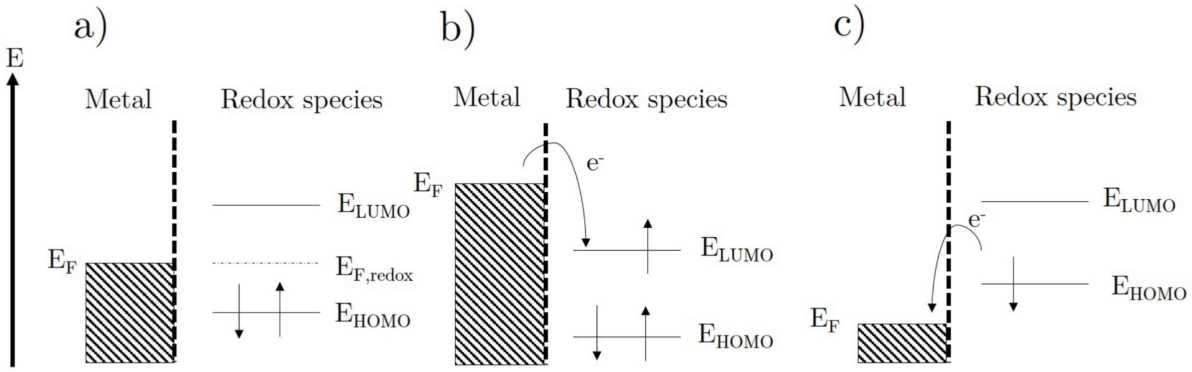

Figure 3.2: Schematic of a junction between a metal electrode and an electrolyte a) in equilibrium, b) during a reduction and c) during an oxidation.

These considerations remain the same in a system of two electrodes immersed in an electrolyte. In that case at equilibrium E_F equals $E_{F,\,redox}$, at both electrode-electrolyte interfaces. This condition implies that no net electric current flows through the cell and thus the voltage drop between the two metal electrodes, in these conditions, is called the open-circuit potential (OCP). The value of the OCP will depend on the relative position between the Fermi levels of both electrodes. An external potential (or voltage) must be applied between the two electrodes for charge transfer and a redox reaction to occur. The voltage bias causes the Fermi levels of the two metals to shift in energy and thus electron transfer phenomena become favourable. When applying a negative voltage to the WE previously described, its Fermi level rises and thus the redox species is reduced (cf. Fig. 3.2b)), whereas applying a positive voltage to the WE results in a decrease of its Fermi level. In this case, the redox species is oxidised as seen in Fig. 3.2c). This approach implies that by application of a voltage to the WE the opposite reaction occurs at the CE, in order to maintain charge neutrality. In the case of metal cations in solution, a reduction will imply the deposition of metal on the working electrode and a subsequent oxidation will remove (or strip) the metal from the electrode surface.

3.1.3 Potential considerations for controlled plating

Since the application of a potential difference is necessary for electrochemical deposition, one needs to be able to measure potentials. This subsection thus considers the requirements for measuring potential differences in the electrochemical system and potential conditions that are necessary for the plating to occur.

Use of reference electrode in three-electrode cell

The OCP cannot be directly measured as it corresponds to a potential difference between a solid and a liquid phase. However, the OCP can be measured respectively to another electrode whose standard reduction potential is known. This third electrode added to the electrochemical cell is called the reference electrode (RE). It forms a separate electrochemical system separated from the two other electrodes by a porous membrane. A scheme of a standard three-electrode electrochemical cell for deposition is shown in Fig. 3.3 where the potential applied to the WE is measured relatively to the RE. The resulting current flows between the WE and the CE. This setup is especially suited for electrodepositions in restricted volumes (i.e small WE areas around 2.5x2.5 cm^2) as the RE and WE need to remain close to each other for potential monitoring.

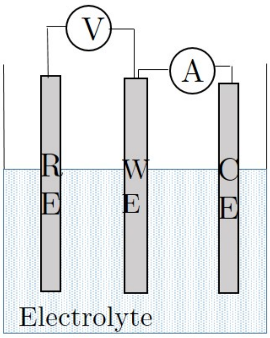

Figure 3.3: Schematics of the electrical setup for electrodeposition, consisting of a three-electrode setup immersed in an electrolyte and connected to a potentiostat monitoring potential and measuring the current flow. WE refers to the working electrode, RE to the reference electrode and CE to the counter electrode.

No current is passed through the RE as it could easily affect the sensitive redox couple it contains. At the laboratory scale, an Ag/AgCl electrode is used as RE. The redox reaction occurs between pure Ag and its AgCl salt. Again, the standard reduction potential of the RE is expressed relatively to another electrochemical system, which is the standard hydrogen electrode.

Standard hydrogen electrode as universal reference

The standard hydrogen electrode (SHE) is the universal RE against which all potential differences are set. The SHE consists in a half cell with a platinum wire immersed in a solution of hydrochloric acid HCl, with H_2 gas being bubbled onto the platinum electrode. The concentration of protons in the aqueous HCl is 1.18 M, the pressure of hydrogen gas is fixed at atmospheric pressure (1013 mbar) and the temperature is 298 K. By definition the reduction potential of the SHE equals 0 V and consists in the following redox half cell reaction:

$$\mathrm{H_{(aq)}}^{+} + \mathrm{e}^{-} \leftrightharpoons \frac{1}{2}\mathrm{H_{2(g)}} \tag{3.3}$$

A potential difference for a specific redox couple is measured with the SHE under standard conditions (298 K, 1013 mbar). To account for deviations to these conditions, the Nernst equation expresses the reduction potential E of a redox couple as function of the standard reduction potential E^0, following:

$$E = E_0 + \frac{RT}{nF} ln \frac{[Ox]}{[Re]} \tag{3.4}$$

with R the molar gas constant, F the Faraday constant and $[Ox]/[Re]$ the concentrations of the oxidant/reductant species in the electrolyte.

Applied overpotential for deposition

To induce the redox reactions necessary for deposition, the system must be moved away from equilibrium. For this reason, an external potential is applied to the system. The overpotential η_V is described as the difference between the applied potential E at which the reaction occurs at the cathode-electrolyte interface (thus current flows) and the equilibrium potential of the redox couple, OCP, such as:

$$\eta_V = E - \mathrm{OCP}. \tag{3.5}$$

Cyclic voltammograms (CV) are recorded when the external potential E applied to the WE (and monitored by the RE) is swept across and the resulting current response measured between WE and CE. The shape of a typical CV is shown in Fig. 3.4 for an aqueous electrolyte where a metallic layer is coated on a Mo substrate. The measurement of the CV starts at OCP conditions, where the net current is zero.

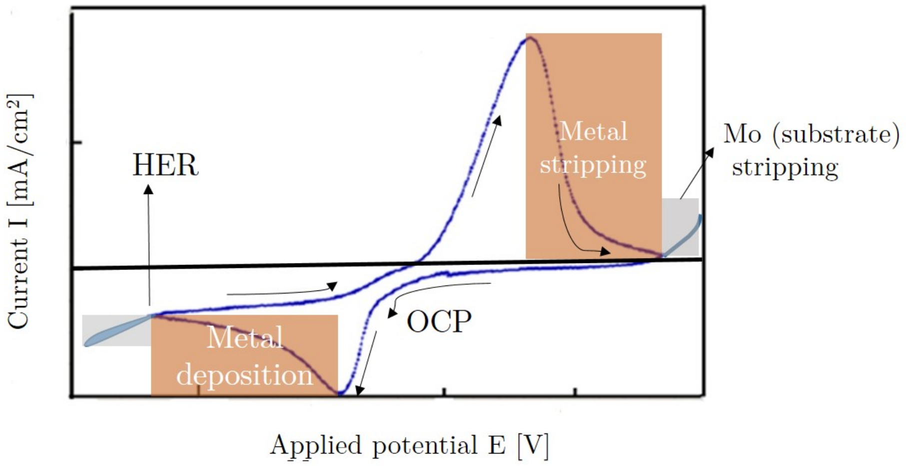

Figure 3.4: Sketch of a typical cyclic voltammogram (CV) showing the current I measured between the counter and working electrodes as a function of the potential E applied between the working and reference electrodes. The arrows show the direction of the potential sweep. Regions where both metal deposition on the Mo electrode and metal stripping off the Mo electrode occur are indicated, as well as the hydrogen evolution reaction (HER) for low negative E.

As seen in Fig. 3.4, when $E < OCP$, $\eta_V < 0$ and the current increases, becoming negative. It is explained by the deposition of the metal M which is taking place following Eq. (3.1). Due to the depletion of ions around the WE, the reduction process eventually slows down, leading to a decrease of the current. This current does not reach zero because ion diffusion thanks to high concentration in the electrolyte from the bulk to the electrode still provides replenishment of the ions for the reduction to happen. At highly negative potentials the metal reduction on the WE competes with the hydrogen evolution reaction (abbreviated as HER). The HER is specific to aqueous electrolytes and will be explained in the next paragraph. When $\eta_V > 0$, stripping of metal off the WE happens, where metal atoms are oxidised following Eq. (3.2). The current drop observed is due to the complete removal of the deposited metal from the WE. If E is further increased, the substrate itself (such as Mo used for solar cell purposes) can also be stripped off the electrode. Care should be taken in choosing potentials for deposition, that are not too close to the HER reduction potential, as we will see it is detrimental to the reduction process. The rate of the CV can be increased by two means: either by an increase of the potential scanning rate during the sweeping or by an increase of the cation concentration near the cathode. The cation concentration near the electrode can be increased by providing a higher replenishment of cations at the electrode interface from the bulk solution, and that is usually done by stirring the electrolyte during the deposition.

3.1.4 Hydrogen evolution reaction in aqueous electrolytes

Generally, water is used as a solvent for preparation of the electrolyte from metal salts. Samples deposited at the University of Luxembourg in this work use aqueous solutions. However many compounds and elements (such as germanium) have a reduction potential E^0 that is close or

even below that of water decomposition, which corresponds to the hydrogen evolution reaction [62].
The HER happens at the cathode and is represented by Eq. (3.6), written as:

$$2\,\mathrm{H}^+_{(\mathrm{aq})} + 2\,\mathrm{e}^- \longrightarrow \mathrm{H}_{2(g)}, \mathrm{E}^0 = 0.00\mathrm{V}, \tag{3.6}$$

where E^0 indicates the standard reduction potential (measured relatively to the SHE).
In parallel at the anode, the following oxidation happens:

$$2\,\mathrm{H_2O_{(l)}} \longrightarrow \mathrm{O_{2(g)}} + 4\,\mathrm{H}^+_{(\mathrm{aq})} + 4\,\mathrm{e}^-, \mathrm{E}^0 = +1.23\mathrm{V}. \tag{3.7}$$

The two half-reactions constitute the water splitting into hydrogen and oxygen gases, such as:

$$2\,\mathrm{H_2O_{(l)}} \longrightarrow 2\,\mathrm{H_{2(g)}} + \mathrm{O_{2(g)}}, \mathrm{E}^0 = -1.23\mathrm{V}, \tag{3.8}$$

Thus instead of depositing germanium, in aqueous electrolytes, the HER will dominate and the mass of germanium deposited will be lower than expected. In those cases, the deposit of Ge should be analysed and compared to the charge passed during the deposition process. To avoid this parasitic reaction, solvents such as ionic liquids and various organic compounds are employed instead of aqueous electrolytes. These alternative solvents have larger electrochemical windows, meaning a larger range of potentials can be applied in which the solvent does not get reduced or oxidised. In this work, a CGS film was prepared from Ge-containing precursors deposited by Dr João Malaquias at the KU Leuven (Belgium) with organic solvents. This occurrence is the single one of this work using electrodeposited precursors out of non-aqueous solutions. Since only analysis of the annealed absorber has been made by the author of this work, but not the deposition of the precursors, the latter will only be briefly mentioned.
Theory can give some predictions on the mass of the deposit from charge considerations, described in the next section.

3.1.5 Quantity of deposited matter

Following Eq. (3.1), one first assumes that each cation in solution is converted to a metal atom by the uptake of n electrons. In this case the mass m_F deposited onto the substrate can be calculated as function of the net charge Q ($= nq$, with q the elementary charge) passed through the circuit (in Coulomb) thanks to Faraday's law of electrolysis, considering that $Q = I \cdot t$ with I constant current applied for a time t:

$$m_F = \frac{QM}{nF} \tag{3.9}$$

where M is the molar mass, n the number of transferred electrons and F the Faraday constant. Using the density and substrate surface area, m can be converted back into a deposit thickness. Alternatively, using the molar mass and Avogadro's number N_A, m can be converted back into a number of atoms. This equation gives a hint on the charge to be passed through the circuit to obtain the wished thickness. However, this equation describes an ideal situation where the amount of charge Q at the electrode is directly proportional to the current I. Side reactions (such as the HER) happening at the cathode will, in reality, affect the deposit thickness. The current efficiency usually expressed as a percentage $P_e < 100\,\%$, thus describes real cases with the ratio between the theoretical deposited mass m calculated from Eq. (3.9) and the real deposit mass m, as follows:

$$P_e = 100 \times m_F/m, \tag{3.10}$$

where m is measured with techniques such as X-ray fluorescence (XRF) or atomic force microscopy (AFM).
Comparative studies between AFM and XRF on electroplated copper layers (2.5x2.5 cm^2) have shown P_e reaches about 80 to 90%, which is a satisfactory experimental reproduction of the expected deposit calculated with Eq.(3.9). Standard deviations among thicknesses of layers prepared with similar Q are below 5 %, which we consider as proof of reproducibility of the deposit thickness.

3.2 Electrodeposition of thin films of copper and tin

In this work, the electrodeposition of thin elemental Cu films or Cu and Sn stacks is done onto molybdenum-coated soda-lime glass (SLG) substrates. Molybdenum is commonly used as conductive substrate and back contact for thin film technologies, such as in CIGS, as it offers a good ohmic contact [60].

3.2.1 Upscaled electroplating setup

Instead of the potentiostatic mode using a reference electrode within a three-electrode cell, two-electrode galvanostatic electrochemical cells that do not include the RE but only a CE with the WE can also be employed for electroplating (as in Fig. 3.1). Due to the absence of the RE for potential monitoring, the process is controlled by applying a constant current between the two electrodes. What results is a variation of E with time. This system is adequate when deposition is meant to occur on substrates immersed in larger vessels because the electrodes are automatically further apart while the use of a RE requires it to be close to the WE. The galvanostatic mode is therefore interesting when one wishes to upscale the deposition to larger surface areas. Electrodeposition on larger substrates can be attempted at the laboratory scale and has been successfully performed in this thesis, for substrates with four times the standard surface, i.e 45×50 mm^2. Thus with an upscale of the surface area of the substrate requiring vessels of two litres for the electrolyte, the galvanostatic mode was more frequently used in this thesis.

3.2.2 Substrate preparation

All Cu or Cu-Sn precursors are deposited onto a 45×50 mm^2 substrate which consists of 2 mm SLG sputtered with a thin film (500 nm) of Mo. Prior to deposition, the Mo surface is etched in NH_4OH solution to remove possible surface oxides and is then further rinsed in deionized water. Immediately after etching, the substrate is dried with a N_2 gun and fixed onto a glass holder, as seen in Fig. 3.5. Electrical contacts are made between the Mo surface and a crocodile clip connected with the WE wiring to a potentiostat. A chemically resistant tape is stuck on top of the copper tape, to protect it from the electrolyte. The quality of the contact between the front of the Mo film and the crocodile clip connecting it to the potentiostat is checked with an ohmmeter ($< 1.5\,\Omega$). The CE is made out of a large inert Platinum electrode.

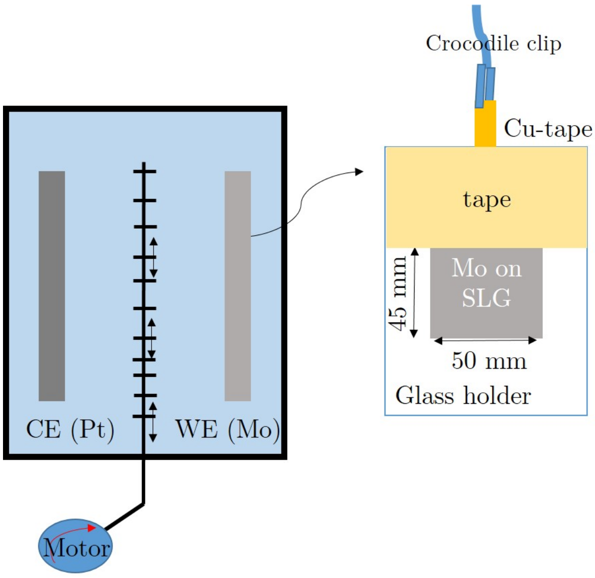

Figure 3.5: Top view of the 2L electrodeposition bath with the CE and WE immersed in the electrolyte containing the Cu or Sn cations. A motor ensures the stirring of the solution. On the right the configuration of the Mo substrate onto the glass holder is described.

Constant stirring of the solution is done via a motor attached to a stirring grid immersed in solution. Plating of copper and tin on upscaled Mo substrates is thus performed that way.

3.2.3 Precursor configurations

The two different precursor configurations, electroplated from aqueous baths, are shown in Fig. 3.6. Essentially the deposition is performed with the Mo electrode (WE) immersed in the electrolyte containing either copper or tin cations.

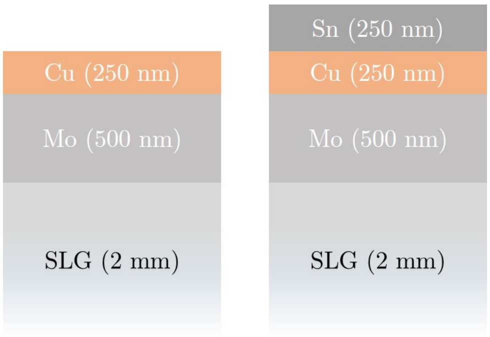

Figure 3.6: Schematics (dimensions not to scale) of the two different configurations of precursors (copper layer and copper-tin stacks) deposited from aqueous baths on SLG/Mo in this work.

The deposition of Cu occurs with the reduction of the $Cu^{2+}_{(aq)}$ cations and the deposition of Sn with reduction of the $Sn^{2+}_{(aq)}$ cations, such as (with indications of the standard reduction potentials against SHE):

$$\mathrm{Cu^{2+}_{(aq)}} + 2\,\mathrm{e^-} \rightarrow \mathrm{Cu_{(s)}}, \mathrm{E^0} = +0.342\,V \tag{3.11}$$

and:

$$\mathrm{Sn^{2+}_{(aq)}} + 2\,\mathrm{e^-} \rightarrow \mathrm{Sn_{(s)}}, \mathrm{E^0} = -0.136\,V. \tag{3.12}$$

As seen in Fig. 3.6, due to the difference in E^0 observed, Cu has to be deposited first on Mo. If Sn was deposited first on Mo, the potential needed to deposit Cu on top would oxidise the Sn layer, leading to its stripping out of the substrate. Therefore to avoid stripping of the layers from the Mo and be able to control the final composition, it is necessary to electrodeposit the metals in a stacking order following an increasingly negative standard reduction potential.

3.2.4 Nature of aqueous electrolytes

The aqueous electrolytes used for the plating of copper and tin films were previously tested and their recipes updated at the University of Luxembourg (UL) for small-scale plating (25x25 mm^2). The upscaled deposition of Cu and Sn stacks was suggested to require a thin seed layer of acidic copper bath before standard basic copper is deposited. The overall smoothness of the plating copper is enhanced with this added seed. However, the adhesion of the tin layer to the stack has shown to be very poor, with the layer peeling off during annealing. The choice was made to avoid the seed and plate thicker layers of copper and tin on the upscaled substrate ($\sim$250 nm each), that showed not to peel off the substrate during the annealing process. The copper cations are provided thanks to 1 L of basic aqueous bath of $CuSO_4$ containing the following compounds with their respective concentrations: 3 M NaOH (Sigma-Aldrich, $\geq$ 98%), 0.2 M Sorbitol (Sigma-Aldrich, $\geq$ 98%), 0.1 M $CuSO_4 \cdot 7H_2O$ (Alfa Aesar, 99%) and 0.932 mM Empigen BB detergent (VWR, 30% in solution).

For the deposition of tin, an acidic tin bath is used containing the cations of interest, Sn^{2+} with the following composition: 1 M Methanesulfonic acid (Sigma-Aldrich, $\geq$ 99 %) , 50 mM Sn(II) methane sulfonate (Sigma-Aldrich, 50% wt.% solution in H_2O, 3.6 mM Empigen BB detergent (VWR, 30% in solution).

3.3 Configuration and deposition techniques for Ge-containing precursors

3.3.1 Summary of all precursors, with/out Ge

As mentioned previously, the electrodeposition of Ge from aqueous baths is difficult due to the competing hydrogen evolution [62]. Therefore to produce Ge-containing ternary and ternary alloy semiconductors, alternative deposition techniques avoiding this issue were employed outside of the UL. The depositions were performed by members of other institutions and the precursors further annealed and characterised at the University of Luxembourg. All the precursor configurations characterised within this work are presented in table 3.1 with references to the respective thesis chapters. Electrodeposition from an organic solvent and DC magnetron sputtering were used as alternative techniques to aqueous electrodeposition to study both the influence of deposition technique as well as varying stacking orders.

As it can be seen in Table 3.1, Cu/Sn stacks with no Ge were also DC sputtered, so additional

Precursor configuration	Technique	Provenance	Ref. Chapter	Target
Cu	ED (aq)	UL	4, 5	-
Cu/Sn	ED (aq)	UL	3, 7	-
	sputtering	HZB	7	(A)
Sn/Cu:Ge	ED (organic)	KU Leuven	4	-
Cu:Sn/Cu:Ge	sputtering	Uni.Liverpool	6	(A)
Cu:Ge/Cu:Sn	sputtering	Uni.Oldenburg	6	(B)
Cu:Sn/Cu:Ge/Cu:Sn	sputtering	Uni.Oldenburg	6	(B)
Cu:Ge/Cu:Sn/Cu:Ge	sputtering	Uni.Oldenburg	6	(B)

Table 3.1: Stacking configurations and origin of the various precursors used in this thesis. ED refers to the electrodeposition technique and sputtering to the DC-magnetron sputtering. Stacks are described by ”/” and codeposited elements by ”:”.(A) refers to DC magnetron sputtering from separate pure Cu, Sn or Ge targets and (B) to DC magnetron sputtering from binary Cu:IV targets with composition 64:36 at.%, respectively. References to the chapters of interest in this thesis are also given.

comparisons are possible between various techniques, stack orderings or annealings. Description of the DC sputtering and organic ED techniques are done in the next paragraphs.

3.3.2 Alternative deposition techniques for Ge-containing precursors

Coelectrodeposition of Cu and Ge from organic solvents

To avoid the hydrogen evolution reaction from aqueous electrolytes, co-electrodeposition of Cu-Ge on SLG/Mo/Sn was performed from an organic solvent. Dr J. Malaquias (KU Leuven, Belgium) successfully deposited homogeneous Cu_3Ge films from a propylene-glycol-based electrolyte at room temperature [63]. The resulting Cu_3Ge alloy showed a higher plating efficiency than pure Ge. The final Mo/Sn/Cu_3Ge precursors were annealed at the University of Luxembourg to form a CTGS alloy. Results are presented in Chapter 4.

Cosputtering of Cu-Sn and Cu-Ge

To study various Ge-containing precursor configurations without additional limitations due to the electrodeposition technique, the physical DC sputtering technique was employed to produce precursors in three different institutions: the University of Liverpool, the Helmholtz-Zentrum Berlin (HZB) and the University of Oldenburg giving us different stacking orders to anneal. Sputtering is a physical vapour deposition technique. It makes use of a high vacuum environment into which a low pressure of inert gas is added (typically Argon). The Ar atoms are ionised into a plasma by application of a DC voltage between the target and the substrate to be coated. By acceleration of those ions, they collide with the target and eject its atoms which come to condense onto the substrate. Electrons created during the ionisation process are accelerated to the substrate and collide with more Ar atoms, further ionising them so the sputtering continues. DC sputtering was used to produce Cu/Sn/Ge-containing precursors onto the standard SLG-Mo substrate, presented previously in table 3.1.

3.3.3 Interdiffusion

The as-deposited Cu-Sn and Cu-Sn-Ge precursors all have depth composition gradients, defined by their stacking configuration. To minimise its Gibbs free energy, a layered matrix tends to achieve a uniform atomic distribution. This uniformisation process occurs via atomic interdiffusion, starting at room temperature. Driven by concentration gradients, this mass transport via atomic motion occurs in solids via vacancy or interstitial diffusion. The kinetics of interdiffusion can also be increased by a pre-annealing thermal treatment of the precursors, called 'pre-alloying'. A pre-alloying treatment was performed on some precursors in this thesis to form a stable alloy. The interdiffusion will thus define the phases present in the precursors before their annealing. These phases are alloys that can either be intermetallic compounds (i.e mixtures of chemical elements with defined proportions), or solid solutions (i.e mixtures of chemical elements which are completely soluble in each other and could thus span a larger compositional range). In this work, the Cu-Sn, Cu-Ge and Ge-Sn binary systems constitute the three metallic interfaces that might be found in the precursors and could lead to various intermetallic or solid solutions. To acknowledge the possible existing phases in the precursors before their annealing it is thus relevant to look at existing phase diagrams for these three binary systems. The precursors used in this work are not subject to temperatures higher than 550°C during pre-alloying and annealing, to prevent degradation of the glass substrate. Therefore focus will be made on the temperature range from room temperature to 550°C, and the following phase diagrams are only shown up to 600°C.

The Cu-Sn system

When Cu and Sn are in contact, interdiffusion occurs already between both metals at room temperature. The interdiffusion occurs mostly via movement of the copper atoms into tin at the interface, as demonstrated by the high diffusion coefficient of copper atoms in a tin matrix at room temperature of $2.0\times10^{-10}\,m^2s^{-1}$ [64] (compared to the diffusion coefficient of tin atoms in a copper matrix, $1.3\times10^{-27}\,m^2s^{-1}$ [65]). Multiple Cu-Sn phases, such as bronze alloys, exist in the Cu-Sn phase diagram, as taken from [66] and presented in Fig.3.7. Below 350°C, the phase diagram shows the existence of the following phases: a Cu-rich solid solution with up to 10 at.% Sn, Cu_3Sn and Cu_6Sn_5 intermetallics, as well as a Sn-rich solid solution with up to 50 at.% Cu. Cu_6Sn_5 is known to form already at room temperature while Cu_3Sn forms when the precursors are annealed above 100°C [64] either when in copper excess or leaving Sn as a by-product. Elemental Cu and Sn can thus also be present in the precursor after alloying. Cu_3Sn has an eutectic point at 227°C for 0.5 at.% Cu, above which it thus becomes a liquid phase. The melting point of pure Sn (231.9°C) is therefore lowered by the slight presence of Cu atoms. From 350°C on, the Cu_4Sn intermetallic compound exists on the Cu-rich side of the diagram. To evaluate the nature of the alloy, electrodeposited Cu-Sn stacks are analysed with X-ray diffraction at room temperature before their annealing. The resulting diffractogram is shown in Fig. 3.8.

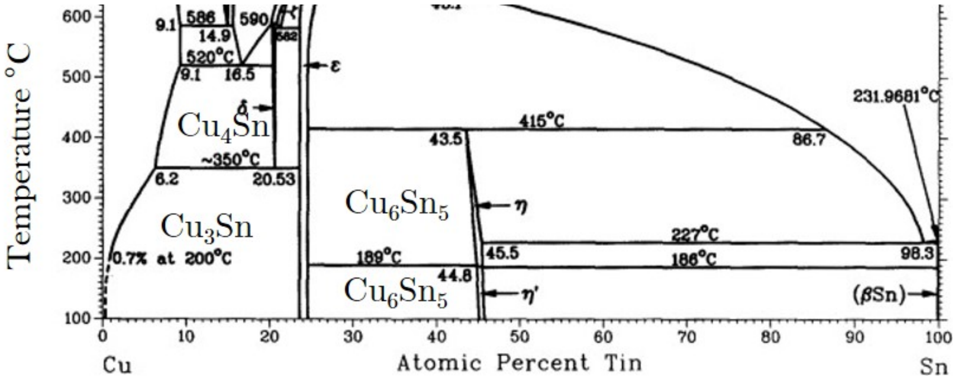

Figure 3.7: Cu-Sn phase diagram, as reproduced from [66] between 100 and 600°C.

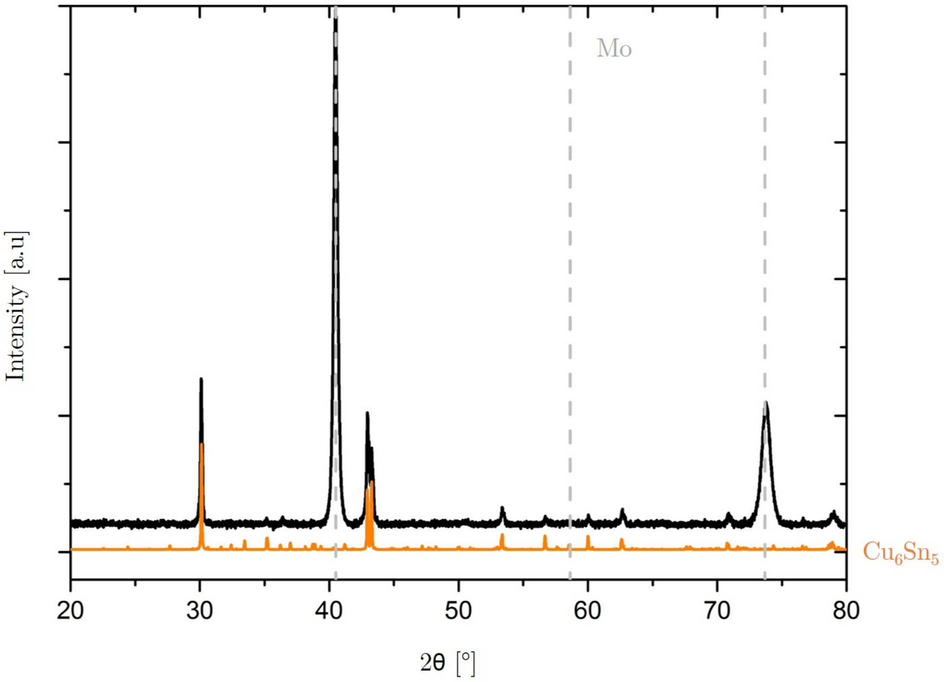

Figure 3.8: XRD of electrodeposited Cu-Sn stacked precursors at room temperature. The peaks relative to the Mo substrate are indicated by the dashed grey lines. Reference to the Cu_6Sn_5 alloy is given by the orange pattern taken from [47].

Fig. 3.8 demonstrates the existence of the Cu_6Sn_5 alloy in Cu-Sn precursors already at room temperature [41, 67].
As explained later in Chapter 4 the high vapour pressure of SnS during annealing leads to the formation of Cu-poor absorbers, for all types of precursors.

The Cu-Ge system

The interdiffusion of copper and germanium at room temperature is controlled by the movement of copper atoms into the germanium matrix [68]. The Cu-Ge phase diagram, as taken from [69] and presented in Fig. 3.9 shows the phases existing between 200°C up to 600°C as: a Ge-rich solid solution, the alloy Cu_3Ge (ε_1), a Cu-rich disordered alloy (ξ) and a Cu-rich solid solution with up to 10 % Ge at 550°C. Cu_3Ge was shown to exist at room temperature [63].

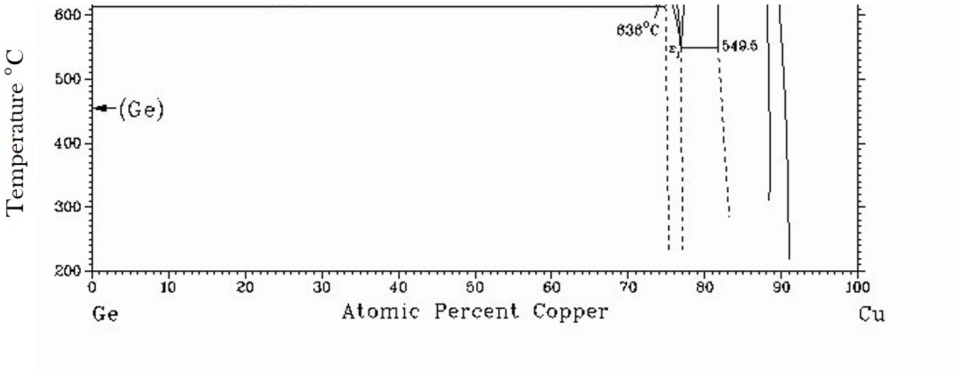

Figure 3.9: Cu-Ge phase diagram, as reproduced from [69].

Cu_3Ge is measured in sputtered Ge-based precursors with GI-XRD, as presented in Fig 3.10. As explained later in Chapter 4 the high vapour pressure of GeS during annealing leads to the formation of Cu-poor absorbers, for all types of precursors.

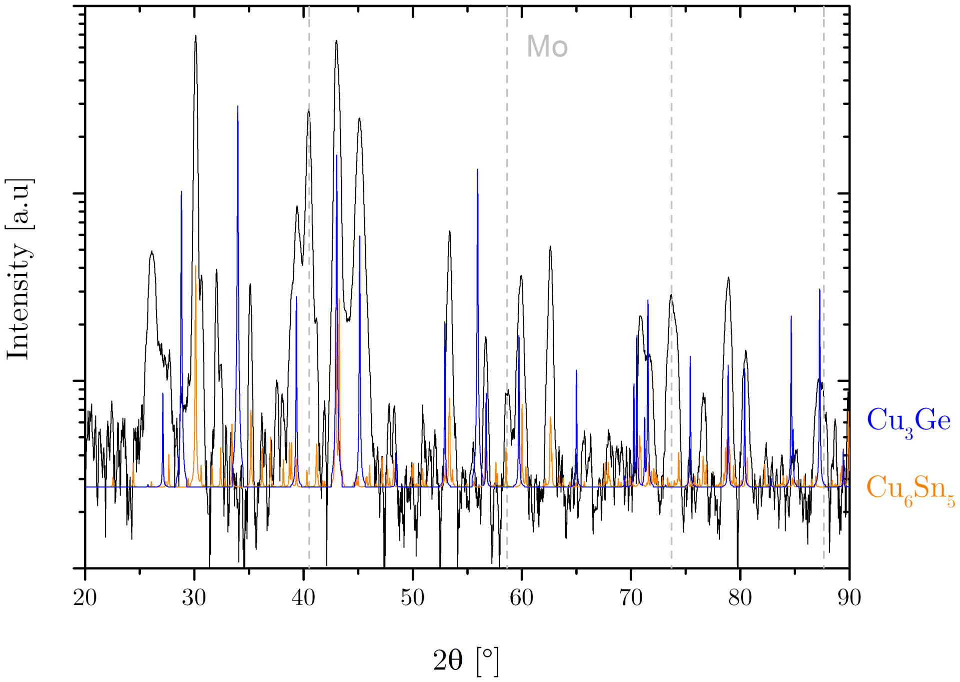

Figure 3.10: XRD of sputtered Cu:Sn/Cu:Ge stacked precursors at room temperature. The peaks relative to the Mo substrate are indicated by the dashed grey lines. Reference to the Cu_6Sn_5 and Cu_3Ge alloys are given by the orange and blue patterns taken from [47].

The Ge-Sn system

The Ge-Sn phase diagram, as reproduced from [70] and presented in Fig. 3.11 shows a very Ge-rich solid solution (Ge) (less than 1.1 at.% Sn), a continuous solid solution of Ge and Sn for most compositions and a solid solution of Ge in Sn (βSn) melting above the eutectic point at 232°C (which equals the melting point of Sn).

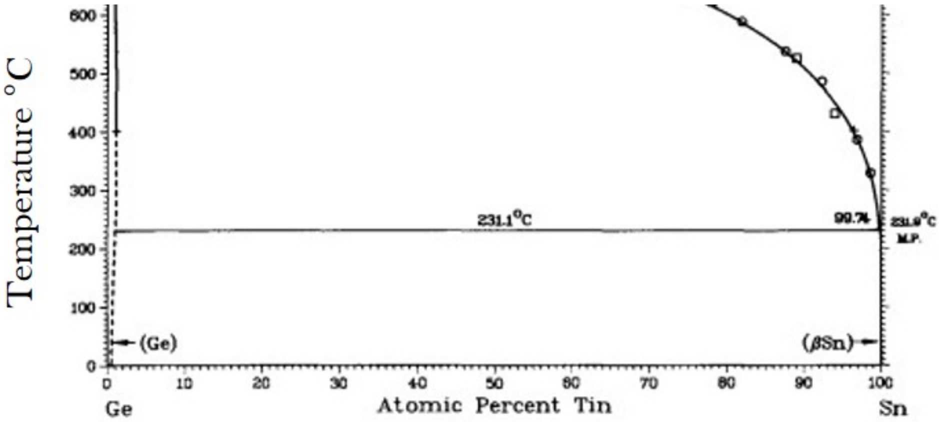

Figure 3.11: Ge-Sn phase diagram, as reproduced from [70], between 0 and 600°C.

Dewetting in Cu-Sn and Ge-Sn thin films

As seen in the phases diagrams of the Cu-Sn (Fig. 3.7) and Ge-Sn (Fig. 3.11) systems, the presence of Sn with a low melting point at 232°C affects the stability of solid compounds. Table 3.2 reports the melting points of the pure Cu, Ge and Sn at atmospheric pressure, demonstrating that only Sn is subject to melting in the annealing temperature range. As seen in the Cu-Sn diagram only a little bit of Cu incorporation suffices to lower the melting point of Sn. However, the domain of existence of the solid solution is low compared to the intermetallics (bronzes) with high melting points. The phenomenon worsens in the case of Ge-Sn which shows an extended eutectic for most compositions of the Sn-rich solid solution.

Chemical element	melting point (°C)
Cu	1085
Sn	232
Ge	931

Table 3.2: Melting points of pure Cu, Sn and Ge at atmospheric pressure.

Consequently, if Cu/Sn stacks are heated to temperatures above the melting point of Sn with a sufficiently high heating rate, Sn melts before Cu diffuses in the Sn matrix. This melting leads to uncoverage of the Mo substrate, and is called dewetting, as observed after attempts of prealloying in Fig. 3.12c).

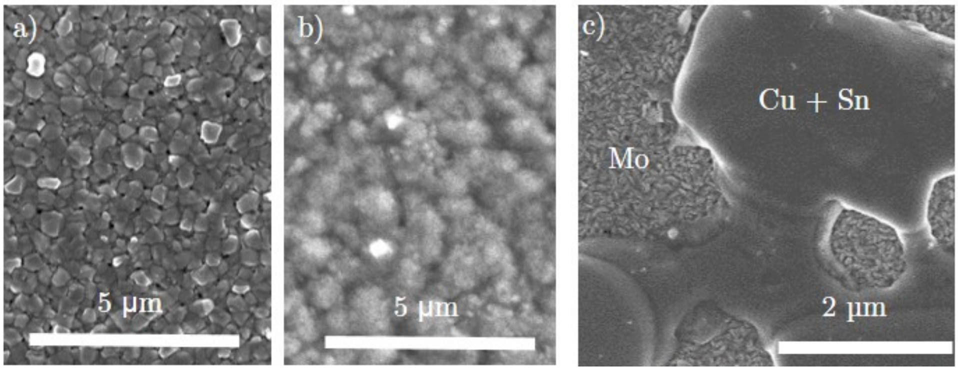

Figure 3.12: SEM top view of a) an electrodeposited Cu/Sn stack b) the same stack after pre-alloying to 250°C, c) the same stack after pre-alloying to 350°C.

If prealloying is to be made on the precursor stacks, one should thus be careful of the temperature and heating rate or dewetting occurs uncovering the substrate as in Fig. 3.12c). As a clear effect of surface improvement is not observed between Fig. 3.12a) and b), prealloying was not performed on the precursors before annealing. The case is worse for Ge-Sn, where the alloy formed will most likely always melt. In this work a decision was made to avoid this Ge-Sn interface, where dewetting definitely will lead to pinholes and thus shunting which is no good for solar cell applications. This explains why only Cu-Ge and Cu-Sn were chosen as the basis of alloys for the precursors in the synthesis of CTGS.

3.4 Conclusion of the chapter

The chapter presented the basics of aqueous electrodeposition used to deposit Cu or Cu and Sn stacks on SLG/Mo substrates. There, one concludes that the hydrogen evolution reaction is detrimental to the deposition of Ge, which explains the choice made in this work to have Ge deposited within the precursors from alternative techniques: electrodeposition from organic solvents and DC sputtering. In particular, the DC sputtering allowed to obtain various stacking orders of Cu:Sn and Cu:Ge alloys on Mo. Due to the low melting point of Sn, prealloying tests of Cu/Sn stacks showed dewetting which uncovers the substrate and can detrimental to future solar cells. It was chosen not to perform prealloying treatments on the precursors before annealing. The precursors described here are used in the following chapters where they are annealed in the presence of chalcogen and group IV chalcogen vapours to form CTS, CTSe, CGS and CTGS films. In order to study the formation path to CTS(e) and CGS layers during annealing a simple configuration of precursor is chosen: a single electrodeposited Cu layer.

CHAPTER 4

Annealing of Cu_2SnS_3, Cu_2GeS_3 and Cu_2SnSe_3 thin films

4.1 Goal

This chapter investigates the annealing of three candidate absorber layers for thin film solar cells: the ternary compounds Cu_2SnS_3 (CTS), Cu_2SnSe_3 (CTSe) and Cu_2GeS_3 (CGS). As demonstrated in the introduction to this work their sufficient light absorption above $10^4\,\mathrm{cm}^{-1}$ directly at the conduction band edge makes CTS, CTSe and CGS suitable candidates for the production of films with thicknesses down to two microns. After introducing in Chapter 3 the precursor deposition, the goal of this chapter is to investigate the growth of CTS, CTSe and CGS films during chalcogenisation of the metallic precursors. In this respect, I have chosen to anneal a single precursor layer of copper in chalcogen and group IV chalcogenide vapours. Three themes of interest will be first discussed in this chapter:

1. Background: theoretical assessment of thermodynamics and kinetics of reaction in the Cu-Sn-Ge-S and Cu-Sn-Se systems
2. Experiment: Time-resolved phase evolution studies during chalcogenisation of a metallic Cu precursor and derivation of the formation mechanism for the CTS, CTSe and CGS absorbers
3. Combined theoretical and experimental study of the generation of group IV chalcogenide species in a vapour as a rate-limiting step of the chalcogenisation process,

where parts 2 & 3 were published in Ref.[71]. Finally, these results are used at the end of this chapter to study the formation mechanism of the CTGS alloy, as an opening to the Chapter 6.

4.2 Background

Considering a solid chalcogen source X (S or Se) placed at a given distance ($\sim 2\,\mathrm{cm}$) from the edge of a metallic precursor M ($2.5 \times 2.5\,\mathrm{cm}^2$), both placed inside a thermally homogeneous graphite box (see Fig. 4.1), the formation of the chalcogenide compound from the precursor during annealing will be related to the mass transfer of reactants and the reaction rates. A kinetic reaction scheme for the reaction between M and X can be defined in three steps drawn in Fig. 4.1.

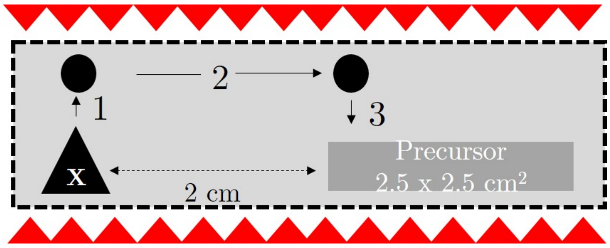

Figure 4.1: Schematics of the three processes (vapour generation, diffusion, reaction) for chalcogenide formation during annealing in the sealed and heated graphite box where the precursor lie together with a source of chalcogen X = S or Se (shown as a triangle). The filled circles correspond to the vapour molecules generated from the chalcogen source by sublimation.

1. Generation of the vapour phase from the chalcogen source X
2. Diffusion of the vapour phase to and over the entire precursor sample
3. Absorption & chemical reaction between the vapour phase and the precursor sample.

Once the chalcogen has reached the reaction front (2), thermodynamic conditions will determine whether the chalcogen metal reaction could be theoretically spontaneous (3).
In this background section, the equilibrium phase diagrams of the Cu-Sn-S, Cu-Sn-Se, Cu-Ge-S and their respective sub systems are first reported. Secondly the thermodynamics of chalcogen-metal reactions will be used to explain the relative stability of secondary phases. Thirdly, using the standard Gibbs free energy of formation the equilibrium partial pressure of X required for chalcogenisation of each of the metals will be determined. Finally, the temperature behaviour of the equilibrium vapour pressures of all species is presented, as a major indicator for the kinetics of generation (1).

4.2.1 The Cu-Sn-S, Cu-Sn-Se and Cu-Ge-S material systems

The Cu-Sn-S system

The Cu-Sn-S system was studied by Fiechter et al. with the report of 18 stable Cu-Sn-S phases of various stoichiometries (at all temperatures) [72], as shown in Fig. 4.2(a). The Cu_2S-SnS_2 tie line (shown in Fig. 4.2b)) was also studied by Olekseyuk et al. [73] where a smaller number of phases is reported (three on the tie line instead of nine in[72]).
The Cu_2SnS_3 phase is observed along the Cu_2S-SnS_2 tie line and was suggested as the most promising candidate for photovoltaic applications [74]. The tie line around Cu_2SnS_3 shows the existence of the copper-rich phase Cu_4SnS_4 or copper poor $Cu_4Sn_3S_8$ and $Cu_2Sn_4S_9$, that would be formed as secondary phases. Only more recently Baranowski et al. suggested a stability region for single phase Cu_2SnS_3 at about 300°C [21]. The outcome is shown in Fig. 4.3 and corresponds to a single temperature version of the survey triangle by Fiechter at al., shown in Fig. 4.2a). The single phase region is only a very narrow stripe on the Cu-Sn-S ternary diagram extending from Cu/Sn $\sim$ 1.6 to 2.7 and S/Sn $\sim$ 2.3 to 4.2. The narrow region is surrounded by three alternative Cu-Sn-S phases and SnS. Cu_4SnS_4 is found for low sulphur pressures, while at high pressures Cu_3SnS_4 and $Cu_4Sn_7S_{16}$ are found. However, the diagram suggests deviations

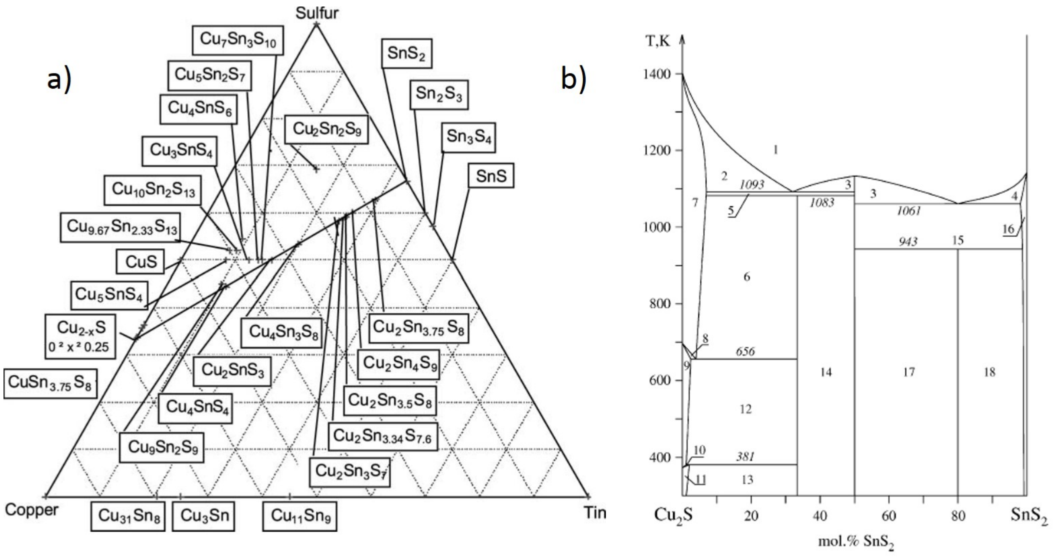

Figure 4.2: a) Survey of all Cu-Sn-S phases observed over all temperatures [72], b) Phase diagram of the Cu_2SSnS_2 system found in [73] with: (1) L, (2) L + α, (3) L + Cu_2SnS_3, (4) L + γ, (5) Cu_2SnS_3 + α, (6) Cu_4SnS_4 + α, (7) α, (8) α + α', (9) α', (10) α' + α, (11) α, (12) Cu_4SnS_4 + α, (13) Cu_4SnS_4 + α, (14) Cu_2SnS_3 + Cu_4SnS_4, (15) Cu_2SnS_3 + γ, (16) γ, (17) Cu_2SnS_3 + $Cu_2Sn_4S_9$, (18) $Cu_2Sn_4S_9$ + γ, where L refers to a liquid phase, α, α', α" to different Cu_2S phases and γ to an SnS_2 phase.

to the stoichiometry of 4 at.% (absolute) in composition can still produce single phase material while in CZTS, the single phase region does not extend above 1-2 at.% at the growth temperature [18]. Thus, it should be easier to avoid making secondary phases in Cu_2SnS_3, than in CZTS.

The Cu-Sn-Se system

The Cu-Sn-Se system is less investigated than the Cu-Sn-S system. The few reported Cu-Sn-Se compounds with other stoichiometries than Cu_2SnSe_3 can not be neglected but there is not enough evidence of their actual existence [75]: $Cu_4Sn_3Se_5$ has been observed once in the literature, Cu_3SnSe_3 is most probably representing the limit of Cu solubility in Cu_2SnSe_3 and Cu_2SnSe_4 another extension of the solid solution to Se-rich compositions. However Cu_2SnSe_3 is observed as a major Cu-Sn-Se phase with a congruent melting point at 695°C. The Cu_2S-$SnSe_2$ tie line [75] is shown in Fig. 4.4 It indicates a small solid solubility region (τ) for Sn in Cu_2SnSe_3.

The Cu-Ge-S system

The Cu-Ge-S system has also been less investigated than the Cu-Sn-S system. In literature only the Cu_2S-GeS_2 tie line was published by Khanafer et al. [76], as shown in Fig. 4.5. It shows the existence of two ternary compounds: the monoclinic Cu_2GeS_3 and the copper-rich Cu_8GeS_6. Cu_8GeS_6 has a phase change at 55°C from the low-temperature phase α (monoclinic) to the β-structure (orthorhombic).

Although no Cu-Ge-S ternary phase diagram has been published, due to the similar properties of group IV elements it is suggested that Cu_2GeS_3 should obey a similar diagram as Cu_2SnS_3

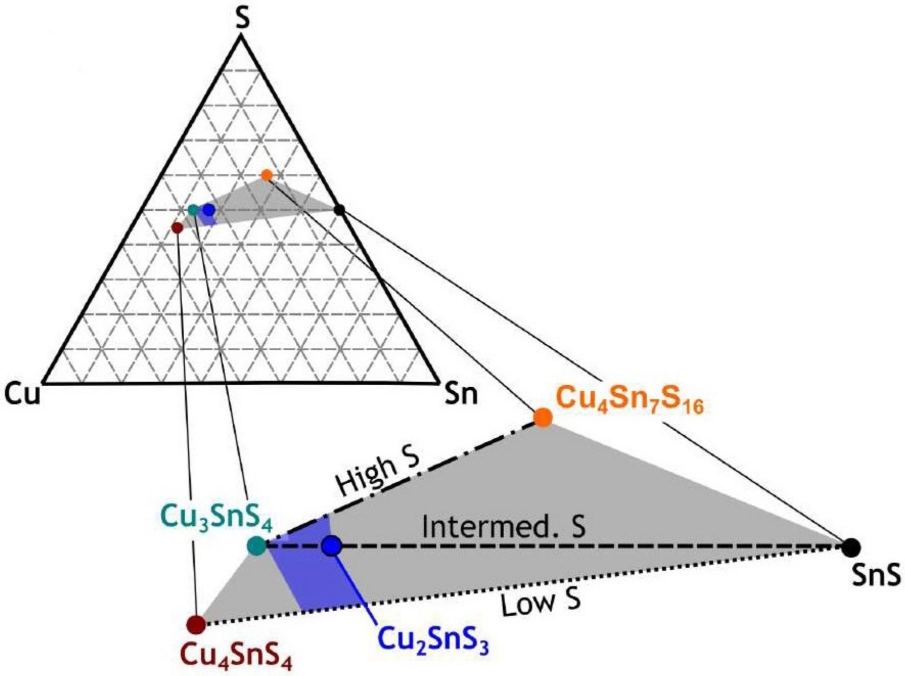

Figure 4.3: Cu-Sn-S phase diagram reproduced from [21], showing in blue the very narrow single phase space of Cu_2SnS_3. Library samples prepared under different sulphur partial pressures (at 275°C for the high and intermediate lines and at 325°C for the low line) have allowed the experimental assessment of the single phase space, surrounded by several alternative Cu-Sn-S phases.

with a narrow single phase region. Khanafer et al. also suggest that some phases might have been omitted on the tie line.

Nomenclature for composition

The general nomenclature used to describe the composition of a CTS, CTSe or CGS film is described in Table 4.1 where Sn and Ge are the two group IV components. As it is difficult to aim towards stoichiometry, corresponding to one point in the phase diagram, more frequently off-stoichiometric material is formed and thus final composition expressed in terms of copper and chalcogen (X = S or Se) poor or rich compositions. As seen previously, compositions with both Cu/Sn $\sim$ 1.6 to 2.7 and S/Sn $\sim$ 2.3 to 4.2 lie in the single phase region predicted in [21].

4.2.2 Chalcogenide metal binaries in the (sub) Cu-Sn-Ge-S(e) system

After report of the knowledge of Cu-Sn-S, Cu-Sn-Se and Cu-Ge-S systems, a closer look at the sub- systems is done in this section. The sub-system that is of interest regarding the annealing process corresponds to chalcogenide binaries, i.e the reaction of Cu, Ge and Sn metals with S or Se. All phase diagrams are shown up to temperatures of 600°C. First, sulphides are presented, followed by the selenide compounds. Only the Ge-Se diagram is absent because as explained

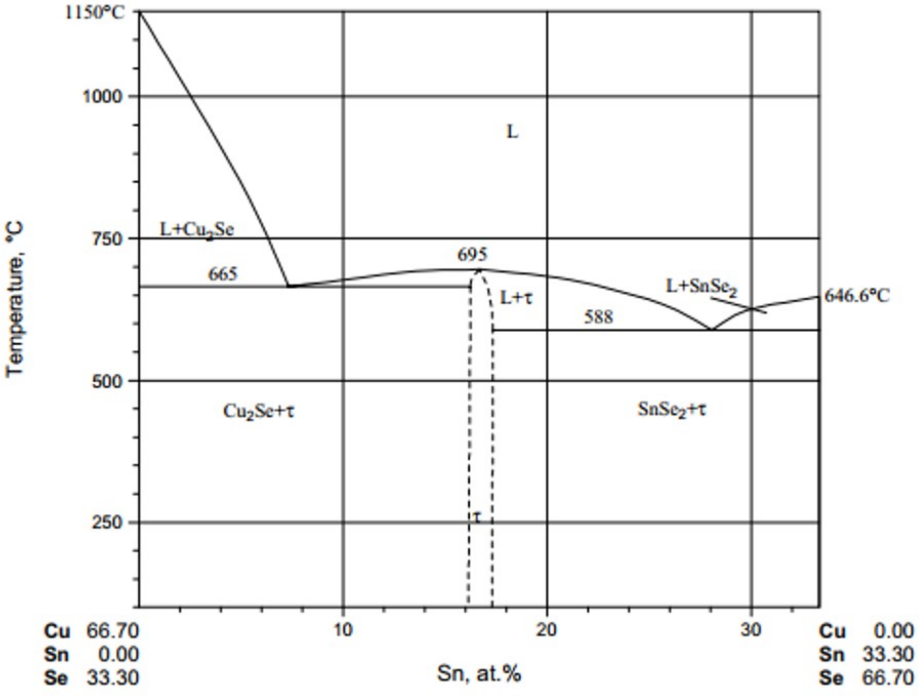

Figure 4.4: Phase diagram of the $Cu_2S-SnSe_2$ system, reproduced from [75].

	Cu-poor	stoichiometric	Cu-rich
Cu/IV	< 2	2	> 2
	S(e)-poor	stoichiometric	S(e)-rich
S(e)/IV	< 3	3	> 3

Table 4.1: Definition of Cu-poor vs Cu-rich and S-poor vs S-rich compositions in $Cu_2(Sn, Ge)S_3$ material. "IV" is used to describe contributions of group IV elements of the periodic table: Sn, Ge or Sn+Ge [at.%].

in the introduction, the Cu_2GeSe_3 ternary will not be studied in this work.

The Cu-S system

The phase diagram of the Cu-S system is shown in Fig. 4.6 [77]. Copper sulfides $Cu_{2-x}S$ ($x = 0...1$) are reported to be p-type semiconductors [78, 79]. Their conductivity decreases from copper rich ($x = 0$) to copper poor ($x = 1$) with charge carrier concentrations as high as 10^{21-22} cm^{-3} [79] down to 10^{12-13} cm^{-3} [78]. Direct bandgaps are reported between 1.2 and 3.1 eV [78–82]. Indirect bandgaps were also reported below 2 eV [79]. The uncertainty in the bandgap values is pretty large due to a broad range of compositions and bandgap determination methods.

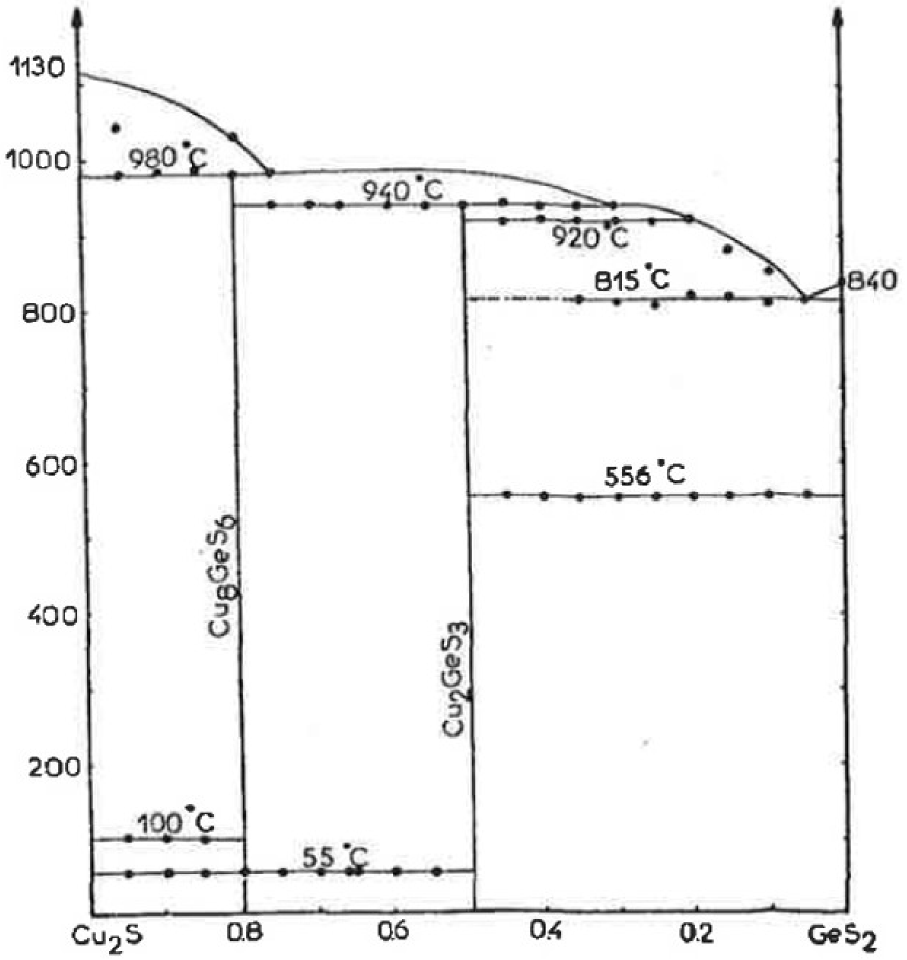

Figure 4.5: Phase diagram of the Cu_2S-GeS_2 system reproduced from [76].

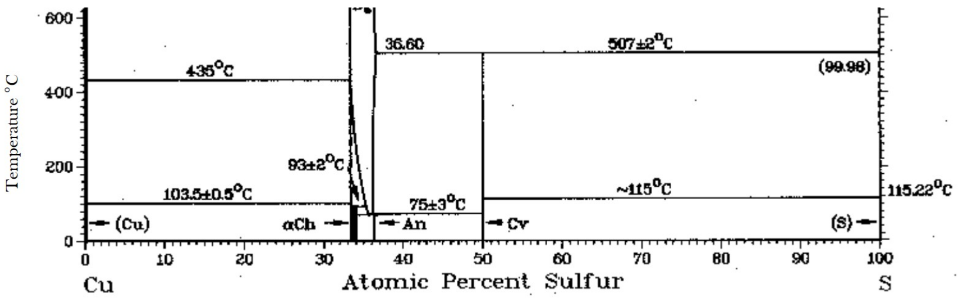

Figure 4.6: Cu-S phase diagram, as reproduced from [77] between 0 and 600°C.

Seven different Cu-S binary chalcogenides are observed in the phase diagram in Fig. 4.6. On the copper rich side of the phase diagram, the α-chalcocite Cu_2S phase (α-Ch) is shown to be stable between room temperature and 103.5°C following a monoclinic crystal structure. Above 103.5°C Cu_2S becomes hexagonal and is described as β-chalcocite. The chalcocite phase eventually decays into the less Cu-rich digenite phase $Cu_{2-x}S$ (cubic) above 435°C, where x has values below 0.3 [83]. The digenite phase is stable down to 72°C, under which it becomes the orthorhombic anilite phase Cu_7S_4. On the copper rich side of anilite, the monoclinic $Cu_{31}S_{16}$ phase, stable up to 72°C. Above 72°C this phase decays into the digenite $Cu_{2-x}S$ and chalcocite Cu_2S phases. On the copper poor side of the diagram, the hexagonal covellite phase CuS phase is present together with an orthorhombic solid solution of copper in sulphur with restricted copper miscibility. CuS is stable up to 507°C. Above this temperature it decays into digenite $Cu_{2-x}S$.

The Sn-S system

The phase diagram of the Sn-S system is shown in Fig. 4.7 [84]. The diagram shows the existence of three different phases with increasing amounts of sulphur: SnS, Sn_2S_3, and SnS_2. SnS crystallises in an orthorhombic structure (α). Tin monosulphide SnS is a p-type compound with charge carrier concentration in the order of $10^{13\text{-}16}\,\mathrm{cm}^{-3}$ [85]. It has a direct bandgap around 1.3-1.4 eV [85, 86]. Sn_2S_3 and SnS_2 are instead n-type semiconductors with higher optical bandgaps about 2.0 and 2.5 eV, respectively [87].

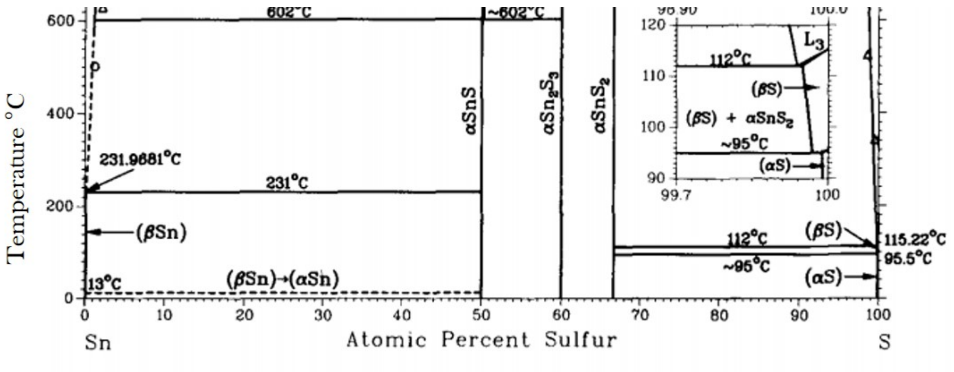

Figure 4.7: Sn-S phase diagram, reproduced from [84] between 0 and 600°C.

The Ge-S system

The phase diagram of the Ge-S system is shown in Fig. 4.8 [88]. Controversy exists on the properties of the germanium sulphide phases since they have been poorly investigated, for example, the bandgap of GeS is reported as both direct and indirect between 1.1 and 1.6 eV [89].

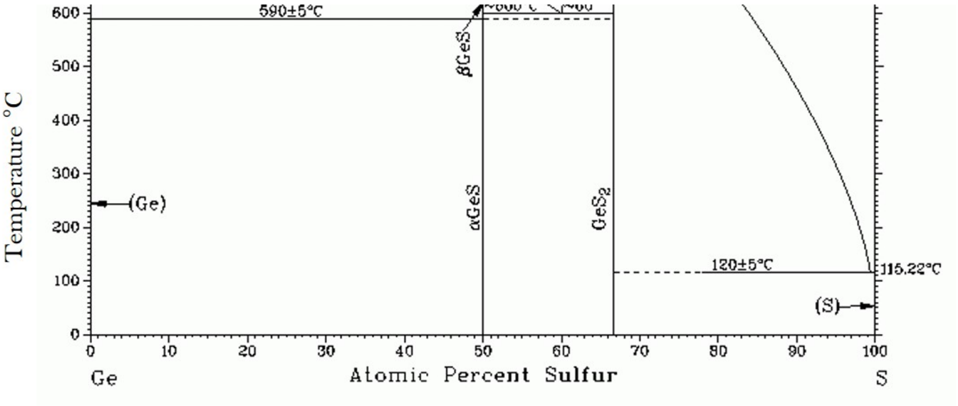

Figure 4.8: Ge-S phase diagram, reproduced from [84] where the temperature range used in this work is shown in grey.

The GeS phase was introduced by [90] as an orthorhombic phase (α), and is substituted by the orthorhombic GeS_2 on the germanium-poor side of the diagram.

4.2.3 The Cu-Se system

The phase diagram of the Cu-Se system is shown in Fig. 4.9 [91]. Copper selenides are reported to be p-type semiconductors with carrier concentrations as high as in copper sulphides around 10^{20-22} cm^{-3} [92]. Direct bandgaps are found between 2.0 and 2.3 eV and indirect from 1.25 to 1.5 eV [93].

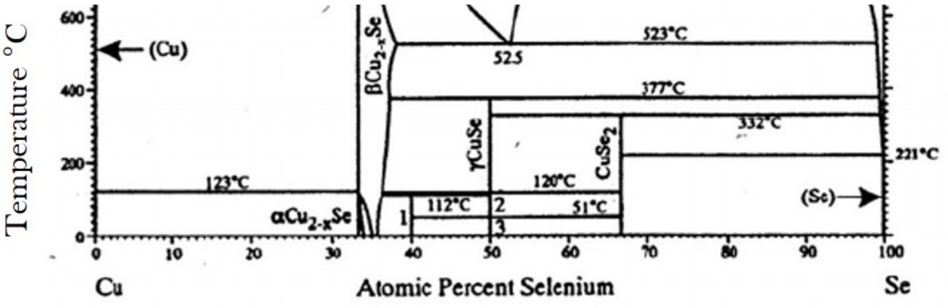

Figure 4.9: Cu-Se phase diagram, as reproduced from [91] between 0 and 600°C.

On the copper rich side of the phase diagram, the α-Cu_2Se phase is shown to be stable between room temperature and 123°C following a monoclinic crystal structure. Above 123°C it becomes cubic and is described as β-Cu_2Se. This phase extends to the Se side as $Cu_{2-x}Se$ with various values of x: the tetragonal Cu_3Se_2 stable up to 112°C, the hexagonal CuSe stable up to 51°C, the orthorhombic β-CuSe stable between 51 and 120°C, the hexagonal γ-CuSe stable between 120 and 377°C and finally the orthorhombic $CuSe_2$ stable up to 332°C. As also observed during the growth of $CuInSe_2$ [94]and more recently with Cu_2SnSe_3 [41], $CuSe_2$ melts incongruently at 332°C to CuSe and a Se-rich liquid, before CuSe converts to $Cu_{2-x}Se$ at 377°C. Thus, for $T > 377$°C we can write:

$$2\,\mathrm{CuSe}_{(\mathrm{s})} \leftrightarrows \mathrm{Cu}_{2-x}\mathrm{Se}_{(\mathrm{s})} + \mathrm{Se}_{(\mathrm{l})} \tag{4.1}$$

with:

$$\mathrm{Se}_{(\mathrm{l})} \leftrightarrows \mathrm{Se}_{(\mathrm{g})} \tag{4.2}$$

where $\leftrightarrows$ indicate reversible reactions.

4.2.4 The Sn-Se system

The phase diagram of the Sn-Se system is shown in Fig. 4.10 [84]. The diagram shows the existence of two different phases with increasing amounts of selenium: the orthorhombic SnSe and the hexagonal $SnSe_2$.

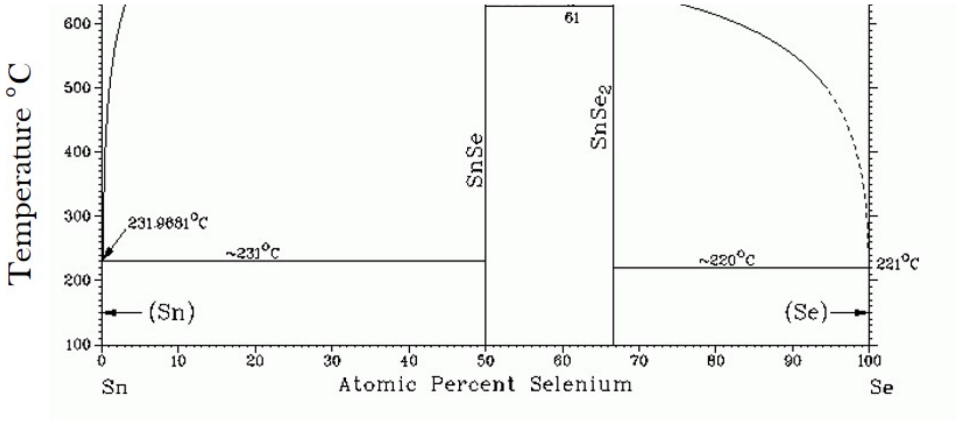

Figure 4.10: Sn-Se phase diagram reproduced from [84] between 100 and 600°C.

4.2.5 Thermodynamics and kinetics of chemical reactions

After the previous section introduced the expected ternary and binary chalcogenide phases in the Cu-Sn-S, Cu-Ge-S and Cu-Sn-Se systems in thermodynamic equilibrium, this section introduces the background theory of thermodynamics of chemical reactions. The section starts with a summary of the basic principles of equilibrium reaction theory before the free energies of the various possible formation reactions for chalcogenide metal binaries are shown. Finally, calculation of the minimum required partial pressures of chalcogen X for those binaries is performed together with the presentation of the vapour pressures of the most common elements and compounds in this quaternary system. More details on the theory of thermodynamics can be found in [95].

Gibbs free energy

The outcome of a chemical reaction is governed by both thermodynamics and kinetics. Kinetics have to do with reaction rates, determining whether a reaction occurs slowly or rapidly, while thermodynamics deal with energy changes and spontaneity. In thermodynamics, the Gibbs free energy G is the key to evaluating the spontaneity of a chemical reaction. Particularly the difference in Gibbs free energy between products and reactants of a chemical reaction $\triangle G$, which for constant p and T is expressed as:

$$\triangle G = \triangle H - T\triangle S \tag{4.3}$$

where $\triangle H$ is the change in enthalpy and $\triangle S$ the change in entropy. A positive $\triangle G$ indicates that the chemical reaction of interest is not spontaneous in the forward direction.

Any chemical reaction of the following form with A, B reactants, and C, D products (a, b, c, d indicating their respective amounts):

$$\mathrm{aA} + \mathrm{bB} \leftrightarrows \mathrm{cC} + \mathrm{dD} \tag{4.4}$$

is an equilibrium reaction, which as its name says, eventually reaches thermodynamic equilibrium. Equilibrium occurs when the rate of the forward reaction $aA + bB \rightarrow cC + dD$ equals the rate of the reverse reaction $cC + dD \rightarrow aA + bB$. At equilibrium reactants and products are thus both present in the system but due to the equal rates there is no net change in concentrations, i.e the reaction 'stops'.

Along with the reaction process until equilibrium, $\triangle G$ changes as proportions of reactants and products change and it reaches a minimum at equilibrium. Before the equilibrium $\triangle G$ can be expressed as:

$$\triangle G = \triangle G^0 + RT \ln Q \tag{4.5}$$

with $\triangle G^0$ the standard Gibbs free energy of formation (defined as the change in Gibbs free energy when one mol of a compound is formed at 1 bar from its elements in their standard states), R the gas constant and Q the reaction quotient.

Q is defined for the equilibrium reaction (4.4) as the ratio of activities 'a' of the respective products and reactants, such as:

$$Q = \frac{{a_C}^c \cdot {a_D}^d}{{a_A}^a \cdot {a_b}^b} \tag{4.6}$$

where the activity would refer to a partial pressure for a gas phase. For a solid or liquid phase, $a = 1$. At equilibrium, $Q = K_{eq}$ described as the equilibrium constant with:

$$K_{eq} = \exp(-\frac{\triangle G^0}{RT}), \tag{4.7}$$

from which $\triangle G^0$ can be extracted and substituted by its expression in Eq. (4.5), giving out:

$$\triangle G = RT \ln \frac{Q}{K_{eq}} \tag{4.8}$$

meaning that when $Q < K_{eq}$, $\triangle G < 0$ so the forward reaction will occur spontaneously, and vice-versa, until $Q = K_{eq}$.

Following Eq.(4.5) and (4.6) if the equilibrium reaction (4.4) corresponds to the sulphurisation of a solid metal M via a vapour of sulphur or selenium (described as $X_{(g)}$ for generalisation), of the following form:

$$\mathrm{M_{(s)}} + \mathrm{X_{(g)}} \leftrightarrows \mathrm{MX_{(s)}}, \tag{4.9}$$

then Eq.(4.5) resumes for this solid-vapour reaction to:

$$\begin{aligned}\triangle G &= \triangle G^0 + RT\ln\frac{a_{MX}}{a_M \cdot a_X},\\ \triangle G &= \triangle G^0 + RT\ln\frac{1}{1\cdot p_p},\end{aligned} \tag{4.10}$$

with p_p partial pressure of $X_{(g)}$.

Free energy of formation for binary metal chalcogenide phases

The chalcogenisation of metals during annealing correspond to equilibrium reactions in the form of Eq. (4.9). The main stoichiometric binary chalcogenide phases observed at thermodynamic equilibrium in the Cu-S, Sn-S, Ge-S, Cu-Se and Sn-Se phase diagrams of the previous section are: CuS, Cu_2S, SnS, Sn_2S_3, SnS_2, GeS, GeS_2, Cu_2Se, $CuSe_2$, SnSe and $SnSe_2$ with their formation reactions written as follows (assuming sulphur is present as S_2 and selenium as Se_2 in the gas phase - which is a correct approximation for $T > 330$°C and $p < 100$ mbar - details of allotropes are explicated in section 4.2.5):

$4\,Cu_{(s)} + S_{2(g)} \longrightarrow 2\,Cu_2S_{(g)}$
$2\,Cu_{(s)} + S_{2(g)} \longrightarrow 2\,CuS_{(g)}$
$Cu_{(s)} + Se_{2(g)} \longrightarrow CuSe_{2(g)}$
$4\,Cu_{(s)} + Se_{2(g)} \longrightarrow 2\,Cu_2Se_{(g)}$

$2\,Sn_{(s)} + S_{2(g)} \longrightarrow 2\,SnS_{(g)}$
$2\,Sn_2S_{3(s)} + S_{2(g)} \longrightarrow 4\,SnS_{2(g)}$
$4\,SnS_{(s)} + S_{2(g)} \longrightarrow Sn_2S_{3(g)}$
$2\,SnSe_{(s)} + Se_{2(g)} \longrightarrow 2\,SnSe_{2(g)}$
$2\,Sn_{(s)} + Se_{2(g)} \longrightarrow 2\,SnSe_{(g)}$

$2\,Ge_{(s)} + S_{2(g)} \longrightarrow 2\,GeS_{(g)}$
$Ge_{(s)} + S_{2(g)} \longrightarrow GeS_{2(g)}$

Table 4.2: Main chalcogenisation reactions in the Cu-S, Sn-S, Cu-Se, Sn-Se and Ge-S systems, whose thermodynamical data are found in literature [96–99].

From thermodynamical data found in literature ([96, 97] for Cu-S and Sn-S, [99] for Sn-Se and [98] for Ge-S), the Gibbs free energy of formation $\triangle G_f$ per mole X_2 for those compounds is calculated and plotted in Fig. 4.11a) as function of T ($350 \leq T \leq 600$°C). Each line indicates the equilibrium between the metal M, the chalcogen X and the corresponding binary metal chalcogenide MX.

Below the line pure M can be expected while above the line MX is favoured. The metals that show less negative values of the standard Gibbs free energy and appear higher up on the diagram are more stable and more likely to be found in their pure solid form. As we move towards the bottom of the diagram, towards large negative values of the Gibbs free energy of formation, M becomes progressively more reactive and MX becomes harder to reduce. Knowing the Gibbs free energy of formation of the MX it is possible to determine the critical partial pressure of chalcogen X required to avoid decomposition of the binary compounds. The partial pressures of X required to reach equilibrium can be calculated from equation (4.10) using the values of $\triangle G_f$ presented in Fig. 4.11a). The resulting partial pressures of all considered reactions are presented in Fig. 4.11b) as function of temperature. Each line on the graph represents the equilibrium between X, M and MX. If the partial pressure of X is below the equilibrium value, the chalcogenisation reaction lies more to the reactant side and the binary will dissociate to form the respective M and X. If the partial pressure of X is greater than the equilibrium partial pressure, the reaction likes more to the product side and the metal will be chalcogenised. In this

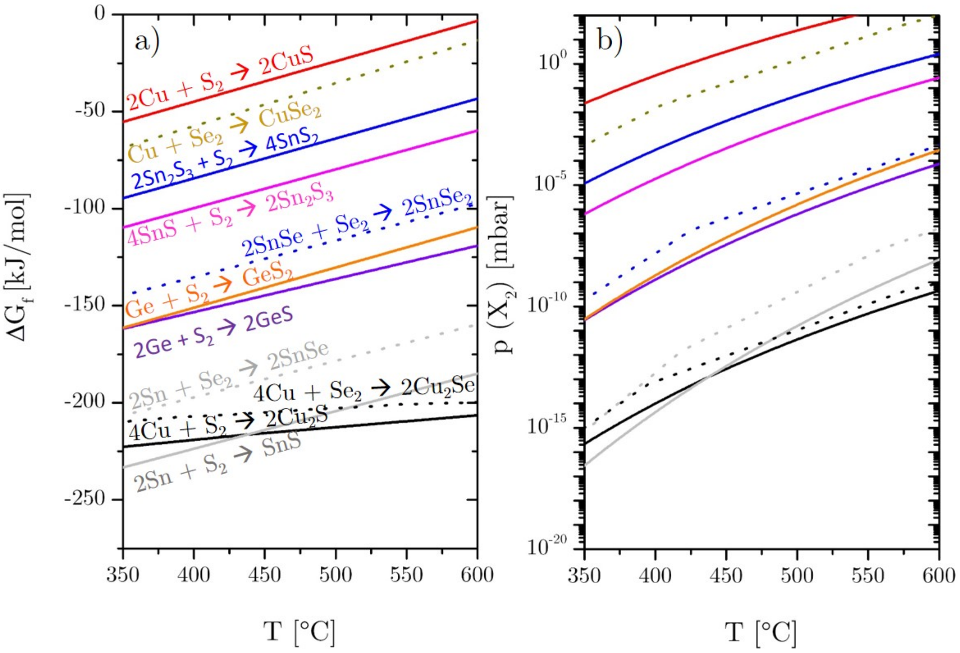

Figure 4.11: a) Temperature dependence of the Gibbs free energy of formation $\triangle G_f$ per mole of X_2 of the expected reactions in the Cu-S, Sn-S, Ge-S, Cu-Se and Sn-Se systems according to [96–99]. b) Minimum partial pressure of X_2 required to form the respective phases at equilibrium. Each color represents a unique chalcogenisation reaction, as labelled.

case the partial pressure of X will drop until the equilibrium pressure is reached. It is observed for example that to reach equilibrium a lower partial pressure of sulphur is required for SnS to form, than for GeS or CuS. Therefore in the case where the precursors and sulphur piles follow the heating ramp during the annealing and thus have the same temperature, we expect the sulphur vapor to react more readily with metallic Sn than with Cu or Ge for $T > 350$°C. But necessarily the kinetics of the process should also be considered, as sufficient chalcogen supply is required for these reactions to occur. The vapour pressures of these elements are reported in the next section as they give relevant hints on the generation of the vapour phases and should also be taken into account.

Vapour pressures

The vapour pressure of a species MX describes the pressure exerted by its vapour over the respective solid phase, following the reaction:

$$\mathrm{MX_{(s)}} \longrightarrow \mathrm{MX_{(g)}} \tag{4.11}$$

The temperature dependence of vapour pressures for all chalcogens X, metal chalcogenides MX and metal M species of interest in this work is presented in Fig. 4.12 between 0 and 1400°C [100–107]. The vapour pressures shown for S and Se represent the mixture of chalcogen allotropes, well approximated by their predominant species: S_8 and Se_6 for $T < 330$°C, S_2 and Se_5

+ Se_2 above (cf subsection 4.2.5). As seen in Fig. 4.12, S, Se, SnS, SnSe, $SnSe_2$ and GeS have high vapour pressures between 350 and 600°C, meaning they are highly volatile, while Cu, Sn and Ge metals are not in this temperature range. No Cu-S or CuSe vapour pressure is shown for the reason that the vapour pressures of Cu-X species are to be expressed as the vapour pressure of $X_{(g)}$ into which they decompose [108].

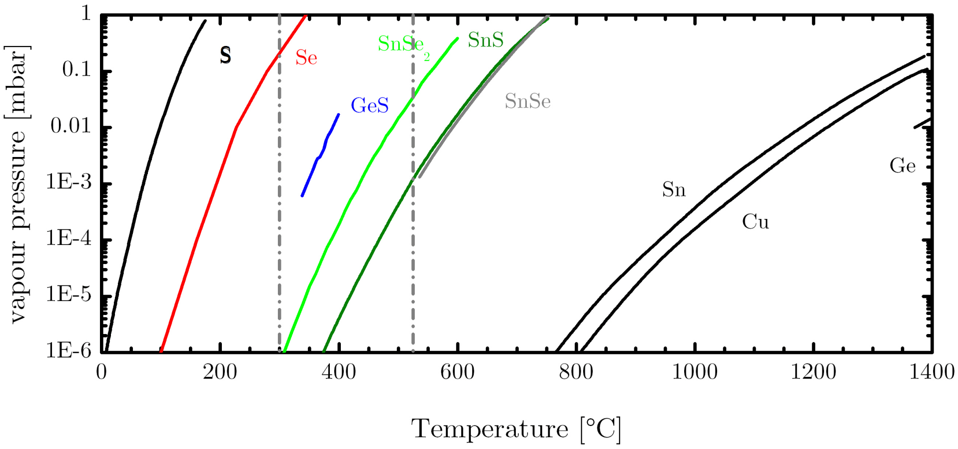

Figure 4.12: Vapour pressures of gaseous X (S, Se), MX (GeS, SnS, $SnSe_2$, SnSe) and M species (Sn, Cu and Ge) above their respective solid phase as function of temperature [100–107] shown between 0 and 1400°C.

Allotropes

Case of SnS, SnSe and GeS Other allotropes of binary chalcogenides may exist in the vapour phase, such as $SnSe_2$ reported to exist as a predominant tin selenide gaseous phase with a higher vapour pressure than SnSe [107], as shown in Fig. 4.12. Due to the scarcity of reports on the matter, no SnS_2 vapour analogue being reported at all and GeS_2 reported as vapour phase having a vapour pressure very similar to GeS [107], the $SnSe_2$ vapour species will not be considered further in this work.

Case of S and Se Sulphur and selenium both exist in a large number of allotropes. In the case of sulphur those various allotropes (S_2 to S_8 [109]) have been debated for a while, but more recent chemical potential calculations have shown the predominance of both S_2 and S_8 allotropes in most temperature regimes [110] but showing a high pressure dependence. For background pressures below 100 mbar in our system and $T < 330$°C, S_8 is shown to describe the gaseous mixture as the majority species while above this temperature S_2 predominates instead. For selenium, Se_6 is considered as the major species for $T < 330$°C while Se_5 and Se_2 become predominant at higher temperatures [99]. The vapour pressures of mixtures of S and Se allotropes can thus be approximated by the vapour pressures of the predominant allotropes. Fig. 4.12 shows the experimental vapour pressures curves.

4.3 Formation mechanism of CTS, CTSe and CGS

The first result section consists in the derivation of the formation mechanism for CTS, CTSe and CGS during annealing. For that, thin copper films electrodeposited on SLG/Mo are annealed in a tube furnace (Elite Thermal System Ltd - Type ”TSH12/38/250-2416”) to a maximum temperature T of 525°C for 30 minutes, sufficiently below the temperature where the SLG starts to bend and still providing sufficient thermal energy for grain growth [111]. The thermodynamics of the system at the reaction front are derived for these given kinetic conditions by analysis of the composition of the resulting CTS, CTSe and CGS films along the heating ramp.

4.3.1 Volatility of MX species

X and group IV-based species MX were reported in Fig. 4.2.5 to have high vapour pressures between 100 and 600°C. Investigations in the quaternary system of $Cu_2ZnSnSSe_4$ have shown Sn losses from the film via desorption of $SnSSe_{(g)}$ during annealing [112, 113]. The loss is diminished by adding a partial pressure of $SnSSe_{(g)}$ to the annealing atmosphere. As similar material systems, CTS and CTSe could similarly lose Sn via desorption of SnS(e)(g) during annealing. Respectively, CGS could lose Ge via desorption of GeS (g) following:

$$2\,\mathrm{Cu_2MX_{3(s)}} \rightarrow {}_2\,\mathrm{Cu_2X_{(s)}} + \mathrm{MX_{(g)}} + \mathrm{X_{2(g)}}, \tag{4.12}$$

Reaction (4.12) was shown to be spontaneous ($\triangle G < 0$) in the case of CTS when the annealing of a CTS film was performed in a high vacuum with a constant supply of $X_{2(g)}$ [114]. The film after only 1 hour of annealing only contained the binary Cu_2S. The Sn loss rate has been reduced in CZTS when an additional partial pressure of SnS was added to the annealing atmosphere [112]. During the annealing of CTGS(e) films, losses of group IV elements could be similarly expected and should be avoided.

4.3.2 Annealing with X and MX partial pressures

Supply of group-IV based chalcogenide powders

To compensate for group IV losses via desorption, additional MX supplies could be added to the annealing atmosphere in the form of solid powders. Prior to this work, it has been shown that a supply of $SnSe_{(g)}$ to the annealing environment decreases the amount of secondary Cu_2Se phases in CTSe films [41, 115]. This supply was insured via sublimation of a solid source of SnSe. The benefit of MX(g) during the annealing of CTS and CGS films was however not known until the start of this work. Only since then it has been employed in a few occurrences, mostly for CGS growth [29], without showing the investigation of its actual benefit. The relevance of SnS (g) has been only investigated during the growth of CZTS films where SnS (g) shows to be essential in the atmosphere to reduce Sn losses. We expect a similar outcome in the Cu-Sn-S system. Berg et al. [116] showed that CZTS can be formed from Cu-Zn precursors annealed in a S and $SnS_{(g)}$-containing atmosphere, as described by Eq. (4.13) [116]. Sn was provided during annealing only, showing completion of the formation reaction happened thanks to the sublimation of solid powder of SnS and reaction with the Sn-free precursors, following:

$$4\,\mathrm{Cu_{(s)}} + 2\,\mathrm{Zn_{(s)}} + 2\,\mathrm{SnS_{(g)}} + 3\,\mathrm{S_{2(g)}} \leftrightarrows \mathrm{Cu_2ZnSnS_{4(s)}} \tag{4.13}$$

We want to evaluate the importance of having both X and MX partial pressures during the annealing process and the impact on composition of the CTS, CTSe and CGS thin films. Fig. 4.13 presents a schematic of the heated zone of the annealing furnace used in this work, consisting of a graphite box enclosed within a quartz tube. The precursor sample to anneal is always introduced in the middle of the graphite box, at a constant distance from the powder supplies on the left-hand side of it. The powders supplies consist in the chalcogen X and the additional binary chalcogen MX previously mentioned, highlighted in red in Fig. 4.13, and described in Table 4.3.

Semiconductor compound to be formed	CTS	CTSe	CGS
Annealing of Cu with powders of:	S and SnS	Se and SnSe	S and GeS

Table 4.3: Description of powder supplies added to a copper layer for synthesis of CTS, CTSe and CGS semiconductors during annealing

The quartz tube around the graphite box is filled with a pressure of inert gas suggested, instead of vacuum, as a necessary background to slow down the film decomposition back into chalcogenide binaries [41, 114]. Since the species from the solid supplies are highly volatile due to their high vapour pressures, an additional background pressure of forming gas p_{back} allows to build up a longer lasting partial pressure within the graphite box, and thus allow longer time for the ternary formation to occur. We make use of forming gas H_2/N_2 as background inert gas (mixture of H_2 and N_2 gases with ratio 10%/90%). Pure N_2 or Ar are more commonly used as background inert gases for the annealing of thin films [117], but H_2-assisted annealing processes have been shown to be beneficial for solar cell applications, at least in CIGS [118], and forming gas usage avoids the toxic $H_2(S, Se)$. Assuming a high thermal conductivity of graphite and glass, it is considered that all elements within the heating zone follow the same heating ramp shown in Fig. 4.14 as also measured with a thermocouple, thus $T_{precursor} \sim T_{powders}$. Before the start, the entire annealing zone is filled with high purity nitrogen N_2 and forming gases H_2/N_2 to atmospheric pressure and further vented to the lowest reachable pressure (low vacuum $\sim 10^{-3}$ mbar). After this, the furnace is re-filled with p_{back} and the heating ramp follows a rate of approx. $0.5\,°\mathrm{C/s}$ (determined by linear fitting of the slope in Fig. 4.14) to the wished annealing temperature (e.g 525°C in this case) where it stays for a tunable duration (usually thirty minutes). At this point, the furnace cools down naturally to room temperature.

Using this annealing system we want to quantify the importance of both chalcogen and group IV chalcogen partial pressures on the S/IV and Cu/IV ratio. Starting from this the simplest formation reaction to the compound can be written as a reversible reaction such as:

$$2\,\mathrm{Cu_{(s)}} + \mathrm{MX_{(g)}} + \frac{2}{\mathrm{x}}\mathrm{X_{x(g)}} \rightleftharpoons \mathrm{Cu_2MX_{3(s)}} \tag{4.14}$$

where the allotrope form of X (thus its subscript x) depends on temperature (see subsection 4.2.5 for details) and $MX_{(g)}$ and $X_{x(g)}$ are vapour species coming from the sublimation of the solid powders of $MX_{(s)}$, and $X_{(s)}$. As the temperature rises the generated vapour phases react with the copper layer, as observed during Kesterite formation [116] and following the three steps explicated in the introduction in Fig. 4.1. The idea is to verify this formation reaction experimentally, noticing that if true, its equilibrium could easily depend on the partial pressures of the two vapour phases.

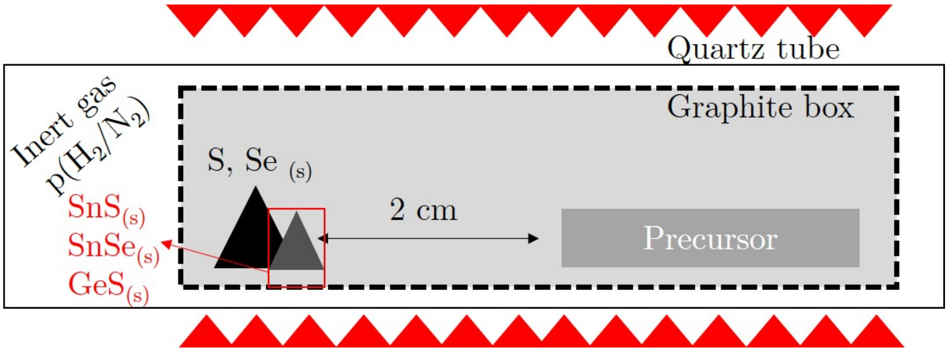

Figure 4.13: Annealing furnace configuration showing the precursor sample in the graphite box with chalcogen and group IV chalcogen powders, surrounded by inert gas H_2/N_2 in a sealed space.

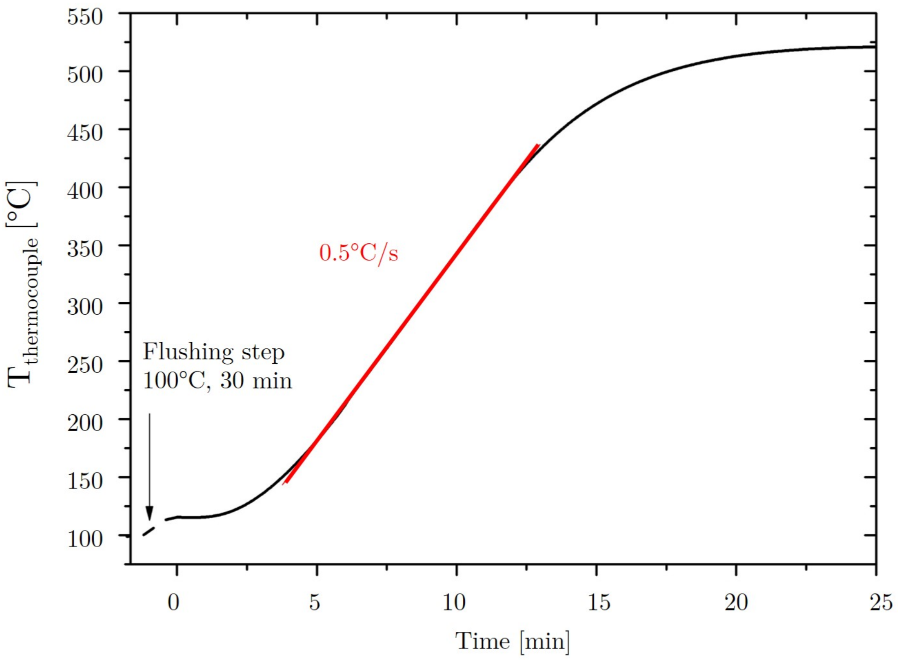

Figure 4.14: Heating ramp of the used annealing furnace, evaluated with a thermocouple, showing the increase of temperature to 525°C directly after the flushing step at 100°C. After the annealing is complete the heating stops and the oven cools down to room temperature in a few hours (not shown). The heating rate is evaluated from the slope of the ramp.

4.4 Assessment of formation reactions

To verify the formation reaction of the CTS, CTSe and CGS, i.e investigate phase formation and the importance of the partial pressures of X and MX vapour phases in approaching target composition, copper layers (SLG/Mo/Cu, refer to Chapter 3 for details about the precursor deposition) were annealed to temperatures from 300 to 525°C in the presence of sources of

X and MX, as shown in the furnace in Fig. 4.13 and described in Table 4.3. Details on the provenance, purities, and amounts of the X and MX sources used are given in Appendix A. In this way the resulting composition and crystallographic structure are studied along the heating ramp. All reference patterns of XRD are taken from the ICDD database and referenced in Appendix B.

4.4.1 Chalcogenisation of the metallic precursors

Formation of $Cu_{2-x}(S, Se)$ from Cu

Annealing to 300°C: formation of CuS and $CuSe_2$ Fig. 4.15 presents GI-XRD recorded on the copper samples annealed to 300°C with immediate cooling. Fig. 4.15a) recorded on copper annealed in S and SnS at 300 °C shows the presence of the CuS phase only. There is no trace of a Sn-related phase in the XRD and the SnS powder in the box remained visibly intact. EDX studies (sensitive down to 1 at.%) done in parallel on individual grains confirmed this absence of Sn [120]. This means only the vapour sulphur phase has reacted with the sample and not the tin sulphide. The observed CuS is expected from the copper-sulphur phase diagram at this temperature (cf.section 4.2.2). The copper sample annealed in S and GeS shown in Fig. 4.15c) gives the same result with only CuS present. No trace of Ge is detected in the sample. The copper annealed in Se and SnSe to 300°C in Fig. 4.15b) shows instead the presence of the $CuSe_2$ binary, in agreement with the copper-selenium phase diagram (cf. section 4.2.3), and again no Sn. Therefore at 300°C the SnS, SnSe and GeS powders have not reacted with the

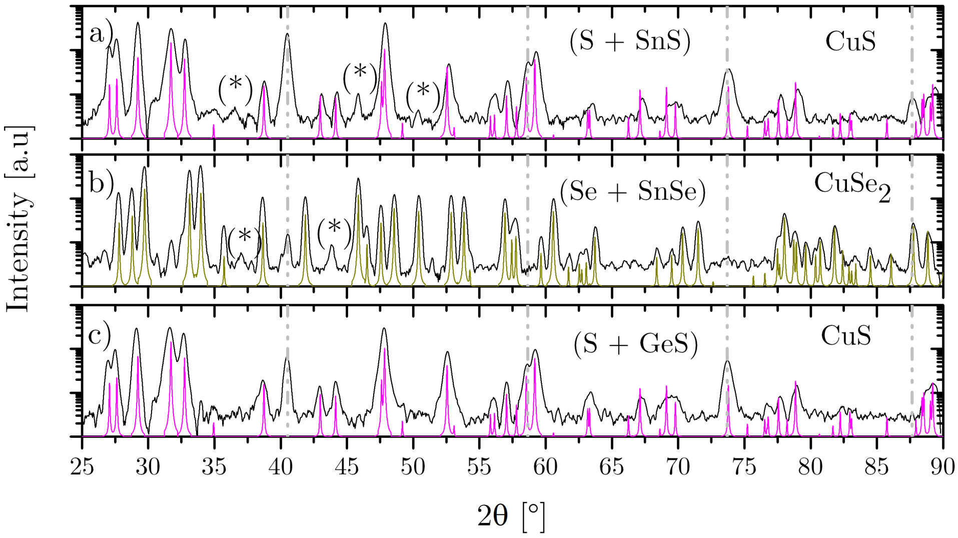

Figure 4.15: GI-XRD of the copper layer annealed up to 300°C following by immediate cooling, in the presence of a) S and SnS powders, b) Se and SnSe powders, c) S and GeS powders. The pink pattern corresponds to covellite, CuS, and the green to marcasite, $CuSe_2$. The dashed grey lines indicate the contribution of the Mo substrate. Potassium cyanide, KCN, is known as an etchant for copper sulphide phases [119]. Unidentified peaks labelled with a star disappeared with the rest of the peaks after KCN etching [30] and are thus attributed to various minor non stoichiometric Cu-S (or Cu-Se) binaries.

sample yet, but only the pure chalcogen S and Se that have 10^4 times higher vapour pressures than the binaries at this temperature (above 0.1 mbar for the chalcogens and below 10^{-6} mbar for the binary chalcogens) as seen in Fig. 4.12).

The difference in vapour pressure explains the first reaction of S and Se species with the copper. The reaction with the SnS, SnSe and GeS species is only expected for $T > 300°C$ where they have higher vapour pressures and therefore provide stoichiometric amounts of group IV elements. Considering the predominant allotropes of the chalcogens for $T < 330°C$ (cf subsection 4.2.5), the first two chemical reactions can, therefore, be written as follows:

$$\mathrm{Cu(s)} + \frac{1}{8}\mathrm{S}_{8(\mathrm{g})} \rightarrow \mathrm{CuS}_{(\mathrm{s})} \tag{4.15}$$

corresponding to reactions in Fig. 4.15a) and c), while for b)

$$\mathrm{Cu}_{(\mathrm{s})} + \frac{1}{3}\mathrm{Se}_{6(\mathrm{g})} \rightarrow \mathrm{CuSe}_{2(\mathrm{s})} \tag{4.16}$$

This is only an intermediate step in the formation of the absorber layers, thus similar annealings are performed at higher temperatures.

Annealing to 400°C: formation of $Cu_{2-x}(S, Se)$ Here the case of SnS is considered first, where a copper layer is annealed in the presence of S and SnS up to 400°C for 30 minutes. GI-XRD is performed on the sample extracted out of the oven after cooling down to room temperature. The resulting diffractogram is presented in Fig.4.16. It shows the presence of the CuS binary together with the copper-rich Cu_9S_5 binary at 400°C. Similarly to the sample annealed at 300°C, neither metallic Sn nor SnS binaries are detected in the sample with WDX and XRD. The diffractogram shows minor unidentified peaks, that disappeared after KCN etching, similarly to the 300°C samples, and are therefore attributed to non stoichiometric Cu-S binaries.

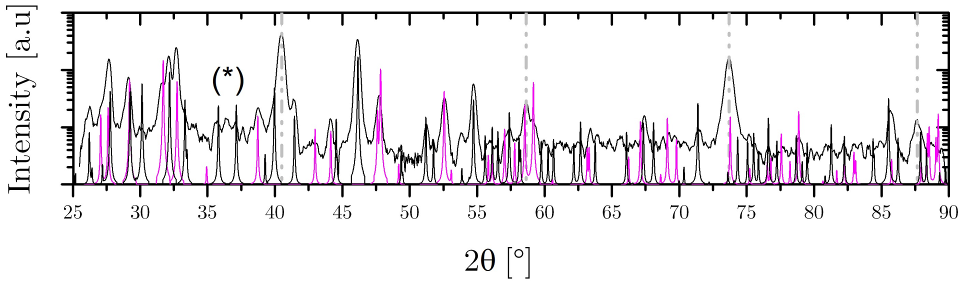

Figure 4.16: GI-XRD of the copper layer annealed up to 400°C for 30 minutes in the presence of S and SnS powders, followed by immediate cooling. The pink pattern corresponds to covellite (CuS) and the black to Cu_9S_5. The dashed grey lines indicate the contribution of the Mo substrate. Unidentified peaks labelled with a star disappeared with the rest after KCN etching [30] and are thus attributed to various minor non stoichiometric Cu-S binaries.

The transition from the CuS to the Cu_9S_5 binary is predicted from the phase diagram at 507°C (cf. section 4.2.2 [77]) but happens at lower temperatures here, suggesting that sulphur escapes the graphite box. This is also seen as sulphur comes to condense on the cold sides of the quartz tube outside of the graphite box. The reaction occurring here between copper sulphide phases is described as a decomposition reaction, written as follows, considering S_2 as the predominant sulphur allotrope for temperatures >330°C [110]:

$$2\,\mathrm{CuS}_{(s)} \rightarrow \mathrm{Cu_2S}_{(s)} + \frac{1}{2}\mathrm{S}_{2(g)} \tag{4.17}$$

so the covellite CuS transforms to chalcocite Cu_2S via desorption of $S_{2(g)}$ (as previously mentioned in section 4.2.5). The absence of Sn in the sample can be again explained by the low vapour pressure of SnS ($< 10^{-5}$ mbar) at this temperature. The absence of Sn is therefore also expected if copper was annealed with Se and SnSe as p(SnSe) $\sim$ p(SnS). However the equilibrium vapour pressure of GeS is 10^4 times higher than SnS or SnSe, thus the presence of Ge could be expected in the sample at 400°C and the hypothesis will be checked in the next subsection.

When copper is annealed with Se and SnSe, no tin is expected but a look at the Cu-Se phase diagram in section 4.2.3 with Eq.(4.1) and (4.2) suggest that under a high vapour pressure of $Se_{(g)}$, $Cu_{2-x}Se(s)$ would coexist with CuSe(s) in thermal equilibrium. The similarity between copper sulphide (Eq.(4.17)) and copper selenide (Eq.(4.1)) decomposition reactions is to be noted, but the liquid selenium phase resulting from the copper selenide binary is detrimental for both morphology and composition. A copper sample was annealed up to 390°C for 30 minutes in the presence of Se and SnSe and the following EDX analysis confirmed Eq. (4.1). The resulting EDX shows a tin-free sample with a very open morphology where various copper selenide binaries with stoichiometries from 1.8:1 ($Cu_{2-x}Se(s)$) to 1:1 (CuSe) coexist. The open morphology observed where the substrate is exposed between the grains is a detrimental source of shunt paths for future solar devices if they are not filled during the final synthesis steps. The next step is to increase the temperature and see if Sn reacts with the sample (and investigate the case of Ge).

Annealing to 450°C: formation of low temperature Cu-Sn-S ternary A copper sample is annealed to 450°C for 30 minutes in presence of S and SnS powders. The resulting GI-XRD presented in Fig. 4.17 shows again the copper rich binary Cu_9S_5 together with a Cu-Sn-S ternary compound. This pattern associated with the ternary fits the best with the reference pattern for cubic Cu_2SnS_3 from the ICDD database [47]. Among available reference diffractograms for Cu-Sn-S phases, the cubic CTS is concluded to have the best cross-comparison of peaks to the measured data. However neither a SnS phase is observed in XRD, nor Sn-rich compositions are measured with EDX, revealing that the reaction between the vapour of SnS and solid Cu_9S_5 must be immediate when SnS(g) reaches the sample.

A copper sample is annealed to 480°C for 30 minutes in presence of S and GeS powders. The resulting GI-XRD presented in Fig. 4.18 shows, similarly to the case of the annealing in SnS, a Cu-Ge-S ternary compound associated with the reference pattern for cubic Cu_2GeS_3 [47]. The absence of copper sulfides can be explained by the higher annealing temperature used for this run.

However due to the higher vapour pressure of GeS compared to SnS and SnSe (cf Fig. 4.12), it would be expected that the reaction of GeS(g) with copper sulphide happens at lower tem-

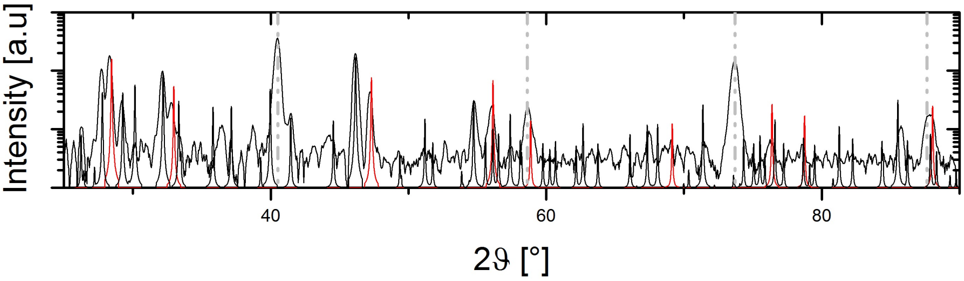

Figure 4.17: GI-XRD of the copper layer annealed up to 450°C for 30 minutes, followed by immediate cooling, in the presence of S and SnS powders. The black pattern corresponds to Cu_9S_5 and the red to cubic Cu_2SnS_3.The dashed grey lines indicate the contribution of the Mo substrate.

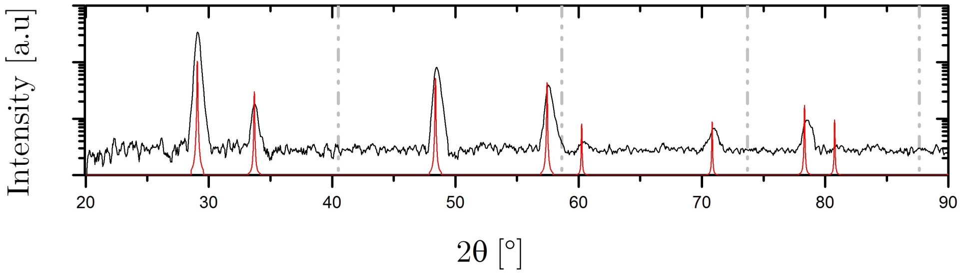

Figure 4.18: GI-XRD of the copper layer annealed up to 480°C for 30 minutes, followed by immediate cooling, in the presence of S and GeS powders. The red pattern corresponds to cubic Cu_2GeS_3.The dashed grey lines indicate the contribution of the Mo substrate.

peratures. It should be noted that at 350°C, the equilibrium vapour pressure of GeS equals the vapour pressure of SnS at 450°C when Sn reacts with copper sulphides. The formation of Cu_2GeS_3 is thus expected at 350°C. This hypothesis will be tested in the next section.

4.4.2 Uptake of group IV vapour species MX

Reaction of $MX_{(g)}$ with Cu-S is limited by stoichiometry

To check for the hypothesis that GeS(g) should react with Cu-S at lower temperatures than SnS(g) a copper sample is annealed up to 350°C in presence of GeS and S powders. At this temperature the vapour pressure of GeS equals the vapour pressure of SnS at 450°C, so the formation of the CGS ternary would be expected (cf Fig. 4.12).

The resulting XRD, presented in Fig. 4.19, shows instead the absence of GeS in the sample, or even Ge, as determined with WDX analysis. Only CuS is detected in the sample, giving the same pattern as in Fig.4.15. GeS is thus only present as a vapour above the sample and/or as a condensate on the CuS at this stage of the annealing and these results suggest that the

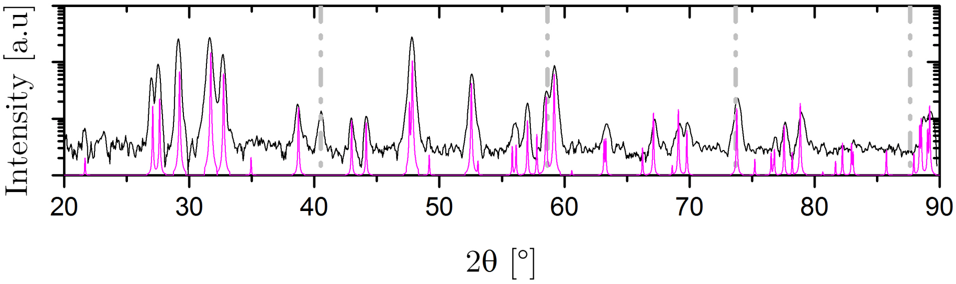

Figure 4.19: GI-XRD of the copper layer annealed up to 350°C for 30 minutes, followed by immediate cooling, in the presence of S and GeS powders. The pattern is identical to Fig.4.15 at 300°C, giving the single CuS phase. The dashed grey lines indicate the contribution of the Mo substrate.

sufficient vapour pressure of the metal chalcogenide and thus its presence above the sample and/or on the sample is not sufficient for the reaction between CuS and GeS to happen. Instead, the stoichiometry of the copper sulphide may be relevant and required to be copper rich (1.8:1) for the direct reaction of SnS or GeS with the sample to happen, and form the final ternary compound, i.e $\triangle G < 0$.

Formation of monoclinic $Cu_2(Sn, Ge)S_3$ via direct reaction with $Cu_{2-x}(S, Se)$

Annealing up to 525°C The annealing of copper layers is repeated up to the final temperature of 525°C for 30 minutes. The resulting XRD are presented in Fig. 4.20 for a) S and SnS, b)S and GeS and c) Se and SnSe. They indicate the formation of monoclinic CTS, CGS and CTSe, respectively, which present a different diffractogram than the cubic phase observed at annealing temperatures below 500°C. This phase transition was observed in other CTS samples prepared from Cu-Sn alloyed precursors [54], suggesting that the annealing temperature has an impact on the arrangement of Cu and Sn cations around the sulphur anions in the crystalline structure [54]. Results on the investigation of the crystalline structure for CGS are presented in Chapter 5. In Fig. 4.20, the monoclinic CTS and CGS samples appear as single phase ternary compounds with the exception of the very few minor and unidentified peaks indicated by arrows. On the other hand, CTSe coexists with the $Cu_{2-x}Se$ binary. Looking back to Eq.(4.1) it means some CuSe decomposed into $Cu_{2-x}Se$ via the escape of selenium vapour from the box, thus decreasing its partial pressure. The reaction with SnSe(g) is however still incomplete, compared to the case of SnS. This suggests either that the partial pressure of SnSe(g) is insufficient to fulfil the ternary formation (i.e low mass transport for the duration of annealing) or that the free energy of formation of CTSe is very close to the free energy of formation of its binaries so that binaries and ternary coexist.

To check for the hypothesis, another copper precursor was annealed in presence of more Sn. The tin was provided directly to the precursor, as an additional layer electrodeposited on top of the copper (cf Chapter 3). The resulting sample showed a reduced amount of $Cu_{2-x}Se$ on its surface, and more CTSe instead. However the reaction, despite the additional Sn layer, has not reached completion. Therefore we expect the free energies of formation of CTSe and its binaries to be close.

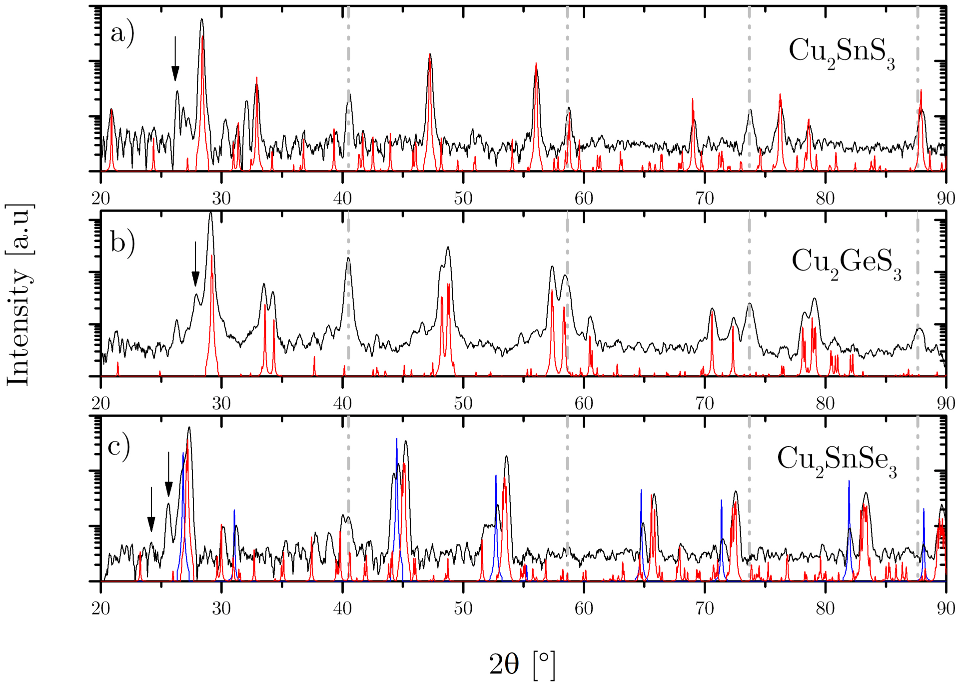

Figure 4.20: GI-XRD of the copper layer annealed up to 525°C for 30 minutes, followed by immediate cooling, in the presence of a) S and SnS powders, b) S and GeS powders, c) Se and SnSe powders. The dashed grey lines indicate the contribution of the Mo substrate. The red patterns indicate the monoclinic CTS, CTSe and CGS phases, respectively. The blue pattern indicates the presence of $Cu_{2-x}Se$. Unidentified peaks labelled with an arrow disappeared after KCN etching [30] and are thus attributed to various minor non stoichiometric Cu-S binaries.

Verification of model of study: relevance of two partial pressures In order to check for the reversibility of Eq. (4.14), the prepared CTS, CGS and CTSe films are re-annealed to 525°C in vacuum. The oven stays at 525°C for durations of 3, 5 or 12 hours. Those long annealing durations chosen arbitrarily (compared to 30 minutes) under vacuum conditions should allow sufficient time for full desorption of the vapour phase and total escape from the graphite box. SEM top view images of the samples re-annealed for the longest time of 12 hours are presented in Fig. 4.21 overlaid with EDX line scan for Cu and group IV elements. The line scans show the total absence of group IV element within the absorber layer after the re-annealing. Preliminary WDX analysis showed the absence of group IV element on CTS and CGS samples re-annealed for 3 and 6 hours as well, with the exception of the CTS sample annealed for 6 hours. This can be explained by a Sn-contaminated annealing environment supplying an unwanted partial pressure of SnS, i.e the graphite box being very porous. Similarly, absorbers re-annealed in the presence of chalcogen show no group IV loss.

Establishment of complete formation reaction The studies made in this chapter allowed us to establish the complete and reversible formation reactions for CTS, CTSe and CGS

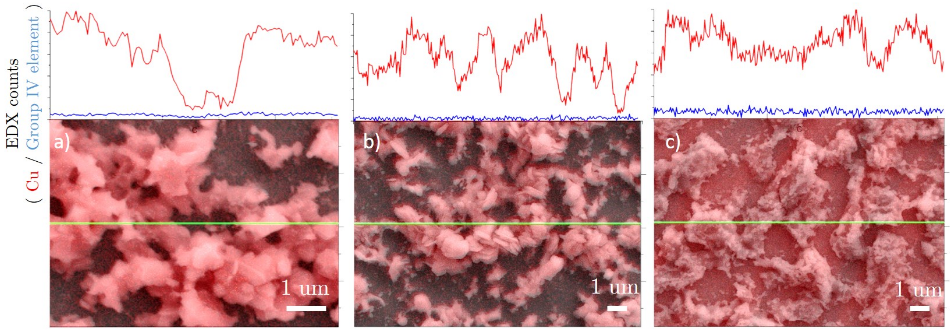

Figure 4.21: EDX line scan for Cu (red) and group IV element Sn or Ge (blue) overlaid with SEM top views where the scan position is indicated by the green line.

semiconductors as follows.

$$\mathrm{Cu_2X_{(s)}} + \mathrm{MX_{(g)}} + \frac{1}{2}\mathrm{X}_{2(g)} \leftrightarrows \mathrm{Cu_2MX_{3(s)}}, \tag{4.18}$$

revealing the importance of the vapour species during annealing, as well as the background pressure. However the formation of CTSe did not reach completion, even with an additional tin supply and secondary Cu_{2-x}Se phases were still present.

4.5 Film composition

The previous section highlighted the importance of partial pressures of both chalcogen and group IV-based chalcogen species during the annealing of CTS, CTSe and CGS thin films. The study showed a full decomposition of these ternary compounds into copper sulfide or copper selenide binaries via desorption of Sn or Ge, in the absence of powder supplies.

4.5.1 Lateral compositional gradient

The samples annealed to 525°C at $p_{back} = 10$ mbar showed in Fig. 8.1 the presence of minor Cu-S or Cu-Se binaries which actually happen to follow a specific lateral distribution when one carefully observes them with the EDX mapping tool. From lateral EDX/WDX measurements, distribution of binaries within the films was deduced and sketched in Fig. 4.22. It shows the annealing box in the tube in the model of Fig. 4.13, after completion of the annealings of CTS, CGS and CTSe. For CTSe, SEM top views of the sample are presented underneath the box sketch overlaid with EDX chemical mapping for Cu and Sn. Due to their high vapour pressure, there is no visible leftover of S, GeS or Se powder in the box. As described in the previous section, monoclinic CTS and CGS have been synthesised uniformly, while Cu_{2-x}Se phases are found to coexist with monoclinic CTSe for annealing temperatures of 525°C. However next to this open morphology present in CTSe surrounded by copper selenides, an additional composition gradient is visible at larger distances from the powders, i.e. the right-hand side of the sample, and also for CTS and CGS but particularly enhanced in the case of CTSe. The schematics (not to scale) in the three cases aim to help for visualisation.

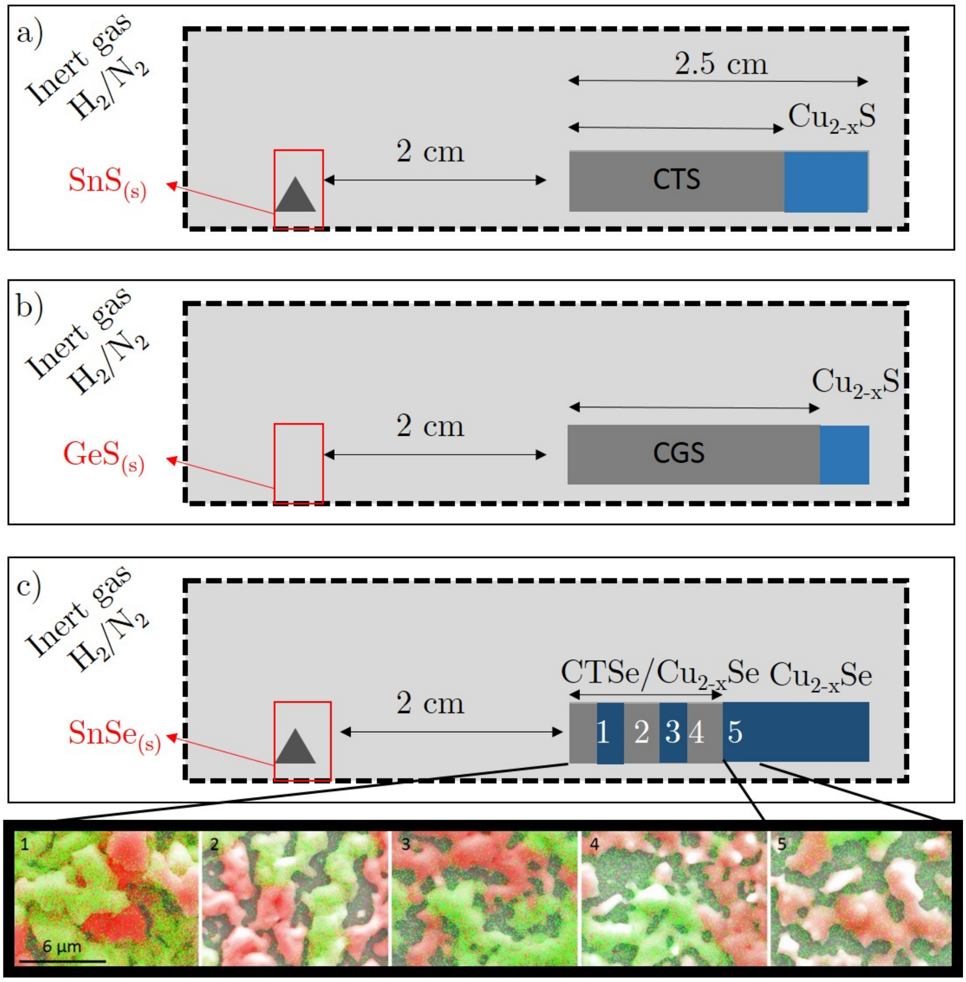

Figure 4.22: Schematic of the annealing furnace configuration after completion of the process showing the sample in the graphite box in the case of a) CTS annealed with S and SnS, b) CGS annealed with S and GeS and c) CTSe annealed with Se and SnSe. For the CTSe sample, SEM top views are shown below (20 kV, 5k) recorded at different distances of the sample left edge (1 mm, 2 mm, 3 mm, 4 mm and 5 mm) where chemical mapping for Cu and Sn is performed with EDX. The green colour is associated to the presence of tin and the red to the presence of copper.

The right-hand side of all samples show a lateral composition gradient with $Cu_{2-x}(S,Se)$ and no group IV species. The CTSe sample shows the largest surface without group IV species while the CGS sample shows to be the most uniformly covered with the CGS ternary and a reduced Cu-S volume.

Relevance of background pressure

The background pressure of forming gas p_{back} appeared as another relevant and tunable parameter during annealing. Annealings of CTS, CTSe and CGS were repeated at lower background pressures of 0.1 and 1 mbar. EDX analysis performed on single grains allow for the study of the Cu/IV ratio as function of the distance to the powders, as presented in Fig. 4.23a), b), and

c) for all ternaries. The EDX data was corrected in the case of CTSe in c) due to the additional composition gradient seen in Fig. 4.22c) where the coverage by copper sulphides increases from the left to the right of the sample (from 1 mm to 5 mm) until the sample becomes tin-free on its right edge. It suggests that the amount of SnSe vapour is not sufficient to reach the right end of the sample and react with it. The Cu/IV ratio for CTSe could thus obviously only be extracted from the grains that do contain tin. Thus it is averaged over Cu-Sn containing grains and afterwards corrected by the total surface area of copper.

It is observed in Fig. 4.23a) that the Cu_2GeS_3 film is of a uniform copper-poor composition with $1.6 < 2\text{Cu/IV} < 2$ at all background pressures, as it could be expected from the high vapour pressure of GeS.

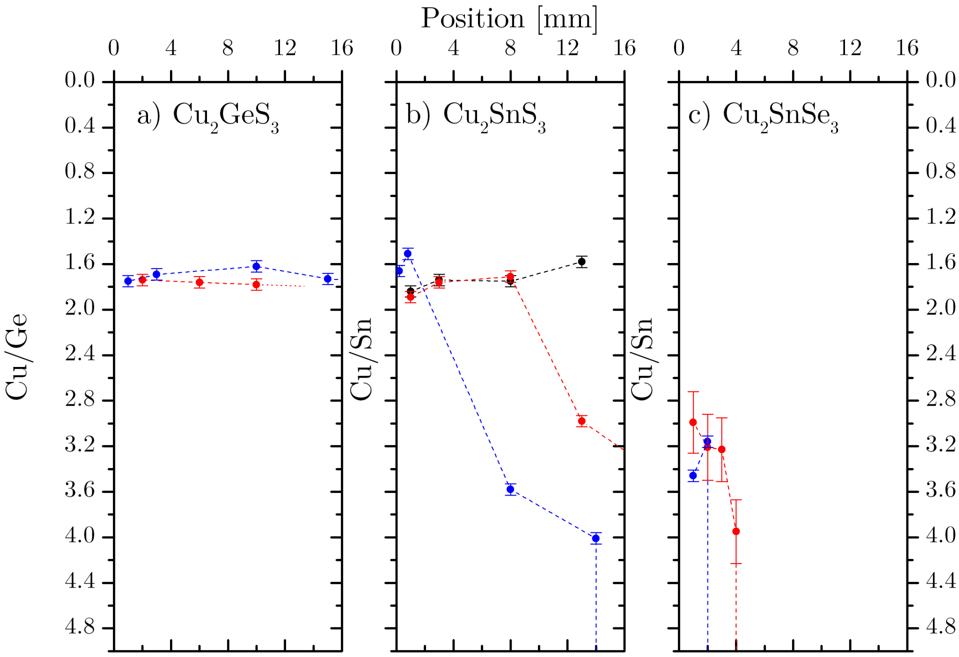

Figure 4.23: Lateral evaluation of final Cu/IV ratio from EDX/WDX measurement after annealing a Cu layer in a) S and GeS, b) S and SnS and c) Se and SnSe at 525°C for 30 minutes under different background pressures of H_2/N_2 : black 0.1 mbar, red 1 mbar, blue - 10 mbar.

However, the CTS sample in Fig. 4.23b) only presents a uniform copper-poor composition on the totality of the sample for the lowest p_{back} of 0.1 mbar. With increasing background pressures of 1 to 10 mbar, a gradient is observed with the absence of Sn after 13 mm for the sample annealed under the highest pressure. The sample also shows a Cu/Sn ratio increasing to about 4 towards the left of the sample before it becomes tin-free. These copper-rich compositions are explained by the formation of the Cu_4SnS_4 ternary, seen in GI-XRD presented in Fig. 4.24.

The gradient is the most enhanced in the CTSe sample. The Sn has reacted with no more than 4 mm of the sample from its left edge at 1 mbar. Due to the dewetting phenomenon followed by data correction, the Cu/Sn ratio of the CTSe reaches high values above 2.8. This would not happen if we had Sn on all the grains where we could and compare the absolute values with CTS.

The CTSe sample prepared at the highest p_{back} of 10 mbar shows the presence of tin over 2 mm

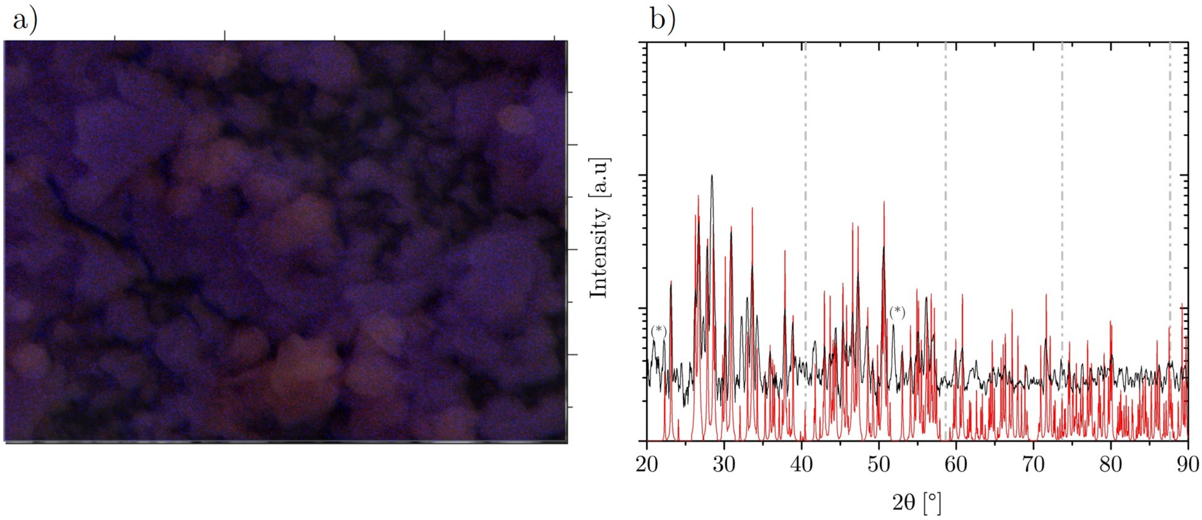

Figure 4.24: a) EDX mapping with copper (red) and Sn (blue) and b) GI-XRD of the CTS sample annealed at 1 mbar, measured at 14 mm of the left sample edge, where the Cu/Sn ratio shows to be increasing. The red pattern represents the Cu_4SnS_4, although secondary phases (unknown peaks) can be seen marked with stars. They likely correspond to Cu-S binaries as seen on the image (red grains)

only, which is in the error of the measurement of the position of the sample in the box. Therefore the trend between maps at 1 mm and 2 mm corrected by the area, is not conclusive. We can only say that the coverage by Sn is lower when annealed at 10 mbar than at 1 mbar.
The next section aims to unify theory to these experimental observations to understand the reasons for this lateral gradient.

4.5.2 Study of reaction kinetics to avoid lateral gradient

The investigation of the reason for the lateral composition gradient in Sn-based ternaries is done via division of the annealing process in three steps (generation, diffusion and reaction), as introduced in Fig. 4.1. We find which step is responsible for the Sn gradient by using a combined theoretical and experimental approach. The theoretical description of the generation and diffusion steps require the kinetic molecular theory, introduced in the next section.

Kinetic molecular theory

The kinetic molecular theory describes a gas as an ensemble of many particles being hard spheres of diameter d where $d << \lambda_t$, the average distance between two particles. They move constantly and randomly along straight lines, and there is no force of attraction between them. Fig 4.25 presents a schematics of this theory applied to our annealing system described previously. The particle trajectory is only deviated when it collides elastically with another particle or the walls of their container (i.e the graphite box). Collisions with the walls of the graphite box define the total pressure of the gas p_t, as an applied force on the surface area of the walls. When different vapours X and MX coexist in the same box, the Dalton's law describes p_t as the

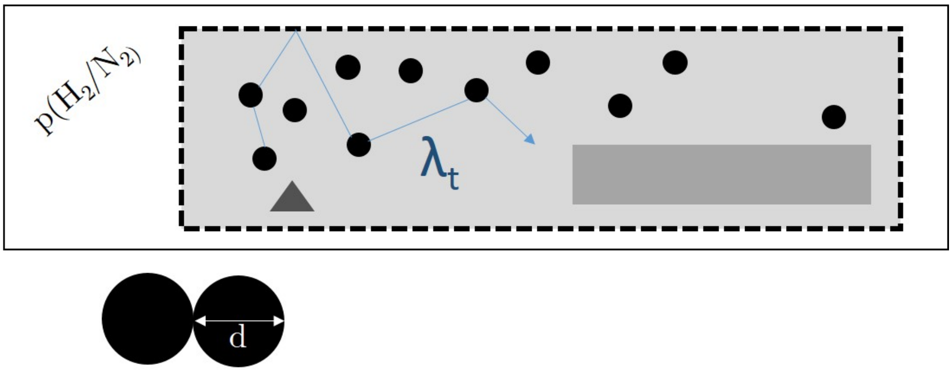

Figure 4.25: Application of the kinetic molecular theory in the annealing box, with definition of the molecular diameter d and the free mean path, λ_t.

sum of partial pressures of all coexisting species, following:

$$p_t = p(X) + p(MX) + p_{back}, \tag{4.19}$$

where p_{back} is included as the box is not a complete sealed element, so X and MX will tend to escape as soon as their partial pressures is high enough, but also the forming gas exerts a force on the outer box walls.
The average distance between particles λ_t (in m), better described as the average travelling distance between two collisions is called free mean path and is calculated as follows at constant temperature T:

$$\lambda_t = \frac{k_B \cdot T}{\sqrt{2} \cdot \pi \cdot d^2 \cdot p_t} \tag{4.20}$$

with k_B the Boltzmann constant and d the molecular diameter. The average speed of diffusion of the particles at T (in m.s^{-1}), expressed as "the root mean square speed" v_{rms} (m/s) can also be computed:

$$v_{rms} = \sqrt{\frac{3 \cdot k_B \cdot T}{m}}, \tag{4.21}$$

with m the molecular weight.
From both λ (Eq. (4.20)) and v_{rms} (Eq. (4.21)) the diffusion coefficient of particles D (m^2.s^{-1}) is then calculated as:

$$D = \frac{1}{3} \cdot \lambda_t \cdot v_{rms}, \tag{4.22}$$

leading to the following definition of D:

$$\begin{aligned} D &= \frac{3 \cdot \pi \cdot v_{rms}(T,m) \cdot \lambda(d,p_t)}{16 \cdot \sqrt{2}} \\ D &= C \cdot v_{rms}(T,m) \cdot \lambda(d,p_t) \end{aligned} \tag{4.23}$$

with C a constant. Therefore D can be calculated at any T as long as m and d are known for the species of interest.

Molecular weights and diameters Most of the molecules present in the annealing atmosphere (and previously introduced in section 4.2.5) are diatomic: S_2, Se_2, SnS, SnSe and GeS. Therefore they also have a linear geometry and rough values of their diameter d, required for the calculation of D, can be computed from covalent radii r_{cov} and bond lengths r_e found in literature [121] and presented in Table 4.4. The table shows the resulting average molecular diameters $d \sim r_e + 2 \cdot r_{cov}$ together with molecular weights calculated from individual atomic weights found in the periodic table. There is one exception of non-linear molecule present in the annealing environment which is the crown-like S_8, whose diameter is directly taken from literature [122].

Atomic species	r_{cov} [Å]		
S	1.02		
Se	1.22		
Sn	1.46		
Ge	1.17		
Molecule	r_e [Å]	d [Å]	m [u]
S_2	1.89	3.93	64.13
S_8	(-)	7.6 [122]	256.52
Se_2	2.16	4.6	157.92
SnS	2.21	4.69	150.77
SnSe	2.33	5.01	197.66
GeS	2.01	4.01	104.71

Table 4.4: Report of atomic covalent radii r_{cov} and molecular bond lengths d taken from [121], used to calculate the average molecular diameters d, with the exception of d for S_8 found in [122]. The molecular weights m (in u) are calculated by summing the weights of individual chemical elements found in the periodic table.

Step 1: Generation of vapour phase

Theoretical minimum generation rate As suggested in section 4.2.5, the generation of the MX-related vapour phase in the graphite box by sublimation of a solid powder of MX is quantified by the vapour pressure. Therefore it also varies with temperature. A minimum vapour generation rate r_{min} of $MX_{(g)}$ is necessary to complete the ternary formation on the entire sample surface by sufficient uptake of group IV element. A theoretical value for r_{min} can be calculated considering the number of copper atoms present in the precursor layer and the target stoichiometry (Cu/IV = 2). Using the surface area S of the copper precursor ($25 \times 25\,\text{mm}^2$), its thickness a ($\sim$ 250 nm and the annealing duration t of 30 minutes at 525°C:

$$r_{min} = \frac{a \times S \times \rho(Cu) \times N_A}{2M(Cu) \times t} \tag{4.24}$$

with $\rho(Cu)$ the density of copper, $M(Cu)$ the molar mass of copper, and N_A the Avogadro number, giving out:

$$r_{min} \sim 6.1\,\text{nmol}\,\text{s}^{-1} \tag{4.25}$$

as a theoretical minimum value of MX molecules to complete the formation. r_{min} should be compared to an experimental value. An experimental value of the maximum generation rate can be calculated by making assumptions on the partial pressure of the X species.

Experimental upper limit for the generation rate From experimental conditions it is possible to calculate an upper limit for the generation rate, described as the maximum rate of sublimation r_{max}. The Hertz-Knudsen equation expresses r_{max} for a source X in vacuum at the constant temperature T [123]. Under those conditions the maximum number of molecules created per second for a 1 m^2 surface area solid source is given as:

$$r_{\text{max}} = \frac{\alpha \cdot v_{rms} \cdot p(X)}{4 \cdot R \cdot T} \tag{4.26}$$

with v_{rms} the root mean square speed described in Eq. (4.21), R the gas constant, $p(X)$ the vapour pressure of the species X and α the sticking coefficient of gas molecules onto the surface of the condensate. α takes values between 0 and 1 and is unknown for the considered species here. In the current situation, Eq. (4.26) has to be modified to consider the total surrounding pressure, p_t. The derived form of the Hertz-Knudsen law gives out r_{max} as:

$$r_{\text{max}} = \frac{\frac{\alpha \cdot v_{rms} \cdot p(X)}{4 \cdot R \cdot T}}{1 + \alpha \frac{v_{rms}}{4} \frac{L}{D}}, \tag{4.27}$$

with L the distance travelled by the vapour from its source (cf Fig. 4.26) and D the diffusion coefficient function of p_t as expressed in Eq. (4.23).

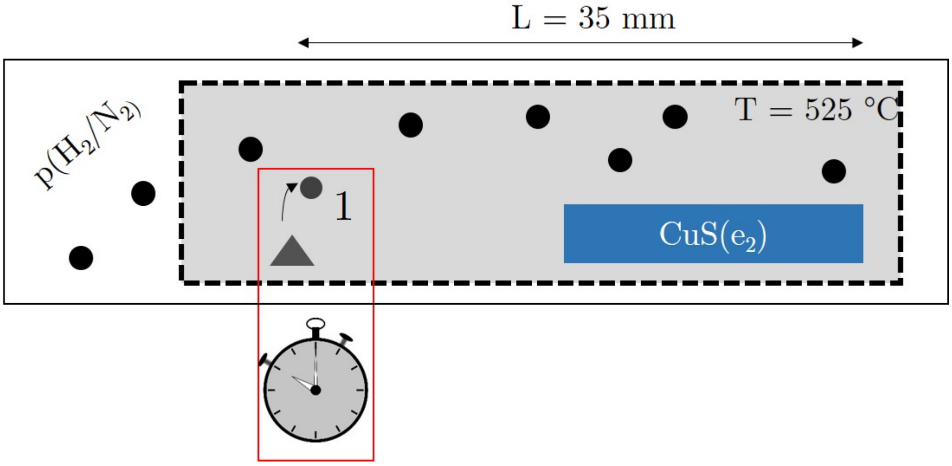

Figure 4.26: Schematic of the annealing configuration used for calculation of r_{max}, where MX sublimes in the presence of $p(X)$ and p_{back}

Eq. (4.27) can be simplified as $\alpha \frac{v_{rms}}{4} \frac{L}{D} \gg 1$, thus

$$r_{\text{max}} = \frac{D \cdot p(MX)}{RTL} \tag{4.28}$$

where D is function of p_t. To calculate r_{max}, $p_t = p_{back} + p_p(X)$ is required so an assumption has to be made on the partial pressure of X, $p_p(X)$. One considers two different situations when X = S or X = Se. When one performs an annealing in the presence of sulphur, one rapidly notices a condensation of sulphur on the cold quartz tube at the edges of the heating zone where the graphite box lies. Therefore we can easily consider that at $T = 525$°C sulphur vapour has already escaped the graphite box. We hypothesise that at the same T there is still selenium vapour in the box. From this, we can write:

$$p_t = p_{back} = 10\,\text{mbar for annealings in S} \tag{4.29}$$

$$p_t = p_{back} + p_p(Se) \sim p_p(Se) \sim 100\,\text{mbar for annealings in Se} \tag{4.30}$$

while the vapour pressures of interest (= p) at 525°C are reported in Table 4.5. The values calculated for r_{max} following Eq. (4.28) are reported in Table 4.5 as well, considering a 1 cm^2 powder source. Finally, as seen in Table 4.5 r_{max} amounts to values that are much below the required value of r_{min} calculated in Eq. (4.25) for annealings of CTS and CTSe. This means that at p_{back} = 10 mbar the annealings will not reach completion. If p_{back} is decreased by a factor of 100 (0.1 mbar), as $r_{max} \propto \frac{p(MX)}{p_t}$, in the case of CTS r_{max} increases to $9\,\text{nmol}\,\text{s}^{-1}$ which is in the same order of magnitude as the required r_{min} for full completion of semiconductor formation. CTS annealed at background pressures of 1 and 10 mbar is thus predicted to have a Cu/Sn gradient whilst the 0.1 mbar should not. In the case of CTSe, the p_{back} should be even below 0.1 mbar or the sample always shows a gradient. In the case of GeS which has a 100 times higher vapour pressure than SnS for any given temperature, the generation rate is predicted to be sufficiently high even at p_{back} = 10 mbar to form a uniform sample.

Vapour	SnS	SnSe	GeS
$p(MX)$[mbar]	10^{-3}	10^{-3}	1
r_{max}[mol/(s · cm^2)]	0.06	0.005	4.5

Table 4.5: Vapour pressures used for calculation of r_{max} at T = 525°C and p_{back} = 10 mbar together with the resulting r_{max}.

Step 2: Diffusion of gas phase to the sample

The diffusion is calculated by means of the diffusion coefficient D from the kinetic molecular theory as presented previously in Eq. (4.23). The resulting D is presented in Fig. 4.27 as function of p_t for all vapour species considered in this work.

It is observed in Fig. 4.27 that for all species considered here, the diffusion happens really fast and the box is filled in one second only. Therefore, the diffusion cannot be the limiting process for semiconductor formation during the annealing.

Step 3: Reaction gas phase-sample

We have seen that while diffusion is very fast, generation is a slow process that can be accelerated by decreasing the background pressure. The gas-solid reaction is the third and last step of the series to consider as a potential limiting step for completion of semiconductor formation. Studies have shown the complete of Kesterite formation in less than five minutes, by a full incorporation of gaseous Se in the solid precursors [124]. Also, the experimental part showed us

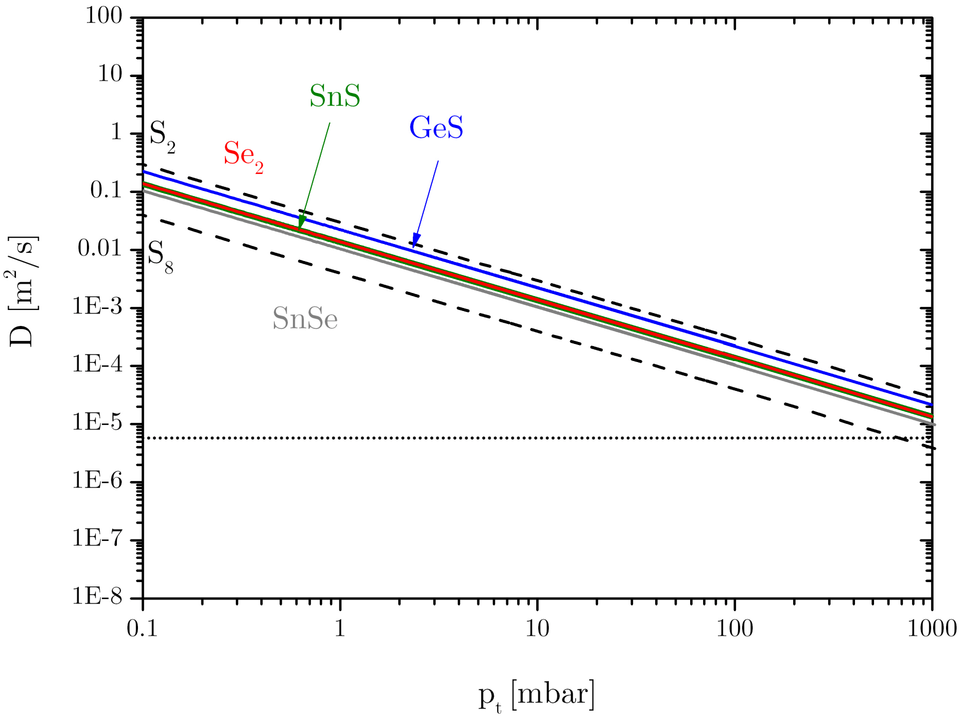

Figure 4.27: Diffusion coefficient of all species as function of the total pressure p_t, calculated from Eq. (4.23). The horizontal dashed line represents the surface area of the box that the vapour phase should travel to fullfill the box in one second.

that MX can not be found in $Cu_{2-x}(S, Se)$ samples where the ternary compound is suggested to form directly when the 2:1 stoichiometry is obtained in the copper sulphide and MX can react with it. Therefore from the experimental evidence the reaction between vapour and sample is assumed to happen within a short fraction of time, that is much smaller than the 30 minutes usually given as annealing time. It does not appear to be a limiting step.

4.6 Generation as limiting step and final suggestions for a uniform target composition

Table 4.6 recapitulates the kinetics of the three processes stated in Fig. 4.1 accessed in this chapter by a combination of theory and experiments. Unification of experimental observations

Step	1.Generation	2.Diffusion	3.Reaction
Timescale [s]	1800	1	$\ll 300$

Table 4.6: Recap of timescales for the three steps of the annealing as sketched in Fig. 4.1

and theory have enabled to evaluate the generation of Sn(S,Se) gaseous molecules as the critical step for completion of CTS and CTSe formation. A lateral composition gradient can be avoided in CTS or reduced in CTSe, when p_{back} is decreased, which increases the generation rate.

Therefore using minimal background pressures is a necessity.

4.7 Formation reaction for ternary alloy $Cu_2Sn_{1-x}Ge_xS_3$

This study on the annealing of CTS and CGS ternary compounds gives some indication on how to proceed for the synthesis of the CTGS ternary alloy. The background pressure p_{back} is lowered to 1 mbar for all further annealing processes to avoid lateral composition gradients in the produced samples, by maximising the partial pressures of GeS & SnS vapours. That means 1 mbar of H_2/N_2 are introduced into the annealing furnace under "low" vacuum ("low vacuum" $\sim 10^{-3}$ mbar). Using both $SnS_{(s)}$ and $GeS_{(s)}$ in the annealing box for supplies of Sn and Ge, similar annealing studies could be repeated from a single layer of copper to try and produce a uniform CTGS absorber.

4.7.1 Expectations of alloy composition: $x \sim 1$

The difference in vapour pressures of S, GeS and SnS (cf Fig. 4.27) suggests , as previously the first reaction of Cu with gaseous S. The reaction of the gas phases with the precursor were shown to depend not only on the presence of the gas phase above the sample but also on the stoichiometry of the copper sulphide phase in the precursor. $SnS_{(g)}$ was shown to react with the sulphurised precursor between 400 and 450°C to form Cu_2SnS_3. Due to its higher vapor pressure, $GeS_{(g)}$ was expected first to incorporate at around 350°C but since the Cu_9S_5 forms only around 400°C, the formation of Cu_2GeS_3 only happens above 400°C as well. The formation of the CTGS alloy is thus also expected above 400°C as only then the presence of Cu_9S_5 allows for incorporation of Sn and Ge. However, since GeS owns a higher vapour pressure than SnS, $GeS_{(g)}$ is expected to be above the sample before $SnS_{(g)}$, and thus could react with it to form $Cu_2GeS_{3(s)}$ as soon as Cu_9S_5 is available. In the model of Eq. (4.18), the following formation reaction model would then be expected for $CuSn_{1-x}Ge_xS_3$:

$$\mathrm{Cu_2S_{(s)}} + x\,\mathrm{GeS_{(s)}} + (1\text{-}x)\,\mathrm{SnS_{(s)}} + \frac{1}{2}\mathrm{S}_{2(g)} \leftrightarrows \mathrm{Cu_2Ge}_x\mathrm{Sn}_{1-x}\mathrm{S}_{3(s)}, \tag{4.31}$$

with the chalcogen binaries in equilibrium with their respective gas phases following:

$$\mathrm{GeS_{(s)}} \leftrightarrows \mathrm{GeS_{(g)}}, \tag{4.32}$$

and:

$$\mathrm{SnS_{(s)}} \leftrightarrows \mathrm{SnS_{(g)}}. \tag{4.33}$$

If $GeS_{(g)}$ reacts immediately with $Cu_{2-x}S_{(s)}$ to form $Cu_2GeS_{3(s)}$, the final composition of the alloy will depend on whether $SnS_{(g)}$ can incorporate in Cu_2GeS_3 during the rest of the annealing. Therefore if correct the final composition of the CTGS alloy depends on the following equilibrium reaction:

$$\mathrm{Cu_2GeS_{3(s)}} \leftrightarrows \mathrm{Cu_2S_{(s)}} + \mathrm{GeS_{(g)}}. \tag{4.34}$$

If it rather lies on the right hand side, some Ge is lost via desorption in the gas phase, and $SnS_{(g)}$ could incorporate. The annealing being done in the presence of p_{back} in a saturated box with S and GeS, reaction (4.34) is rather lies to the left. A final CTGS with $x \sim 1$ is thus expected.

4.7.2 Verification of expectations: Establishment of formation reaction

Annealing to 430℃: formation of $Cu_{2-x}S$

A copper sample is annealed to 430°C for 30 minutes in the presence of S, GeS and SnS powders. After annealing the sample is mapped with EDX for analysis of Cu, Sn and Ge contents, at the micron scale. The amount of Sn detected is below sensitivity (< 1 at.%) at any position, while Ge is found locally in amounts that range between 1 and 2 at.% with no specific distribution. For this reason the resulting EDX map (presenting mostly copper) is not shown. However for further analysis the produced sample is also analysed with GI-XRD, as shown in Fig. 4.28. Fig. 4.28 shows the coexistence of two phases in the sample: the binary Cu_9S_5 and the ternary Cu_2GeS_3 (cubic). Only the two main peaks of the cubic Cu_2GeS_3 are detected in the XRD, demonstrating a preferred orientation along the (111) and (220) planes and confirming the local incorporation of Ge. At 430°C the formation reaction can be therefore expressed as:

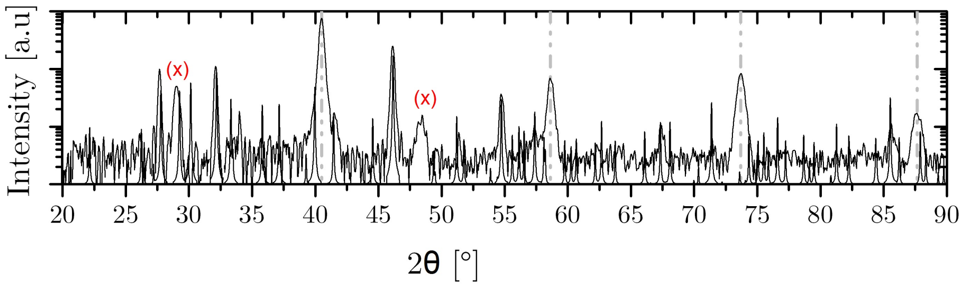

Figure 4.28: GI-XRD of the copper layer annealed up to 430°C for 30 minutes in the presence of S, GeS and SnS powders. The black pattern corresponds to Cu_9S_5 binary while the red stars refer to two single major peaks from the cubic Cu_2GeS_3. The dashed grey lines indicate the contribution of the Mo substrate.

$$Cu_{2-x}S_{(s)} + GeS_{(g)} \leftrightarrows Cu_2GeS_{3(s)} (T = 430°C), \tag{4.35}$$

with the equilibrium rather on the left hand side, as EDX demonstrates a very poor Ge content. It also confirms that $SnS_{(g)}$ has not yet reacted with the sample.

Annealing to 470℃: formation of Cu_2GeS_3 and Sn-secondary phases

A copper sample is annealed to 470°C for 30 minutes in the presence of S, GeS and SnS powders. The XRD measured on the resulting sample (presented in Fig. 4.29) show the coexistence of the cubic Cu_2GeS_3 together with Sn-containing secondary phases. EDX studies done in parallel suggest a rather homogeneous Sn distribution varying between 0.5 and 2 at.% which is still low to draw a clear conclusion. One relies on the XRD which suggests Sn rather belongs to a minor secondary phase than incorporated within a CTGS alloy.

The resulting EDX mapping analysis demonstrates the existence of Sn above 1 at.%. Delamination problems due to stress in the precursor layer have affected the sample with shows an open morphology with islands surrounded by an uncovered Mo layer. The islands of about 2 microns

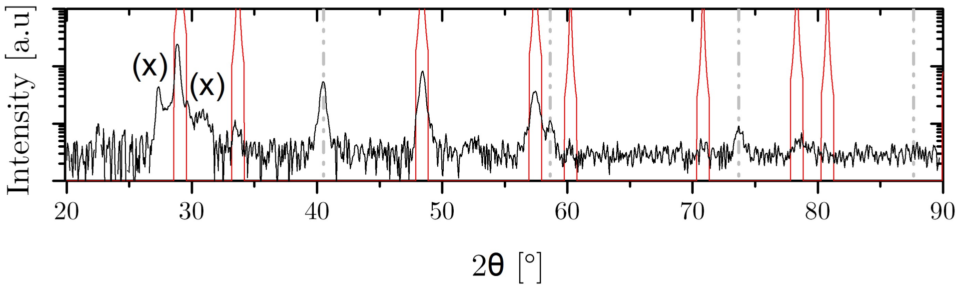

Figure 4.29: GI-XRD of the copper layer annealed up to 470°C for 30 minutes in the presence of S, GeS and SnS powders. The red pattern refers to the cubic phase of Cu_2GeS_3 and the dashed grey lines indicate the contribution of the Mo substrate. The two black stars highlight the two broad shoulder peaks suggesting the presence of one or several unidentified secondary phases, very likely to contain Sn, as measured with EDX.

size can be analysed with point EDX to establish the Cu/IV ratio. The average of the Cu/IV ratio is around 1.4, which, lower than the 1.8 standards in the ternaries, suggest the presence of a minimum of one Sn-containing secondary phase. The results suggest the poor incorporation of Sn in the sample, and most of all the fact it does not mix with the existing Cu_2GeS_3 ternary already present.

Annealing to 525°C: formation of Cu_2GeS_3

A copper sample is annealed to 525°C for 30 minutes in the presence of S, GeS and SnS powders. An EDX mapping is performed on the sample after annealing. The resulting map is presented in Fig. 4.30 together with data from a line scan. Low amounts of Sn are detected

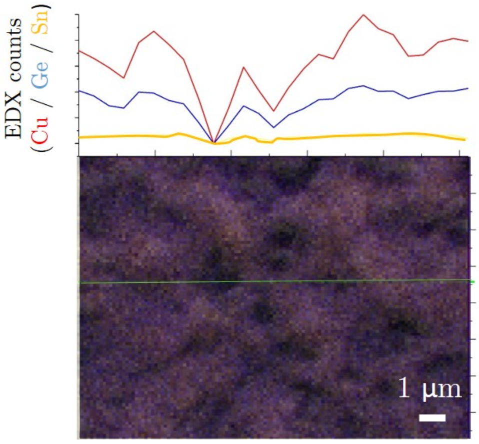

Figure 4.30: EDX line scan for Cu (red), Ge (blue) and Sn (yellow) overlaid with SEM top views where the scan position is indicated by the green line.

which are just slightly above the sensitivity limit at 1 at.%. As seen in Fig. 4.30, the Ge/IV and Cu/IV ratio vary from point to point. GI-XRD results presented in Fig. 4.31 show the existence of pure Cu_2GeS_3 together with minor Sn-containing phases which suggest that Sn does not incorporate well in CGS to form CTGS.

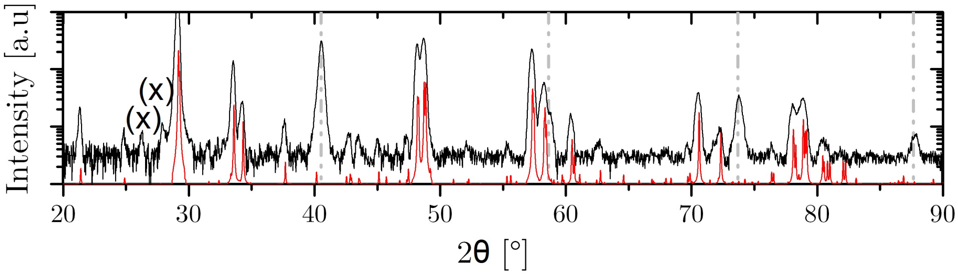

Figure 4.31: GI-XRD of the copper layer annealed up to 525°C for 30 minutes in the presence of S, GeS and SnS powders. The red pattern refers to the monoclinic phase of Cu_2GeS_3 and the dashed grey lines indicate the contribution of the Mo substrate. The unidentified peak highlighted by a cross refers to secondary Sn-containing phases.

Therefore Sn incorporation does not occur as wished in Cu_2GeS_3, at best a very Ge rich CTGS is formed with Sn-containing secondary phases. The experiment suggests that to form a single phase CTGS alloy, Sn should already be present in the precursor.

Annealing to 525°C of Sn-containing precursors

The Sn/Cu_3Ge precursors deposited on Mo from organic solvents, as described in section 3.3.2, are annealed at 525°C for 30 minutes in the presence of S and GeS powders and $p_{back} = 1$ mbar. As reported in [63], the precursor stack was plated with a chemical composition of Cu/IV = 2.0 and Ge/IV = 0.7. After annealing, the chemical composition of the absorber was determined by EDX to Cu/IV = 1.9 and Ge/IV = 0.8, showing the loss of Sn during annealing, as it could be expected from the absence of SnS vapour in the atmosphere. GI-XRD of the absorber also shows the poor Sn content with angular positions close to Cu_2GeS_3. Therefore, it is highlighted that to form CTGS alloys, Sn should be present in the precursor but also in the annealing environment to prevent its desorption as $SnS_{(g)}$.

4.8 Conclusion of the chapter

The chapter showed the successful synthesis of thin films of Cu_2SnS_3, Cu_2GeS_3 and Cu_2SnSe_3 by a two-step method consisting in the annealing of single copper layers in chalcogen and group IV chalcogenide vapours. Respective formation routes are described, a method which is simple and can be used for any type of Cu-based semiconductor compound as long as the vapour pressures of the other constituent elements are sufficiently high. To avoid film decomposition during annealing it is necessary to provide both S and SnS, Se and SnSe or S and GeS vapour phases to the annealing atmosphere. The final compositions follow copper and sulphur-poor conditions. Large compositional gradients were observed in the films, especially in SnSe-containing films. By calculation of the diffusion and generation constants, it was established and verified experimentally that generation of the group IV containing vapour from the solid pile of group IV chalcogenide is slow, which hinders the formation of a film of uniform composition. It is further expected and verified that increasing the background pressure has the dramatic effect of lowering the kinetics of formation, leading to enhanced compositional gradients in the film. However, increasing the duration of the annealing would not help as the vapour phases eventually escape the annealing box. During the formation route, we also have observed that CTS, CTSe and CGS show different predominant crystalline structures (cubic when the films are annealed at temperatures below 500°C and monoclinic when annealed at higher temperatures). In Chapter 5 one would like to extend get further insight into the crystalline structure and optical properties of the CGS polymorph, on the model of a study performed on CTS. An attempt at forming CTGS from Cu was performed by annealing in group IV containing vapours. However, the resulting films mostly show a CGS phase or very Ge-rich and/or minor Sn-containing secondary phases. Additionally, a Cu-Sn-Ge precursor was annealed in GeS, and lost all its Sn, confirming that to form CTGS alloys of various compositions in Ge, one should anneal not only Sn and Ge containing precursors but also provide all group IV chalcogenide species. Alloys will be prepared in Chapter 6.

CHAPTER 5

Characterisation of the Cu_2GeS_3 ternary compound

5.1 Goal

This chapter is based upon the X-ray diffraction results presented in Chapter 4, suggesting a change in the crystallographic structure of Cu_2SnS_3 and Cu_2GeS_3 from cubic to monoclinic when their annealing temperature is increased above 500°C. In the case of Cu_2SnS_3, these results correlate with the report of the same structure transition by de Wild et al. [54], from the reactive annealing of Cu-Sn precursors. More insight into the crystallographic properties of the ternary compounds and their respective optoelectronic properties is essential for future photovoltaic applications, especially if one of the phases shows better characteristics than another.
After the presentation of the initial background literature on Cu_2SnS_3, this chapter shows investigations of the predominant crystallographic structures in Cu_2GeS_3 and respective bandgap energies, absent of literature at the start of this work. Four themes of interest will be thus discussed in this chapter:

1. Background literature on the Cu_2SnS_3 & Cu_2GeS_3 polymorphs
2. Change in the Cu_2GeS_3 polymorph with annealing temperature
3. Estimation of bandgap energies for the polymorph by three different optical methods
4. Assessment of Raman spectra of the polymorph

Parts 2 & 3 were published in Ref.[125].

5.2 Background

At the start of this work, the existing literature focuses on Cu_2SnS_3 reporting a broad range of bandgaps between 0.93 and 1.35 eV [30, 32, 33], suggested to correlate to different crystal structures of Cu_2SnS_3 which is a polymorphic material. Four structures are often cited: a high-temperature cubic phase grown at temperatures above 775°C and the less ordered triclinic, tetragonal and monoclinic phases prepared at lower temperatures [30]. The different bandgaps reported are suggested to relate to the formation of different structures of Cu_2SnS_3, without much of a consensus. The calculations of Zhai et al. [126] brought more insight on the several structures found in Cu_2SnS_3. Despite being derived from the zinc blende structure like Kesterite CZTS with tetragonal arrangements of cations around each sulphur anion (cf. Fig. 1.2), CTS does not respect the octet rule. There is no configuration of Cu and Sn cations around S anions that adds up to 8 valence electrons. Out of 5 possible motifs (Cu_2Sn_2, Cu_3Sn, $CuSn_3$, Cu_4, Sn_4), the two that are the closest to the octet rule, Cu_2Sn_2 and Cu_3Sn, were calculated to be energetically the most stable [126] and arranged into the monoclinic structure of Cu_2SnS_3. It was suggested that larger deviations to the octet rule would lead to highly disordered structures. The study of de Wild et al.[54] within this thesis project was one of the first steps in studying the polymorphic transitions of Cu_2SnS_3 and first optoelectronic properties, in the temperature range adequate for annealing of samples grown on soda-lime glass, therefore between 450°C and 550°C. The phase identification is performed by cross-comparison of measured X-ray diffractograms with CTS phases from the ICDD database [47], as presented in Appendix B. In literature, the selected measurement range is often too narrow to allow a fair differentiation of the different phases as their peaks show many overlaps. In the studies done at the UL, the measurement range of 2θ is therefore extended down from 10-20°to 90°, which allows to evaluate the nature of the predominant crystallographic structures. It is shown in [54] by cross-comparison of X-ray diffraction and Raman data that Cu_2SnS_3 shows a predominant cubic structure at annealing temperatures below 500°C and a predominant monoclinic structure above 500°C. The monoclinic phase also shows higher luminescence than the cubic phase which suggests a higher quasi-fermi level splitting and a larger open-circuit voltage when implemented in solar cell devices [54]. The monoclinic phase is reported to have a bandgap of about 0.95 eV. In parallel, the best CTS-based devices reported are from monoclinic absorbers [31], which would favour annealing temperatures above 500°C.

This chapter is based on the hypothesis that different CGS polymorphs and/or secondary phases are formed at different process temperatures. Recent studies of Cu_2GeS_3 reported bandgaps between 1.3 and 1.6 eV [127–129]. Similarly to CTS, the deviations in measured bandgap should be clarified. Cubic [130], tetragonal [131] and monoclinic [132, 133] crystallographic structures have all been presented in the literature as possible configurations of the CGS lattice, from both single crystal or thin films XRD studies. However, there is no agreement on secondary phases or consistency on the existence of polymorphs and the temperature range in which the polymorphs and secondary phases are formed. This chapter aims to get more insight into this and check whether CGS follows similar trends as for CTS in terms of polymorphism and optoelectronic properties.

5.3 Structural characterisation

Thin films of Cu_2GeS_3 were prepared with a similar methodology as in Chapter 4 [71]. The method uses the high vapour pressure and diffusion coefficient of germanium monosulphide GeS to grow uniform Cu_2GeS_3 films by annealing copper layers deposited on Mo, in GeS and S vapours. The background pressure of 1 mbar is set via input of forming gas H_2/N_2 (10/90) around the graphite box. It was shown in Chapter 4 that the incorporation of Ge into the film only happens at temperatures above 450°C, hence setting the minimum annealing temperature required to prepare CGS via this method. To study the existing polymorphs of CGS present across the annealing temperature range, annealings of similar Cu precursors are repeated at 480, 500 and 520°C and the resulting samples studied with GI-XRD. The resulting GI-XRD are presented in Fig. 5.1. The structural analysis is done by cross-comparison of measured peak positions with reference patterns found in the ICDD database [47] and presented in Appendix B. In the film annealed at 480°C a cubic CGS phase is formed, as seen in Fig 5.1a). The film annealed at 500°C in b) shows peaks belonging to the monoclinic structure as well, indicating likely a mixture of the cubic and monoclinic phases. When annealed at 520°C in c) the CGS structure suggests the presence of a predominant monoclinic phase.

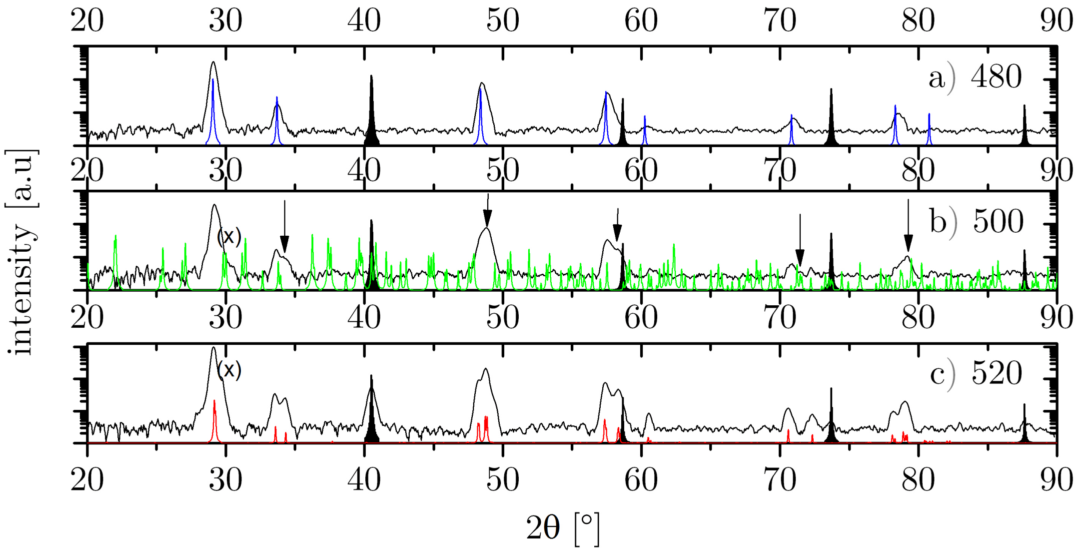

Figure 5.1: GI-XRD measured on the Cu_2GeS_3 films after annealing at a) 480, b) 500, c) 520°C. The blue pattern corresponds to the cubic CGS, the red to monoclinic CGS, the green to orthorhombic Cu_8GeS_6 and the black to the Mo substrate (refer to Table 8.2 in Appendix B for details on the reference patterns). The crosses (×) in the diffractograms b) and c) indicate the reflection that also remains after KCN etching, likely belonging to the Cu-rich Cu_8GeS_6 phase. The arrows on b) show the transition of the diffractogram from the cubic to the monoclinic polymorph at 500°C when the main reflections double.

The signature of an additional component is present as a shoulder on the right-hand side of the main peak at 30°in the diffractograms b) and c). The film annealed at 520°C in c) was etched in KCN for surface cleaning [119]. The etched sample presented in c) after KCN etch still shows the CGS monoclinic phase together with the additional shoulder, which suggests it could be a minor Cu-Ge-S phase that cannot be etched away. The unknown component was further identified to likely belong to the Cu-rich Cu_8GeS_6 phase (orthorhombic, as reported in Table 8.2) and also observed along the Cu_2S-GeS_2 tie line. The diffractogram of the Cu_2GeS_3 sample presented in Chapter 4 in Fig. 4.20b) and annealed at a similar temperature might contain the Cu_8GeS_6 impurity as well. It is only described as an impurity as only seen in one peak of the GI-XRD and is suggested to refer to some copper left unreacted. The crystal structures of the monoclinic and cubic CGS are presented in Fig. 5.2a) and b), respectively, as plotted with the software VESTA [134] from lattice parameters and atomic positions found in the ICDD database and corresponding to the reference XRD patterns used in Fig. 5.1. In the monoclinic structure, each atom has a defined position. The monoclinic structure in CTS was calculated to be the most stable structure with only two Cu-Sn clusters around S anions: Cu_3Sn and Cu_2Sn_2

that approach the octet rule [126]. One sees it is the same in CGS. In the cubic structure, each cation site could be occupied either by a Cu or a Ge atom, leading to local disorder. This low-temperature cubic structure is seen as highly disordered.

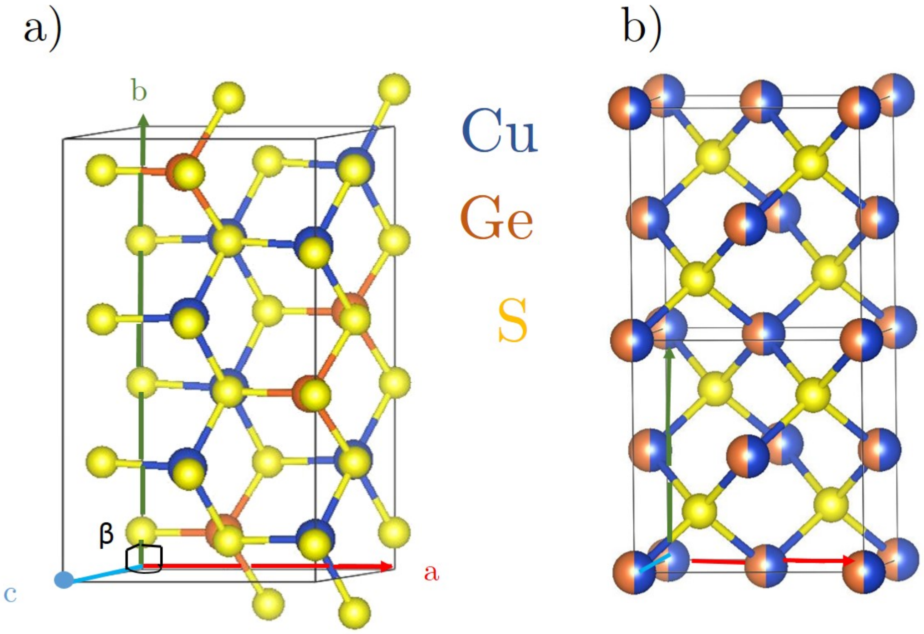

Figure 5.2: a) Unit cell of monoclinic Cu_2GeS_3 and b) two unit cells of cubic Cu_2GeS_3, all drawn with VESTA [134], using lattice parameters in Table 8.2 and respective atomic positions found in the ICDD database.

A highly disordered phase could easily lead to local fluctuations in E_G and does not lead to any good for device application [126, 135, 136]. However one is interested in estimating the bandgap E_G for the polymorph. E_G will be determined by a combination of PL and light $T-R$ measurements.

5.4 Bandgap extraction for the Cu_2GeS_3 polymorph

5.4.1 Transmission-reflection measurements

Light transmission and reflection measurements were performed on CGS absorbers directly grown on SLG substrates from a Cu precursor deposited on SLG, as described in section 2.1.4. The annealing of the copper film is performed at 480 or 525°C. The films annealed on SLG present the same crystallographic structures as the films prepared on Mo.
Using Eq. (2.10) with the film thickness $x\ \sim 1$ micron, the absorption coefficient α of Cu_2GeS_3 prepared at different temperatures can be calculated from the measured T and R. Finally, the bandgaps of the cubic and monoclinic phases can be estimated either from inflection points or Tauc plots, as described in section 2.1.4. The absorption coefficients calculated for the film annealed below 500°C and above are presented in Fig. 5.3a) in the range from 0.8 to 1.8 eV. The absolute values of α below $10^4\,\mathrm{cm}^{-1}$ are most likely underestimated due to the high number of

pinholes in the layers. Fig. 5.3b) presents the inflection points calculated from α, and c) the respective Tauc plots. It is seen in b) that the cubic sample only shows one inflection point at 1.23 eV while the monoclinic sample shows two inflection points at 1.55 and 1.68 eV. Instead, the Tauc plots allow to extract one bandgap value for each sample, 1.06 eV for the cubic sample and 1.41 eV for the monoclinic one. The two plots confirm the that the cubic and monoclinic phases have different E_G.
The first inflection point observed in monoclinic Cu_2GeS_3 at 1.55 eV was attributed to the VB-CB transition, corresponding to E_G, while the second inflection point at 1.68 eV was attributed to a second VB validated by theoretical calculations and also present in Cu_2SnS_3 [53]. The transition from the second VB to the CB is not seen in the Tauc plot as it lies above E_G. Combination of both methods is thus essential to determining all optical transitions. Despite the offset in E_G from the two methods, the cubic polymorph can be thought of having a bandgap below 1.3 eV and the monoclinic above 1.4 eV. PL measurements were also done as an additional method for bandgap extraction and are presented in the next section.

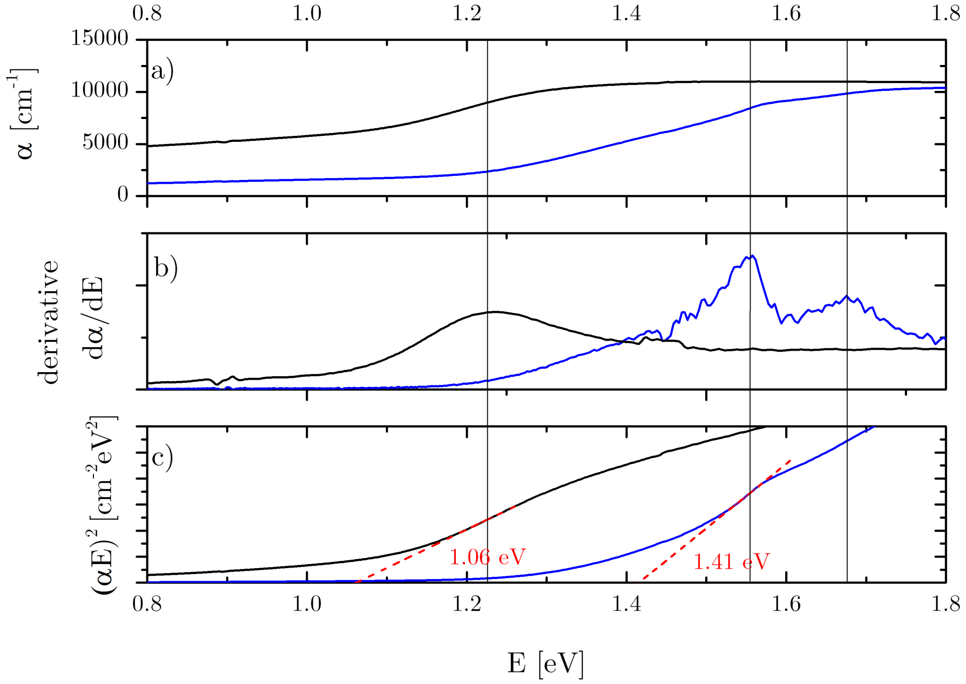

Figure 5.3: a) Experimental absorption spectrum of cubic CGS (black) and monoclinic CGS (blue), b) First derivative of both absorption spectra, with the three vertical lines showing their respective inflection points, (c) Tauc plots. Only the first transition could be determined from the Tauc plot, while the second transition gives a value below the main band gap.

5.4.2 Photoluminescence measurements

Photoluminescence measurements were performed on the bare absorbers on Mo annealed at different temperatures. The resulting spectra are presented in Fig. 5.4. The samples annealed below 500°C presenting a cubic phase in GI-XRD in Fig. 5.1 do not show any measurable PL yield between 1.0 and 1.7 eV. The only yield is recorded for the samples annealed at T $>$ 500°C, with a peak maximum located at 1.57 eV.

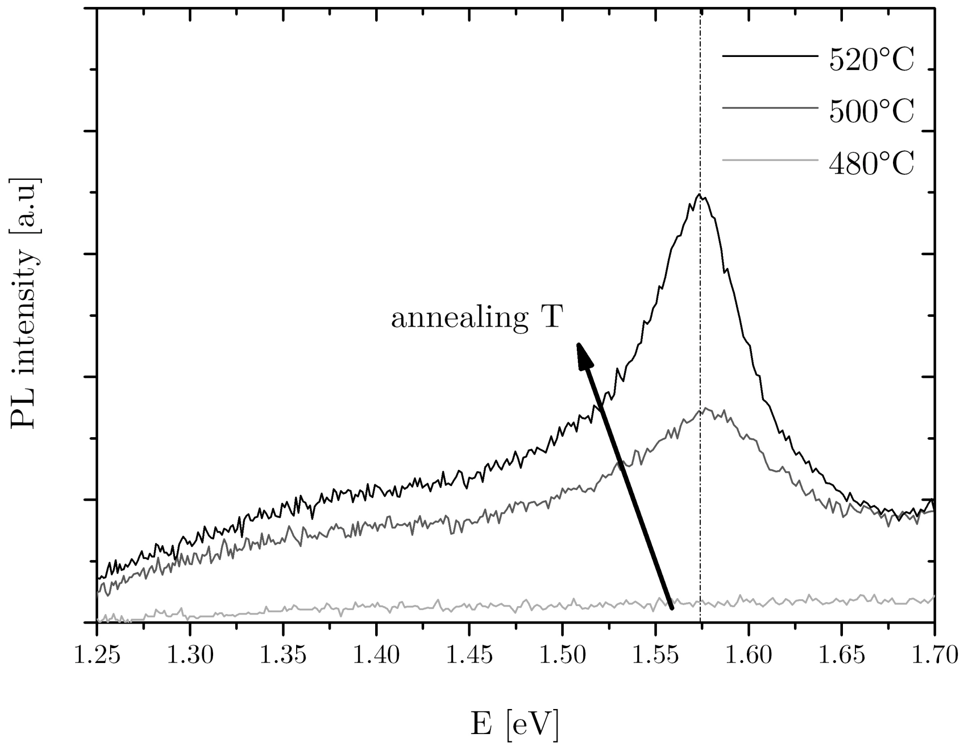

Figure 5.4: PL yield of the Cu_2GeS_3 annealed at $T = 480$, 500 and 520°C. The line shows the maximum of the 520°C sample at 1.57 eV.

The PL peak seen at 1.57 eV is close to the inflection point of the monoclinic polymorph at 1.55 eV as determined from the absorption spectrum in Fig. 5.3b). Since this transition refers to the band-to-band transition [53], monoclinic absorbers are the most likely giving the highest QFLS (cf. Eq. (2.8)). The large tailing, unfortunately, does not allow quantification of the QFLS by fitting of the high energy side of the signal so that the comparison between the samples annealed at 500 and 520°C is not possible. However, one can conclude that annealing at temperatures above 500°C is absolutely required for synthesis since the QFLS gives the highest limit for the open circuit voltage that we want as close as possible to the bandgap. An additional broad feature is recorded at lower energies below 1.5 eV which could refer to the existence of secondary phase(s). However, due to its too broad width, the estimation of the CGS bandgap energy is not possible precisely.

5.5 Raman spectra as other signature of the material

Raman measurements were performed on the cubic and monoclinic CGS samples. A first excitation wavelength of 633 nm was used and the resulting spectra are shown in Fig. 5.6 for wavenumbers between 50 and 500 cm^{-1}. This work constitutes the first report of Raman data for the low-temperature cubic phase and additionally is extending the measurement range of the monoclinic phase where usually peaks are only shown between 250 and 500 cm^{-1} [51, 137, 138]. All spectra were averaged over several positions on the samples to discard the possible influence of local defects. For instance, in order to verify the homogeneity of the monoclinic sample a rapid mapping was made on approximately twenty thousand positions, where no evidence for another phase could be made. The peak maxima of both cubic and monoclinic-related spectra in wavenumbers are reported in Table 5.1. Despite the fact that a lot of modes are found to be common, the intensity ratio of peaks between cubic and monoclinic phases are different,and the most intense modes are located at different wavenumbers. Additionally, the cubic phase shows larger broadening of the modes, which eventually confirm in parallel to the XRD the different nature of both samples.

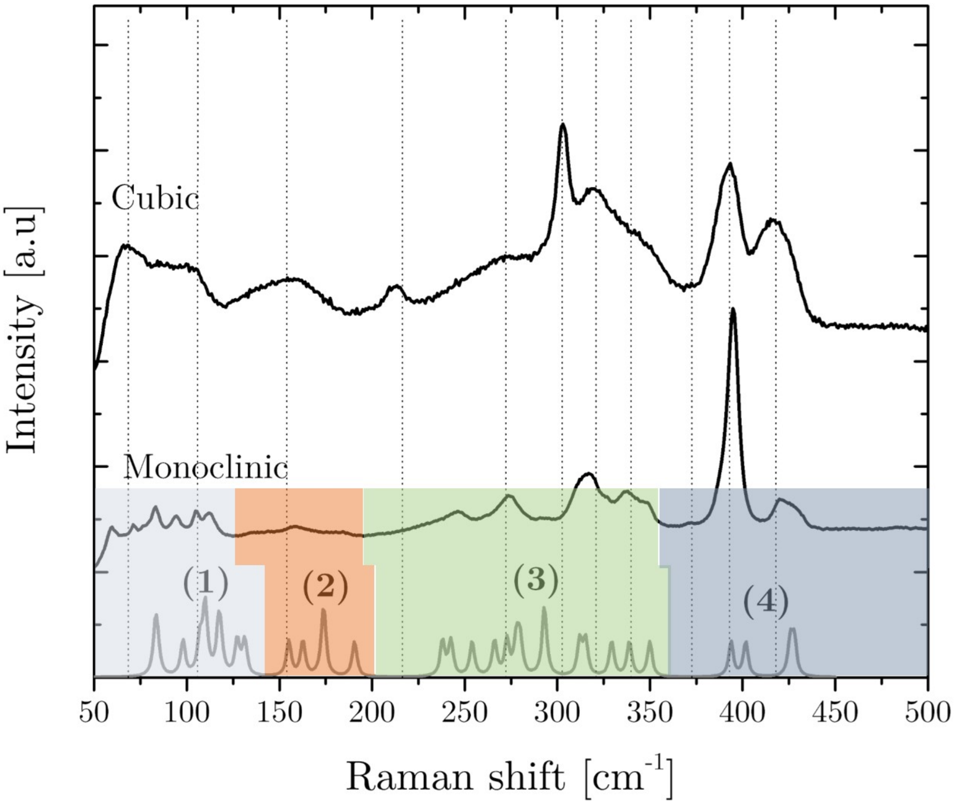

Figure 5.5: Raman spectra of the Cu_2GeS_3 annealed at $T = 480$°C (cubic) and 520°C (monoclinic). The dashed vertical lines highlight the peak maxima of the cubic sample. The grey line at the bottom shows the sketch of the Raman modes calculated for monoclinic CGS represented with constant width. Higher intensities correspond to the overlap of several modes.

As seen in Fig. 5.6, the Raman spectra of the cubic and monoclinic samples are different with maxima located at different wavenumbers [cm^{-1}] which as given in Table 5.1, amount to 317 cm^{-1} for cubic CGS and 395 cm^{-1} for monoclinic CGS. Theoretical physicists at the UL calculated the phonon modes expected in a monoclinic structure of CGS. With N = 12 atoms in its primitive unit cell, 3 N - 3 or 33 Raman active modes are present in the spectrum, shown together with the experimental data in Fig. 5.6. The calculated modes allow to confirm that modes reported here between 50 and 250 cm^{-1} well belong to the sample and not to a secondary phase. Thus, it is useful to extend the measurement range to obtain a full signature of vibrational modes of CGS. Even though overlaps between modes in the experiment do not allow to count modes and compare them to the calculation, four regions of modes are identified, as highlighted in Fig. 5.6.

The same measurements were repeated at other λ of 442, 532 and 785 nm. The resulting spectra are shown in Fig. 5.6 and the positions of peak maxima added to Table 5.1. It is seen that the intensity of the Raman modes varies with the laser source, suggesting different resonance phenomena. Generally, most of the modes are found at all wavelengths within the measurement error of less than 4 cm^{-1}. However even if more insight is currently not available those measurements lead to the conclusion that measurement ranges and conditions should be multiplied to get a full picture of the material and progress.

	monoclinic CGS							cubic CGS			
Nr.	442 nm	532 nm	660 nm	785 nm	[137]	[138]	[51]	442 nm	532 nm	660 nm	785 nm
1			60	60							62
2	73	72	73						72		68
3		84	83	83							89
4	99	96	95	94					95		
5	107	105	105					104		106	
6	113	114	112	112							
7	140	140		139							
8		160	159					154	156	158	155
9		184	182								
10								217	214	213	212
11		246	246	247							
12	276	275	274	275		275	276	273		272	269
13		294		293		296	292				
14							303	303	302		
15	320	318	317	315	321	320	319	323	320	321	317
16	339	338	338	337	339		340			340	
17			349	349		348	355				
18			370	372			373	373	367	373	
19	396	395	395	395	396	397	397	393	392	396	391
20		421	420		421	420		416	416	418	416
21	424	428		429	427		424				

Table 5.1: Report of peaks positions extracted from the Raman spectra of cubic and monoclinic CGS. Literature references [51, 137, 138] measured on monoclinic CGS between 250 and 450 cm^{-1} with $\lambda = 532$ nm, are added for comparison.

5.6 Conclusion of the chapter

This chapter showed that Cu_2GeS_3 follows a similar crystallographic transition as Cu_2SnS_3 from a low-temperature cubic structure to a more ordered predominant monoclinic structure, when the annealing temperature is increased above 500°C. Both materials are polymorphs and

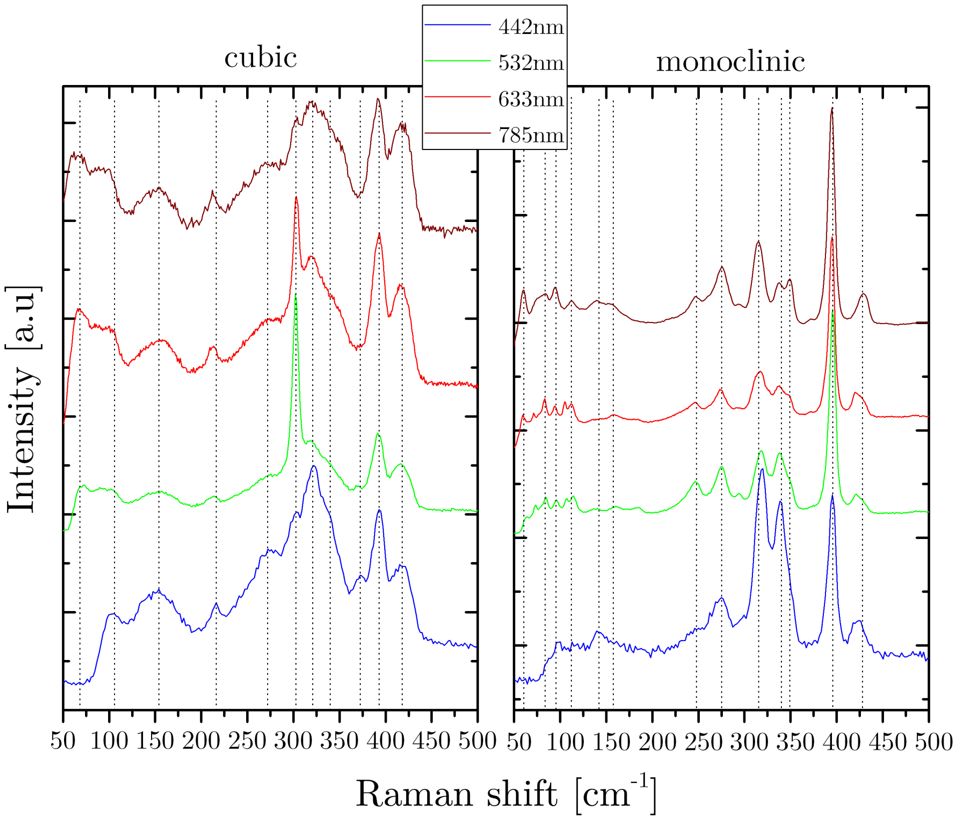

Figure 5.6: Raman spectra of the cubic (left) and monoclinic (right) Cu_2GeS_3 measured with $\lambda = 442$, 532, 633 and 785 nm. The dashed vertical lines are guidelines to the eye, to highlight the common peaks.

the cubic structure seems to be subject to local composition fluctuations, as Cu-Ge clusters can arrange themselves differently. In the monoclinic structure, atom positions are well defined while the low-temperature cubic phase is highly disordered. Photoluminescence measurements combined with absorption spectra suggest the presence of two absorption onsets as in Cu_2SnS_3, with a second valence band close to the first one. The band-to-band transition allows to determine a bandgap of 1.56 eV for the monoclinic sample. Absorption spectra allowed to determine the bandgap of cubic phase at 1.21 eV where the inflection point is found. Despite the complexity of the disordered phase, we have now developed its Raman database and bandgaps, which were not reported previously. Additionally one suggests that measurement range and conditions should be extended to fully characterise the material.

The recorded photoluminescence yield suggests that annealing temperatures above 500°C should be preferentially used for preparing absorbers designed for solar cell implementation. Those conditions are chosen to prepare CTGS alloys in Chapter 6.

CHAPTER 6

Synthesis and characterisation of $Cu_2Sn_{1-x}Ge_xS_3$ ternary alloys

6.1 Goal

Alloying Cu_2SnS_3 layers with germanium Ge offers great opportunities to better fit the bandgap of pure Cu_2SnS_3 to the maximum of the Shockley-Queisser limit (cf Fig.1.3) and tailor other optoelectronic properties to the specific requirements of a solar cell device. Recent investigations such as in Ref. [29] showed device power conversion efficiencies could be improved from 2% for Cu_2SnS_3 to 6% for $Cu_2Sn_{1-x}Ge_xS_3$-based devices ($x = 0.17$), which motivated to start researching on this material. A precise control of the elemental composition, particularly of the [Ge]/([Sn]+[Ge]) ratio, x, of a $Cu_2Sn_{1-x}Ge_xS_3$ (CTGS) absorber layer is a prerequisite in order to influence the film formation towards a desired Ge concentration or respectively, a specific bandgap profile through the depth, as done in highly efficient $CuIn_{1-x}Ga_xSe_2$ (CIGSe)-based devices [139]. To be able to control the composition and possibly further engineer graded absorbers one first needs a fundamental understanding of the reactive processes which govern the growth of the thin film between precursor and annealing stages. A stable alloy corresponds to the configuration with the lowest Gibbs free energy but the phase diagram of the Cu-Sn-Ge system is not available. The free energies could also be in favour of the absence of wide solid solution range. Therefore thin film analysis of Ge-containing $Cu_2Sn_{1-x}Ge_xS_3$ absorber layers synthesised by annealing of Cu-(Sn,Ge) precursor stacks in a sulphur atmosphere, has been performed to check for the nature of the intermixing. This chapter splits this theme in four sections in the following sequence:

1. Theoretical background of alloying and literature review of Ge-alloying in Cu_2SnS_3
2. Growth of Ge-containing Cu_2SnS_3 absorber
3. Study of miscibility and existence of $Cu_2Sn_{1-x}Ge_xS_3$ alloys
4. Estimation of doping densities for future device applications

These results were published in Ref.[140].

6.2 Background

This section groups the basics of the theory of semiconductor alloys. For more information the reader is referred to Ref.[141]. Alloying is widely used in semiconductors to tune properties of pure compounds into ones that are more suitable for electronic devices, such as solar cells. The primary goal of alloying is to engineer the minimum energy gap of the semiconductor, but it usually also influences others like the lattice parameters or mechanical constants. To be technologically useful, semiconductor alloys must be single phase with nearly perfect mixing. The perfect mixing results from a high solubility of the starting pure elements or compounds. Several types of alloys exist such as binary (mixtures of two elemental semiconductors), ternary (mixtures of two compound semiconductors) or quaternary alloys (mixtures of a larger number of compounds). This work focuses on ternary alloys as the mixture of two crystalline semiconductor compounds, Cu_2GeS_3 and Cu_2SnS_3. Depending on the relative size of the atoms replaced in the crystal structure, the average lattice parameter of the resulting alloy crystals will vary compared to the pure compounds. The lattice parameter of a crystal alloy $a_{A_{1-x}b_x}$, mixture of two compound semiconductors A and B, is generally described as the average of the lattice constants of the pure compounds a_A and a_B, weighted by the alloy composition. The resulting linear rule is known as Vegard's law:

$$a_{A_{1-x}B_x} = (1-x) \cdot a_A + x \cdot a_B \tag{6.1}$$

suggesting a linear evolution of the lattice constant between the starting parameters of the pure compounds A and B. Vegard's law represents an average over sufficiently large crystal volumes where local composition fluctuations do not affect the overall property. However, optoelectronic properties such as the bandgap E_g are localised to first and second neighbour bonds in the crystal structure and thus do not necessarily scale linearly with the alloy composition. A non-linear behavior of an alloy is then described by a bowing parameter c such as for E_G:

$$E_{G(A_{1-x}B_x)} = E_{G(A)} + (E_{G(B)} - E_{G(A)})x - cx(1-x). \tag{6.2}$$

A larger bowing is synonymous with poorer miscibility (i.e local phase separation) and most measurements techniques such as PL are sensitive to those local bandgaps. The solubility range of a new semiconductor alloy (or range of solid solution) is essential to know. The stability of an alloy is determined by the change in Gibbs energy $\triangle G$ (see Chapter 4 for the definition) with the change in composition. $\triangle G$ is defined as follows:

$$\triangle G = \Sigma \mu_i \triangle N_i = \triangle E - T\triangle S + p\triangle V, \tag{6.3}$$

wITH μ_i the chemical potential of the species i and N_i the number of atoms or molecules of that species. $\triangle E$ corresponds to the change in bond energy with the alloying, $\triangle S$ the change in entropy at constant T. Usually $\triangle V = 0$. The alloy will choose the crystallographic configuration that owns the smallest $\triangle G$ and is thus the most stable. The extent of miscibility of Ge in Cu_2SnS_3 was unknown at the start of this thesis. Mostly attempts at forming $Cu_2Sn_{1-x}Ge_xS_3$ layers with $x \sim 0.2$, single value of solid solution were performed, as reported in Table 6.2. The study of a solid solution in the CTGS system is complexified by the polymorph character of the pure CTS and CGS ternaries. Optoelectronic properties such as the bandgap energy vary with the polymorph structure. Therefore one should be very careful in attributing a property to a polymorph material and make sure good quality XRD data is reported to match a property to a certain crystal structure. The bandgap values E_G reported for the data presented in table 6.2 are shown in Fig. 6.1, showing the deviation between values, especially for large x, likely arising from different crystal structures.

Reference	Year	Nature	Composition(s) x $(0 < x < 1)$	η [%]
[29]	2013	TF	0 ; 0.17	6.0
[129]	2015	TF	0 ; 0.18 ; 0.40 ; 0.63 ; 0.83 ; 1	(-)
[142]	2016	TF	0.17	(-)
[51]	2017	P	0 ; 0.1 ; 0.2 $\longrightarrow$... 0.9 ; 1	(-)
[143]	2017	TF	0.07	3.8
[144]	2017	TF	0 ; 0.14 ; 0.66 ; 1	3.4
[145]	2018	TF	0.1	2.1

Table 6.1: Literature review of all studies for CTGS solid solutions with report of the best device efficiencies if any, TF refers to thin film and P to powder data.

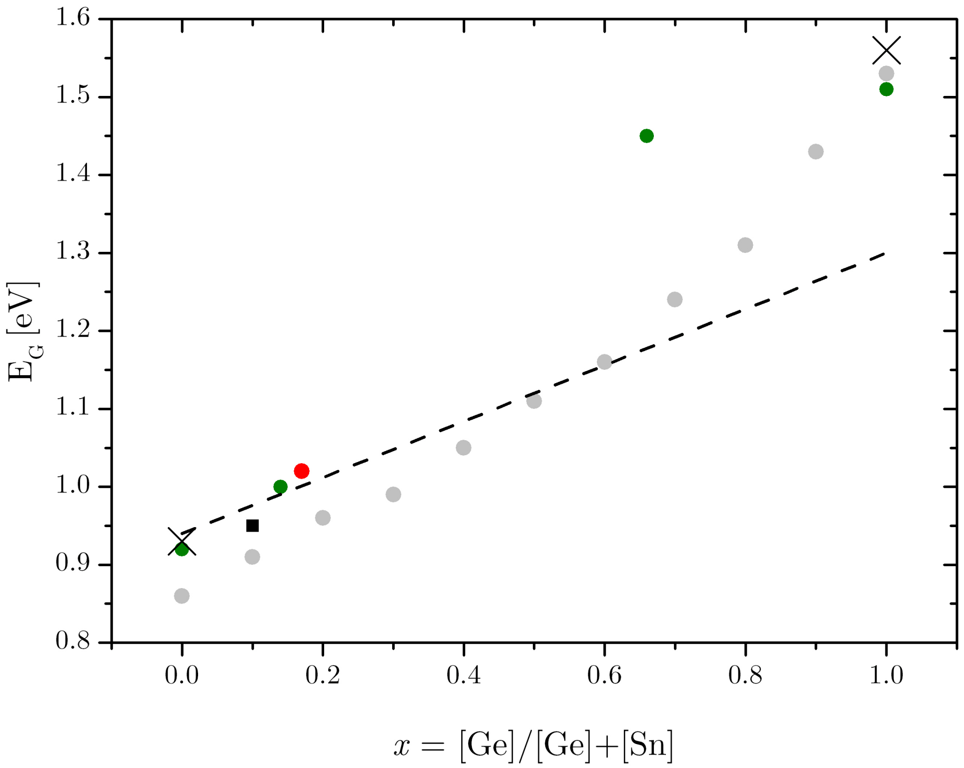

Figure 6.1: Report of bandgap energies E_g measured on CTGS thin films (the dashed line refers to the linear extrapolation of data in [129], the red dot to [29], the green dots to [144], the black square to [145], the light grey dots to the powder samples in [51]), together with black crosses from PL measurements done at the UL [53, 125]).

The lower bandgap for CGS ($x = 1$) reported in Fig. 6.1, as reproduced from [129], matches with the cubic structure of CGS measured in [125]. Therefore depending on synthesis conditions

polymorphs show deviations in their reported bandgap values. The powder study is the most complete. However, miscibility in the powder form does not necessarily mean thin films of CTGS show a solid solution for all x as well, depending on the kinetics of reaction. Araki et al. prepared CTGS powders by heating pure elements in a sealed ampoule for durations of more than a week at temperatures up to 1000°C [51]. Those extended durations go in favour of any thermodynamically stable reaction to occur, and the respective products form. However for thin films, annealing is usually around half an hour only, in an environment prone to vapour losses (cf chap 4), thus much more sensitive to kinetics. In this work it is investigated whether stable and uniform alloys can form, and on which composition range of x.
As seen previously in Chapter 5 the structures of both Cu_2SnS_3 and Cu_2GeS_3 ternaries are based on tetrahedral atomic arrangements where the sulphur anion is tetradrehally coordinated to four cations [146] that are Cu and group IV atoms. The only bonds are between sulphur anions and Cu or sulphur anions and group IV cations. The Cu-S and Sn-S average bond lengths in Cu_2SnS_3 were evaluated to be between 2.30-2.33 $\mathring{A}$ and 2.50-2.60 $\mathring{A}$, respectively [146–148]. Ge-S bond lengths are smaller around 2.21-2.25 $\mathring{A}$ [146], which reflect the smaller size of the Ge atoms. Replacing a fraction x of the Sn atoms in Cu_2SnS_3 by Ge should therefore lead to a decrease of the average bond length in the crystal lattice. It is therefore expected, according to Bragg's law (Eq. (2.1)) that an incorporation of Ge atoms in Cu_2SnS_3 to form $Cu_2Sn_{1-x}Ge_xS_3$ reduces the average interplanar distance and thus shifts the reflections of its X-ray diffractogram to larger 2θ angles. GI-XRD is thus a tool of importance for analysing the structure and composition of CTGS films with high depth resolution. The result section begins with the study of the effect of stacking order on the final CTGS composition.

6.3 Growth of Ge-containing $Cu_2Sn_{1-x}Ge_xS_3$ films

6.3.1 Importance of stacking order in precursor

Cu,Ge,Sn-containing precursors with different stacking orders are annealed under the same conditions to form CTGS alloys. Standard and fixed annealing conditions are chosen in accordance with previous research (cf chap 4, T = 550 °C, p_{back} = 1 mbar, t = 30 min) to form the monoclinic structure of Cu_2SnS_3 and Cu_2GeS_3. CTGS is likely a polymorph as well and one makes the hypothesis that a monoclinic structure of CTGS will be formed as well under these same annealing conditions. Isostructural alloying (starting with two compounds of the same crystallographic structure) is the most likely to form a solid solution [141]. The importance of the stacking order on the final CTGS composition is evaluated for three different Cu-Sn-Ge-containing precursors, presented in table 6.3.1. The annealing is performed in the furnace presented in Chapter 4 in the presence of a sulphur source and GI-XRD measured on the films after annealing. The precursors were sputtered from from binary Cu:IV targets with composition 64:36 at.%. The target composition matches the precursor composition. The different stacking orders allow to study the interdiffusion of Sn and Ge.

1	Cu:Ge/Cu:Sn
2	Cu:Sn/Cu:Ge/Cu:Sn
3	Cu:Ge/Cu:Sn/Cu:Ge

Table 6.2: Stacking configurations of the DC sputtered precursors from binary Cu:IV targets with composition 64:36 at.%, used to prepare $Cu_2Sn_{1-x}Ge_xS_3$ thin films. Stacks are described by "/" and codeposited elements by ":".

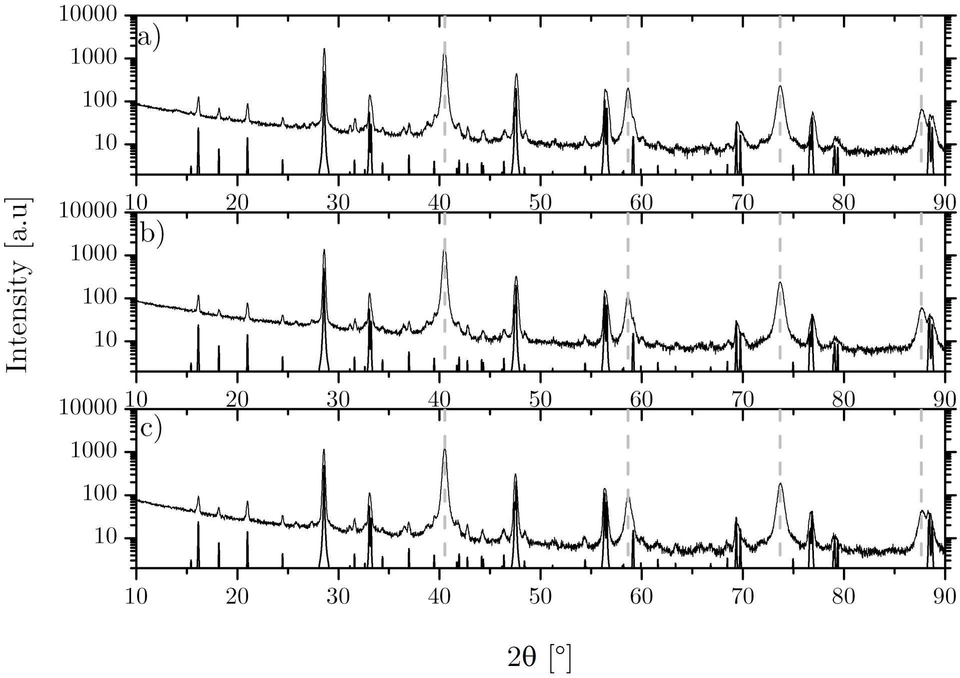

Figure 6.2: GI-XRD (α = 2°) of the annealed a) Cu:Ge/Cu:Sn, b) Cu:Sn/Cu:Ge/Cu:Sn and c) Cu:Ge/Cu:Sn/Cu:Ge precursors, in S at 550°C for 30 minutes, cross compared with the theoretical XRD generated with PowderCell [149], for a monoclinic CTGS layer with x = 0.2. Mo peaks are indicated by the dashed grey lines.

The resulting GI-XRD in 6.2 show the same Bragg peaks for all three resulting films. Theoretical X-ray patterns for the CTGS alloys ($0 < x < 1$) considering a uniform intermixing of Ge and Sn can be generated with the software PowderCell [149] for any x. The software calculates the X-ray diffractogram after input of the crystallographic details (lattice parameters, space group, atomic positions and site occupation). Assuming that CTS and CGS both follow a monoclinic structure under the chosen annealing conditions and that their alloy forms a solid solution on the entire composition range ($0 < x < 1$), Vegard's law (Eq. (6.1)) can be used to estimate lattice parameters for all x [150], i.e the lattice parameters decrease linearly between the reference values for pure CTS [151] and pure CGS [133], reported in Table 8.2. Thus follows for a:

$$a_{\mathrm{Cu_2Sn_{1-x}Ge_xS_3}} = (1-x) \cdot a_{CTS} + x \cdot a_{CGS} \tag{6.4}$$

and similarly for b, c and β. The atomic positions are not known for the alloys $0 < x < 1$. Instead atomic positions of the atoms in pure CGS are used arbitrarily. One therefore makes the hypothesis that the atomic positions do not vary much when changing x. The occupation of cationic sites by Sn and Ge are written respectively as $1 - x$ and x. Such an examplary unit cell for $Cu_2Sn_{1-x}Ge_xS_3$ with $x = 0.5$ is represented in Fig. 6.3.

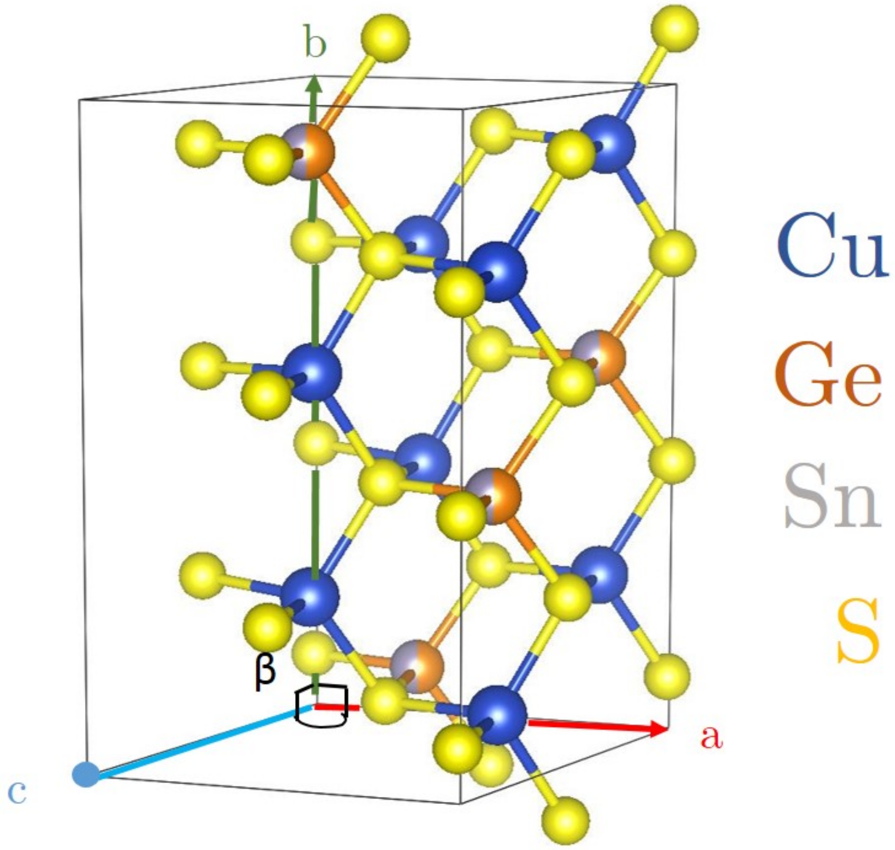

Figure 6.3: Conventional unit cell of $Cu_2Sn_{0.5}Ge_{0.5}S_3$ drawn with VESTA [134], using lattice parameters calculated considering a solid solution with Vegard's law (Eq. 6.4) and atomic positions of Cu_2GeS_3. The occupation site reflects the replacement of a randomised fraction of Sn sites by Ge.

Visual inspection of the three GI-XRD in Fig.6.2 is done with a diffractogram generated for x = 0.2, showing the same identical Bragg peaks for all precursors a), b) and c). The three GI-XRD were taken with sufficiently high incident angle α to probe the entirety of the film (cf.2.1.2) and also peaks related to the Mo substrate are recorded. This cross comparison suggests a similar outcome in composition of CTGS for different precursor stacks with formation of a single alloy. This means that in the thirty minutes allowed for the annealing the Sn and Ge could perfectly interdiffuse. Engineering a gradient in $Cu_2Sn_{1-x}Ge_xS_3$ would certainly necessit shorter annealing times. Kinetics of formation of the alloy seem sufficiently quick to avoid gradients and thus alloy the study of $Cu_2Sn_{1-x}Ge_xS_3$ bulk. Deeper studies of depth uniformity on a series of absorbers with various x are performed. These absorbers are produced from one type of Cu:Sn/Cu:Ge precursors annealed to produce several x that can be analysed.

6.3.2 Lateral uniformity of the $Cu_2Sn_{1-x}Ge_xS_3$ films

Since the precursor stacking has shown no influence on the composition of the final CTGS films which seem to show no apparent grading, one of the precursor types is selected. When various CTGS alloys with different x can be synthesised from those precursors with sufficient volume without lateral and depth compositional grading, one could evaluate the structural and optoelectronic properties of the alloy, and study in parallel the width of the solid solution. Precursors with Ge at the top (Cu:Sn/Cu:Ge) are chosen for the highest vapour pressure of GeS and the ability to tune Ge content with annealing duration. Five of those same precursors are annealed with S at 550 °C between 15 and 30 minutes. Films of pure Cu_2SnS_3 and Cu_2GeS_3 (x = 0 and 1) are prepared from single copper layers annealed in S and group IV atmosphere, by the method described in Chapter 4. All seven resulting films are measured with WDX to check for their lateral composition, both on micron-sized points and 60 μm^2 areas randomly selected on the sample surface. Considering that WDX allows an elemental accuracy down to about ± 1 at%, all measured ratios on a sample, x, Cu/IV and Ge/IV are found to be identical since their variation from spot to spot are lower than the accuracy limit. Thus, the seven samples are considered as uniform and for each sample the compositional ratios are averaged over three large areas and reported in Table 6.3.2.

Sample	1	2	3	4	5	6	7
x	0	0.24	0.26	0.43	0.47	0.63	1.00
Cu/IV	1.95	1.83	1.94	1.94	1.98	1.84	1.86
S/IV	2.90	2.69	2.64	2.66	2.73	2.98	3.11

Table 6.3: Report of compositional ratios $x = \frac{Ge}{Ge+Sn}$, Cu/IV $= \frac{Cu}{Ge+Sn}$ and S/IV $= \frac{S}{Ge+Sn}$ of the seven CTGS thin films under investigation.

The compositional ratio reported in Table 6.3.2 demonstrate the successful synthesis of a series of laterally uniform alloys with increasing Sn substitution by Ge. Only no sample could be produced with a composition x between 0.65 and 1. This is explained by the high vapours pressures of GeS and SnS during annealing and their desorption, which makes control of the final composition after annealing difficult. Also, powders with a larger compositional range could be produced and measured [51]. The Cu/IV ratio for the seven samples can be considered as identical with values between 1.83 and 1.98. Thus, all films are copper poor as Cu/IV < 2, which can be explained by the high partial pressure of SnS or GeS during the annealing [71]. The films are S-poor with S/IV < 3, at the exception of sample 7 which shows a higher sulphur content. This higher sulphur is attributed to the formation of MoS_2 during annealing as the film has peeled off and thus Mo was exposed to the chalcogen vapours. In the Raman spectrum of this sample, one peak suggests the existence of MoS_2.

6.3.3 Depth uniformity of the $Cu_2Sn_{1-x}GexS_3$ films

The same films are analysed with depth-resolved GI-XRD for several grazing incidence angles α (cf. section 2.1.2). α values of 0.5, 3 and 6 ° are chosen to study from the first 200 nm to the entire depth of the film (3 microns) of the absorber, as demonstrated in section 2.1.2. The average thickness of the films was evaluated from SEM cross-sections to 2.4 microns. Fig. 6.4

presents all diffractograms recorded with α = 0.5°. The assessment of present phases and their crystallographic structures is done by direct cross-comparison with reference patterns for monoclinic CTGS and cubic Mo (substrate). The XRD references for Mo, monoclinic CTS and CGS are taken from literature, as reported in Table 8.2 [47]. For the Le Bail fitting we make the assumption that CTGS alloys with $0 < x < 1$ also follow a monoclinic structure. However the XRD references for CTGS alloys with $0 < x < 1$ do not exist in literature.

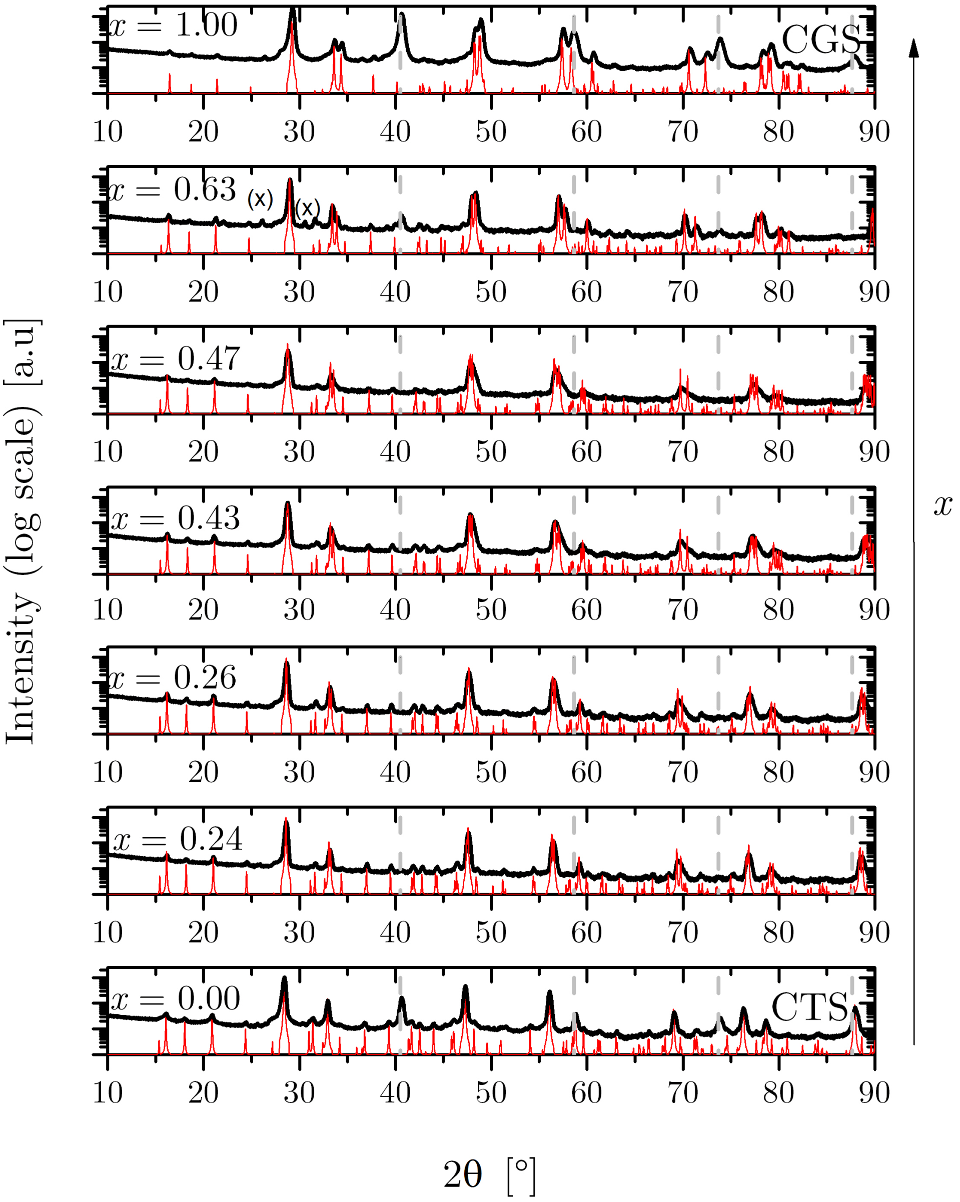

Figure 6.4: GI-XRD recorded with α = 0.5° on CTGS absorbers with x = 0 ; 0.24 ; 0.26 ; 0.43 ; 0.47 ; 0.63 ; 1 (as labelled on the graphs). The dashed grey lines indicate the Mo contribution and the stars (×) the SnS-related peaks, both taken from literature, as reported in Table 8.2. Theoretical patterns (shown in red) are generated with PowderCell for all x from the atomic positions of pure CGS and the lattice parameters of both CTS and CGS reported in Table 8.2.

As seen in Fig. 6.4 the theoretical patterns calculated with PowderCell for monoclinic (space group C1c1) lattices of CTGS are directly comparable with the experimental data for all x: despite the hypothesis made on atomic positions, all visible reflections in the experimental data are explained by the theoretical patterns, together with the signal referring to the Mo substrate. The GI-XRD therefore suggest the alloying of CTS with Ge with various concentrations x. Only the sample with x= 0.58 contains additional Bragg peaks, only two, which could be tin sulphide SnS. To study the depth phase uniformity, GI-XRD are also recorded with α = 3 and 6° and presented in Fig. 6.5 for all x, together with the data recorded with α = 0.5° .

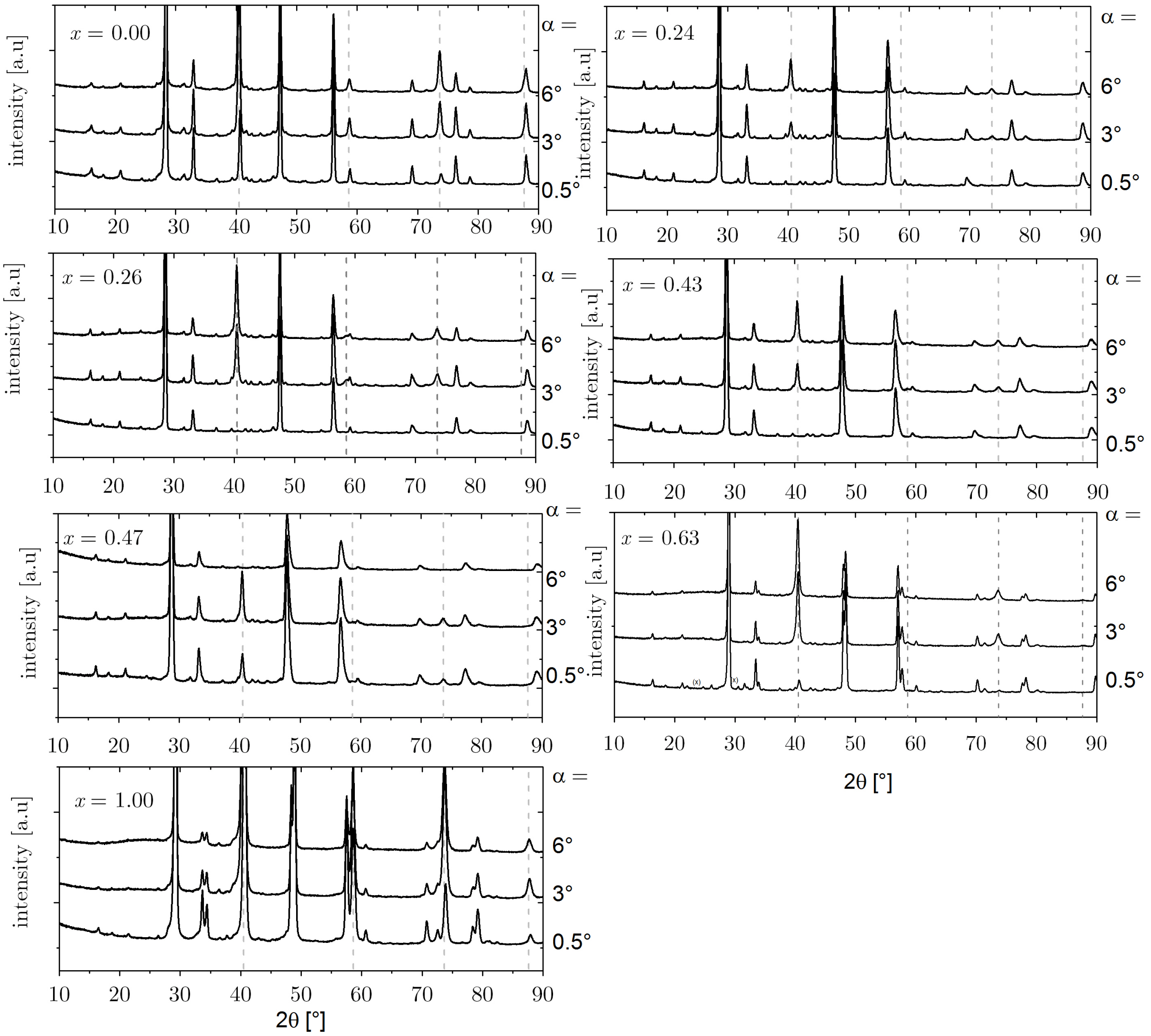

Figure 6.5: GI-XRD recorded for α = 0.5; 3 and 6° for each x. The dashed grey lines show the reference pattern for the Mo substrate.

After visual inspection the XRD recorded at various depths seem to show identical Bragg peaks as on the sample surface (first 200 nm). The sample with x = 0.63 shows the two SnS-related peaks at the surface only. This SnS phase, not seen in powder data prepared in cleaner environments [51], is attributed to an impurity from the graphite box.

The depth uniformity is studied via extraction of lattice parameters of the CTGS alloys. The extraction of lattice parameters is done with Le Bail refinement method with the software FullProf (as described in section 2.1.2). The overlay of all GI-XRD data with the respective Le Bail fittings is presented in Appendix C. Since the method requires a starting crystal structure and space group, one inputs a monoclinic C1c1 structure, for all x, as this seems fair for the annealing temperature used [71]. The lattice parameters extracted from the refinement are presented in Fig. 6.6 as function of the incidence angle α.

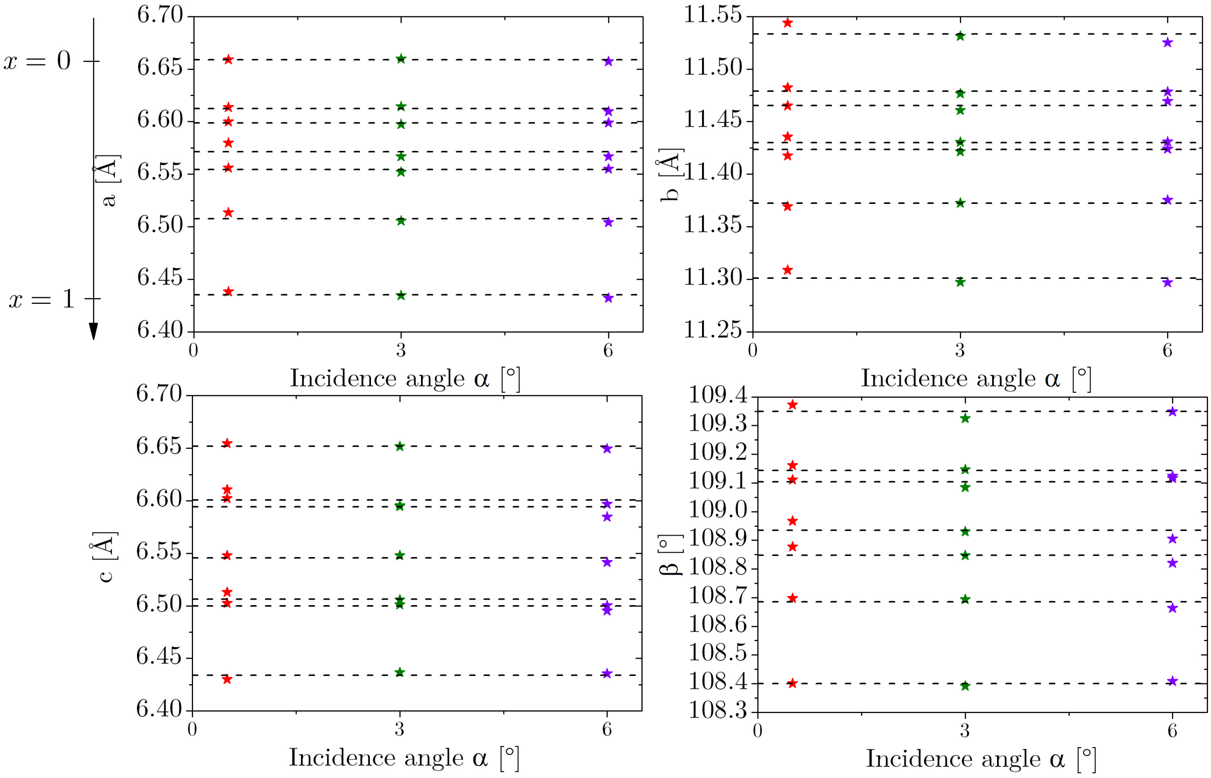

Figure 6.6: Lattice parameters a, b, c and β extracted from Le Bail refinement, on a monoclinic structure (space group C1c1) shown as function of the incidence angle α (0.5° (red stars), 3° (green stars), 6° (purple stars)). All compositions from $x = 0$ to 1 are shown ordered as labelled on the left hand side. The dashed lines represent the average of a set of three values.

Fig. 6.6 shows the lattice parameters are constant in depth. The few visible fluctuations to the average within the sample depth are of a negligible value. As treated in the background section to this chapter, Vegard's law (Eq. (6.1)) averages the lattice properties over large volumes and thus linear extrapolation of the data can be done. The same lattice parameters extracted with Le Bail are presented in Fig. 6.7 as function of x together with lattice parameters extracted from powder diffraction data in [51].

The direct cross-comparison between thin film and literature powder data [51], presented in Fig. 6.7 shows satisfactory trends with very similar outcomes. A linear fit $y = ax + b$ is calculated for each parameter and each incidence angle α. The resulting linear equations are given in table 6.3.3 together with standard deviations. Within the errors all fits for each lattice parameter are identical.

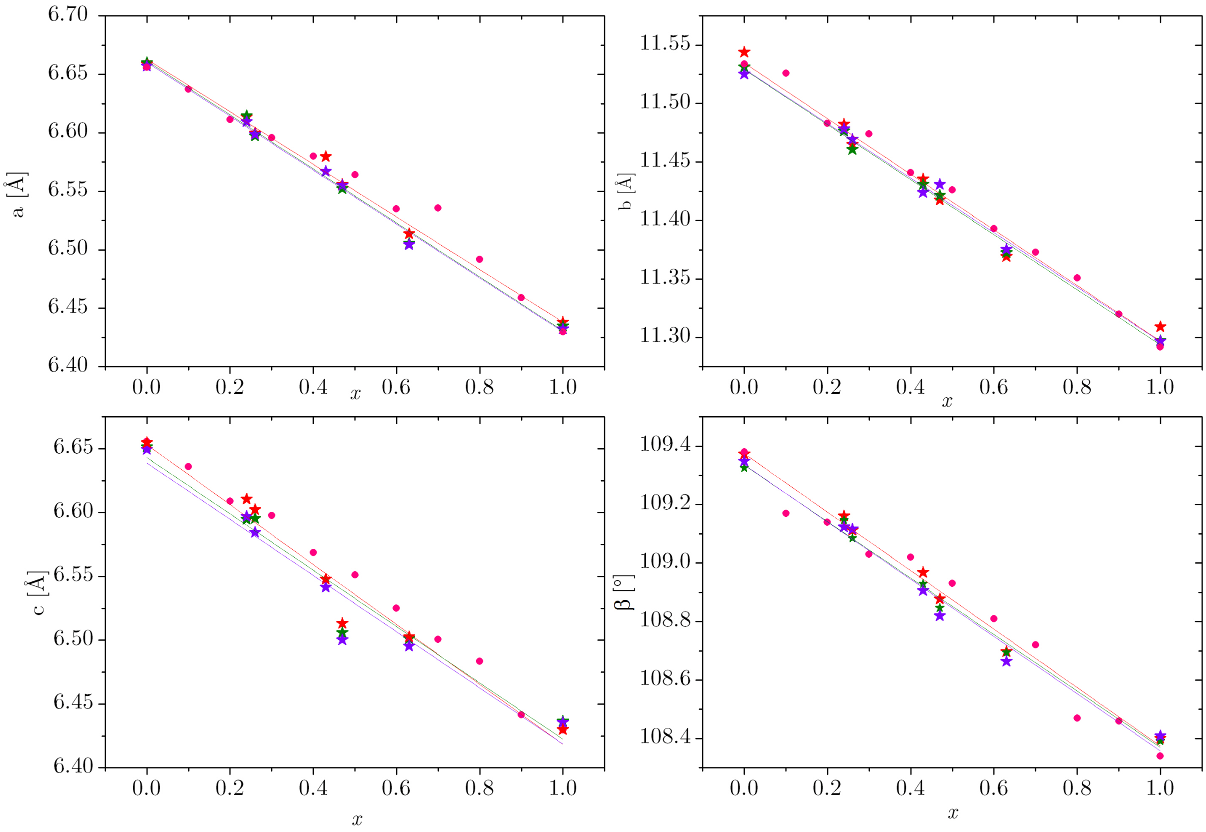

Figure 6.7: Lattice parameters a, b, c and β extracted from Le Bail refinement for all incidence angles α ((0.5° (red stars), 3° (green stars), 6° (purple stars)), on a monoclinic structure (space group C1c1) shown as function of the composition x. The pink dots are literature powder data extracted from [51]. Linear fits are drawn for all lattice parameters at every α.

The overall shift of lattice parameters with x thus scales linearly with x, as shown in Table 6.3.3, and is in agreement with the powder data. With this section we have shown that a wide solid solution range of Sn-Ge alloying exists, uniform in depth and laterally. Unlike CIGSe, gradients could be engineered and do not naturally form under standard annealing conditions.

6.4 Bandgap extraction with photoluminescence

PL spectra were measured for all x. The resulting spectra are shown in Fig 6.8a) normalised to their maxima labelled as E_2. An additional feature is visible at about 0.9 eV in almost all spectra, labelled as E_1. Fig 6.8b) shows the peaks E_2 overlaid. E_2 is considered as the band-to-band transition, as both the maximum of E_2 for $x = 0$ and $x = 1$ fit to expectations in bandgap for pure CTS and pure CGS [116, 125, 127]. CTS and CGS also have been reported to have an intrinsic feature with a second optical transition at slightly higher energies than the bandgap [53], however for this analysis one considers it does not change the position of the main peak, as no clear feature is observed. One therefore considers E_2 relates to the main band-to-band transition from the maximum valence band to the lower conduction band.

Lattice parameter	α	Slope a [Å or °]	Y-intercept b [Å or °]
a	0.5	-0.00225 (±9.86E-5)	6.66301(±0.00517)
	3	-0.0023(±8.09E-5)	6.66032(±0.00425)
	6	-0.00231(±8.86E-5)	6.66152(±0.00465)
b	0.5	-0.00238(±1.39E-4)	11.53471(±0.0073)
	3	-0.00235(±7.34E-5)	11.5291(±0.0039)
	6	-0.00233(±8.87E-5)	11.52948(±0.00466)
c	0.5	-0.00235(±2.09E-4)	6.65322(±0.01096)
	3	-0.00221(±2.22E-4)	6.6431(±0.01163)
	6	-0.0022(±2.40E-4)	6.63877(±0.01261)
β	0.5	-0.01(4±00E-4)	109.37405(±0.02098)
	3	-0.01(±3.95E-4)	109.33469(±0.02073)
	6	-0.01(±5.94E-4)	109.33607(±0.03115)

Table 6.4: Slope a and y-intercept b of linear fits $y = ax + b$ of lattice parameters vs x, presented in Fig 6.7 for a, b, c and β.

The overlay in Fig. 6.8b) of all E_2 peaks shows that the full width at half maximum (FWMH) do not exceed 115 meV. For FWHM < 120 meV extraction of the bandgap E_G can be done by taking the value of the peak maxima E_2 [153], which can underestimate the real E_G only by 20 meV. The bandgap values obtained from E_2 are presented in Fig 6.9 as function of x, together with the optical light transmission-reflection data measured on CTGS powders in [51], and theoretical bandgap values (top valence band to conduction band) extracted for CTS, CGS and CTGS with x = 0.5 [53, 154]. A linear fit of the thin film data is performed and shown in Fig 6.9, which would correspond to a bowing $c = 0$ which may be an approximation due to the number of data points present. It has to be noted that transmission-reflection measurements make the bandgap extraction complex due to the several optical transitions in the material [53]. In this regard, PL likely offers a more accurate description.

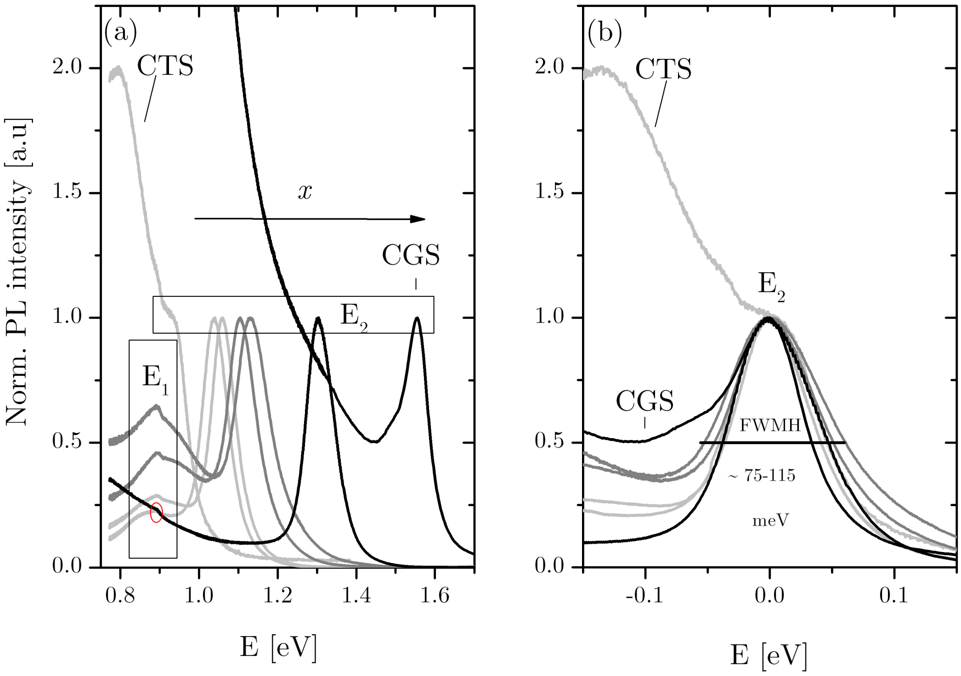

Figure 6.8: (a) PL spectra normalised to the peak maximum E_2, highlighted in rectangle for all x ($0 \leq x \leq 1$, with shading from light grey for $x = 0$ to black for $x = 1$). The luminescence peak E_1 is also highlighted in a separate vertically orientated rectangle. Only $x = 0.63$ shows large tailing and no E_1 but a feature around 0.9 eV (circled in red) possibly related to water absorption [152], (b) Overlay of all normalized PL spectra shifted by their maximum E_{max} for comparison of peak widths (FWHM).

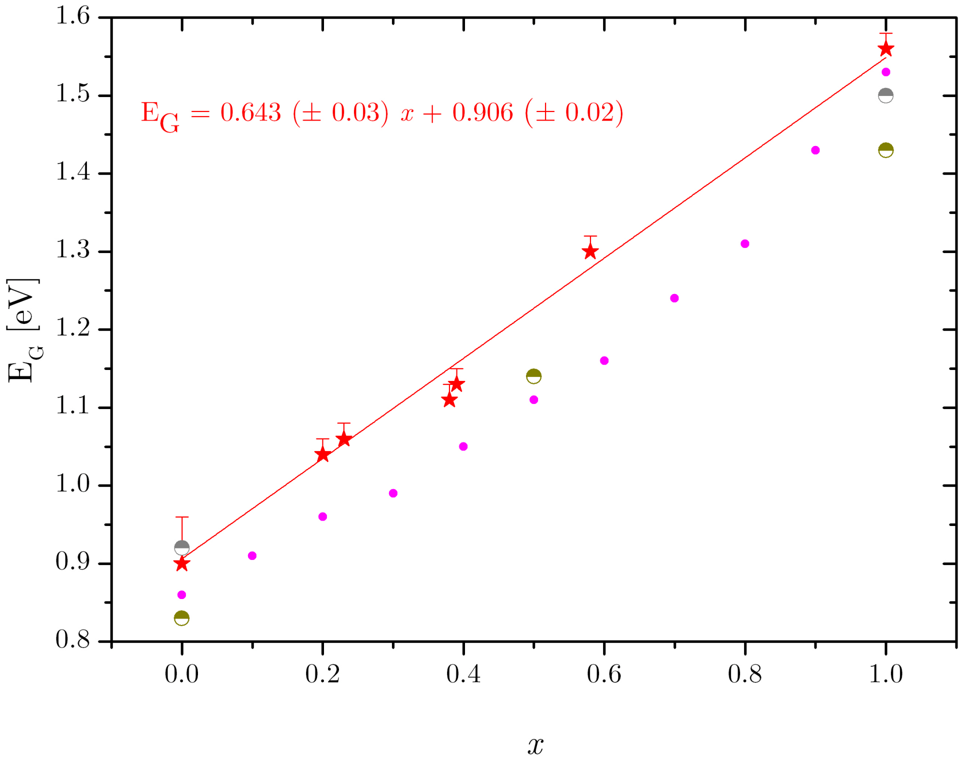

Figure 6.9: Bandgap energies E_G (shown as red stars) extracted from the PL peak maximum E_2 for all x and fitted linearly, plotted together with the E_G extracted from light transmission-reflection measurements on CTGS powder samples (pink dots) [51]. Using the maximum of E_2, E_G is underestimated by 20 meV only (error bars) . Only the error on CTS is a bit larger due to the PL tailing. Additionally theoretical bandgaps from [53] are shown as half-filled grey circles for pure CTS, CGS and as

6.5 Raman spectroscopy

Raman spectroscopy was measured for all x with a wavelength of 633 nm, as shown in Fig.6.10a). Additionally, theoretical physicists at the UL calculated the Raman modes expected in CTGS materials of the same composition and sketched in b) for the same x, plus one at 0.8 which was not produced experimentally, similarly as in Chapter 5 for $x = 1$.

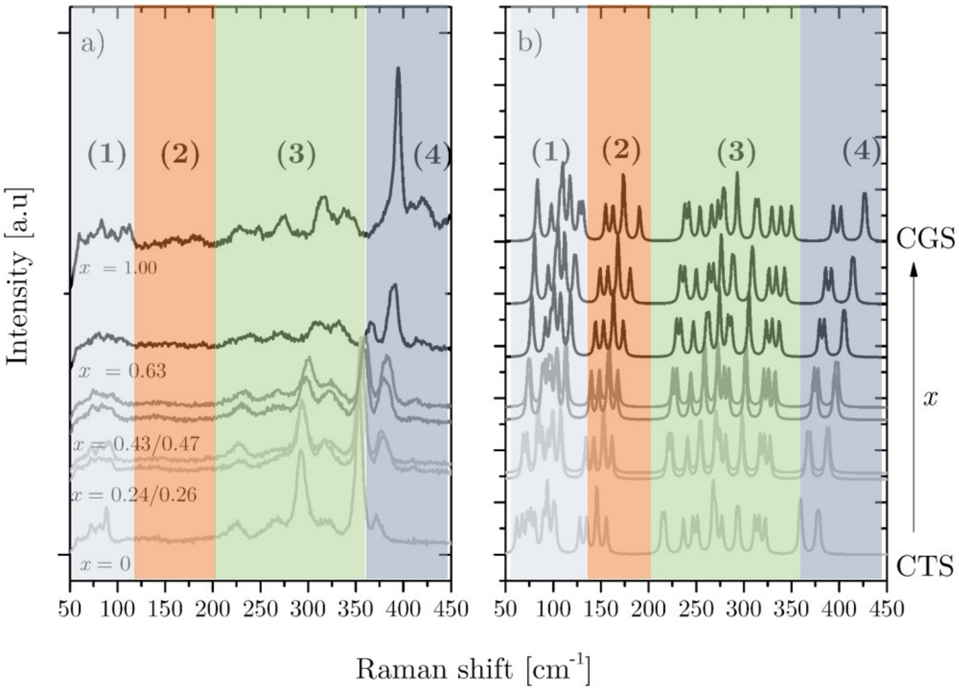

Figure 6.10: Raman spectra recorded for all x (as labelled on the right hand side and shaded from light grey (no Ge) to black (100% Ge). Each spectra is y-shifted to a value its composition, in order to follow the peak shifts more easily. The major peaks of interest are highlighted with red dashed lines and their respective Raman shift positions. For x = 0.63 the modes known for SnS are highlighted by vertical lines [155].

The experimental Raman spectra show a fair comparison to the phonon sketch with identification of four separate regions of modes, although in the experiment the modes in region 2 have almost vanishing intensity. The experimental spectra also all have fewer peaks than the calculated phonon sketch (where all phonons contribute with equal intensity). The theoretical calculations simply show the possible phonon modes, but not their likely intensity. The calculations confirm the existence of the Raman modes measured between 50 and 100 cm^{-1} in region 1, never reported previously. We also note the good agreement in the degree of peak shifting between theoretical and experimental data as x increases from 0 to 1. For example the most intense mode in CTS at 353 cm^{-1} shifts to 394 cm^{-1} for CGS in Fig.6.10b), revealing a shift to higher frequencies by about 40 cm^{-1}. This corresponds rather well to the theoretically expected shift of the main peak from 360.2 to 401.6 cm^{-1} in Fig.6.10a). Examining regions 3 and 4 in Fig.6.10b), the four modes observed in the CTS sample at frequencies between 290 and 450 cm^{-1} were previously reported in literature for the monoclinic structure of CTS in both thin film [30] and powder [51] forms. Similarly the seven modes observed in the CGS sample at frequencies between 275 and 450 cm^{-1} were also previously reported in the literature for a monoclinic structure in CGS bulk crystals and/or powders as explained in Chapter 5, at the exception of the mode at 408 cm^{-1} which was not reported previously but is visible in the spectra and likely relates to MoS_2 [156]. The presence of SnS suggested by XRD at the surface of the sample $x = 0.63$ is not observed with Raman spectroscopy (160 and 191 cm^{-1} [85]) which could mean that it is in low concentration, or that it is preferentially orientated in such a way that its modes are not visible, as also seen by the lack of multiple reflections in XRD.

6.6 Electrical measurements

CTGS films could be implemented in solar cell devices. In this regard doping concentrations below $10^{17}\,\mathrm{cm}^{-3}$ are required to achieve a large space-charge width W in typical p-n junction thin film photovoltaic devices. After adding aluminium front contacts to the films, capacitances are measured for a range of applied voltages where resulting Mott-Schottky plots allow to extract both doping type and concentrations. The doping concentration corresponds to the slope of the linear fit to the Mott-Schottky plot. Only the pure CTS sample ($x = 0$) could not be evaluated as it was electrically shunted due to a high number of pinholes. All other samples showed a linear response similar to Fig. 6.11 showing the Mott-Schottky plot evaluated for $x = 0.24$. The negative slope confirms the p-type character of the films, and is thus suitable for creation of pn junction photovoltaic devices. However, the apparent net doping concentration, N_A, is in the order of $10^{17}\,\mathrm{cm}^{-3}$ for this sample. Doping concentrations for all x (except $x = 0$) are reported in Table 6.6. N_A varies from 4 to 35 × $10^{17}\,\mathrm{cm}^{-3}$ with no clear trend with respect to the group IV composition.

x	0.00	0.24	0.26	0.43	0.47	0.63	1.00
$N_A \times 10^{17}[\mathrm{cm}^{-3}]$	(-)	4	22	8	35	11	18

Table 6.5: Report of apparent doping concentrations N_A [cm^{-3}] estimated from C-V measurements

In two of the films N_A below $10^{18}\,\mathrm{cm}^{-3}$ are estimated which is consistent with the work of Baranowski et al. [21] but remain at least one order of magnitude too high for device applications.

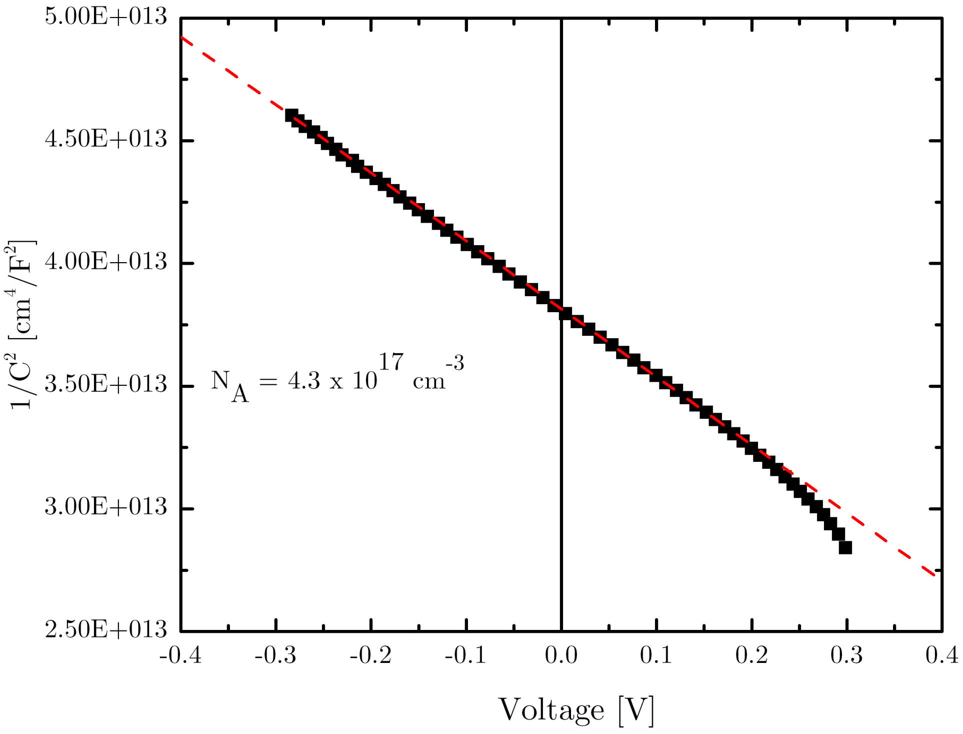

Figure 6.11: Exemplary Mott-Schottky plot measured on the sample with $x = 0.24$ whose slope is used to extract the doping density N_A.

6.7 Conclusion of the chapter

Ge-alloying of Cu_2SnS_3 offers a wide range of solid solution for monoclinic CTGS, where lattice parameters and bandgaps can be extrapolated linearly for all x. Samples with composition between 0.65 and 1 being not available, one can not be sure that the entire compositional range offers a solid solution of CTGS. One however knows that without SnS and GeS in the atmosphere, high desorption of SnS and GeS occur, which make it complex to control final composition. Powder results have demonstrated a wide solution on the entire range, which correlates with our results for x between 0 and 0.6. The powders are known to be synthesised in closed and cleaner annealing environments, where thermodynamic conditions have higher impact than the kinetics. Contrarily to CIGS, the kinetics of annealing of the films offer rapid formation of an homogeneous CTGS absorber with no depth gradient. To engineer graded bandgaps in the future, annealing durations should be minimised. For implementation in working solar cell devices, investigation in lowering the doping density is a requirement. The high doping density likely arise from the large density of copper vacancies in the material. Compensating those acceptor defects by donors could result in a reduced doping density. Such doping can be for instance done with silver if Cu has an oxidation state of +1, as suggested in Ref. [157]. The next chapter consists in the study of the completion of CTGS absorbers into finished solar cell devices. As in CIGS, depth gradients and thus bandgap gradients are known to be beneficial to performance, one finds a way to engineer a gradient in CTGS absorbers and produce working solar cells with a performance close to 3% which represents half of the current world record's device.

CHAPTER 7

What limits the efficiency of $Cu_2Sn_{1-x}Ge_xS_3$-based solar cell devices?

7.1 Goal

This chapter investigates the completion of the CTGS absorber layers into thin-film solar cell devices. Preliminary studies on the completion of the pure Cu_2SnS_3 ($x = 0$) and Cu_2GeS_3 ($x = 1$) ternaries into similar devices demonstrate power conversion efficiencies below 2% for CTS and below 1% for CGS in this thesis, when the best device efficiencies reported do not exceed 4.6% for CTS [31] and 2.7% for CGS [158], respectively. Improvement of Ge-alloy based devices to above 6% [29] with the same heterojunction motivated research on the mixture of Ge and Sn, as developed in chapter 6. Although the device efficiency was improved to 6%, large power losses still limit these thin film solar cells whose performance is far behind CZTS and CIGS. It is a requirement now to try and understand the origin of power losses in order to reduce them in the future. In this objective three themes of interest will be discussed in this chapter:

1. Literature background of non-ideal solar cells
2. Assessment of the main power loss factor in CTS and CGS-based solar cells
3. Presentation of the CTGS-based device obtained and discussion

7.2 Background

Solar cell devices function upon solar irradiation via the photovoltaic effect. Solar cells presented in this chapter were prepared from CTGS absorber layers completed in a p-n heterojunction structure copied from CIGSe technologies, with n-type CdS buffer and ZnO window layers on top of it, as seen in Fig. 1.4. The reader is referred to Refs.[43, 159] for more information about the solar cell working principles.

When a device is illuminated, incident photons with an energy above the bandgap of the absorber layer (CTGS), $E > E_G$, are absorbed by the CTGS layer, generating electron-hole pairs. The CdS and ZnO top window and buffer layers completing the p-n junction as n-type contact have bandgaps of 2.4 and 3.3 eV respectively, therefore they can absorb some of the high energy photons of the solar spectrum and this decreases the total number of photons being absorbed in the CTGS. The charge carrier generation following photon absorption can occur anywhere in

the absorber layer: either near the interface with the n-type CdS layer, within the space-charge region (SCR), or deeper in the bulk. The photocurrent that one wants to extract out of the solar device is described by the flow of minority carriers (electrons in the p-type layer) through an external circuit. For an external current to flow, any electron generated in the bulk should diffuse to the SCR where it is separated from holes by the existing electric field and is transported through to the CdS layer. The holes are separated by the electric field in direction of the back contact and thus diffuse through the bulk.
Several CTS, CGS and CTGS working solar cell devices have been reported in the literature, such as those presented in Table 1.4 and more recently up to 4.6% for CTS [31] and 2.7% for CGS [158]. However, these devices are still far below the efficiencies produced by CIGSe-based or even CZTS-based devices. A requirement for the future is to give an attempt to understand the origin of losses.

As defined in Eq. (2.20), the power conversion efficiency of the solar cell device η is defined by the product of J_{sc}, V_{oc} and FF for a fixed illumination power. Thus losses in the real device will reflect in the decrease of at least one of these three parameters compared to the ideal device defined in the SQ-limit (cf. Fig 1.3). The maximum J_{sc}, V_{oc} and FF reachable in an ideal CTS, CGS and CTGS device will be calculated next. However, first one wants to differentiate the different loss factors.
Losses in the short-circuit current density J_{sc} are mostly optical losses. Optical losses are constituted of:

- the parasitic photon absorption by the n-type CdS (2.4 eV) and ZnO (3.3 eV) layers,
- the incomplete photon absorption by the p-type CTGS layer (via reflection or transmission)
- the shadowing by the Ni:Al top surface grids on the device,

where a film thickness below the light penetration depth can also lead to incomplete photon absorption.

In highly efficient CIGSe devices, only 10-15% of the incoming photons are lost, which results in an EQE spectrum at 85-90% below the bandgap of CdS, $E < 2.4\,\text{eV}$ (cf. Fig.2.7, Eq. (2.25)). The example of CIGSe devices in Ref.[160] is taken where a 15% loss is considered. However, the highly efficient devices also contain a top anti-reflective coating (ARC) on the ZnO to help in further reducing optical losses. In an ideal solar cell device without ARC a maximum of 24% loss in J_{sc} can be considered.
Poorly efficient devices also do show a weak collection of the charge carriers generated in the bulk of the absorber. Due to a restricted minority carrier diffusion length, L_d the photogenerated electrons do not get to the space-charge region as they should. A poor collection due to a low L_d is reflected in a reduced EQE at long wavelengths (cf Eq. (2.25)) also reflecting in a J_{sc} loss. The collection probability is however considered to equal 100% in the SQ limit where each absorbed photon leads to one electron flowing out of the device.

On the other hand, **losses in the open-circuit voltage** V_{oc} are due to the recombination of electron-hole pairs. Recombination processes occur radiatively via band-to-band transitions or through defect levels (cf. section 2.1.3), and this anywhere in the absorber: in the bulk or rather towards the interface with the buffer layer. Non-radiative recombination via defects leads to an increase of the saturation current density J_0 which reduces the V_{oc} (cf Eq. (2.16)). Recombination also results in a poor collection of charge carriers, which as just mentioned, reduces the J_{sc}.

Losses in the fill factor FF (cf. Eq. (2.18)) reflect a non-ideal behavior of the diode, with a diode ideality factor $n,$ 1, large series resistance R_s and/or low shunt resistance R_{sh}. Highly efficient CIGSe devices have FF values $\sim 80\%$ [160]. The increase of R_s directly affects FF and might reduce the J_{sc} as well when too high. On the other hand, the reduction of R_{sh} directly affects FF and might also reduce the V_{oc} when too low. This means obviously that in solar devices largely affected by resistance losses (i.e far from the ideal diode model $n >> 1$) and/or poor charge carrier collection it is more difficult to determine the exact origins of power losses as more factors combine to reduce the J_{sc} and V_{oc}.

Table 7.2 gives a short summary of the different factors just discussed that lead to the reduction of J_{sc}, V_{oc} and FF.

	J_{sc}	V_{oc}	FF
Optical losses	Yes	-	-
Charge carrier recombination (electrical losses)	Yes	Yes	-
Low charge carrier collection probability (electrical losses)	Yes	-	-
Resistive losses	Yes (R_s)	Yes (R_{sh})	Yes, both

Table 7.1: Summary of factors leading to a reduction of J_{sc}, V_{oc} and FF, mostly separated into optical, electrical & resistive losses.

In the following section, one would like to estimate what of J_{sc}, V_{oc} or FF are the most affected in real current CTGS solar cell devices.

7.3 Main power loss factor in CTS and CGS-based solar cells

The produced CTGS absorbers are converted into completed photovoltaic devices with the same structure as CIGS-based devices. This structure is shown in Fig. 1.4. KCN etching is always performed on the absorber before device completion, where it is mostly known as an etchant for Cu_xS_y phases in devices based on Cu-rich absorbers (Cu/IV > 2) [119]. In this work we produce Cu-poor absorbers as seen in Chapter 4 so KCN is not always mentioned as mandatory step, nevertheless it might as well clean the surface of the absorber from other possible segregated phases such as Sn_xS_y [119] still present after annealing due to incomplete reaction of the binary chalcogenides [125].

As seen in the previous section power losses in CTGS could have several origins. One can first see whether J_{sc}, V_{oc} and/or FF losses are the most detrimental to decide whether to pursue optical, recombination or resistivity losses, first. The maximum power conversion efficiencies of ideal CTS- (E_G = 0.93 eV), CGS- (E_G = 1.56 eV) and alloyed CTGS-based devices can be calculated in the Shockley-Queisser limit reported in Fig. 1.3. The bandgap E_G of the CTGS alloy is considered for the calculation to equal 1.4 eV, which should correspond to a Ge-rich composition $x \sim 0.77$ as seen in Chapter 6. A device of similar bandgap (the lower bandgap seen in the EQE, as seen later in Fig 7.3) has been produced from a graded CTGS absorber layer.

The maximum $J_{sc,SQ}$, $V_{oc,SQ}$ and FF reachable for the three 'ideal' devices can be calculated in the SQ limit [43, 161] which considers the only power losses find their origin in the loss of photons with energies below the bandgap of the absorber, that are thus not absorbed as well as thermalisation losses (loss of energy through heat when charge carriers thermalise to the band edges) and the radiative recombination losses.

In this respect almost all incident photons with $E > E_G$ are considered to be absorbed by the film, except 24%, which as stated in the background introduction to this chapter account for current reduction in real devices due to grid shadowing, parasitic absorption by ZnO and CdS, as well as incomplete absorption, in a CTGS device without top ARC. The calculation, therefore, amounts to a more realistic Schockley-Queisser limit 'with optical losses', as established in Refs.[16, 160], from highly efficient CIGSe devices. The J_{sc}, V_{oc} and FF calculated in this limit are described as $J_{sc,SQ,opt}$, $V_{oc,SQ,opt}$ and $FF_{SQ,opt}$, respectively and calculated in the following paragraphs.

7.3.1 Calculation of a maximum short-circuit current density

$J_{sc,SQ,opt}$ is obtained by integration of the incident photon flux ϕ_{inc} on the device over all photon energies, considering a sharp absorption edge where the absorptivity factor A = 0 for $E < E_G$ and A = 0.76 for $E > E_G$.

$$J_{sc,SQ,opt} = q \int_0^{\lambda_g} 0.76 \cdot \phi_{inc}(\lambda) d\lambda \tag{7.1}$$

where q is the elementary charge, λ_g corresponds to the bandgap of the semiconductor material in nm and the incident photon flux ϕ_{inc} in $\mathrm{s^{-1}cm^{-2}}$ is calculated from ϕ_{sun},the 'AM1.5G' solar spectrum in $\mathrm{Wm^{-2}nm^{-1}}$ divided by the photon energy.

7.3.2 Calculation of a maximum short-circuit current density

The open-circuit voltage V_{oc} can be computed in an ideal device as $V_{oc,SQ,opt}$, following Eq. (2.16) with $n = 1$:

$$V_{oc,SQ,opt} = \frac{k_b T}{q} \ln \frac{J_{ill}}{J_0}, \tag{7.2}$$

assuming that the only loss, reflected in an increase in the reverse saturation current J_0, balances the blackbody radiation emitted at 300 K following Planck's radiation law:

$$V_{oc,SQ,opt} = \frac{k_b T}{q} \ln\left(\frac{\int_0^{\lambda_g} \phi_{sun}(\lambda) d\lambda}{2 \int_0^{\lambda_g} \phi_{BB}(\lambda) d\lambda}\right) \tag{7.3}$$

with ϕ_{BB} the blackbody radiation spectrum at 300 K.

7.3.3 Calculation of a maximum fill factor

The fill factor FF is expressed as in Eq. (2.18) by the ratio of the maximum power point on the JV curve to the product of J_{sc} and V_{oc}. In an ideal solar cell, the maximum value of the fill factor in the SQ limit, representing thus the device without resistive loss, $FF_{SQ,opt}$ can be determined empirically from $V_{oc,SQ,opt}$ following Ref. [161]:

$$FF_{SQ,opt} = \frac{\frac{q}{nk_bT} \cdot V_{oc,SQ,opt} - \ln(\frac{q}{nk_bT} \cdot V_{oc,SQ,opt} + 0.72)}{\frac{q}{nk_bT} \cdot V_{oc,SQ,opt} + 1} \tag{7.4}$$

7.3.4 Estimation of open-circuit voltage and fill factor as main power loss factors

The resulting values for $J_{sc,SQ,opt}$, $V_{oc,SQ,opt}$ and $FF_{SQ,opt}$ calculated for ideal CTS-based, CGS-based and CTGS-based devices, all without ARC are reported in Table 7.3.4. These optimum values are compared with the J_{sc}, V_{oc} and FF of real CTS, CGS and CTGS-based devices produced by the author of this thesis with the same E_G (University of Luxembourg, UL), as well as CTS and CGS-based world record devices (WR) up-to-date with similar E_G, and referenced.

The CTS and CTGS (UL) full devices were air annealed on a hot plate for 1 hour at 250 °C as the treatment was shown to improve the device performance of Sn-containing devices via an increase of the V_{oc} and the FF, majoritarily [162]. No change in the JV curve was observed after the same treatment on the CGS device.

As seen in Table 7.3.4 the largest power losses in the real CTS and CGS devices, either the best ones reported (WR) or the ones produced at the University of Luxembourg (UL), compared to the ideal device in the Shockley-Queisser limit (SQ) are reflected mostly in the V_{oc} and FF and are to a lesser extent in terms of J_{sc}, as seen by the lowest ratio around 1.

This all means that losses in real CTS and CGS devices mostly come from recombination of photogenerated charge carriers affecting their collection and resistive losses affecting the diode behaviour, rather than optical losses due to not enough photons being absorbed.

Since the loss in V_{oc} is larger than the loss in J_{sc} it seems to suggest that the highest recombination of photogenerated carriers occurs at the interface, and is less pronounced in the bulk. Also, since both FF and V_{oc} are particularly low, one could have a very low R_{SH}. The CGS-based device shows a lower J_{sc} and a lower FF than the CTS device, which could be due to a larger R_s.

On the other hand, in the CTGS-based device the J_{sc} losses are equally important to V_{oc} losses in efficiency reduction while FF is higher. It suggests that the device shows less resistive problems but rather increased optical and/or collection losses.

The J-V curves of the pure CTS and CGS UL devices are reported first in Fig. 7.1. As it can be noticed directly, both JV curves do not follow an ideal diode behavior as the light curve can not be obtained by a simple shift of the dark curve with the light-generated current. Especially in the case of the CGS device, the JV curve deviates too much from the one diode model (cf. Eq. (2.15)) to fit the data and extract reasonable values for R_s, R_{sh} and J_0 [163]. Instead, one can just extract tendencies by looking at the shape of the curve, knowing that R_{sh} and R_s can be extracted from the inverse of the slopes at V_{oc} and J_{sc}, respectively, as indicated by the blue

	CTS-based	CTGS-based	CGS-based
Ref η [%] WR	4.6 [31]	-	2.7 [158]
η [%] UL	1.8	2.9	0.3
E_G [eV]	0.93	1.40	1.56
$J_{sc,SQ,opt}$ [mA.cm^{-1}]	39	25	20
J_{sc} UL [mA.cm^{-1}]	26	10	6
J_{sc} WR [mA.cm^{-1}]	37	-	15
$J_{sc,SQ}/J_{sc}$ UL	1.5	2.5	3.3
$J_{sc,SQ}/J_{sc}$ WR	1.0	-	1.3
$V_{oc,SQ}$ [mV]	690	1121	1270
V_{oc}UL [mV]	181	463	194
V_{oc} WR [mV]	283	-	592
$V_{oc,SQ,opt}/V_{oc}$ UL	3.8	2.4	6.5
$V_{oc,SQ,opt}/V_{oc}$ WR	2.4	-	2.1
$FF_{SQ,opt}$ [%]	84	89	90
FF UL [%]	38	51	33
FF WR [%]	44	-	30
$FF_{SQ,opt}/FF$ UL	2.2	1.8	2.7
$FF_{SQ,opt}/FF$ WR	1.9	-	3

Table 7.2: Report of maximum J_{sc}, V_{oc} and FF in the Shockley-Queisser limit for ideal CTS and CGS-based p-n junction devices as well as a CTGS-based device with E_G = 1.3 eV, together with the maximum J_{sc} and V_{oc} measured from real devices prepared at the University of Luxembourg (UL), and the world record devices up to date (WR). There is no device reported for the chosen CTGS alloy. The ratio of current, voltage and fill factor between ideal and real devices are also calculated and reported and highlighted by the bold lines.

and green dashed lines on the JV curves in Fig. 7.1. It suggests that the series resistance in the CGS device is particularly high, which was already expected previously. Also the CTS device shows a low shunt resistance, which was expected from the lower FF and V_{oc} but the resistive issues are overall less dramatic than in CGS. If the V_{oc} still shows a large reduction in CTS compared to an ideal device, it means for sure that recombination is a detrimental factor that should be suppressed. Added to the resistances, the diode factor is increased with the curves either crossing in forward bias for CTS or showing a large kink in reverse bias for CGS under illumination. The crossover was observed on other CTS devices at the UL and attributed to defects in the CdS buffer layer or voltage-dependent current collection [162]. Similarly, a kink was observed with low energy photoexcitation and thus referred to an interface issue in Ref.[162]. The kink was reduced for air annealed devices and it is thus not surprising it is not observed here in Cu_2SnS_3. The JV curves of the CTGS device are presented much later in this chapter in Fig. 7.4, and indicate slightly better resistive behaviour for both R_s and R_{sh} which explains the increase in FF.

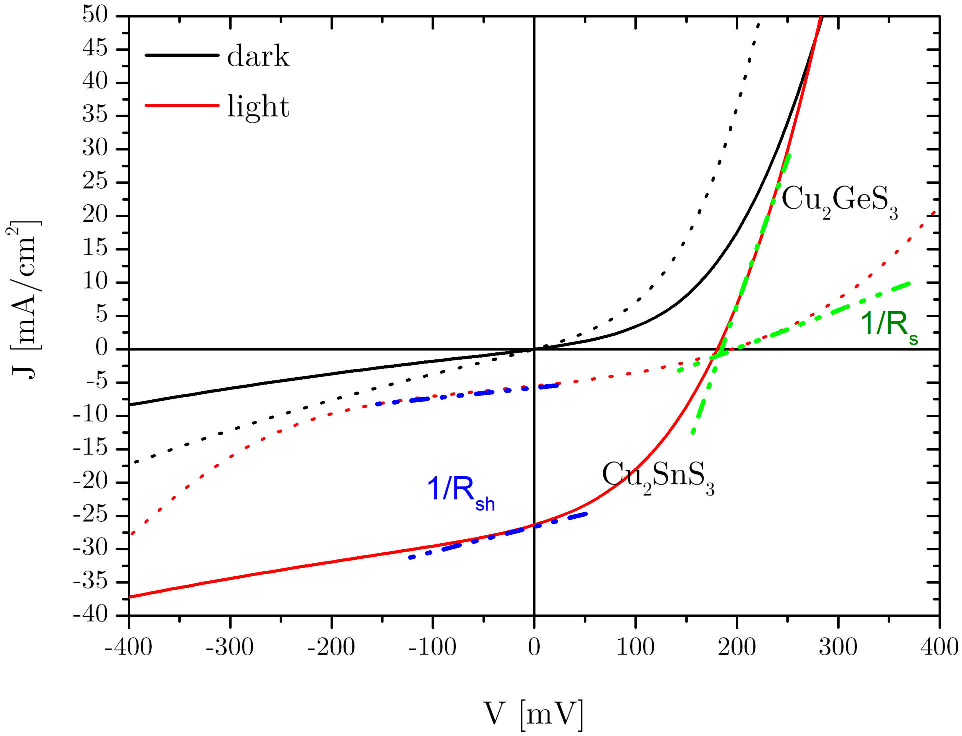

Figure 7.1: Dark (black) and light (red) J-V curves of best (UL) CTS (solid lines) and CGS-based (dotted lines) devices.

Analysis of the JV curves and JV parameters suggested that CTS and CGS devices suffer from charge carrier recombination, which might be more pronounced at the pn junction interface than in the bulk. In CTGS there is an improvement of the resistances as well as an increase of the V_{oc}. Looking at the EQE spectra of these devices could help in refining those observations. Before studying the EQE spectra the possible current (optical and collection losses) and voltage losses (recombination losses) are studied in more detail.

7.3.5 Sources of open-circuit voltage loss in CTGS solar cells

Poor carrier collection at long wavelengths: bulk recombination

The p-type material has been reported as having a large net acceptor density N_A with a minimum of 10^{18} cm^{-3} [21, 164, 165], also measured in the several CTGS alloys prepared in Chapter 6. In high-efficiency CIGSe-based devices (with η >19%) the hole density is evaluated in the order of 10^{16} cm^{-3} [166] which is two orders of magnitude lower than in CTGS. The total space-charge region width (or depletion width) W of the pn junction is fixed by the doping level of the p and n-type materials with:

$$W = x_p + x_n, \tag{7.5}$$

where x_p and x_n are the depletion widths in the p- and n-type materials, respectively, which add up to form W. For lightly p-doped materials such as good CIGSe absorbers, $N_D >> N_A$ thus one can make the approximation that $W \sim x_p$ and the depletion width mostly extends in the p-type region. Since one wants to collect photogenerated carriers that are generated in the p-type CTGS material, one wishes to maximise x_p.
x_p can be expressed as in Ref.[141]:

$$x_p = W \cdot \frac{N_D}{N_D + N_A} \tag{7.6}$$

with N_D the donor density of the n-type material. For a fixed N_D, the lower the N_A, i.e the least intrinsically doped the p-type material is, the higher the resulting x_p is. Said differently, high doping leads to the formation of a narrow depletion width. Baranowski et al. [21] suggested a moderate p-type doping of $\sim 10^{17}\,\mathrm{cm}^{-3}$ can be obtained under Cu and S-poor conditions, which is likely still one order of magnitude too high. Doping densities in CIGS in the order of 10^{16} cm^{-3} lead to depletion widths W that could rise up to 500 nm [167]. Narrower W, as observed in CZTS below 250 nm [168], would then require a larger minority carrier diffusion length L_d as large as the thickness of the absorber, to collect the photoexcited electrons that are generated far from the pn-junction, before they recombine with holes. After thermalising back to the conduction band edge, the photoexcited electrons eventually recombine with holes in the valence band after a duration described as their lifetime or τ. It is suggested that CTS has a short 'minority charge carrier lifetime' τ of a few picoseconds [136] while τ reaches 250 picoseconds in highly efficient CIGSe devices [169]. It is therefore very likely that bulk recombination affects CTGS devices, even though we suggest from the JV curves that interface recombination is more important.

Band alignment CdS/CTGS: a disputed case in interface recombination

The bandgap of monoclinic CTGS was shown in chapter 6 to vary from about 0.9 eV ($x = 0$) to 1.6 eV ($x = 1$) which represents a maximum increase of about 0.7 eV with the increase in Ge content. CdS owns a larger bandgap of 2.4 eV. The VB states arise in CTS and CGS due to the hybridization of the Cu 3d and S 3p orbitals while the CBM is composed of S 3p and Sn 5s for CTS or Ge 4s components for CGS, respectively [38]. Therefore by increase of the Ge content from CTS to CGS, we only expect an increase of the energy level of the CBM, while the VBM would remain constant for all x. However, the positions of VBM and CBM of CTGS compared to the vacuum level are unknown, which means we do not know the relative positions of CTGS bands to CdS. Two situations can occur: either the CBM of CdS lies above the CBM of CTGS (described as a 'spike-like' interface) so there is an energetic barrier which prevents the photoexcited electrons to cross the SCR and diffuse to the CdS where they are collected so the FF is reduced, or the CBM of CTGS lies above the CBM of CdS and the junction is described as 'cliff-like' where photoexcited electrons can easily diffuse to the CdS. However, in the last case, the recombination between holes in CTGS and electrons in CdS is increased due to a reduction of the bandgap at the CTGS-CdS interface. This enhanced interface recombination reduces the V_{oc} of the device. The nature of the interface in CTGS is still disputed in literature. A 'cliff'-like interface was measured between CdS and CTS by photoelectron spectroscopy in Ref.[170] which was presented as a possible phenomenon for the low activation energy measured by temperature-dependent JV measurements in Ref.[171], which suggests a large interface recombination. Other experimentalists have suggested a 'spike'-like interface instead, in the CTGS alloy [172], which does not correlate with the former as one can not go from a cliff to a spike-like interface by a rise of the conduction band of the CTGS absorber. In a spike-like situation, a high density of gap states could also be responsible for an increased recombination, which is likely to be the case as well in CTS. The case of the nature interface remains therefore very disputed, despite one suggests a high interface recombination, the source of it is still unclear and one often mentions a 'non-optimised' interface. Attempts in changing the buffer layer from CdS to In_2S_3 [173] were also performed experimentally, but not resulting in a drastic change in the V_{oc}. In this regard, the synthesis of the absorber needs to be optimised first or improvements would be first seen in the J_{sc}. Even though similar attempts were tried at the UL with ZnO instead of CdS, there was no resulting device efficiency that allowed to draw comparisons. Therefore one can not conclude here at this stage.

Back contact recombination

The formation of a stable Cu_2SnS_3 ternary material was reported to occur in the presence of MoS_2 [174] which forms during annealing and is observed on cross-sectional images by a doubling of the initial Mo thickness. The MoS_2 was shown to generate an electronic barrier for holes at the back contact, decreasing recombination of charge carriers and reducing the V_{oc} [171]. Therefore, one can have back contact recombination together with interface recombination.

Local bandgap and electrostatic potential fluctuations

As explained in Chapter 5 the CTS and CGS ternaries are of a stoichiometry that does not allow respect of the octet rule. Instead, two different motifs of the Cu-Sn and Cu-Ge atoms, Cu_3Sn and Cu_2Sn_2, exist only approaching the number of 8 valence electrons. As a result, (sub)-nanometer clustering leading to local composition fluctuations and non-detectable by most experimental techniques were calculated to cause both bandgap and electrostatic potential fluctuations [175]. Both hamper device performance [135, 176]. The monoclinic structures of CTS and CGS have been demonstrated as the adequate phases for solar cells, showing a higher quasi-Fermi level splitting than the low-temperature cubic phase [54, 125]. It is thus more suitable to use synthesis conditions (high temperatures) that restrict the absorber formation to the monoclinic phase [71] of the polymorph, or at least to a predominant monoclinic phase [176] and avoid the existence of the low-temperature cubic phase. Chapter 6 has also demonstrated the existence of a solid solution of CTGS with a monoclinic structure under similar annealing conditions. The existence of local composition fluctuations is also likely.

Charge carrier recombination at grain boundaries

The difference between UL and WR devices particularly lies in the V_{oc} loss which is more pronounced at the UL. An obvious difference between the CGS devices produced at the UL and the world records is seen in top view images of similar cross sections, where the average grain size of the record device sums to 1-2 microns while the average grain size in UL devices does not exceed a hundred of nanometers. This difference is attributed to the annealing process and leads to the multiplication of grain boundaries. Grain boundaries are known as extended defects which could be easily detrimental to the V_{oc} [43]. The difference in cross-sections between the UL and the WR device is not that sharp in CTS, where the difference in V_{oc} is not that high. It could suggest that the synthesis process should be optimised, as the size of the grains could be a parameter to enhance.

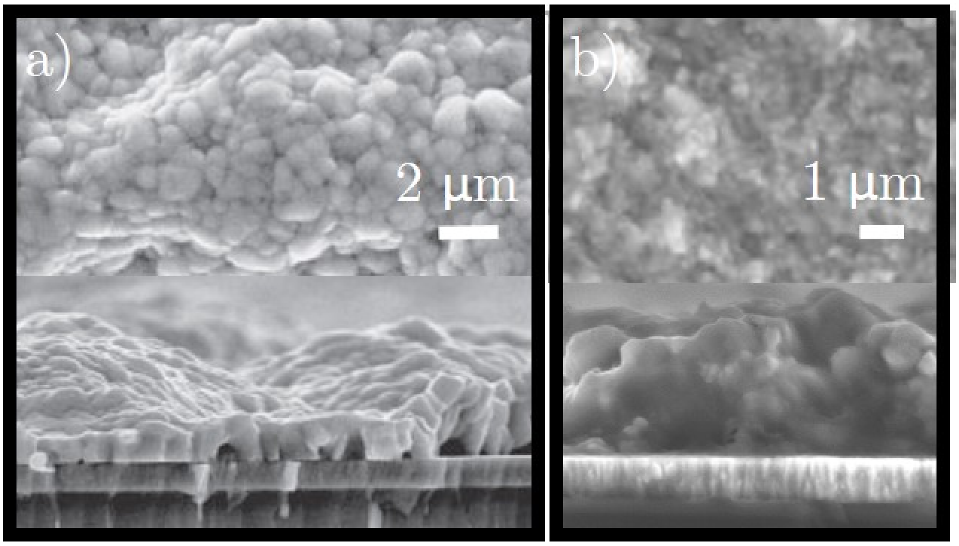

Figure 7.2: a) Top surface SEM image, and cross section of the record CGS device found in [51], b) Top surface SEM image, and cross section of the CGS device prepared at the UL.

7.3.6 Source of short-circuit current loss in CTGS devices

Second optical transition above the bandgap

A double step observed in light absorption data [53, 177], and attributed with theoretical studies to the valence band splitting of the CTGS was attributed as responsible for losses of J_{sc}. A second valence band whose maximum lies about 50 meV below the first is visible in the absorption coefficient plot versus wavelength (and in most EQE spectra) is responsible for a 5% loss in J_{sc}. This loss is however not sufficient to explain all J_{sc} losses but could be one of the contributors. We therefore mostly attribute the J_{sc} losses to low R_{sh} in CTS/CGS added to a poor charge carrier collection. In the graded CTGS device, optical losses are likely increasing instead, due to the graded bandgap.

7.3.7 Analysis of external quantum efficiency spectra

Analysis of the EQE spectra of the devices give more information on the collection and recombination issues that could exist. It is an easy method to employ for a first quantification of existing challenges.

In particular, a modelling method developed by de Wild et al [162] for the EQE spectra of Cu_2SnS_3-based devices allows to extract electrical properties such as the space-charge region width W, the minority carrier diffusion length L_d and the magnitude of interface recombination. The EQE spectrum of the solar cell is fitted using the Gärtner equation (Eq. (2.24)), which expresses the EQE as function of L_d and α. However, in poorly efficient devices without an optimised p-n interface, Eq. (2.24) is not sufficient to mathematically describe the EQE. A global decrease of the EQE intensity is explained in CTS by a large recombination of charge carriers at the p-n junction interface. To account for this loss the modelling is performed by adding a multiplicative term 'g' to Eq. (2.24) which becomes:

$$\mathrm{EQE} = g \cdot (1 - \frac{\exp(-\alpha W)}{1 + \alpha L}), \tag{7.7}$$

with 'g' expressed as:

$$g = (1 + \frac{S}{\mu_e \cdot E_0})^{-1} \cdot \exp(-\alpha_{CdS} \cdot d_{CdS}) \exp(-\alpha_{ZnO} \cdot d_{ZnO})$$

with S the interface recombination velocity, μ_e the electron mobility, and E_0 the maximum field at the p-n junction. The last two exponential terms account for the absorption of photons in the top CdS and ZnO layers using the Beer-Lambert law, with α their respective absorption coefficients and d the respective thicknesses of both layers. The fit of CTS and CGS-based solar cells is performed with the absorption data for CdS and ZnO found in the SCAPS software [178].

All EQE of study and their final modellings and values of W and L_d are shown in Fig.7.3. The EQE of the modelled CTS solar cell is the one of the UL device while the CGS device is a WR device [127] because the UL CGS device shows a large sub bandgap tailing that suggests Sn contamination during annealing and therefore can not be used.

The absorption spectra of CTS and CGS are taken from theoretical calculations [53]. Additionally the CTGS device does not present the double absorption onset which would allow the modelling from the absorption spectrum of CGS, shifted by the difference in bandgap. Therefore only the CTS and CGS EQE are modelled.

The modelling is based on the following equations that allow to calculate W from the acceptor density in the p-type film. The intrinsic carrier concentration n_i can be expressed as function of temperature T following [43]:

$$n_i^2 = N_V N_C \exp(\frac{-E_g}{k_B T}) \tag{7.8}$$

with N_V and N_C the effective density of states in the valence and conduction bands of the absorber, respectively, and E_G the semiconductor bandgap which equals 0.93 eV for CTS [116] and 1.56 eV for CGS [125]. The intrinsic carrier concentration at room temperature (T = 300 K) can be calculated assuming default values proposed by Scheer and Schock for N_C and N_V of $2 \cdot 10^{18}$ cm$^-3$ [179]. The built-in potential at the pn junction is computed from n_i^2, using [141]:

$$V_{bi} = \frac{k_b T}{q} \ln(\frac{N_A N_D}{n_i^2}) \tag{7.9}$$

with N_A the acceptor concentration on the p-type side of the junction (the absorber layer) and N_D the donor concentration on the n-type side of the junction (CdS). A default value of $1 \cdot 10^{18}$ cm^{-3} is taken for N_D, which is a standard value for n-type CdS in CdS/CIGS junctions [179]. W is calculated as function of the total voltage at the junction ($V_{bi} - V_{\text{applied}}$):

$$W = [\frac{2\varepsilon}{q}\frac{N_A + N_D}{N_A \cdot N_D}(V_{bi} - V_{\text{applied}})]^{\frac{1}{2}} \tag{7.10}$$

with q the elementary charge and ε the dielectric constant, such as:

$$\varepsilon = \varepsilon_r \cdot \varepsilon_0, \tag{7.11}$$

where ε_0 is a constant (the permittivity of free space) and ε_r the relative dielectric constant of the absorber material, unknown for CTS and CGS. The default value ε_r of CZTS of 12 is chosen [16], which allows to calculate ε. At J_{sc} the electric field at the junction can be calculated from W as:

$$E_0 = \frac{2k_bT\ln(\frac{N_AN_D}{n_i^2})}{W}. \tag{7.12}$$

This allows to compare the depletion width W extracted from the EQE modelling, to a calculated W estimated as function of the expected acceptor doping density N_A in the material and check whether electric fields magnitudes correspond in both situations. As seen in Fig. 7.3 the method shows average W and L_d not exceeding 150 nm for CTS, as measured on a CTS-based device after air annealing post-treatment, known to reduce both bulk and interface recombination [53]. For an absorber with a thickness of around 1-2 μm, the collection of charge carriers generated far from the space-charge region is still affected, decreasing the J_{sc}. This is not the only factor because the devices also suffer from a high interface recombination that is modelled by the factor 'g' and decreases the EQE. Interface recombination reduces both the J_{sc} and the V_{oc}.

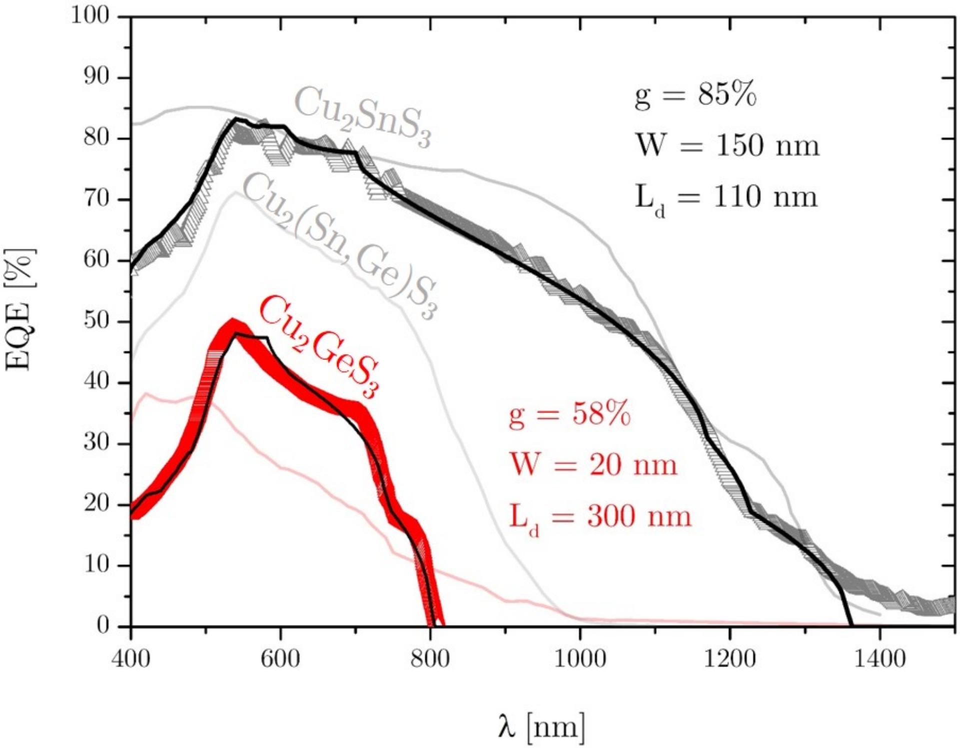

Figure 7.3: Modelling (black lines) of the EQE spectra of a Cu_2SnS_3-based device (grey) and a Cu_2GeS_3-based device (red). The CTS device was prepared by the author while the EQE of CGS is taken from [127]. The thin red line refers to a similar CGS device prepared by the author of this work. The two thin grey lines refer to the graded-CTGS device prepared n this work, and the WR Cu_2SnS_3 device [180], respectively.

The CGS device from [127] whose EQE is shown in Fig. 7.3 presents a shorter space-charge region width than the annealed CTS device, which could relate to a larger doping [162]. However, it shows a larger minority carrier diffusion length, which could relate to larger grain size and fewer grain boundaries as possible recombination paths. Nevertheless, it remains too low and indicates a low τ. For a high acceptor density $N_A \sim 10^{18}$ cm^{-3} (as high doping value measured on the CTGS series), a W of about 45 nm is calculated, which is almost as low as the low value extracted from the fit of 20 nm. The discrepancy in the values could arise from the approximation made in the calculation, or the absorption coefficient used to fit the data. The conclusion remains the same for CTS as for CGS, namely, the space charge region width is too low, with a collection length affected by low carrier lifetimes and high interface recombination 'g', even if the air annealing post-treatment carried out in CTS increases $W + L_d$.

7.4 Production of a 2.9% depth-graded CTGS-based device

In this work, no working device could be prepared from depth-uniform absorbers similar to the ones presented in Chapter 6. The high doping value measured did anyway not suggest an increase of the space-charge region compared to the pure ternaries. For device applications, graded structures are preferred to uniform absorbers, as known from CIGS, which allow to change locally the bandgap and improve device performances. The best solar cell (A = 0.58 cm^2) produced in this thesis was processed from a Cu/Sn precursor stack annealed in GeS, SnS and S at 550°C with a 1 mbar background pressure of H_2/N_2. The device presents an efficiency of 2.9% as reported in Table 7.3.4, which is higher than any of the CTS and CGS solar cells, thanks to an increase in the V_{oc} to 463 mV (J_{sc} of 17 mA/cm^2, FF of 37%). The dark and light JV curves of the devices are shown in Fig 7.4. A fit of the EQE (shown in Fig. 7.3) cannot be carried out due to a composition depth gradient with a Ge-rich surface ($x \sim 0.9$) down to $x \sim 0.2$, measured with EDX at different acceleration voltages of 20 and 30 keV. Normalised SIMS data x depth content is presented in Fig.7.5. Therefore the composition is graded with higher bandgap towards the surface which could be helping to reduce recombination at the interface. It is only the second attempt of gradient engineering in CTGS, and one can not be too convinced yet which grading is preferred [172]. In a first step the open-circuit voltage and the resistive issues could be slightly improved. The device is more limited by J_{sc} losses than the CTS and CGS. These losses could arise from optical losses due to the non-optimised depth composition gradient.

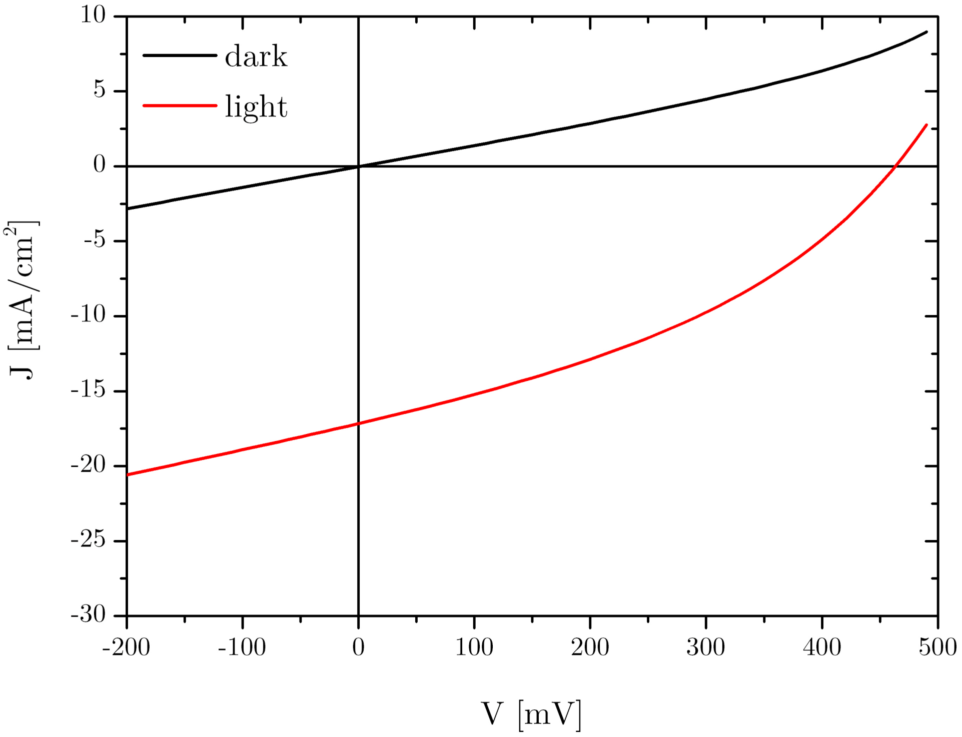

Figure 7.4: Dark (black) and light (red) JV curves of the best CTGS device obtained, with an efficiency of 2.9%.

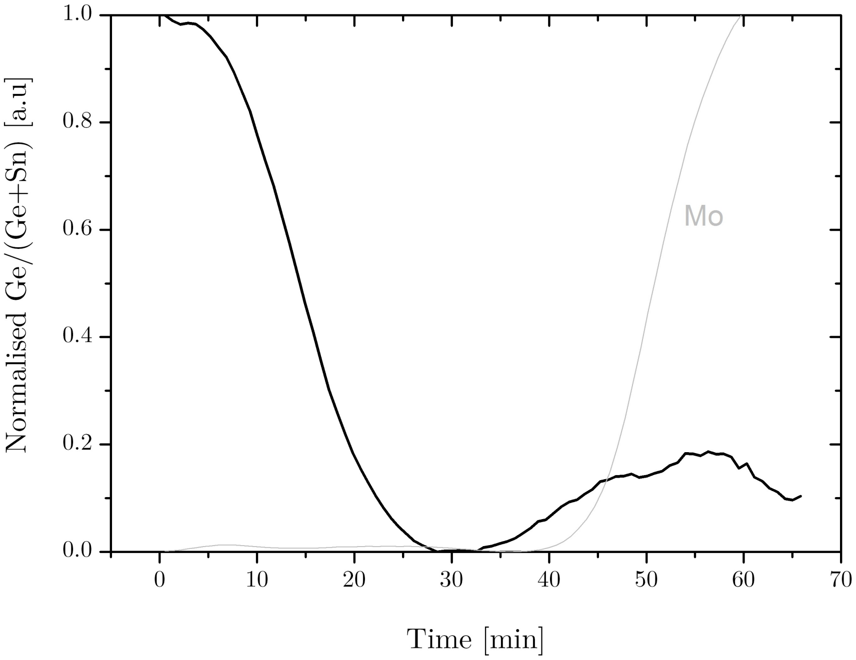

Figure 7.5: Depth information on the trend in Ge/(Ge+Sn) ratio in a similar absorber to the one which produced a 2.9% efficient device, as extracted from Secondary Ion Mass Spectroscopy. The Mo line is indicated (grey).

7.5 Conclusion of the chapter

Study of the CTS and CGS materials implemented in devices have shown particularly low V_{oc}, and resistive losses.
At this stage it is difficult to select a single factor responsible for performance loss. However one can find trends that seem relevant to work on, first.

Modelling of the EQE have shown large interface recombination, and thus if the materials should be pursued, the interface with the CdS should be optimised. Devices also suffer from a narrow space-charge region and low minority carrier diffusion length, impacting both V_{oc} and J_{sc}.

If carried out, future device implementation absolutely requires reduction of doping density that was measured to be two orders of magnitude too high compared to CIGS absorbers producing highly efficient devices. The material is still in its early years and more future experimental evidence is required to have more progress concerning, for instance, the ideal buffer layer to use, or the recombination at the back contact.

A graded absorber could be produced from Cu/Sn precursors after annealing. A maximum device efficiency of 2.9% could be reached from this graded CTGS absorber, showing higher V_{oc}. In the future, several gradings need to be attempted to check if one of them is more beneficial to reducing recombination and improving charge carrier collection.

CHAPTER 8

Summary and outlook

Summary

The aim of this thesis was to investigate material properties of the CTGS semiconductor, for applications as p-type absorber layer in thin film solar cells.
This work showed that the Cu_2SnS_3 and Cu_2GeS_3 materials can be synthesised with a facile two-step route, involving the annealing of copper in a reactive tin/germanium and sulphur atmosphere. From investigations of their chemical formation reactions, one showed the relevance of having chalcogen and group IV chalcogenide vapour species present during the annealing, to suppress secondary phase segregation and film decomposition. It was also demonstrated that the kinetics of vapour-solid reactions are not the critical step to forming layers of uniform compositions, but rather the vapour phase generation of group IV chalcogen species. When kinetics of generation of the vapour phase from the solid supply are insufficient for fulfilling the formation of the ternary compound, copper sulphides binaries will remain in the films, and the case was shown to be particularly dramatic during the annealing of Cu_2SnSe_3. To reduce this, one should minimise the background pressure used during the annealing process.

Before this work, CTGS was previously already described as a polymorphic material without much consensus on the different structures observed, and resulting properties. One recommends to perform X-ray structural analysis over sufficient angular range because it makes it easier to identify the crystallographic phases. The Cu_2SnS_3 and Cu_2GeS_3 were shown in this manner to exist under a low temperature phase, cubic, when annealed below 500°C and a higher temperature phase, monoclinic, which forms under higher annealing temperature. These phases are predominant and to this point one can not say that there is no minor trace of the cubic phase in the monoclinic sample. But definitely the monoclinic phase is more ordered and less defective. In both ternaries, the monoclinic samples therefore show more promising properties for photovoltaic applications. Research done on the annealing has shown that forming $Cu_2(Sn,Ge)S_3$ alloys with controlled composition is a complex process since both SnS and GeS have high vapour pressures. By choosing precursors containing Ge, high kinetics of intermix of Sn-Ge metallic precursors allowed to form uniform $Cu_2(Sn,Ge)S_3$ absorbers in the time given to the annealing process. $Cu_2(Sn,Ge)S_3$ was shown to be a solid solution range with a wide existence domain, where lattice parameters decrease linearly with the Ge composition while bandgaps increase linearly.

However, from the knowledge of CIGS, bandgap graded absorbers are usually favourable to device performance. One develops a way to engineer a graded bandgap by annealing Cu/Sn precursors in GeS, SnS and S atmospheres. A 2.9% CTGS device based on such an absorber has been produced. But even when growth conditions are restricted to the predominance of the monoclinic structure which is the less defective and the most ordered, respective devices have low one-circuit voltages far below the bandgap, and minor open-circuit current losses. By careful analysis of the CTS, CGS and the record CTGS produced, one suggests that recombination of charge carriers is a detrimental factor in this material. Doping densities are measured to values of $10^{18}\,\mathrm{cm}^{-3}$ which is about 2 orders of magnitude higher than in well-performing CIGS devices, and definitely leads to restricted depletion widths and reduced device performances. Additionally, high bulk recombination exists seen in low minority carrier diffusion lengths. The device external quantum efficiency also suffers from a large interface recombination.

Outlook

Study of CTGS properties bring a large consensus to the poor knowledge at the start of this work, from a material point of view.

Bandgaps and lattice parameters of the $Cu_2(Sn,Ge)S_3$ alloys with a monoclinic structure are now known on the full composition range from Ge-free to Sn-free layers. Therefore group IV composition of a new layer can be now both deduced from optical or diffraction measurements.

Additionally, annealings should be performed in the presence of group IV chalcogenide vapours, which should permit to better control composition.

However this study also shows the intrinsic complexity of the material, which brings new challenges to future research when one wants to implement it in efficient solar cell devices.
This work showed the polymorphism of the compound with a transition from cubic to monoclinic. Only absorbers prepared from high temperature conditions are thus likely to rise above efficiency limits. On the other hand, to reduce recombination and increase the device open-circuit voltages one should decrease the intrinsic doping density.
The devices produced in this work with an efficiency of almost 3% are not too far apart from current world record devices. One suggests that the difference relies in the growth process with for instance a reduced grain growth. However, getting beyond the current world record efficiency at 6% will require far more work.

Appendix A

All annealings performed for Chapters 4, 5 and 6 are done in the presence of chalcogenide, $X_{(g)}$, and group IV chalcogenide, $MX_{(g)}$ vapours. These vapours are generated by sublimation of solid powders of X and MX. All solid powders used are presented in Table 8.1 with their provenance and purities. One uses fixed amounts of 100 mg of chalcogen powder and 10 mg of group IV chalcogenide in the annealing box.

Nature	Provenance	Purity [%]
S	Alfa Aesar	99.9995
Se	Alfa Aesar	99.999
SnS	MKnano	99.95
SnSe	Alfa Aesar	99.999
GeS	Sigma Aldrich	99.99

Table 8.1: Nature of X and MX powder supplies used to produce a X+MX vapour atmosphere in the graphite box during annealing of the precursors

Appendix B

This section groups the reference X-ray diffractograms used from the International Centre for Diffraction Data (ICDD PDF-2016) to identify crystallographic structures and compounds obtained within the frame of this thesis. The given PDFs were selected for their quality, as given by the database, when several for the same structure were present. Table 8.3 groups the XRD references for selenium compounds analysed in Chapter 4.

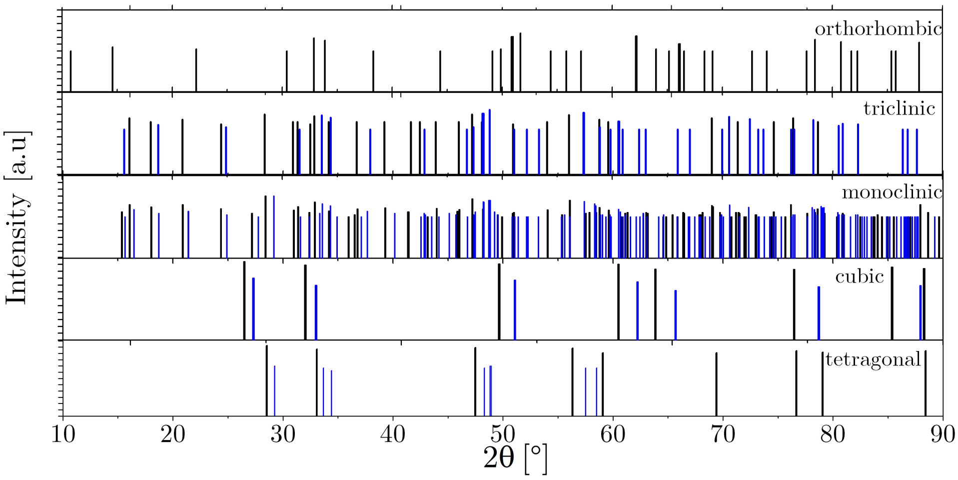

Figure 8.1: Collection of XRD patterns as found in Table 8.2 for the polymorph CTS (blue) and CGS (black) compounds for the reported crystal structures: orthorhombic, triclinic, monoclinic, cubic and tetragonal.

Phase	Structure	Space group	Lattice parameter (Å & °)	PDF Nr.
Mo	cubic	Im-3m	a = b = c = 3.146 $\alpha = \beta = \gamma = 90$	04-001-0059
CuS	hexagonal	$\frac{P63}{mmc}$	a = b = 3.792, c = 16.344 $\alpha = \beta = 90, \gamma = 120$	00-006-0464
Cu_9S_5	rhomboedral	R-3m	a = b = 3.930, c = 48.140 $\alpha = \beta = 90, \gamma = 120$	00-047-1748
SnS	orthorhombic	Pbnm	a = 4.329, b = 11.192, c = 3.984 $\alpha = \beta = \gamma = 90$	00-039-0354
$(Cu_2SnS_3)_{1.333}$	cubic	F-43m	a = b = c = 5.430 $\alpha = \beta = \gamma = 90$	01-089-2877
Cu_2SnS_3	monoclinic	Cc	a = 6.665, b = 11.537, c = 6.653 $\alpha = \gamma = 90, \beta = 109.39$	04-010-5719
Cu_2SnS_3	triclinic	P1	a = 11.510, b = 18.758, c = 6.640 $\alpha = 90.29, \beta = \gamma = 90$	00-027-0198
$Cu_{2.665}Sn_{1.335}S_4$	tetragonal	I-42m	a = b = 5.413, c = 10.824 $\alpha = \gamma = 90, \beta = 109.39$	04-009-7947
Cu_2GeS_3	monoclinic	Cc	a = 6.449, b = 11.319, c = 6.428 $\alpha = \gamma = 90, \beta = 108.37$	04-010-4292
Cu_2GeS_3	cubic	F-43m	a = b = c = 5.317 $\alpha = \beta = \gamma = 90$	03-065-5562
Cu_2GeS_3	tetragonal	I-42d	a = b = 5.326, c = 10.410 $\alpha = \beta = \gamma = 90$	00-041-1035
Cu_2GeS_3	orthorhombic	I2mm	a = 5.210, b = 11.321, c = 3.766 $\alpha = \beta = \gamma = 90$	04-008-8915
Cu_8GeS_6	orthorhombic	Pm21n	a = 7.026, b = 9.841, c = 6.947 $\alpha = \beta = \gamma = 90$	00-039-1902
Cu_8GeS_6	cubic	F-43m	a = b = c = 9.926 $\alpha = \beta = \gamma = 90$	00-040-1190

Table 8.2: XRD references for sulphide compounds used in this thesis

Phase	Structure	Space group	Lattice parameter (Å& °)	PDF Nr.
$CuSe_2$	orthorhombic	Pnnm	a = 5.023, b = 6.196, c = 3.747 $\alpha = \beta = \gamma = 90$	04-004-2178
Cu_2SnSe_3	monoclinic	Cc	a = 6.967, b = 12.049, c = 6.945 $\alpha = \gamma = 90, \beta = 109.19$	04-012-4693

Table 8.3: XRD references for selenide compounds used in Chapter 4

Appendix C

This appendix reports the overlay of all Le Bail fittings (black lines) with raw GI-XRD data (red dots) for Chapter 6, as extracted from the software FullProf [48]. The blue XRD dashed pattern for CTGS is generated for a monoclinic structure (space group C1c1) after refinement of the lattice parameters. The red dashed pattern corresponds to Mo. The blue line at the bottom of each graph represents the residuals ($I_{measured} - I_{calculated}$). The corresponding composition x and incidence angle α are shown at the top of each graph.

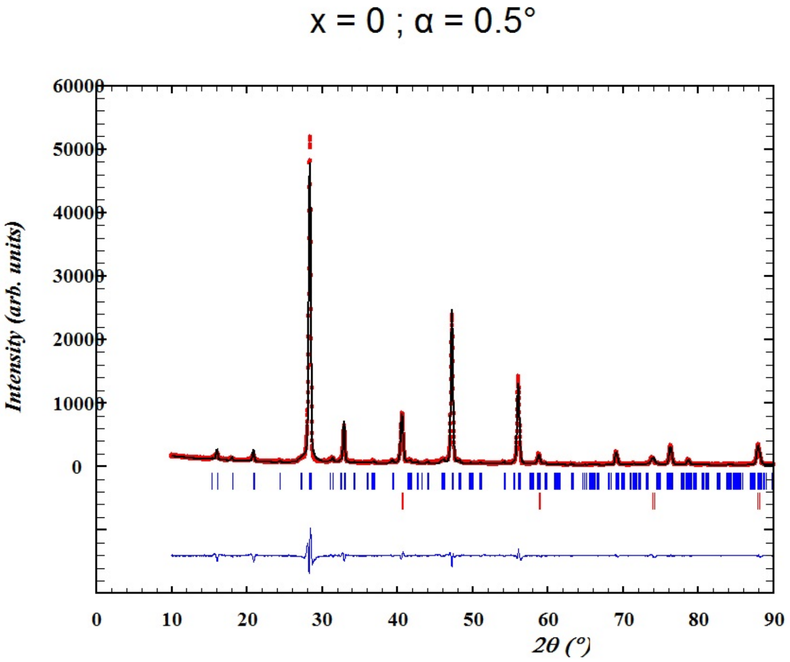

Figure 8.2:

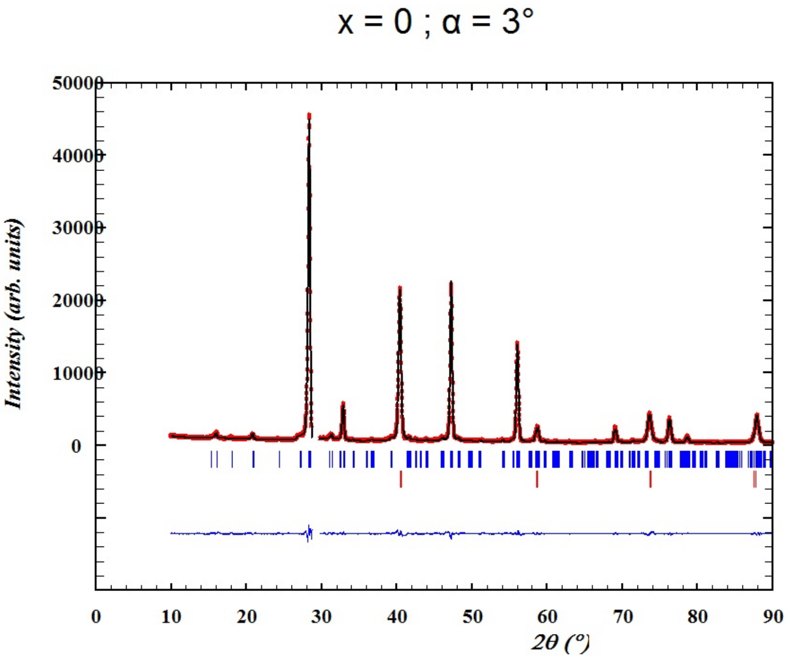

Figure 8.3:

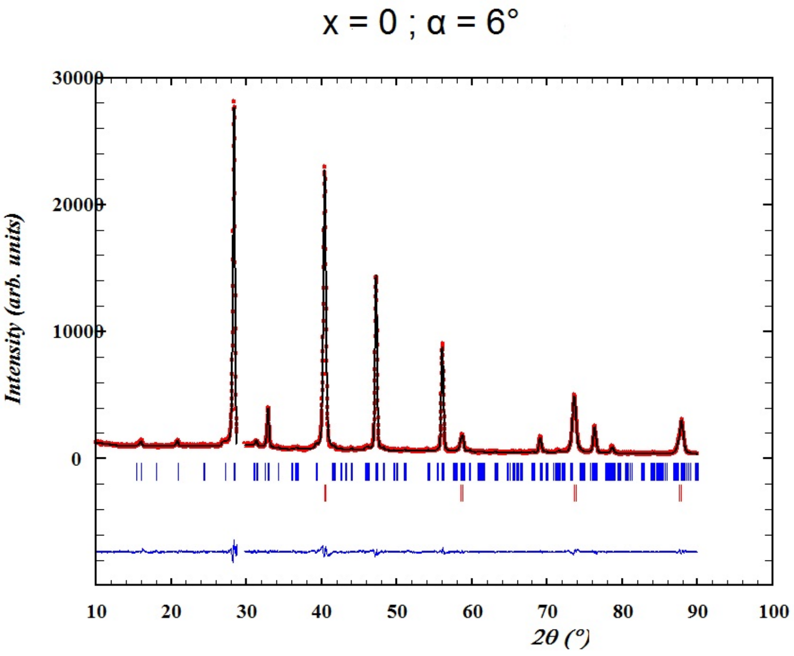

Figure 8.4:

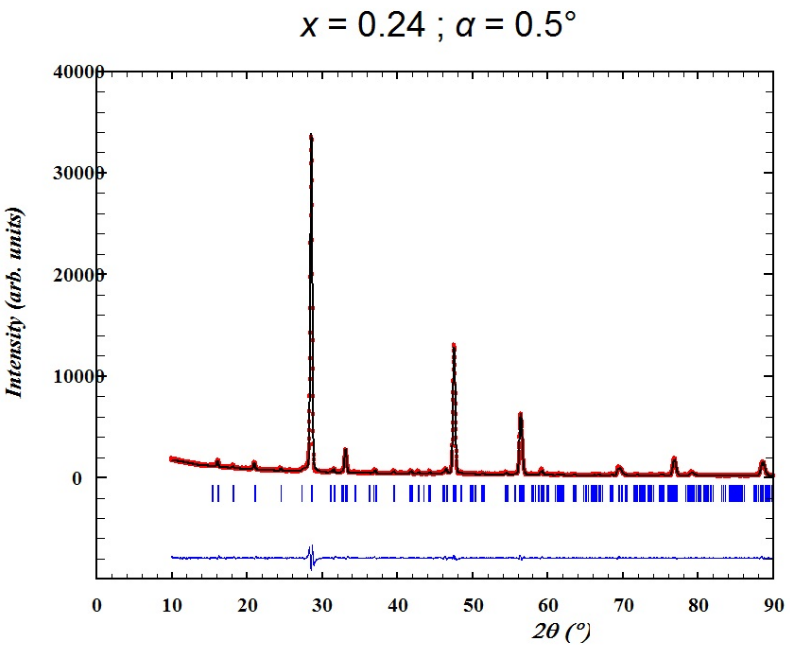

Figure 8.5:

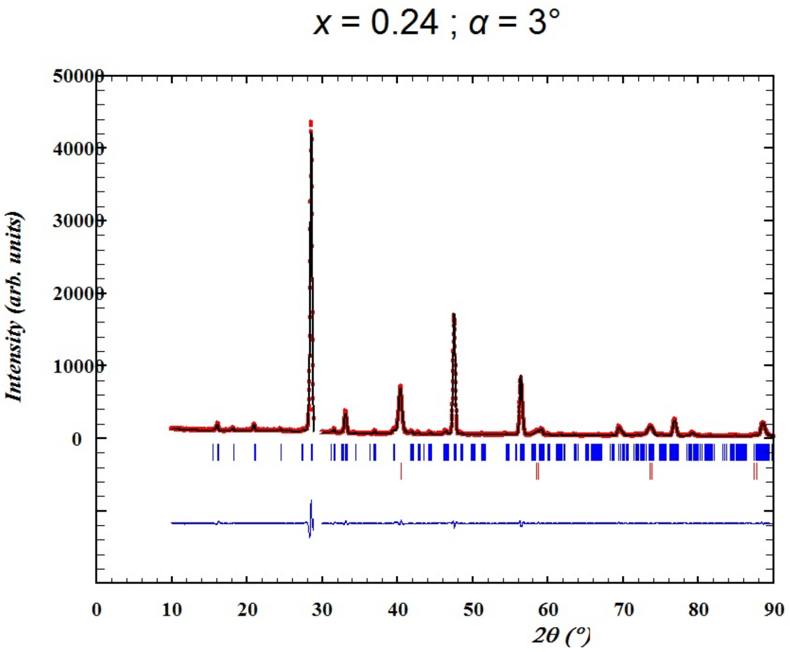

Figure 8.6:

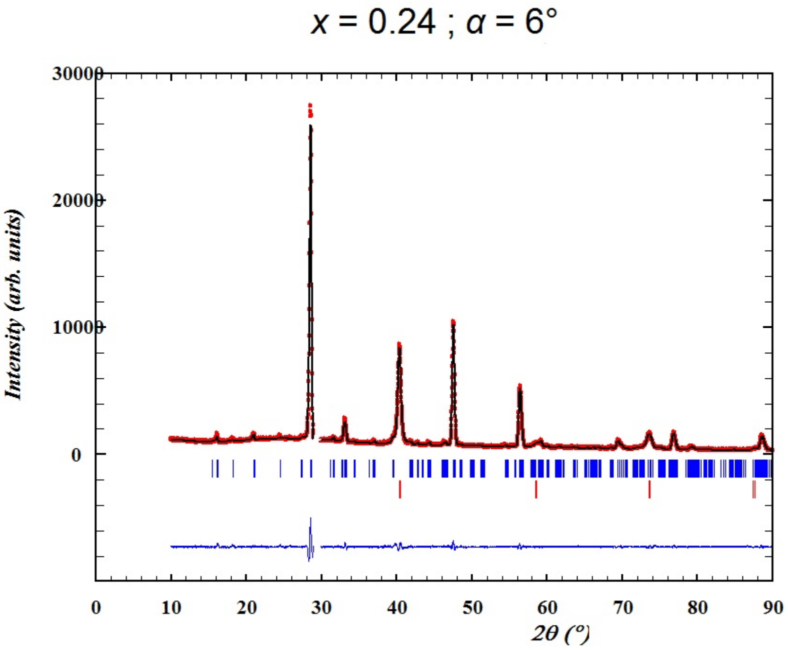

Figure 8.7:

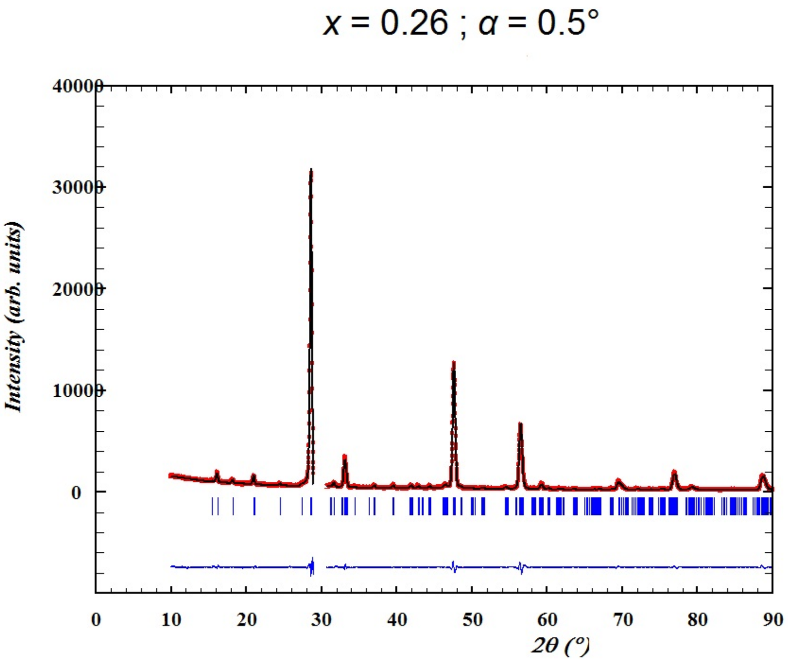

Figure 8.8:

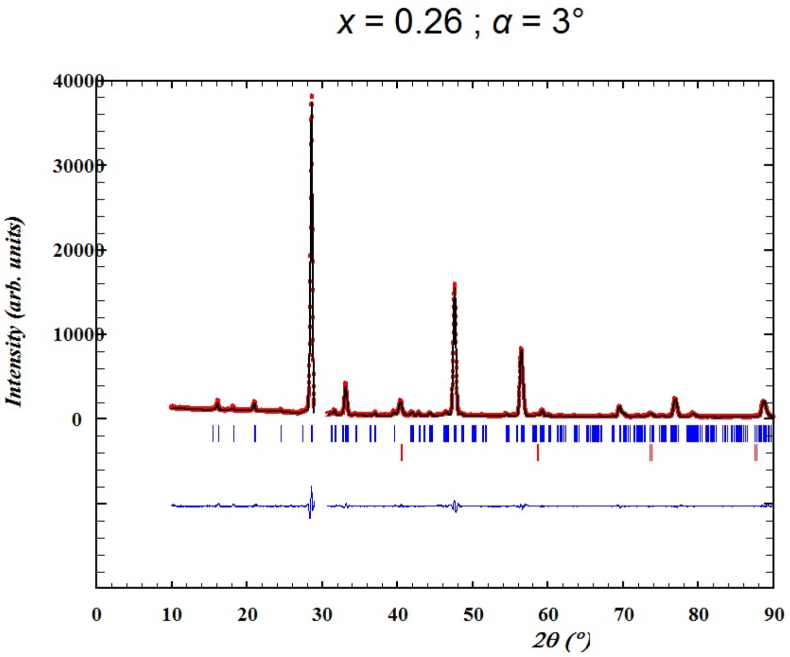

$x = 0.26$; $\alpha = 3°$

Figure 8.9:

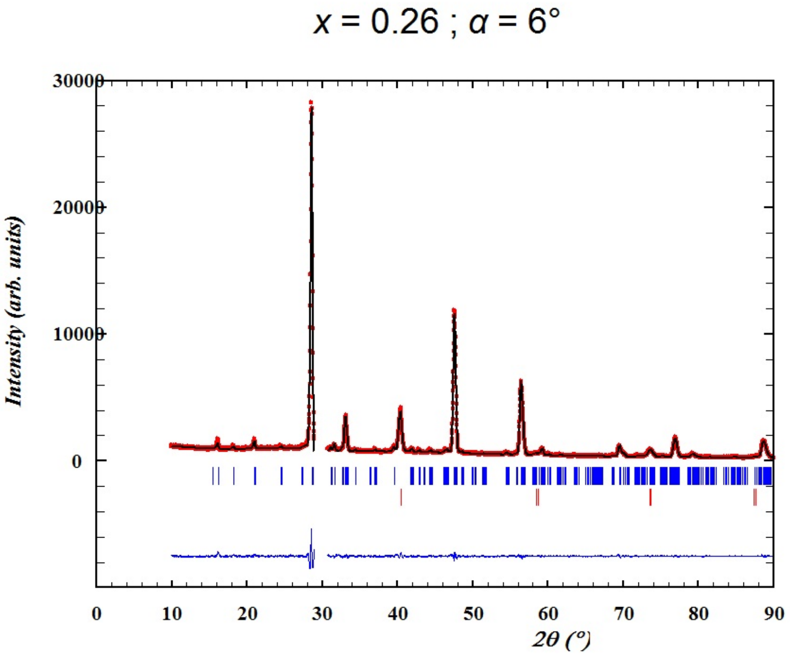

$x = 0.26$; $\alpha = 6°$

Figure 8.10:

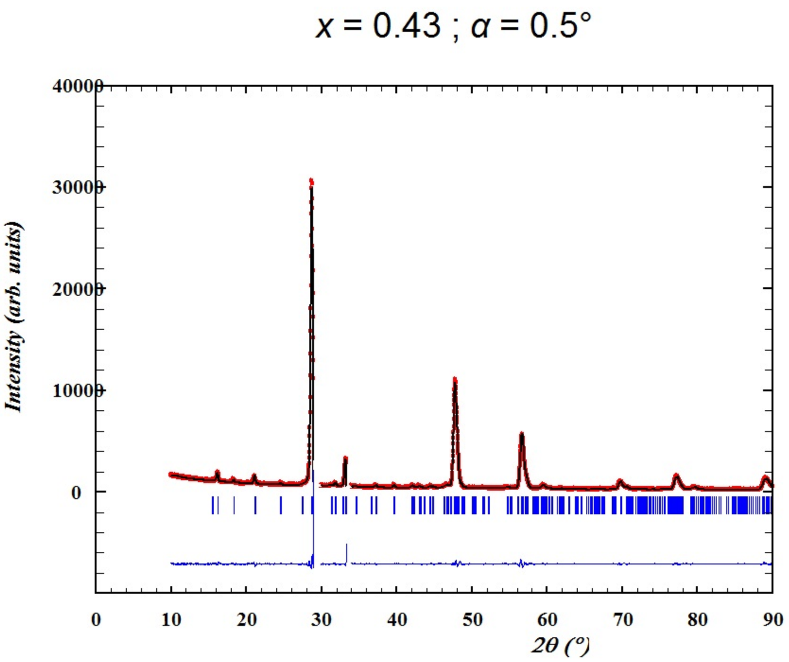

Figure 8.11:

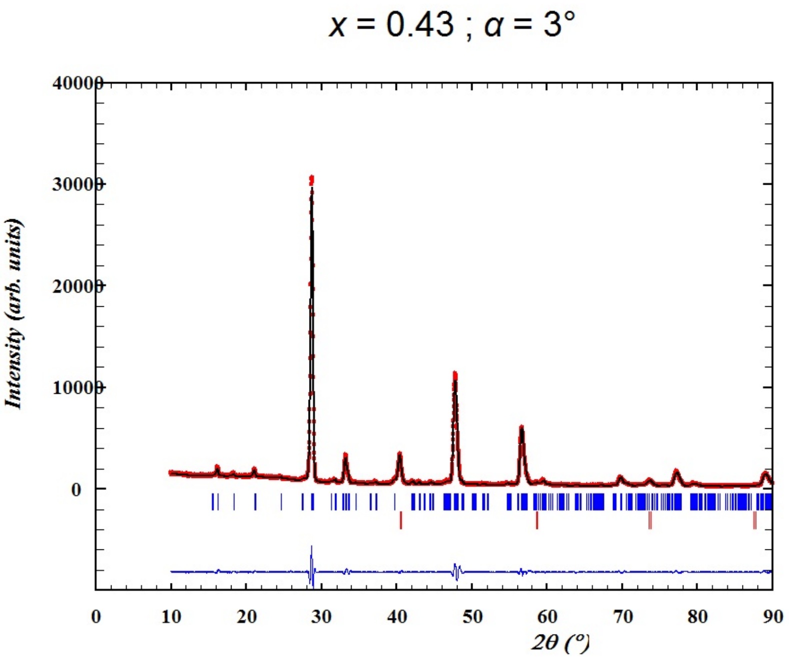

Figure 8.12:

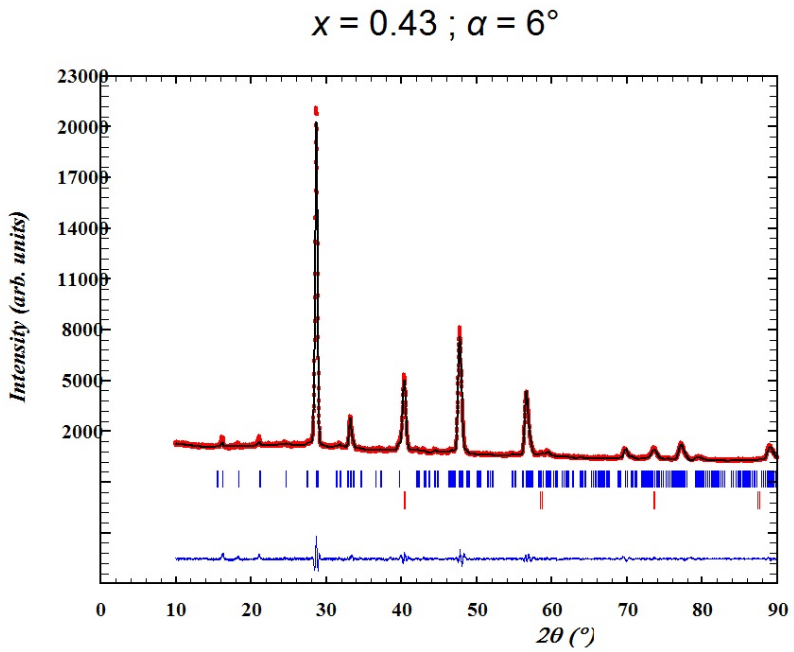

Figure 8.13:

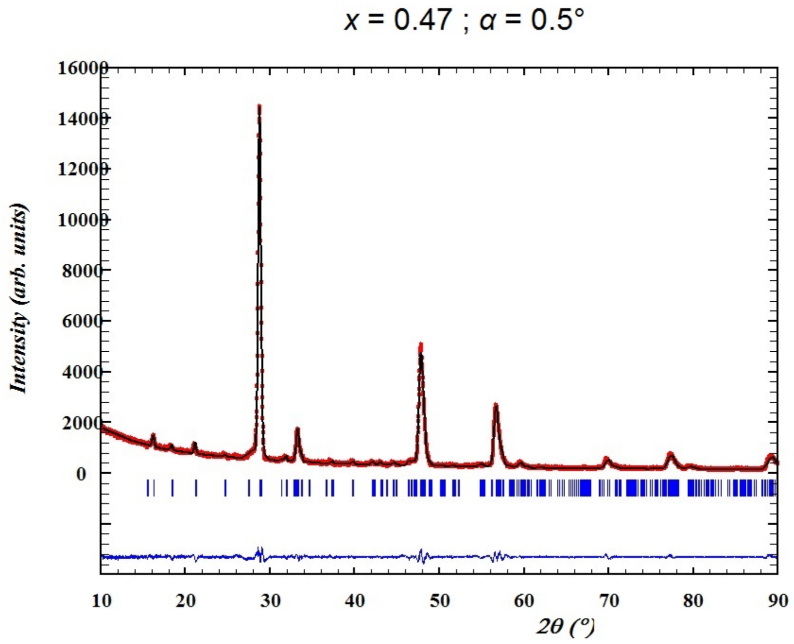

Figure 8.14:

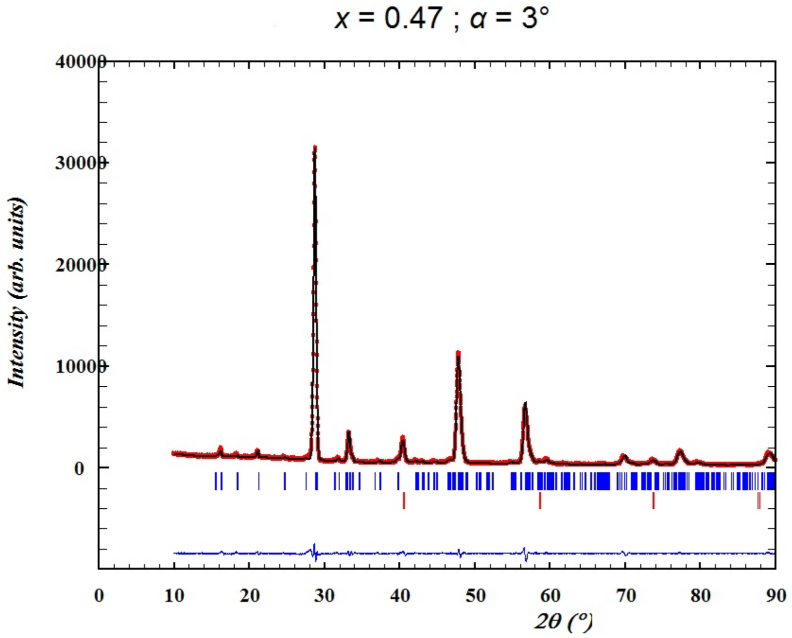

Figure 8.15:

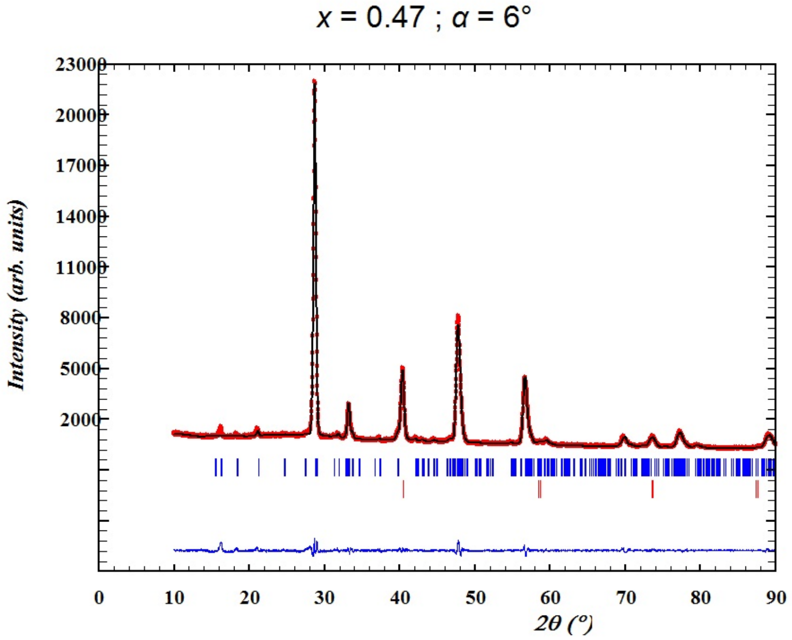

Figure 8.16:

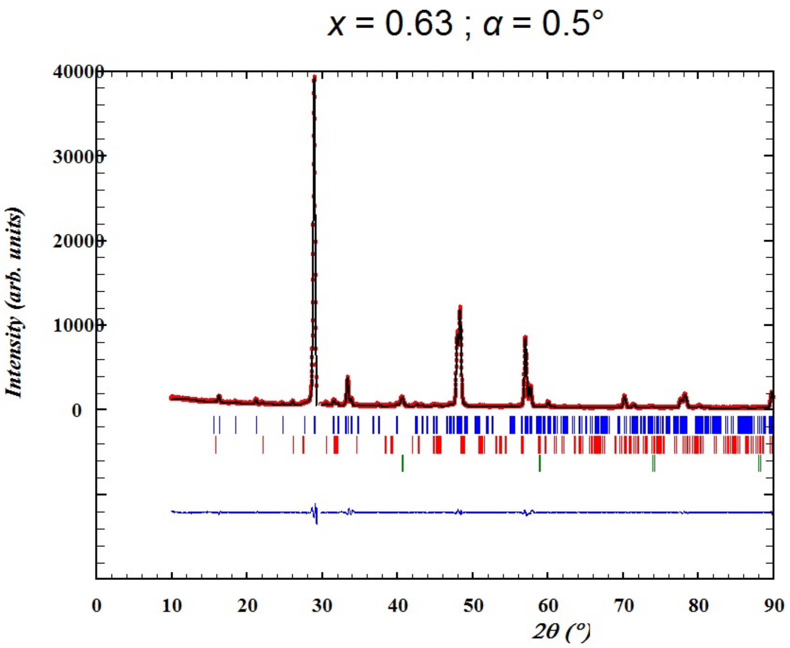

Figure 8.17:

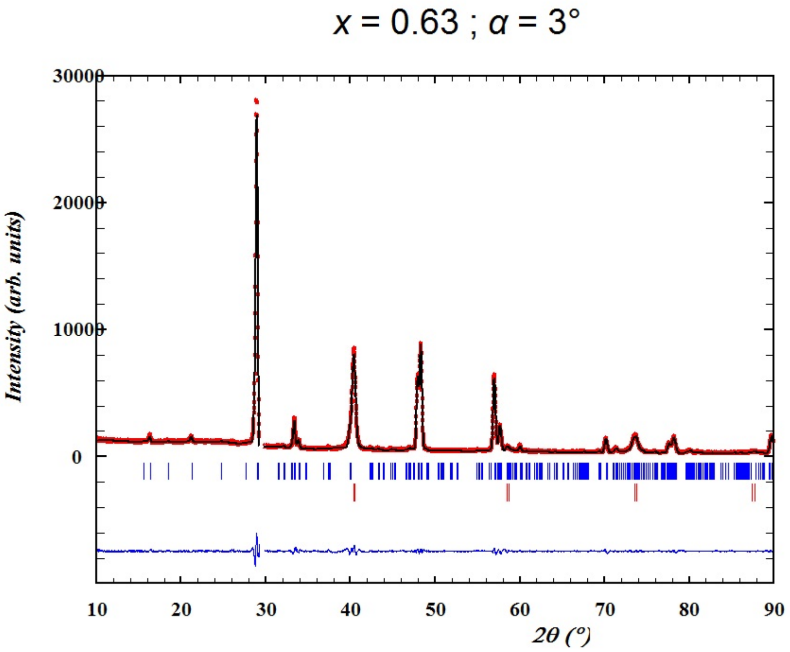

Figure 8.18:

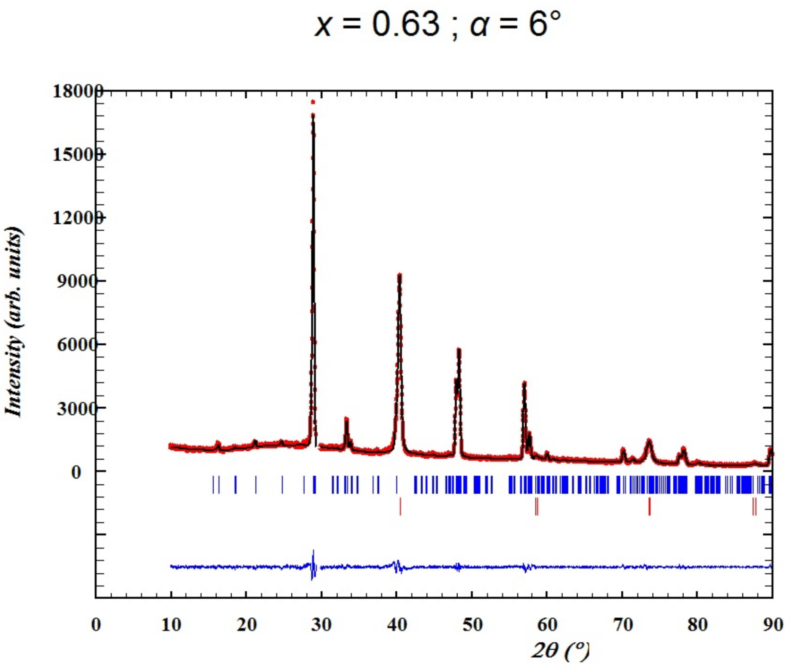

Figure 8.19:

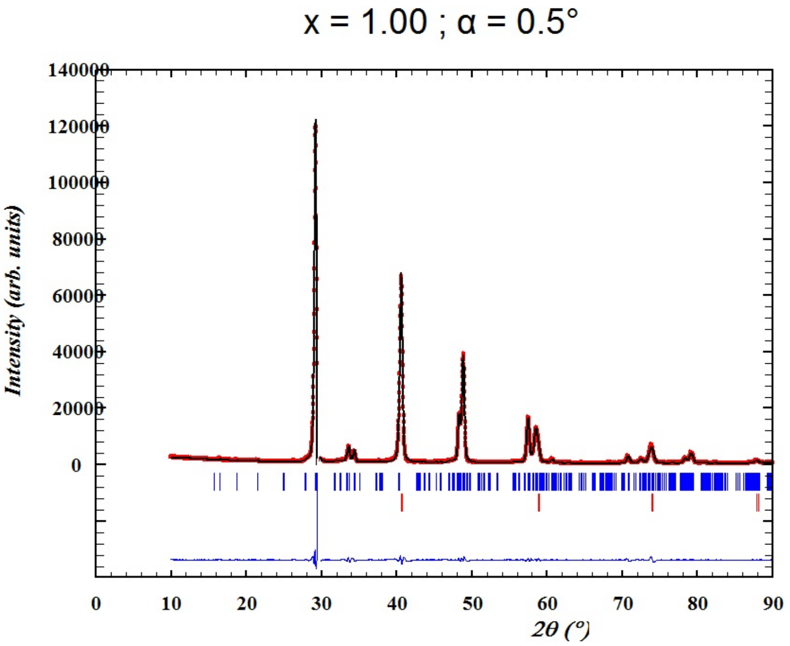

Figure 8.20:

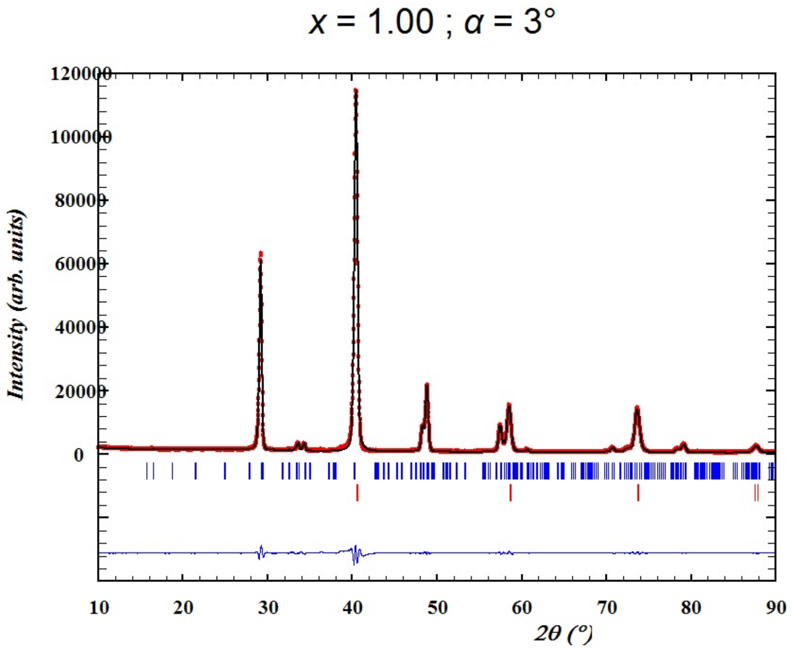

Figure 8.21:

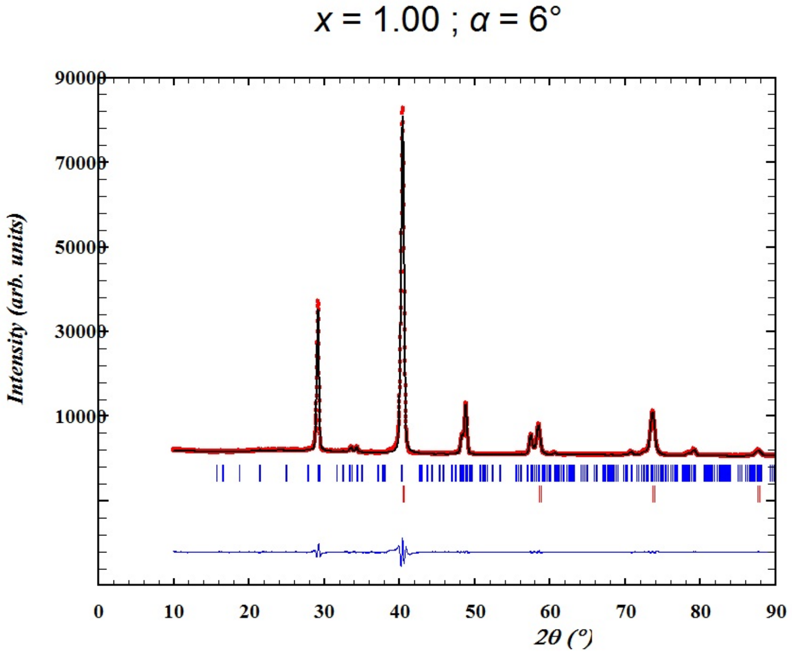

Figure 8.22:

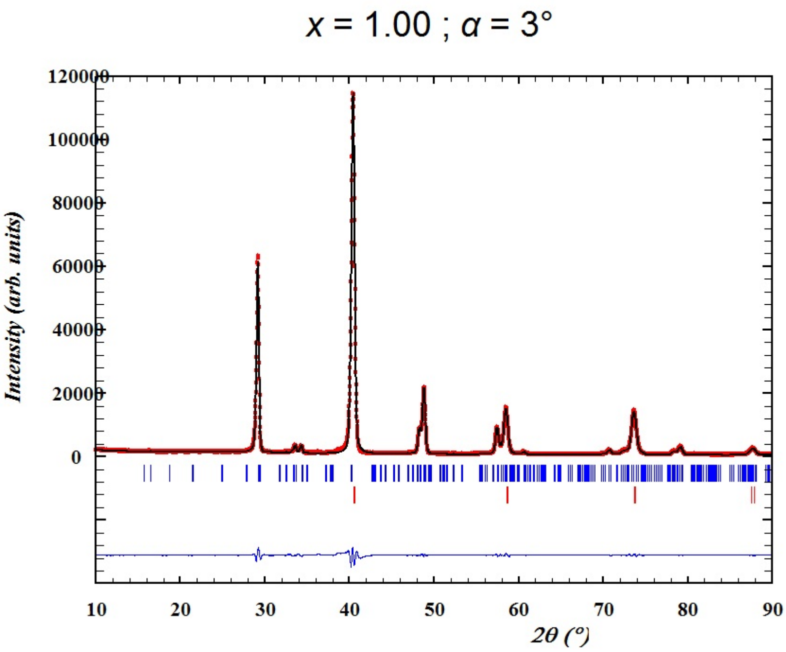

Figure 8.23:

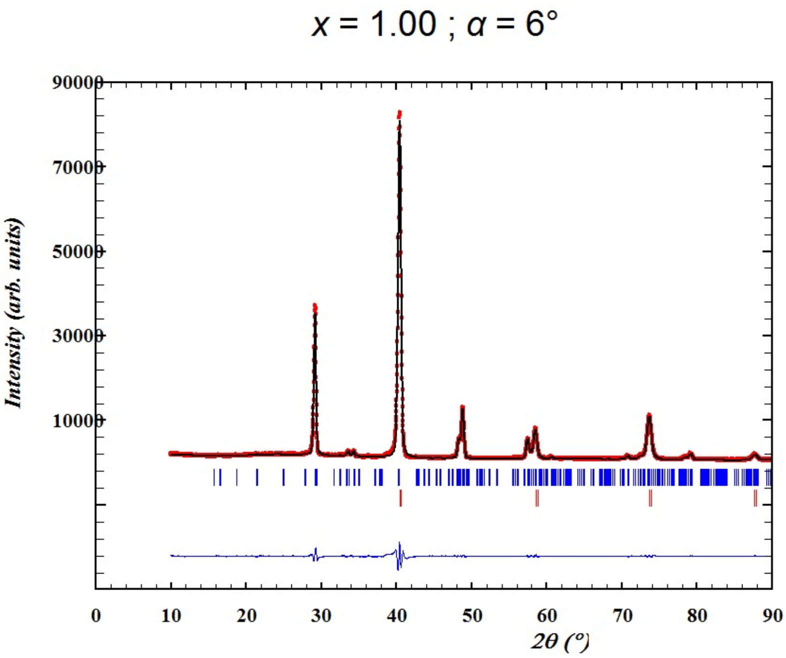

Figure 8.24:

Bibliography

[1] BP Global. BP statistical review of world energy, 2017.

[2] U.S. Energy Information Administration. International energy outlook 2016. Technical report, U.S. Energy Information Administration, 2016.

[3] S. Saomoto. World's highest conversion efficiency of 26.33% achieved in a crystalline silicon solar cell a world first in a practical cell size. http://www.nedo.go.jp/english/news/AA5en_100109.html, September 2016.

[4] V. Fthenakis. Sustainability of photovoltaics: the case for thin-film solar cells. *Renewable and Sustainable Energy Reviews*, 13(9):2746–2750, 2009.

[5] L. M. Peter. Towards sustainable photovoltaics: the search for new materials. *Philosophical Transactions of the Royal Society a-Mathematical Physical and Engineering Sciences*, 369(1942):1840–1856, 2011. Peter, L. M.

[6] M. Osborne. ZSW achieves world record CIGS lab cell efficiency of 22.6%. https://www.pv-tech.org/news/zsw-achieves-world-record-cigs-lab-cell-efficiency-of-22.6, June 2016.

[7] M. Hutchins. Solar frontier hits new thin film cell efficiency record. https://www.pv-magazine.com/2017/12/20/solar-frontier-hits-new-thin-film-cell-efficiency-record/, December 2017.

[8] A. Feltrin and A. Freundlich. Material considerations for terawatt level deployment of photovoltaics. *Renewable Energy*, 33(2):180–185, 2008.

[9] as referenced from Wikipedia WebElements. Abundance in earth's crust. www.webelements.com.

[10] InfoMine. Investment mine. www.infomine.com.

[11] Les Echos. Investir. https://investir.lesechos.fr/marches/matieres-premieres/.

[12] U.S. Department of the Interior. USGS. https://minerals.usgs.gov/minerals/pubs/commodity/selenium/, 2017.

[13] C. H. L. Goodman. The prediction of semiconducting properties in inorganic compounds. *Journal of Physics and Chemistry of Solids*, 6(4):305 – 314, 1958.

[14] E. Parthé. *Crystal chemistry of tetrahedral structures*. CRC Press, 1964.

[15] B. Walker. PV education. http://www.pveducation.org/es/fotovoltaica/czts.

[16] K. Ito. *An overview of CZTS-based thin-film solar cells*, pages 1–41. John Wiley & Sons Ltd, 2014.

[17] W. Wang, M. T. Winkler, O. Gunawan, T. Gokmen, T. K. Todorov, Y. Zhu, and D. B. Mitzi. Device characteristics of CZTSSe thin-film solar cells with 12.6% efficiency. *Advanced Energy Materials*, 4(7):1301465, 2014.

[18] S. Siebentritt and S. Schorr. Kesterites: a challenging material for solar cells. *Progress in Photovoltaics: Research and Applications*, 20(5):512–519, 2012.

[19] S. Bourdais, C. Choné, B. Delatouche, A. Jacob, G. Larramona, C. Moisan, A. Lafond, F. Donatini, G. Rey, S. Siebentritt, A. Walsh, and G. Dennler. Is the Cu/Zn disorder the main culprit for the voltage deficit in Kesterite solar cells? *Advanced Energy Materials*, 6(12):1502276, 2016.

[20] S. K. Wallace, D. B. Wallace, and A. Walsh. The steady rise of kesterite solar cells. *ACS Energy Letters*, 2(4):776–779, 2017.

[21] L. L. Baranowski, P. Zawadzki, S. Christensen, D. Nordlund, S. Lany, A. C. Tamboli, L. Gedvilas, D. S. Ginley, W. Tumas, E. S. Toberer, and A. Zakutayev. Control of doping in Cu_2SnS_3 through defects and alloying. *Chemistry of Materials*, 26(17):4951–4959, 2014.

[22] K. Chino, J. Koike, S. Eguchi, H. Araki, R. Nakamura, K. Jimbo, and H. Katagiri. Preparation of Cu_2SnS_3 thin films by sulfurization of Cu/Sn stacked precursors. *Japanese Journal of Applied Physics*, 51(10), 2012.

[23] D. M. Berg, R. Djemour, L. Guetay, G. Zoppi, S. Siebentritt, and P. J. Dale. Thin film solar cells based on the ternary compound Cu_2SnS_3. *Thin Solid Films*, 520(19):6291–6294, 2012.

[24] W. Shockley and H. J. Queisser. Detailed balance limit of efficiency of p-n junction solar cells. *Journal of Applied Physics*, 32(3):510–519, 1961.

[25] S. Siebentritt. What limits the efficiency of chalcopyrite solar cells? *Solar Energy Materials and Solar Cells*, 95(6):1471–1476, 2011.

[26] J. Koike, K. Chino, N. Aihara, H. Araki, R. Nakamura, K. Jimbo, and H. Katagiri. Cu_2SnS_3 thin-film solar cells from electroplated precursors. *Japanese Journal of Applied Physics*, 51(10), 2012.

[27] D. Abou-Ras, S. Wagner, B. J. Stanbery, H.-W. Schock, R. Scheer, L. Stolt, D. Siebentritt, S.and Lincot, C. Eberspacher, K. Kushiya, and A. N. Tiwari. Innovation highway: breakthrough milestones and key developments in chalcopyrite photovoltaics from a retrospective viewpoint. *Thin Solid Films*, 633(Supplement C):2 – 12, 2017.

[28] J. J. Scragg, J. T. Wätjen, M. Edoff, T. Ericson, T. Kubart, and C. Platzer-Björkman. A detrimental reaction at the molybdenum back contact in $Cu_2ZnSn(S,Se)_4$ thin-film solar cells. *Journal of the American Chemical Society*, 134(47):19330–19333, 2012.

[29] M. Umehara, Y. Takeda, T. Motohiro, T. Sakai, H. Awano, and R. Maekawa. $Cu_2Sn_{1-x}Ge_xS_3$ ($x = 0.17$) thin-film solar cells with high conversion efficiency of 6.0%. *Applied Physics Express*, 6(4), 2013.

[30] D. M. Berg, R. Djemour, L. Guetay, S. Siebentritt, P. J. Dale, X. Fontane, V. Izquierdo-Roca, and A. Perez-Rodriguez. Raman analysis of monoclinic Cu_2SnS_3 thin films. *Applied Physics Letters*, 100(19), 2012.

[31] M. Nakashima, J. Fujimoto, T. Yamaguchi, and M. Izaki. Cu_2SnS_3 thin-film solar cells fabricated by sulfurization from NaF/Cu/Sn stacked precursor. *Applied Physics Express*, 8(4), 2015.

[32] H. Dahman, S. Rabaoui, A. Alyamani, and L. El Mir. Structural, morphological and optical properties of Cu_2SnS_3 thin film synthesized by spin coating technique. *Vacuum*, 101:208–211, 2014.

[33] P. A. Fernandes, P. M. P. Salome, and A. F. da Cunha. Cu_xSnS_{x+1} (x = 2, 3) thin films grown by sulfurization of metallic precursors deposited by DC magnetron sputtering. *Physica Status Solidi C*, 7(3-4):901–904, 2010.

[34] C. Wu, Z. Hu, C. Wang, H. Sheng, J. Yang, and Y. Xie. Hexagonal Cu_2SnS_3 with metallic character: another category of conducting sulfides. *Applied Physics Letters*, 91(14), 2007.

[35] P. A. Fernandes, P. M. P. Salome, and A. F. da Cunha. A study of ternary Cu_2SnS_3 and Cu_3SnS_4 thin films prepared by sulfurizing stacked metal precursors. *Journal of Physics D*, 43(21), 2010.

[36] G. Marcano and L. Nieves. Temperature dependence of the fundamental absorption edge in Cu_2GeSe_3. *Journal of Applied Physics*, 87(3):1284–1286, 2000.

[37] B. K. Sarkar, A. S. Verma, and P. S. Deviprasad. Temperature induced band gap shrinkage in Cu_2GeSe_3: role of electron-phonon interaction. *Physica B-Condensed Matter*, 406(14):2847–2850, 2011.

[38] A. Shigemi, T. Maeda, and T. Wada. First-principles calculation of Cu_2SnS_3 and related compounds. *Physica Status Solidi B-Basic Solid State Physics*, 252(6):1230–1234, 2015.

[39] Y. Hirate, H. Tampo, S. Minoura, H. Kadowaki, A. Nakane, K. M. Kim, H. Shibata, S. Niki, and H. Fujiwara. Dielectric functions of $Cu_2ZnSnSe_4$ and Cu_2SnSe_3 semiconductors. *Journal of Applied Physics*, 117(1), 2015.

[40] K. M. Kim, S. Kim, H. Tampo, H. Shibata, K. Matsubara, and S. Niki. Narrow-bandgap $Cu_2Sn_{1-x}Ge_xSe_3$ thin film solar cells. *Materials Letters*, 158:205–207, 2015.

[41] Z. Tang, K. Aoyagi, Y. Nukui, K. Kosaka, H. Uegaki, J. Chatana, D. Hironiwa, and T. Minemoto. Reaction path for formation of Cu_2SnSe_3 film by selenization of Cu- Sn precursor. *Solar Energy Materials and Solar Cells*, 143:311–318, 2015.

[42] J. Goldstein, D. E. Newbury, D. C. Joy, C. E. Lyman, P. Echlin, E. Lifshin, L. Sawyer, and J. R. Michael. *Scanning electron microscopy and X-ray microanalysis*. Springer US, 2003.

[43] U. Rau, D. Abou-Ras, and T. Kirchartz, editors. *Advanced characterization techniques for thin film solar cells*. Wiley-VCH, 2011.

[44] D. Drouin, A. R. Couture, D. Joly, X. Tastet, V. Aimez, and R. Gauvin. Casino v2.42- a fast and easy-to-use modeling tool for scanning electron microscopy and microanalysis users. *Scanning*, 29(3):92–101, 2007.

[45] R. E Dinnebier. *Powder diffraction*. The Royal Society of Chemistry, 2008.

[46] H. Ibach and H. Lüth. *Festkörperphysik. Eine Einführung in die Grundlagen. 7. Auflage*, volume 62. Springer Verlag, 2008.

[47] edited by Dr. Kabekkodu S. ICDD (2016). PDF-4+ 2016 (database).

[48] J. Rodriguez-Carvajal. Introduction to the program FULLPROF: refinement of crystal and magnetic structures from powder and single crystal data. -, 2014.

[49] R. A. Young. *The Rietveld method*. Oxford Science Publications, 1995.

[50] A. Le Bail. Whole powder pattern decomposition methods and applications: a retrospection. *Powder Diffr.*, 20(4):316–326, 2005.

[51] H. Araki, M. Yamano, G. Nishida, A. Takeuchi, N. Aihara, and K. Tanaka. Synthesis and characterization of $Cu_2Sn_{1-x}Ge_xS_3$. *Phys. Status Solidi C*, 14:1610–1642, 2017.

[52] P. Würfel and W. Ruppel. The chemical potential of luminescent radiation. *Journal of Luminescence*, 24:925–928, 1981.

[53] J. de Wild, E. Kalesaki, L. Wirtz, and P. J. Dale. Valence band splitting in $Cu_2(Sn,Ge,Si)S_3$: Effect on optical absorption spectra. *Phys. Status Solidi RRL*, 11(2):1862–6270, 2017.

[54] J. de Wild, E.V.C Robert, B. El Adib, D. Abou-Ras, and P. J Dale. Secondary phase formation during monoclinic Cu_2SnS_3 growth for solar cell application. *Solar Energy Materials and Solar Cells*, 157(Supplement C):259 – 265, 2016.

[55] S. Siebentritt, G. Rey, A. Finger, D. Regesch, J. Sendler, T. P. Weiss, and T. Bertram. What is the bandgap of kesterite? *Solar Energy Materials and Solar Cells*, 158(2):126–129, 2015.

[56] P. A. Barnes. Capacitance-voltage (C-V) characterization of semiconductors. *Characterization of materials*, pages 1–11, 2002.

[57] S. J. Fonash. *Solar cell device physics (second edition)*. Academic Press, 2010.

[58] W. W. Gärtner. Depletion-layer photoeffects in semiconductors. *Phys. Rev.*, 116(1):84–87, 1959.

[59] D. Colombara, E. V. C. Robert, A. Crossay, A. Taylor, M. Guennou, M. Arasimowicz, J. C. B. Malaquias, R. Djemour, and P. J. Dale. Quantification of surface ZnSe in $Cu_2ZnSnSe_4$-based solar cells by analysis of the spectral response. *Solar Energy Materials and Solar Cells*, 123:220–227, 2014.

[60] D. Colombara, A. Crossay, L. Vauche, S. Jaime, M. Arasimowicz, P.-P. Grand, and P. J. Dale. Electrodeposition of kesterite thin films for photovoltaic applications: Quo vadis? *Physica Status Solidi A*, 212(1):88–102, 2015.

[61] Y. D. Gamburg and G. Zangari. *Theory and practice of metal electrodeposition*. Springer, New York, NY, 2011.

[62] C. G. Fink and V. M. Dokras. Electrodeposition and electrowinning of germanium. *J. Electrochem. Soc.*, 1949.

[63] J. C. Malaquias, M. Wu, L Lin, E. V. C. Robert, J. Sniekers, K. Binnemans, P. J. Dale, and J. Fransaer. Electrodeposition of germanium-containing precursors for $Cu_2(Sn, Ge)S_3$ thin film solar cells. *Electrochimica Acta*, pages –, 2017.

[64] K. N. Tu. Interdiffusion and reaction in bimetallic Cu-Sn thin films. *Acta Metallurgica*, 21(4):347 – 354, 1973.

[65] M. Date, K. Tu, T. Shoji, M. Fujiyoshi, and K. Sato. Interfacial reactions and impact reliability of Sn Zn solder joints on Cu or electroless Au/Ni(P) bond-pads. *Journal of Materials Research*, 19(10):2887–2896, 2004.

[66] R. W. Cahn. *Binary alloy phase diagrams, Second edition.*, volume 3. ASM International, 1990.

[67] R. Schurr, A. Hoelzing, and R. Hock. Real-time investigations on the formation reactions during annealing of sulfurized Cu-Sn precursors. *Thin Solid Films*, 519(21):7412–7415, 2011.

[68] F. M. D'heurle and J. Gupta. Phase formations in the copper-germanium system: reactions, structures and resistivities. *Applied Surface Science*, 73:214 – 224, 1993.

[69] R. W. Olesinski and G. J. Abbaschian. The Cu-Ge (Copper-Germanium) system. *Bulletin of Alloy Phase Diagrams*, 7(1):28–35, Feb 1986.

[70] R. W. Olesinski and G. J. Abbaschian. The Ge-Sn system (Germanium-Tin) system. *Bulletin of Alloy Phase Diagrams*, 5(3), 1984.

[71] E.V.C Robert, J. de Wild, and P. J. Dale. Reaction chemistry of group IV copper chalcogenide semiconductors. *J Alloys Compd*, 2016.

[72] S. Fiechter, M. Martinez, G. Schmidt, W. Henrion, and Y. Tomm. Phase relations and optical properties of semiconducting ternary sulfides in the system Cu-Sn-S. *Journal of Physics and Chemistry of Solids*, 64(9-10):1859–1862, 2003.

[73] I. D. Olekseyuk, I. V. Dudchak, and L. Piskach. Phase equilibria in the $Cu_2S-ZnS-SnS_2$ system. *Journal of Alloys and Compounds*, 368(1):135 – 143, 2004.

[74] P. Zawadzki, L. L. Baranowski, H. Peng, E. S. Toberer, D. S. Ginley, W. Tumas, A. Zakutayev, and S. Lany. Evaluation of photovoltaic materials within the Cu-Sn-S family. *Appl. Phys. Lett.*, 103(25), 2013.

[75] V. Tomashik, Lebrun N., and P. Perrot. *Landolt-Börnstein - group IV physical chemistry (Non-ferrous metal systems. Part 1)*, volume 11C1, chapter Cu-Se-Sn (Copper-Selenium-Tin), pages 1–13. Springer Berlin Heidelberg, 2006.

[76] M. Khanafer, J. Rivet, and J. Flahaut. Etude du composé Cu_2S-GeS_2. surstructure du composé Cu_2GeS_3. transition de phase de Cu_8GeS_6. *Bulletin de la Société Chimique de France*, 1973.

[77] D.J. Chakrabarti and D.E Laughlin. The Cu-S (copper-sulfur) system. *Bulletin of Alloy Phase Diagrams*, 4(3), 1983.

[78] S. K. Maji, N. Mukherjee, A. K. Dutta, D. N. Srivastava, P. Paul, B. Karmakar, A. Mondal, and B. Adhikary. Deposition of nanocrystalline CuS thin film from a single precursor: structural, optical and electrical properties. *Materials Chemistry and Physics*, 130(1):392 – 397, 2011.

[79] Nathanaelle Schneider, Daniel Lincot, and Frederique Donsanti. Atomic layer deposition of copper sulfide thin films. *Thin Solid Films*, 600(Supplement C):103 – 108, 2016.

[80] M. Chen, J. Zhao, and X. Zhao. Scanning electrochemical microscopy studies of micropatterned copper sulfide (Cu_xS) thin films fabricated by a wet chemistry method. *Electrochim Acta*, 56(14-7):5016–5021, 2011.

[81] L. Isac, I. Popovici, A. Enesca, and A. Duta. Copper sulfide (Cu_xS) thin films as possible p-type absorbers in 3D solar cells. *Energy Procedia*, 2(1):71–78, 2010.

[82] I. Grozdanov and M. Najdoski. Optical and electrical properties of copper sulfide films of variable composition. *Journal of Solid State Chemistry*, 114(2):469 – 475, 1995.

[83] Joseph N. Gray and Roy Clarke. Superlattice ordering in digenite, $Cu_{2-x}S$. *Phys. Rev. B*, 1986.

[84] R. C. Sharma and Y. A. Chang. The S-Sn (Sulfur-Tin) system. *Bulletin of Alloy Phase Diagrams*, 7(3):269–273, 1986.

[85] M. Steichen, R. Djemour, L. Guetay, J. Guillot, S. Siebentritt, and P. J. Dale. Direct synthesis of single-phase p-type SnS by electrodeposition from a dicyanamide ionic liquid at high temperature for thin film solar cells. *The Journal of Physical Chemistry C*, 117(9):4383–4393, 2013.

[86] S. Banu, S. J. Ahn, Y. J. Eo, J. Gwak, and A. Cho. Tin monosulfide (SnS) thin films grown by liquid-phase deposition. *Solar Energy*, 145:33 – 41, 2017.

[87] M.S. Mahdi, K. Ibrahim, A. Hmood, N. M. Ahmed, and F. I. Mustafa. Control of phase, structural and optical properties of tin sulfide nanostructured thin films grown via chemical bath deposition. *Journal of Electronic Materials*, 46(7):42274235, 2017.

[88] C. H. Liu, A.S. Pashinkin, and A.V. Novoselova. -. *Dokl. Akad. Nauk SSSR*, 151(6):1335–1338, 1963.

[89] L. Makinistian and E. A. Albanesi. First-principles calculations of the band gap and optical properties of germanium sulfide. *Phys. Rev. B*, 2006.

[90] B. Predel. *Ge-S (Germanium-Sulfur)*, pages 1–2. Springer Berlin Heidelberg, Berlin, Heidelberg, 1996.

[91] D.J. Chakrabarti and D.E Laughlin. The Cu-Se (copper-selenium) system. *Bulletin of Alloy Phase Diagrams*, 2(305-314), 1983.

[92] A. N. Kogut, A. I. Mel'nik, A. G. Mikolaichuk, and B. M. Romanishin. Structure and electrical properties of thin films of copper selenide. *Soviet Physics Journal*, 16(8):1113–1116, Aug 1973.

[93] A. B. M. O. Islam Al-Mamun and A. H. Bhuiyan. Structural, electrical and optical properties of copper selenide thin films deposited by chemical bath deposition technique. *Journal of Materials Science: Materials in Electronics*, 16(5):263–268, 2005.

[94] A. Gobeaut, L. Laffont, J. M. Tarascon, L. Parissi, and O. Kerrec. Influence of secondary phases during annealing on re-crystallization of $CuInSe_2$ electrodeposited films. *Thin Solid Films*, 517(15):4436–4442, 2009.

[95] A. Weber. *Wachstum von Dnnschichten des Materialsystems Cu-Zn-Sn-S*. PhD thesis, Friedrich-Alexander-Universitt Erlangen-Nrnberg, 2009.

[96] J. J. Scragg, T. Ericson, T. Kubart, M. Edoff, and C. Platzer-Björkman. Chemical insights into the instability of Cu_2ZnSnS_4 films during annealing. *Chemistry of Materials*, 23(20):4625–4633, 2011.

[97] D. J. Vaughan and J. R. Craig. *Mineral chemistry of metal sulfides*. Cambridge University Press, 1978.

[98] S. P Jain. A thermodynamic study of the germanium sulphides. Master's thesis, Missouri University of Science and Technology, 1960.

[99] A. Olin, B. Nolang, Osadchii E.G., L-O Ohman, and E. Rosen. *Chemical Thermodynamics of Selenium*. Elsevier, 2005.

[100] D. Y. Peng and J. J. Zhao. Representation of the vapour pressures of sulfur. *Journal of Chemical Thermodynamics*, 33(9):1121–1131, 2001. Peng, DY Zhao, JJ.

[101] R. Hultgren, P. D. Desai, D. T. Hawkins, M. Gleiser, K. K. Kelley, and D. D. Wagman. Selected values of thermodynamic properties of the dlements. *American Society for Metals*, 1973.

[102] E-I. Shimazaki and T. Wada. Vapour pressure of germanium monosulfide. *Bulletin of the Chemical Society of Japan*, 29(3):294–296, 1955.

[103] V. Piacente, S. Foglia, and P. Scardala. Sublimation study of the tin sulphides SnS_2, Sn_2S_3 and SnS. *Journal of Alloys and Compounds*, 177(1):17–30, 1991.

[104] F. Zocchi and V. Piacente. Sublimation enthalpy of tin monoselenide. *J Mater Sci Lett.*, 14(4):235–237, 1995.

[105] F. Geiger, C. A. Busse, and R. I. Loehrke. The vapor pressure of indium, silver, gallium, copper, tin, and gold between 0.1 bar and 3.0 bar. *International Journal of Thermophysics*, 8(4):425–436, 1987.

[106] D. Stull. *American Institute of Physics Handbook*, volume Third edition. McGraw-Hill, 1972.

[107] J. Greenberg. *Thermodynamic Basis of Crystal Growth*. Springer, 2014.

[108] B. Brunetti, V. Piacente, and P. Scardala. Study on sulfur vaporization from covellite (CuS) and anilite ($Cu_{1.75}S$). *Journal of Alloys and Compounds*, 206(1):113 – 119, 1994.

[109] H. Rau. Vapour composition and critical constants of selenium. *J. Chem. Thermodynamics*, 6:525–535, 1974.

[110] A. J. Jackson, D. Tianaa, and A. Walsh. A universal chemical potential for sulfur vapours. *Chemical Science*, 2015.

[111] U. Chalapathi, Y. Jayasree, S. Uthanna, and V. S. Raja. Effect of annealing temperature on the properties of spray deposited Cu_2SnS_3 thin films. *Physica Status Solidi A*, 210(11):2384–2390, 2013.

[112] A. Redinger, D. M. Berg, P. J. Dale, and S. Siebentritt. The consequences of kesterite equilibria for efficient solar cells. *Journal of the American Chemical Society*, 133(10):3320–3323, 2011.

[113] J. J. Scragg, P. J. Dale, D. Colombara, and L. M. Peter. Thermodynamic aspects of the synthesis of thin-film materials for solar cells. *Chem Phys Chem*, 13(12):3035–46, 2012.

[114] A. Weber, R. Mainz, and H. W. Schock. On the Sn loss from thin films of the material system Cu-Zn-Sn-S in high vacuum. *Journal of Applied Physics*, 107(1):013516, 2010.

[115] Z. G. Tang, Y. Nukui, K. Kosaka, N. Ashida, H. Uegaki, and T. Minemoto. Reduction of secondary phases in Cu_2SnSe_3 absorbers for solar cell application. *Journal of Alloys and Compounds*, 608:213–219, 2014.

[116] D. M. Berg, M. Arasimowicz, R. Djemour, L. Gütay, S. Siebentritt, S. Schorr, X. Fontané, V. Izquierdo-Roca, A. Pérez-Rodriguez, and P. J. Dale. Discrimination and detection limits of secondary phases in Cu_2ZnSnS_4 using X-ray diffraction and raman spectroscopy. *Thin Solid Films*, 569:113–123, 2014.

[117] P. S Pawar, S. M. Pawar, K. V. Gurav, S. W. Shin, J. Y. Lee, S. S. Kolekar, and J. H. Kim. Effect of annealing atmosphere on the properties of electrochemically deposited Cu_2ZnSnS_4 (CZTS) thin films. *ISRN Renewable Energy*, page 934575, 2011.

[118] D. Wu, H.and Liu, H. Zhang, C. Wei, B. Zeng, J. Shi, and S. Yang. Solvothermal synthesis and optical limiting properties of carbon nanotube-based hybrids containing ternary chalcogenides. *Carbon*, 50(13):4847–4855, 2012.

[119] M. Buffière, G. Brammertz, S. Sahayaraj, M. Batuk, S. Khelifi, D. Mangin, A.-A. El Mel, L. Arzel, J. Hadermann, M. Meuris, and J. Poortmans. KCN chemical etch for interface engineering in $Cu_2ZnSnSe_4$ solar cells. *ACS Applied Materials & Interfaces*, 7(27):14690–14698, 2015.

[120] D. M. Berg, A. Crossay, J. Guillot, V. Izquierdo-Roca, A. Perez-Rodriguez, S. Ahmed, H. Deligianni, S. Siebentritt, and P. J. Dale. Simplified formation process for Cu_2ZnSnS_4-based solar cells. *Thin Solid Films*, 573:148–158, 2014.

[121] D.R Lide. *Handbook of Chemistry and Physics, 89th edition*. 89th edition. CRC Press, 2008.

[122] J. C. Guo, Y. H. Xu, and C. S. Wang. Sulfur-impregnated disordered carbon nanotubes cathode for lithium-sulfur batteries. *Nano Letters*, 11(10):4288–4294, 2011. Guo, Juchen Xu, Yunhua Wang, Chunsheng.

[123] O. Knacke and I. N. Stranski. The mechanism of evaporation. *Progress in Metal Physics*, 6:181–235, 1956.

[124] Y. Qu, G. Zoppi, and N. S. Beattie. Selenization kinetics in $Cu_2ZnSn(S,Se)_4$ solar cells prepared from nanoparticle inks. *Solar Energy Materials and Solar Cells*, 158:130–137, 2016.

[125] E.V.C Robert, J. de Wild, D. Colombara, and P. J. Dale. Crystallographic and optoelectronic properties of the novel thin film absorber Cu_2GeS_3. *Proc. SPIE 9936*, Thin Films for Solar and Energy Technology VIII:993607, 2016.

[126] Y. T. Zhai, S. Chen, J.-H. Yang, H.-J. Xiang, X.-G. Gong, A. Walsh, J. Kang, and S. H. Wei. Structural diversity and electronic properties of Cu_2SnX_3 (X = S, Se): a first-principles investigation. *Phys. Rev. B*, 84(7):075213, 2011.

[127] H. Araki, K. Chino, K. Kimura, N. Aihara, K. Jimbo, and H. Katagiri. Fabrication of Cu_2GeS_3-based thin film solar cells by sulfurization of cu/ge stacked precursors. *Japanese Journal of Applied Physics*, 53(5S1):05FW10, 2014.

[128] I. Tsuji, Y. Shimodaira, H. Kato, H. Kobayashi, and A. Kudo. Novel stannite-type complex sulfide photocatalysts AI2-Zn-AIV-S_4 (AI = Cu and Ag; AIV = Sn and Ge) for hydrogen evolution under visible-light irradiation. *Chemistry of Materials*, 22(4):1402–1409, 2010.

[129] M. T. Htay, T. Mandokoro, H. Seki, T. Sakaizawa, N. Momose, T. Taishi, Y. Hashimoto, and K. Ito. Influence of Ge composition in the $Cu_2Sn_{1-x}Ge_xS_3$ thin-film photovoltaic absorber prepared by sulfurization of laminated metallic precursor. *Sol. Energy Mater Sol. Cells*, 140:312–319, 2015.

[130] P. Ramasamy and J. Kim. Wurtzite Cu_2GeS_3 nanocrystals: phase- and shape-controlled colloidal synthesis. *Chem Asian J*, 10(7):1468–1473, 2015.

[131] H. Hahn, W. Klingen, P. Ness, and H. Schulze. Ternäre Chalkogenide mit Silicium, Germanium und Zinn. *Naturwissenschaften*, 53(1):18–18, 1966.

[132] M. Khanafer, O. Gorochov, and J. Rivet. Etude des proprietes electriques des phases: Cu_2GeS_3, Cu_2SnS_3, Cu_8GeS_6 et Cu_4SnS_4. *Materials Research Bulletin*, 9(11):1543–1552, 1974.

[133] L. M. de Chalbaud, G. D. deDelgado, J. M. Delgado, A. E. Mora, and V. Sagredo. Synthesis and single-crystal structural study of Cu_2GeS_3. *Materials Research Bulletin*, 32(10):1371–1376, 1997.

[134] K. Momma and F. Izumi. VESTA3 for three-dimensional visualization of crystal, volumetric and morphology data. *Journal of Applied Crystallography*, 44(6):1272–1276, 2011.

[135] L. L. Baranowski, K. McLaughlin, P. Zawadzki, S. Lany, A. Norman, H. Hempel, R. Eichberger, T. Unold, E. S. Toberer, and A. Zakutayev. Effects of disorder on carrier transport in Cu_2SnS_3. *Physical Review Applied*, 4(4), 2015.

[136] L. L. Baranowski, P. Zawadzki, S. Lany, E. S. Toberer, and A. Zakutayev. A review of defects and disorder in multinary tetrahedrally bonded semiconductors. *Semiconductor Science and Technology*, 31(12):123004, 2016.

[137] N. Aihara, Y. Matsumoto, and K. Tanaka. Photoluminescence characterization of Cu_2GeS_3 bulk crystals. *Phys. Status Solidi B*, 254(6):1700118, 2017.

[138] Y. Matsumoto, N. Aihara, N. Saito, and K. Tanaka. Growth of Cu_2GeS_3 bulk single crystals by chemical vapor transport with iodine. *Materials Letters*, 194:16–19, 2017.

[139] C. Frisk, C. Platzer-Björkman, J. Olsson, P. Szaniawski, J. T. Wätjen, V. Fjällström, P. Salomé, and M. Edoff. Optimizing Ga-profiles for highly efficient $Cu(In,Ga)Se_2$ thin film solar cells in simple and complex defect models. *Journal of Physics D-Applied Physics*, 47(48):485104, 2014.

[140] E. V. C. Robert, R. Gunder, J. de Wild, C. Spindler, F. Babbe, H. Elanzeery, B. El Adib, R. Treharne, H. P. C. Miranda, L. Wirtz, S. Schorr, and P. J. Dale. Synthesis, theoretical and experimental characterisation of thin film $Cu_2Sn_{1-x}Ge_xS_3$ ternary alloys ($x = 0$ to 1): Homogeneous intermixing of Sn and Ge. *Acta Materialia*, 151:125–136, 2018.

[141] A. Rockett. *The Materials Science of Semiconductors*, chapter Semiconductor alloys, pages 237–287. Springer US, 2008.

[142] F. Neves, J. B. Correia, K. Hanada, L. F. Santos, R. Gunder, and S. Schorr. Structural characterization of Cu_2SnS_3 and $Cu_2(Sn,Ge)S_3$ compounds. *J Alloys Compd*, 682:489–494, 2016.

[143] K. Hamamura, J. Chantana, K. Suzuki, and T. Minemoto. Influence of Cu/(Ge+Sn) composition ratio on photovoltaic performances of $Cu_2Sn_{1-x}Ge_xS_3$ solar cell. *Solar Energy*, 149:341–346, 2017.

[144] S. Sasagawa, A. Yago, A. Kanai, and H. Araki. $Cu_2(Sn_{1-x}Ge_x)S_3$ solar cells prepared via co-evaporation and annealing in germanium sulfide and sulfur vapor. *Phys. Status Solidi C*, 14(6):1600193, 2017.

[145] M. He, Kim J., M.P. Suryawanshi, A.C. Lokhande, Gang M., Ghorpade U.V., Lee D. S., and Kim J. H. Influence of sulfurization temperature on photovoltaic properties of Ge alloyed Cu_2SnS_3 (CTGS) thin film solar cells. *Solar Energy Materials and Solar Cells*, 174(Supplement C):94–101, 2018.

[146] L. M. de Chalbaud, J. M. Delgado, and V. Sagredo. X-ray powder diffraction data and structural characterization of Cu_2GeS_3 and Cu_2SnS_3. In R. D. Tomlinson, A. E. Hill, and R. D. Pilkington, editors, *Ternary and Multinary Compounds*, volume 152, pages 151–154, 1998.

[147] D. Tiwari, T. K. Chaudhuri, and T. Shripathi. Electrical transport in layer-by-layer solution deposited Cu_2SnS_3 films: effect of thickness and annealing temperature. *Applied Surface Science*, 297:158–166, 2014.

[148] X. A. Chen, H. Wada, A. Sato, and M. Mieno. Synthesis, electrical conductivity, and crystal structure of $Cu_4Sn_7S_{16}$ and structure refinement of Cu_2SnS_3. *Journal of Solid State Chemistry*, 139(1):144–151, 1998.

[149] W. Kraus and G. Nolze. Powdercell a program for the representation and manipulation of crystal structures and calculation of the resulting X-ray powder patterns. *Journal of Applied Crystallography*, 29(3):301–303, 1996.

[150] M. Dimitrievska, A. Fairbrother, R. Gunder, G. Gurieva, H. Xie, E. Saucedo, A. Perez-Rodriguez, V. Izquierdo-Roca, and S. Schorr. Role of S and Se atoms on the microstructural properties of kesterite $Cu_2ZnSn(S_xSe_{1-x})_4$ thin film solar cells. *Phys. Chem. Chem. Phys.*, 18(12):8692–8700, 2016.

[151] M. Onoda, X. A. Chen, A. Sato, and H. Wada. Crystal structure and twinning of monoclinic Cu_2SnS_3. *Mat Res Bull*, 35(9):1563–1570, 2000.

[152] J. A. Curcio and C. C. Petty. The near infrared absorption spectrum of liquid water. *Journal of the optical society of America*, 41(5):302–303, 1951.

[153] J. K. Katahara and H. W. Hillhouse. Quasi-fermi level splitting and sub-bandgap absorptivity from semiconductor photoluminescence. *Journal of Applied Physics*, 116(17):173504, 2014.

[154] R. Chen and C. Persson. Exploring the electronic and optical properties of $Cu_2Sn_{1-x}Ge_xS_3$ and $Cu_2Sn_{1-x}Si_xS_3$ (x = 0, 0.5, and 1). *Phys. Stat. Sol. (b)*, 254(6):1921–3951, 2017.

[155] J. M. Skelton, L. A. Burton, A. J. Jackson, F. Oba, S. C. Parker, and A. Walsh. Lattice dynamics of the tin sulphides SnS_2, SnS and Sn_2S_3: vibrational spectra and thermal transport. *Phys. Chem. Chem. Phys.*, 19:12452–12465, 2017.

[156] E. Blanco, P. Afanasiev, B. Berhault, D. Uzio, and S. Loridant. Resonance raman spectroscopy as a probe of the crystallite size of MoS_2 nanoparticles. *Comptes Rendus Chimie*, 19(10):1310 – 1314, 2016.

[157] F. de Wild, J.and Babbe, E.V.C Robert, A. Redinger, and P. J Dale. Silver-doped Cu_2SnS_3 absorber layers for solar cells application. *IEEE Journal of Photo*, 8(1):299–304, 2017.

[158] X. Jin, L. Zhang, G. Jiang, W. Liu, and C. Zhu. High open-circuit voltage of ternary Cu_2GeS_3 thin film solar cells from combustion synthesized Cu-Ge alloy. *Solar Energy Materials and Solar Cells*, 160:319–327, 2017.

[159] P. Würfel. *Physics of solar cells: from basic principles to advanced concepts, 2nd Edition*. Wiley-VCH, 2009.

[160] W. N. Shafarman, S. Siebentritt, and L. Stolt. *Handbook of photovoltaic science and engineering, second edition*, chapter $Cu(InGa)Se_2$ Solar Cells, pages 546–599. John Wiley & Sons, Ltd, 2011.

[161] M. Green. Solar cell fill factors - general graph and empirical expressions. *Solid State Electronics*, 24:788–789, 1981.

[162] J. de Wild, E. Kalesaki, Robert E.V.C, and P. J. Dale. Quantum efficiency measurements and modeling as tools to monitor air annealing of Cu_2SnS_3 solar cells. *IEEE Journal of Photovoltaics*, 7(1):268–272, 2016.

[163] S. S. Hegedus and W. N. Shafarman. Thin-film solar cells: device measurements and analysis. *Progress in Photovoltaics: Research and Applications*, 12(23):155–176, 2004.

[164] D. Avellaneda, M. T. S. Nair, and P. K. Nair. Cu_2SnS_3 and Cu_4SnS_4 thin films via chemical deposition for photovoltaic application. *Journal of The Electrochemical Society*, 157(6):D346–D352, 2010. Times Cited: 18.

[165] S. Dias, B. Murali, and S. B. Krupanidhi. Transport properties of solution processed Cu_2SnS_3/AZnO heterostructure for low cost photovoltaics. *Solar Energy Materials and Solar Cells*, 143:152–158, 2015.

[166] I. Repins, S. Glynn, Duenow J., T.J. Coutts, W. Metzger, and M. A. Contreras. Required material properties for high-efficiency CIGS modules. In *Society of Photographic Instrumentation Engineers (SPIE)*, 2009.

[167] I. Repins, M. Contreras, M. Romero, Y. Yan, W. Metzger, J. Li, S. Johnston, B. Egaas, C. de Hart, and J. Sharf. Characterization of 19.9%-efficient CIGS absorbers. In *IEEE Photovoltaics Specialists Conference*, 2008.

[168] P.A. Fernandes, P. M. P. Salomé, A. F. Sartori, J. Malaquias, A. F. da Cunha, B.-A. Schubert, J. A. Gonzalez, and G. M. Ribeiro. Effects of sulphurization time on Cu_2ZnSnS_4 absorbers and thin films solar cells obtained from metallic precursors. *Solar Energy Materials and Solar Cells*, 115(Supplement C):157 – 165, 2013.

[169] W. K. Metzger, I. L. Repins, and M. A Contreras. Long lifetimes in high-efficiency $Cu(In, Ga)Se_2$ solar cells. *Applied Physics Letters*, 93(2):022110, 2008.

[170] S. Sato, H. Sumi, G. Shi, and M. Sugiyama. Investigation of the sulfurization process of Cu_2SnS_3 thin films and estimation of band offsets of Cu_2SnS_3-related solar cell structure. *Phys. Status Solidi C*, 2015.

[171] D. Tiwari, T. Koehler, R. Klenk, and D. J. Fermin. Solution processed single-phase Cu_2SnS_3 films: structure and photovoltaic performance. *Sustainable Energy & Fuels*, 1(4):899–906, 2017.

[172] M. Umehara, Y. Takeda, K. Oh-ishi, Y. Aoki, T. Motohiro, T. Sakai, and R. Maekawa. Energy level diagram around Ge-rich grain boundaries in $Cu_2Sn_{1-x}Ge_xS_3$ (CTGS) thin-film solar cells. *Solar Energy Materials and Solar Cells*, 134(Supplement C):1 – 4, 2015.

[173] Q. Chen, X. Dou, Y. Ni, S. Cheng, and S. Zhuang. Study and enhance the photovoltaic properties of narrow-bandgap Cu_2SnS_3 solar cell by p-n junction interface modification. *Journal of Colloid and Interface Science*, 376:327–330, 2012.

[174] J. de Wild, E.V.C Robert, and P. J. Dale. Chemical stability of the Cu_2SnS_3/Mo interface. In *IEEE Proceedings*, 2016.

[175] P. Zawadzki, A. Zakutayev, and S. Lany. Entropy-driven clustering in tetrahedrally bonded multinary materials. *Phys. Rev. Applied*, 3(3), 2015.

[176] F. Oliva, L. Arques, L. Acebo, M. Guc, Y. Sanchez, X. Alcobe, A. Perez-Rodriguez, E. Saucedo, and V. Izquierdo-Roca. Characterization of Cu_2SnS_3 polymorphism and its impact on optoelectronic properties. *J. Mater. Chem. A*, 5:23863–23871, 2017.

[177] A. Crovetto, A. Chen, R. B. Ettlinger, A. C. Cazzaniga, J. Schou, C. Persson, and O. Hansen. Dielectric function and double absorption onset of monoclinic Cu_2SnS_3: origin of experimental features explained by first-principles calculations. *Solar Energy Materials and Solar Cells*, 154(Supplement C):121 – 129, 2016.

[178] SCAPS. http://users.elis.ugent.be/ELISgroups/solar/projects/scaps/SCAPSinstallatie.html.

[179] R. Scheer and H.-W. Schock. *Chalcogenide photovoltaics: physics, technologies, and thin film devices*. Wiley-VCH Verlag GmbH & Co. KGaA, 2011.

[180] A. Kanai, K. Toyonaga, K. Chino, H. Katagiri, and H. Araki. Fabrication of Cu_2SnS_3 thin film solar cells with power conversion efficiency over 4%, 2014.

Acronyms and Symbols

Acronyms

AM1.5G	Standard terrestrial solar spectrum 'Air Mass 1.5 Global'
ARC	Anti-Reflection Coating
BSE	Backscattered Electron
CB	Conduction Band
CBM	Conduction Band Minimum
CBD	Chemical Bath Deposition
CE	Counter Electrode
CGS	Cu_2GeS_3
CIS	$CuInSe_2$
CIGS	$CuIn_{1-x}Ga_xSe_2$
CTGS	$Cu_2Sn_{1-x}Ge_xS_3$
CTS	Cu_2SnS_3
CTSe	Cu_2SnSe_3
CZTS	Cu_2ZnSnS_4
ED	Electrodeposition
EDX	Energy Dispersive X-Ray
EQE	External Quantum Efficiency
FF	Fill Factor
FWHM	Full Width at Half Maximum
GI-XRD	Grazing Incidence X-Ray Diffractogram
HZB	Helmholtz Zentrum Berlin

I-V	Current - voltage characteristics
J-V	Current density -voltage characteristics
KCN	Potassium cyanide
LIST	Luxembourg Institute of Science and Technology
OCP	Open Circuit Potential
RE	Reference Electrode
(RT)-PL	(Room Temperature) Photoluminescence
PV	Photovoltaics
PVD	Physical Vapour Deposition
RE	Reference Electrode
SE	Secondary Electron
SEM	Scanning Electron Microscopy
SHE	Standard Hydrogen Electrode
SIMS	Secondary Ion Mass Spectrometry
SLG	Soda-Lime Glass substrate
SQ	Shockley-Queisser Limit
QE	Quantum Efficiency
QFLS	Quasi-Fermi Level Splitting
T-R	Transmission-Reflection measurements
UL	University of Luxembourg
VB	Valence Band
VBM	Valence Band Maximum
WDX	Wavelength Dispersive X-Ray
WE	Working Electrode
XRD	X-Ray Diffraction

Symbols

α	absorption coefficient
a	activity
a	thickness
A	surface area
α	molecular sticking coefficient
c	speed of light, $c = 3 \cdot 10^8$ m/s
$\frac{\mathrm{Cu}}{\mathrm{IV}}$	$\frac{\mathrm{Cu}}{\mathrm{Ge^{+}Sn}}$
d	molecular diameter
D	diffusion coefficient
E	photon energy $h\nu$
$\mathrm{E_F}$	Fermi level
E_G	bandgap energy
ε_0	permittivity of vacuum, $\varepsilon_0 = 8.85 \cdot 10^{12}$ F/m
F	Faraday constant, $F = 96485$ C.mol^{-1}
G	Gibbs free energy
G_f	Gibbs free energy of formation
G^0	standard Gibbs free energy of formation
h	Planck's constant
η	solar cell device efficiency, %
H	enthalpy
K_{eq}	equilibrium constant
k_B	Boltzmann constant, $k_B = 1.38 \times 10^{-23}$ J K^{-1}
IV	group IV atomic species, Sn+Ge
J	current density
J_0	saturation current density
J_d	current density in the dark
J_{ill}	illumination current density

J_{sc}	short-circuit current density
L	distance travelled by the vapour phase starting at the source
L_d	minority carrier diffusion length
λ	wavelength
λ_t	mean free path
M	Cu or group IV metal
M	molar mass
m	molecular weight
m_F	mass electrodeposited according to Faraday's law
n	diode factor
N_A	Avogadro number, $N_A = 6.02 \times 10^{23}$ mol^{-1}
N_A	net acceptor concentration
N_D	net donor concentration
p	vapour pressure
p_{back}	background pressure
P_e	plating efficiency
P_{in}	incident power
p_p	partial pressure
p_t	total pressure
Φ_{gamma}	photon flux
Q	reaction constant
q	elementary charge, $q = 1.6 \times 10^{-19}$ C
R	gas constant $R = 8.31$ JK^{-1} mol^{1}
r_{cov}	covalent radius
r_e	bond length
r_{max}	maximum vapour generation rate
r_{min}	minimum vapour generation rate
r_s	series resistance

r_{SH}	shunt resistance
ρ	density
$\frac{\mathrm{S}}{\mathrm{IV}}$	$\frac{\mathrm{S}}{\mathrm{Ge}^{+}\mathrm{Sn}}$
S	entropy
t	annealing duration
T	temperature
u	atomic mass unit, u = $1.66 \times 10^{-27}\,\mathrm{kg}$
V_{oc}	open-circuit voltage
v_{rms}	root mean square speed
W	space-charge region (or ’depletion’) width
x	$\frac{\mathrm{Ge}}{\mathrm{IV}} = \frac{\mathrm{Ge}}{\mathrm{Ge}^{+}\mathrm{Sn}}$
X	chalcogen source (S or Se)
X	chalcogen source (S or Se)
Z	atomic number